

# $^{57}\text{Fe}$ MÖSSBAUER STUDIES OF THE HYPERFINE INTERACTIONS IN SOME hcp METALS AND DISORDERED BINARY ALLOYS

by

N. V. NAIR

PHY  
981  
D  
NAI  
MQS

TH  
Phy/1981/D  
N 144 f



DEPARTMENT OF PHYSICS

INDIAN INSTITUTE OF TECHNOLOGY KANPUR

NOVEMBER, 1981

# $^{57}\text{Fe}$ MÖSSBAUER STUDIES OF THE HYPERFINE INTERACTIONS IN SOME hcp METALS AND DISORDERED BINARY ALLOYS

A Thesis Submitted  
in Partial Fulfilment of the Requirements  
for the Degree of  
DOCTOR OF PHILOSOPHY

by  
N. V. NAIR

*to the*

DEPARTMENT OF PHYSICS  
INDIAN INSTITUTE OF TECHNOLOGY KANPUR  
NOVEMBER, 1981

DEDICATED TO

MY

WIFE

1942

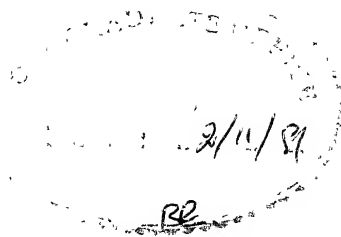
4 JUN 1984

CENTRAL LIBRARY,  
I. I. T., Kanpur.

Acc. No. A 82714

PHY-1981-D-NAI-MOS





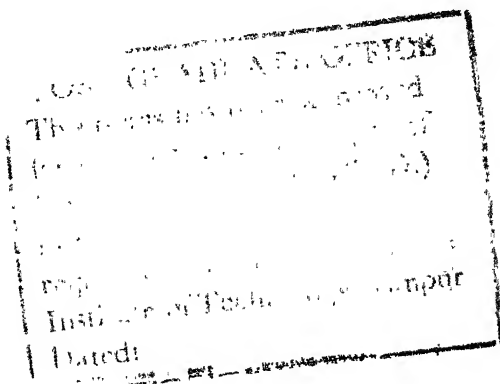
# CERTIFICATE

This is to certify that the work presented in this thesis entitled "<sup>57</sup>Fe Mössbauer studies of the hyperfine interactions in some hcp metals and disordered binary alloys" by N. Vasudevan Nair has been done under my supervision and it has not been submitted elsewhere for a degree or diploma.

*SCKhan*

October 1981

D. C. Khan  
Department of Physics  
Indian Institute of Technology  
Kanpur, India.



### ACKNOWLEDGMENTS

I am deeply grateful to Dr. D.C. Khan for his supervision, encouragement, help and guidance in matters both academic and otherwise through out the course of this work.

I wish to express my sincerest thanks to Professor R.M. Singru for the immense help and encouragement and for the brotherly affection shown to me through out my stay in I.I.T. Kanpur.

I am very thankful to Professor Y.R. Waghmare for his keen interest in the progress of this work and for all those delightful evenings which I could spent with him.

My thanks are due to Professor T.M. Srinivasan, Professor G.K. Mehta and Dr. Sudhir Sen for their kind co-operation and encouragement.

There are no words to express my sincerest thanks to my friends, Dr. Harish Chandra Verma who helped me in innumerable ways in my work and for his active participation in making the computer programmes and Mrs. Veena Joshi who helped me in the XRF measurements.

I take this opportunity to express my deepest sense of gratitude to Professor T.B.K. Menon (Kerala University, Trivandrum) and Professor Radhamma (M.G. College, Trivandrum) for their help, encouragement and support.

I am particularly thankful to Mr. J.S. Sharma of the Physics Workshop who helped me in the fabrication of the cryostat. My thanks are also due to him for the neat tracings

prepared by him for this thesis. My sincere thanks are due to Mrs. Fatima Naqvi, who rendered considerable help in the fabrication and repair of several electronic instruments.

I sincerely thank my friends Dr. J.K. Sharma, Mr. A.K. Sinha, Miss Ratna Mala Roy, Mr. Muddu Krishna, Mr. A.K. Singh, Mr. Akhilesh Prasad, Mr. Atul Sen and all others who helped me willingly in one way or other.

I express my thanks to Mr. L.S. Bajpai for neat typing and Mr. H.K. Panda for cyclostyling this thesis.

Financial assistance from the University Grants Commission, New Delhi (India) in the form of a Teacher Fellowship is gratefully acknowledged.

This work would not have been possible without the emotional support from my mother and brothers and I wish to express my profound regards to them.

Finally I would like to express my deepest appreciation to my wife, Padmini, and my daughters, Malini and Neelima who patiently acquiesced to my staying in I.I.T. Kanpur even if it meant lonely days, months and years.

N. Vasudevan Nair

# LIST OF CONTENTS

	<u>Page</u>
LIST OF TABLES	ix
LIST OF FIGURES	xii
SYNOPSIS	xviii
CHAPTER 1 : FUNDAMENTAL OF MÖSSBAUER SPECTROSCOPY	1
1.1 Introduction	1
1.2 The Mössbauer Effect	1
1.3 Hyperfine Interactions	4
1.3.1 Isomer shift	5
1.3.2 Electric quadrupole interaction	8
1.3.3 Sternheimer antishielding factors	12
1.3.4 Magnetic dipole interaction	13
1.3.5 Relaxation effects in Mössbauer spectroscopy	15
1.3.6 Goldnski-Karyagin effect	20
1.3.7 Asymmetric quadrupole doublet	22
REFERENCES	23
CHAPTER 2 : EXPERIMENTAL	25
2.1 Instruments	25
2.1.1 Electronic equipment	25
2.1.2 Furnace	32
2.1.3 Cryostat	40
2.2 Sources and Absorbers	43

## List of Contents (Continued)

	<u>Page</u>
2.2.1 Sources	43
2.2.2 Standard absorbers for calibration	44
2.2.3 Sample preparation	44
2.2.4 Thickness optimisation	44
2.3 Effect of Geometry	47
2.4 Data Analysis	50
2.4.1 Calibration	50
2.4.2 Computer programmes	50
REFERENCES	53
CHAPTER 3 : <sup>55</sup> MÖSSBAUER STUDIES OF SOME FERROUS COMPLEXES- A NEW LOOK INTO THE OLD SYSTEMS	55
3.1 Introduction	55
3.2 Mössbauer Studies of $\text{FeSO}_4 \cdot 7\text{H}_2\text{O}$ and $\text{Fe}(\text{SO}_4)_2(\text{NH}_4)_2 \cdot 6\text{H}_2\text{O}$ Under Applied Electric Field	55
3.3 Electric Field Gradient and Isomer Shift Distributions from Mössbauer Spectra	63
3.3.1 Introduction	63
3.3.2 Computational methods	65
3.3.3 Results and discussion	67
3.4 Recoilless Fraction	76
REFERENCES	87
CHAPTER 4 :        ELECTRIC FIELD GRADIENT AT IRON IMPURITIES IN hcp METALS	90
4.1 Introduction	90

	<u>Page</u>
4.1.1 The EFG Tensor	90
4.2 Systematic Trends of the EFG's in Metals	92
4.2.1 Correlation between $eq_{ion}$ and $eq_{el}$	92
4.2.2 Dependence of EFG on the Probe Used	95
4.2.3 Dependence of the EFG on Temperature	97
4.3 Theoretical Estimates of EFG's	98
4.3.1 The lattice contribution	98
4.3.2 Electronic contribution	99
4.3.3 Pseudopotential approach and charge screening effects	100
4.3.4 Conduction electron charge shift model of Bodenstein and Perscheid	102
4.4 Quadrupole Interactions at $^{57}\text{Fe}$ in Titanium Metal	108
4.4.1 Introduction	108
4.4.2 Sample preparation	109
4.4.3 Experimental	110
4.4.4 Results and discussion	110
4.4.5 Conclusions	128
4.5 Quadrupole Interactions at $^{57}\text{Fe}$ in trigonal selenium	128
4.5.1 Introduction	128
4.5.2 Crystal structure of hexagonal selenium	130
4.5.3 Sample preparation	130
4.5.4 Results and discussions	132

## List of Contents (Continued)

	<u>Page</u>
4.5.5 Conclusion	141
4.6 Quadrupole Interaction at $^{57}\text{Fe}$ in the hcp Rare-Earth Neodymium as a Dilute Impurity	142
4.6.1 Introduction	142
4.6.2 Sample preparation	143
4.6.3 Results and discussions	143
4.6.4 Some theoretical aspects of EFG in rare earth metals	145
4.6.5 Conclusions	148
4.7 Comparisons	149
REFERENCES	150
CHAPTER 5 : HYPERFINE INTERACTIONS AND PHASE TRANSITIONS IN BINARY IRON ALLOYS	154
5.1 Introduction	154
5.2 Mössbauer Study of the fcc-fct Martensi- tic Transformation in Fe-Pd Alloy	156
5.2.1 Introduction	156
5.2.2 Sample preparation	159
5.2.3 Results and discussions	159
5.2.4 Conclusion	180
5.3 Mössbauer and Magnetic Studies of the Amorphous $\text{Nd}_{0.33}\text{Fe}_{0.67}$ Alloy	180
5.3.1 Introduction	180
5.3.2 Experimental	183
5.3.3 Results and discussions	186

## List of Contents (Continued)

	<u>Page</u>
5.3.4 Conclusion	205
REFERENCES	208



LIST OF TABLES

<u>Table No.</u>	<u>Caption</u>	<u>Page</u>
3.1	The quadrupole splitting obtained by Lorentzian fit, and from $p( V )$ distribution and FWHM of the $P(V)$ distribution.	75
3.2	The recoilless fraction, Debye-temperature and thickness corrected FWHM of some Ferrous Complexes.	84
4.1	Observed Mössbauer parameters for $^{57}\text{FeTi}$ system.	112
4.2	The available data at present on quadrupole interactions at different probes in titanium host.	115
4.3	Electric field gradients in hcp transition metal hosts.	117
4.4	Lattice parameters of titanium at different temperatures.	123
4.5	The value of $eq_{\text{ion}}$ , $eq_{\text{hp}}$ and $eq_{\text{el}}$ for different $c/a$ values of titanium at different temperatures in units of $Z_{\text{eff}} e/4\pi\epsilon_0 a^3$ .	124
4.6	The values of elastic constants of titanium at different temperatures in units of $10^{12}$ dynes/cm <sup>2</sup> .	126
4.7	The values of electric field gradients at $^{57}\text{Fe}$ in titanium host at different temperatures calculated using the charge shift model. The value of $Z_{\text{eff}}$ is taken as 4.	127

## List of Tables (Continued)

<u>Table No.</u>	<u>Caption</u>	<u>Page</u>
4.8	Calculated values of EFG at $^{57}\text{Fe}$ probe at room temperature using charge shift model in various hcp metals and its comparison with experimental results.	129
4.9	Observed Mössbauer parameters of $^{57}\text{FeSe}$ .	135
4.10	The currently available data on quadrupole interactions for different probes in Selenium host. $eq_{\text{el}}^{\text{I}}$ and $eq_{\text{el}}^{\text{II}}$ are calculated values assuming the total EFG to be positive and negative respectively. All the values of EFG are in $10^{17} \text{ V/cm}^2$ .	137
4.11	Observed Mössbauer parameters of $^{57}\text{FeNd}$ .	145a
4.12	Systematics of electric field gradients in pure hexagonal group IIb, IIIb (including the rare earths), IVb, VIIb and VIIIb metals.	146
5.1	The observed Mössbauer parameters of Fe-31.2 % Pd alloy at different temperatures.	161
5.2	The quadrupole splitting of the fct phase of Fe-31.2 % Pd alloy at different temperatures with the corresponding c/a values.	169
5.3	The mean field $H_{\text{eff}}$ , most probable field ( $\bar{H}$ ) and the FWHM ( $\Delta H$ ) of $P(H)$ distribution in Fe-31.2 % Pd as a function of temperature.	176
5.4	Recoilless fraction ( $f_a$ ) and effective thickness ( $t_a$ ) of the fcc phase of Fe-31.2 % Pd as a function of temperature.	179

## List of Tables (Continued)

<u>Table No.</u>	<u>Caption</u>	<u>Page</u>
5.5	Observed Mössbauer parameters of the ferromagnetic phase of $\text{Nd}_{0.33}\text{Fe}_{0.67}$ amorphous alloy.	196
5.6	Temperature dependence of the most probable field ( $H_{\text{eff}}$ ) mean fields ( $\bar{H}$ ) and FWHM ( $\Delta H$ ) of the hyperfine field distribution in $\text{Nd}_{0.33}\text{Fe}_{0.67}$ amorphous alloy.	200
5.7	Quadrupole splitting and isomer shift in the paramagnetic phase of $\text{Nd}_{0.33}\text{Fe}_{0.67}$ amorphous alloy.	201

LIST OF FIGURES

Figure No.	Caption	Page
1.1	Effect of monopole interaction on the energy levels of source and absorbers.	7
1.2a	The quadrupole splitting in $^{57}\text{Fe}$ .	11
1.2b	The quadrupole split Mössbauer spectrum with isomer shift $\delta$ .	11
1.3	Magnetic hyperfine splitting without and with electric quadrupole interaction.	14
2.1	Schematic diagram of the Mössbauer spectrometer.	27
2.2	Schematic design of the electromechanical transducer.	29
2.3	Schematic diagram of the pre-amplifier.	31
2.4	Schematic design of the vacuum furnace.	34
2.5	Schematic diagram of the power oscillator.	37
2.6a	Schematic drawing of the power supply of temperature controller.	38
2.6b	Control amplifier of temperature controller.	39
2.7	The schematic design of the liquid nitrogen dewar used in the Mössbauer experiments at temperature between 80 K and 300 K.	41
3.1	Mössbauer spectra of $\text{FeSO}_4 \cdot 7\text{H}_2\text{O}$ at (a) zero field and (b) 45 KV/cm.	57
3.2	Change in Q.S. with applied field in $\text{FeSO}_4 \cdot 7\text{H}_2\text{O}$ and in $\text{Fe}(\text{SO}_4)_2(\text{NH}_4)_2 \cdot 6\text{H}_2\text{O}$ .	58

Figure No.	Caption	Page
3.3	Change in isomer shift with applied field in $\text{FeSO}_4 \cdot 7\text{H}_2\text{O}$ and in $\text{Fe}(\text{SO}_4)_2(\text{NH}_4)_2 \cdot 6\text{H}_2\text{O}$ .	59
3.4	Variation of intensity ratio of the two peaks with applied field in $\text{Fe}(\text{SO}_4)_2 \cdot 7\text{H}_2\text{O}$ .	60
3.5	Mössbauer spectra of $\text{Fe}(\text{SO}_4)_2(\text{NH}_4)_2 \cdot 6\text{H}_2\text{O}$ at (a) zero field and (b) 30 KV/cm.	62
3.6	Mössbauer spectrum of $\text{Fe}(\text{SO}_4)_2(\text{NH}_4)_2 \cdot 6\text{H}_2\text{O}$ at 35 KV/cm.	64
3.7	Mössbauer spectrum of SNP with (a) pure Lorentzian least square fit and (b) EFG distribution fit.	68
3.8	EFG distribution in SNP at room temperature.	69
3.9	EFG distribution in $\text{FeSO}_4 \cdot 7\text{H}_2\text{O}$ at room temperature.	71
3.10	EFG distribution in $\text{Fe}(\text{SO}_4)_2(\text{NH}_4)_2 \cdot 6\text{H}_2\text{O}$ at room temperature.	72
3.11	The Mössbauer spectrum of sodium silicate glass with (a) pure Lorentzian fit and (b) EFG distribution fit.	73
3.12	EFG distribution in sodium silicate glass at room temperature.	74
3.13	Mössbauer spectrum of pottassium ferrocynide with (a) pure Lorentzian fit and (b) the isomer shift distribution fit.	77

## List of Figures (Continued)

Figure No.	Caption	Page
3.14	Isomer shift distribution in potassium ferrocynide at room temperature.	78
3.15	Isomer shift distribution in 310 stainless steel.	79
4.1	Correlation between the electronic and ionic contributions to EFG based on recent (1981) data. Figure taken from ref. [1].	94
4.2	Correlation between the EFG and the impurity valence. a) The ratio ( $V_{zz}$ at impurity/ $V_{zz}$ in pure metal) vs. impurity valence. Figure taken from ref. [10]. b) Electronic contribution to the EFG vs. impurity valence. Figure taken from ref. [11].	96
4.3	Charge distribution in an hcp metal idealised for Bodendadt calculations.	104
4.4	The dependence of EFG in zinc on the probe used. The solid line represents the prediction of the charge shift model. Figure taken from ref. [21].	107
4.5a	The Mössbauer spectrum of unannealed sample $^{57}\text{FeTi}$ .	113
4.5b	The Mössbauer spectrum of $^{57}\text{FeTi}$ after annealing the sample.	113

Figure No.	Caption	Page
4.6	The correlation between electronic and ionic contributions to the EFG in the transition metal hosts with hcp structure.	119
4.7	Temperature dependence of EFG in $^{57}\text{FeTi}$ system.	120
4.8	EFG distribution in $^{57}\text{FeTi}$ at room temperature.	122
4.9	Crystal structure of hexagonal selenium.	131
4.10	Typical Mössbauer spectrum of trigonal selenium at room temperature.	134
4.11	Typical Mössbauer spectrum of $^{57}\text{FeNd}$ at room temperature.	144
5.1a	The phase diagram of Fe-Pd system (after Shunk [41], p. 340).	158a
5.1b	Schematic drawing of twinning (after Hirabayashi et al. 1962).	158a
5.2	X-ray diffraction pattern corresponding to 220 peak of Fe-31.2 % Pd alloy.	160
5.3	Mössbauer spectra of Fe-31.2 % Pd alloy at various temperatures.	163
5.4	Hyperfine field distribution in Fe-31.2 % Pd alloy.	164
5.5	The variation of $\frac{H_{\text{eff}}(T)}{H(295)}$ with $T/T_c$ in Fe-31.2 % Pd alloy.	166

Figure No.	Caption	Page
5.6	Variation of isomer shift with temperature in the Fe-31.2 % Pd alloy.	167
5.7	Variation of magnetisation and inverse susceptibility with temperature of Fe-31.2 % Pd alloy.	168
5.8	EFG change with temperature in the fct phase of Fe-31.2 % Pd alloy.	171
5.9	Variation of EFG with variation of c/a value in Fe-31.2 % Pd alloy.	173
5.10	The variation of lattice parameters and c/a ratio for the Fe-31.2 % Pd alloy with temperature.	174
5.11	X-ray diffraction pattern of pure neodymium.	184
5.12	X-ray diffraction pattern of amorphous $\text{Nd}_{0.33}\text{Fe}_{0.67}$ .	185
5.13	Temperature dependence of magnetisation and inverse susceptibility of amorphous $\text{Nd}_{0.33}\text{Fe}_{0.67}$ alloy.	187
5.14	Variation of $\frac{d\sigma}{dT}$ with temperature in $\text{Nd}_{0.33}\text{Fe}_{0.67}$ alloy.	189
5.15	$\sigma$ vs H in the amorphous $\text{Nd}_{0.33}\text{Fe}_{0.67}$ alloy (note the lack of saturation).	190
5.16	Temperature dependence of magnetisation at various values of the applied field in $\text{Nd}_{0.33}\text{Fe}_{0.67}$ amorphous alloy.	191
5.17	Arrott plots of $\text{Nd}_{0.33}\text{Fe}_{0.67}$ amorphous alloy.	193



## List of Figures (Continued)

Figure No.	Caption	Page
5.18	Variation of thermodynamic coefficient $c$ with temperature in the amorphous $\text{Nd}_{0.33}\text{Fe}_{0.67}$ alloy.	194
5.19	Mössbauer spectra of the amorphous $\text{Nd}_{0.33}\text{Fe}_{0.67}$ alloy at different temperatures.	195
5.20	Variation of $H_{\text{eff}}$ with $T/T_c$ in the amorphous $\text{Nd}_{0.33}\text{Fe}_{0.67}$ alloy.	198
5.21	Hyperfine field distribution with temperature in amorphous $\text{Nd}_{0.33}\text{Fe}_{0.67}$ alloy.	199
5.22	Quadrupole splitting in the paramagnetic phase of $\text{Nd}_{0.33}\text{Fe}_{0.67}$ plotted against the corresponding $T^{3/2}$ .	202
5.23	Dependence of $H_{\text{hf}}$ at the Fe site upon the size of R.	204
5.24	EFG distribution in the paramagnetic state of $\text{Nd}_{0.33}\text{Fe}_{0.67}$ amorphous alloy.	206

SYNOPSIS

<sup>57</sup>Fe MÖSSBAUER STUDIES OF THE HYPERFINE INTERACTIONS  
IN SOME hcp METALS AND DISORDERED BINARY ALLOYS

By

N. VASUDEVAN NAIR  
DEPARTMENT OF PHYSICS  
INDIAN INSTITUTE OF TECHNOLOGY  
KANPUR 208016, INDIA.

Mössbauer effect, which is the recoilless absorption or emission of gamma rays by nuclei, has provided a powerful technique for studying the interactions of the atomic nucleus with its environment. The interaction of the electric quadrupole moment of the nucleus and the electric field gradients (EFG) present at the nuclear site is called the electric quadrupole interaction, and that of the nuclear magnetic dipole moment with the magnetic field at the nucleus is known as the magnetic hyperfine interaction.

It is found that in many of the non-cubic metals the electronic contribution to the EFG is about 2-4 times the lattice contribution. It is also interesting to note that with all the complexities, the dependence of EFG on temperature obeys a simple  $T^{3/2}$  relationship. More experimental data on the non-cubic metals will be valuable to find the exact systematics and to improve the theoretical understanding of the

origin of EFG. The present thesis, in part, deals with the measurement of EFG and its dependence on temperature in some non-cubic systems. These results are analysed on the basis of some of the available theoretical models.

Mössbauer spectroscopy has been found very useful in the investigations of order-disorder transitions in alloys and its effect on hyperfine magnetic field and quadrupole interaction. The broad distribution of magnetic hyperfine fields in the disordered alloys is notably reduced by atomic ordering. Metal atoms coagulate some times into the non-crystalline form which is in an extraordinarily disordered state called the amorphous state. The amorphous rare-earth based alloys have raised considerable interest because of the possibility of its use in computer memories and thermomagnetic recording. The magnetic properties of these alloys are quite varied and sensitive to the variation of temperature and other parameters. The study of an amorphous system leads to a critical re-examination of the role of lattice in crystalline solids in the structural origin of hyperfine fields. The Mössbauer and magnetic studies of two such disordered binary alloys are reported in this thesis.

The methods of analysis (EFG distribution and recoilless fraction) developed by us were first checked on certain standard systems, e.g.  $\text{Fe}(\text{SO}_4) \cdot 7\text{H}_2\text{O}$ . A thorough systematic study of these old systems yielded some outstanding new results such as identification of the induced Stark effect, which is presented briefly in this thesis.

A general brief introduction to Mössbauer spectroscopy is given in Chapter 1. Mössbauer parameters like the recoilless

fraction, isomer shift, electric quadrupole interaction, magnetic dipole interaction are introduced. Other topics like (a) Relaxation effects (b) Goldanskii-Karyagin effect (c) Sternheimer antishielding effect and (d) Asymmetric doublets in Mössbauer spectra are discussed briefly in this chapter.

Chapter 2 gives the experimental details including the authors contribution in this field, e.g. designing and development of a 'miniature quartz vacuum furnace (Induction heating/ resistance heating) for Mössbauer studies'. The method of preparation of the samples and the optimisation of the thickness for best signal to noise ratio are discussed. The computer programmes used in the analysis of data are also briefly explained.

Chapter 3 presents some new studies done on some well-known ferrous compounds of iron. The effect on EFG by an externally applied electric field to these samples is described at the first part of this chapter. The later part gives the study of the EFG distribution in these compounds by analysing the Mössbauer data by a computer programme developed by the author using a model independent method. The recoilless fraction and the Debye-temperature of some of the ferrous compounds are determined.

In Chapter 4, the present status of the understanding on the origin of EFG's in pure metals and alloys is briefly reviewed. The systematic trends observed in the experimental findings are discussed. The theoretical models suggested for finding the EFG in hexagonal close packed (hcp) metals

are also reviewed, especially the charge screening approach of Nishiyama et al., and the charge shift model suggested by Bodenstein and Perchard. The measurements on  $^{57}\text{FeTi}$ ,  $^{57}\text{FeSe}$  and  $^{57}\text{FeNd}$  systems at various temperatures are reported and discussed in detail.

The quadrupole interaction frequency (QIF), at  $^{57}\text{Fe}$  as a dilute impurity in Ti, as an absorber in the Mössbauer experiments is determined for the first time. The measurements are done from 80 K - 386 K. The dependence of EFG on temperature obeys the  $T^{3/2}$  law as for most of the other systems. The lattice contribution to EFG is calculated using the Das and Pomerantz relation and the electronic contribution is separated from the experimentally observed EFG. The present measurement is in agreement with the correlation observed between the electronic and ionic contribution. The EFG's at  $^{57}\text{Fe}$  in Ti at different temperatures are calculated using the charge shift model and it is found that there is a general agreement between the theoretical and experimental values.

The EFG at  $^{57}\text{Fe}$  probe nuclei in the semiconductor selenium is measured in the temperature range 82 K - 298 K. The present data on  $^{57}\text{FeSe}$  seem to qualitatively support the correlation between the ionic and electronic contribution to EFG if we assume that the experimental and ionic EFG's are of opposite signs. Otherwise the electronic contribution to the total EFG becomes negligible compared to the ionic contribution.

The recoilless fraction of  $^{57}\text{FeSe}$  absorber is measured using the method of Trooster et al. with some modifications.

The EFG at  $^{57}\text{Fe}$  in the light rare-earth metal neodymium is measured for the first time in the temperature range 82 K - 295 K. It is found that this system violates the systematics proposed by Ernst et al. regarding the ratio of the electronic to ionic contribution to EFG. It is also found that the electronic contribution to the EFG is the main source of EFG in this system.

In Chapter 5 the Mössbauer and magnetisation studies done on the Fe-31.2 % at Pd alloy and the  $\text{Nd}_{0.33}\text{Fe}_{0.67}$  amorphous rare-earth alloy are reported. The phase transition from fcc to fct at around 173 K is observed in the Fe-Pd system. The systematic behaviour of the quadrupole interaction with temperature in the fct phase obeys the  $T^{3/2}$  law. The Mössbauer data are analysed by the hyperfine field distribution method developed by Window and the width of the field distribution is found to increase with temperature, which reveals that the range of exchange interaction is short in the Fe-Pd system. The universal correlation that the total EFG is proportional to the lattice contribution is obeyed by the tetragonal phase of Fe-Pd alloy. The recoilless fraction of this alloy at various temperatures are determined by the Trooster et al. method. The paramagnetic Curie temperature is determined by using the PARC vibrating sample magnetometer and also from the variation of  $H_{\text{eff}}$  with temperature and the

agreement between these two values is quite good in this case.

The magnetisation studies done on the amorphous system  $\text{Nd}_{0.33} \text{Fe}_{0.67}$  is presented in detail in this chapter. The Curie temperature is found out from the Mössbauer studies and from the Arrott plots. The average hyperfine field varies from 317 kOe to 109 kOe in the temperature range 90 K to 320 K. The hyperfine field distribution is also found in this temperature range. In the paramagnetic phase this system shows quadrupole splitting with well defined peaks. The quadrupole splitting changes with temperature according to the  $T^{3/2}$  law. The distribution of EFG in the paramagnetic phase is also determined in the  $\text{Nd}_{0.33} \text{Fe}_{0.67}$  system.

It is hoped that the present work has contributed to our knowledge on the systematics of hyperfine interactions in metals, alloys and compounds and has helped bring us closer to the understanding of the origin of the hyperfine fields.

## CHAPTER 1

### FUNDAMENTALS OF MÖSSBAUER SPECTROSCOPY

#### 1.1 Introduction

The discovery by R.L. Mössbauer [1] of the recoilless absorption or emission of gamma rays by nuclei has opened up new vistas in the realm of hyperfine interactions. The unlimited potentialities of this discovery is reflected in its rapid development into a scientific discipline and the impressive position it has occupied in the varied fields of physics, chemistry, metallurgy, biochemistry, earth sciences to name a few. It is exciting to realise that by now a single aspect of Mössbauer effect like the isomer shift could fill the whole volume of a book [2].

The field of hyperfine interactions with special reference to Mössbauer spectroscopy is treated in many reviews and monographs in details [3-7]. Therefore only a broad outline will be given of the nuclear and solid state properties that influence Mössbauer spectra in this chapter.

#### 1.2 The Mössbauer Effect

When a nucleus decays from an excited state  $E^{\text{ex}}$  of energy  $E_0$  with respect to the ground state of energy  $E^{\text{gr}}$ , it will emit a photon of energy  $E_\gamma$ . To conserve the momentum a



recoil energy  $E_R$  is imparted to the emitting nucleus

$$E_R = \frac{E_\gamma^2}{2Mc^2} \quad (1.1)$$

where  $M$  represents the mass of the nucleus and  $c$  the velocity of light. Conservation of energy yields for the photon energy  $E = E_0 - E_R$  similarly to excite such a nucleus from  $E^{gr}$  to  $E^{ex}$ , a photon of energy  $E = E_0 + E_R$  will be required. It is clear therefore that resonant absorption of the emitted photon can only take place, when  $E_R$  is comparable to or smaller than  $\Gamma$ , the line width (full width at half maximum or in short FWHM) of the excited state  $E^{ex}$ . This line width is connected to the mean life  $\tau$  of  $E^{ex}$  by the Heisenberg uncertainty relation

$$\tau \gtrsim \frac{h}{2\pi}$$

where  $h$  is the Plank's constant. In the case of gamma ray transitions, the recoil energy  $E_R$  is much larger ( $\sim 10^8$  times). when compared with typical nuclear line widths thus making resonance absorption almost impossible. However, when the nuclei are embedded in a crystal, a fraction 'f' of the gamma rays are emitted without any energy loss due to recoil, the same being true for absorption also. The probability for this is given by

$$f = \left| \int \varphi_n^*(x) \varphi_n(x) \exp(-i \vec{k} \cdot \vec{x}) dx \right|^2 \quad (1.2)$$

where  $\varphi_n(\vec{x})$  represents the vibrational state of the lattice, which remains the same in the case of recoilless emission.  $\vec{k}$

is the wave vector of the gamma ray and  $\bar{x}$  is the position coordinate of the centre of mass of the emitting nucleus.

A general expression for the probability of emission or absorption without recoil, that is in which no phonons are excited is given by

$$f = \exp [-k^2 \langle x^2 \rangle] \\ = \exp \left[ -\frac{h^2 k^2}{2m} \int_0^{\omega} \frac{g(\omega)}{h} \coth \left( \frac{h\omega}{2k_B T} \right) d\omega \right]$$

$\langle x^2 \rangle$  is the mean square displacement of the nucleus from its equilibrium position, and  $g(\omega)$  is the normalised density of phonon states of angular frequency  $\omega$ . In the Debye model of solids, the frequency distribution function

$$g(\omega) = \text{constant} \cdot \omega^2 \quad \text{for } 0 \leq \omega \leq \omega_{\text{max}} \\ = 0 \quad \text{for } \omega > \omega_{\text{max}}$$

Using this model the expression for 'f' reduces to

$$f = \exp \left\{ -\frac{6hR}{k\theta_D} \left[ \frac{1}{4} + \left( \frac{T}{\theta_D} \right)^2 \int_0^{\theta_D/T} \frac{x dx}{e^x - 1} \right] \right\} \quad (1.3)$$

It is seen that 'f' can be non zero under the conditions mentioned above. The energy distribution of recoilfree emitted radiation can be shown to be

$$I(E) = I_0 f_s \left( \frac{r^2/4}{(E-E_0)^2 + r^2/4} \right) \quad (1.4)$$

while the probability for resonant absorption can similarly be

described by

$$\sigma(E) = \sigma_0 f_s \left( \frac{r^2/4}{(E-E_0)^2 + r^2/4} \right) \quad (1.5)$$

where  $f_s$  and  $f_a$  are the recoilfree fractions in source and absorber respectively.  $I_0$  is intensity of emitted radiation from the source and  $\sigma_0$  is the effective photon cross section of the Mössbauer nucleus in the absorber. This type of recoilless resonant absorption of nuclear gamma radiations is known as Mössbauer effect (ME) after its discoverer.

Mössbauer effect has provided us with an extremely precise method for measuring the small energy shifts experienced by the nuclei such as the hyperfine structure of the nuclear energy levels.

In Mössbauer experiments either the source or the absorber is usually subjected to a velocity programme to give an appropriate Doppler energy shift to the  $\gamma$ -rays so that one may obtain the resonance intensity as a function of energy.

### 1.3 Hyperfine Interactions

When a nucleus is embedded in a solid, the Hamiltonian for interaction between the nucleus and the surrounding charges and currents may be written as

$$\mathcal{H} = E_1 + M_1 + E_2 + \dots$$

where  $E_1$  refers to electric monopole interaction between the nucleus and electrons,  $M_1$  the magnetic dipole interactions and.

$E_2$  to electric quadrupole interactions. Higher terms are usually small.

The electric monopole interaction between the electrons and nucleus shifts the energy levels of the ground and the excited states of the nucleus generally by different amounts. Depending on the chemical form, this change may be different for source and absorber which will cause a shift in the resonance energy. This shift is known as isomer shift or chemical shift.

The electric quadrupole and magnetic interactions result in splitting of the energy levels and consequently give a multiple resonance absorption pattern in the Mössbauer spectra. These interactions will be discussed briefly.

### 1.3.1 Isomer shift

The isomer shift  $\delta$  is the result of the Coulomb interaction of the nuclear charge distribution because of the finite size of the nucleus with the electron charge density at the nucleus ( $s$  electrons). Because of the different environment of the source and absorber nuclei this interaction energy may be also different. So in a resonance experiment the centre of gravity of the spectrum will be shifted by this difference of interaction energies.

This shift can be expressed in non-relativistic approximation, assuming a spherical uniformly charged nucleus, as

$$\delta = \frac{2\pi}{5} Z e^2 [|\varphi_S(0)|_A^2 - |\varphi_S(0)|_S^2] \cdot [\langle r_e^2 \rangle - \langle r_g^2 \rangle] \dots (1.6)$$

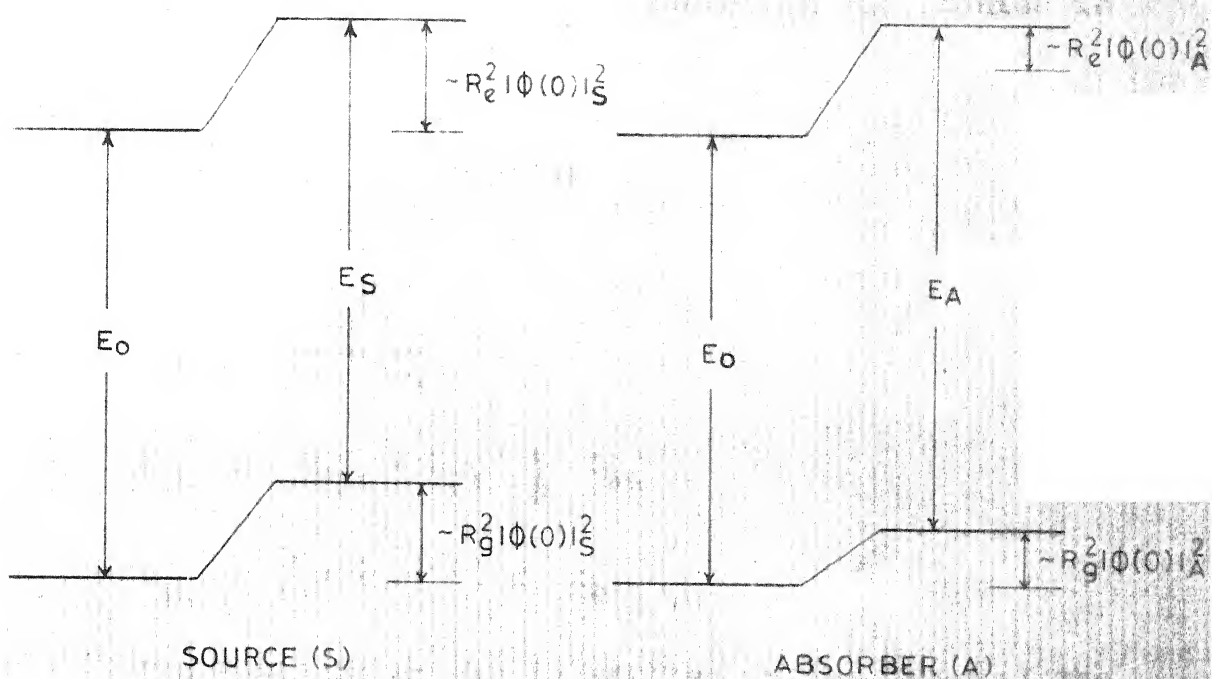
where the suffixes A and S refer to absorber and source respectively.  $\varphi_S(0)$  is the s electron density at the site of nucleus and  $\langle r_e^2 \rangle$  and  $\langle r_g^2 \rangle$  are the mean squared nuclear charge radii in the excited and ground states respectively. (Fig. 1.1). The wealth of information that could be obtained from isomer shift measurements are described in the recent work on isomer shifts edited by G.K. Shenoy et al. [2].

The ratio of isomer shifts of two gamma-transitions A and B in two isotopes of the same element is

$$\frac{[\langle r_e^2 \rangle_A - \langle r_g^2 \rangle]}{[\langle r_e^2 \rangle_B - \langle r_g^2 \rangle]} \approx \frac{\Delta R_A^2}{\Delta R_B^2}$$

which is independent of the electron density. That is, this ratio of isomer shifts gives the ratios of the changes in the mean squared charge radii for different transitions in the same element.

The isomer shift data are commonly used to study the chemical structure, bonding of valence states etc. in compounds. The measured isomer shift values of the same element in different systems are related to changes in the electron densities and are therefore, used to find the structure and phase of the systems.



$$\delta = 2\pi/S \cdot Ze^2 (|\Phi(0)|_A^2 - |\Phi(0)|_S^2) (\langle R_e^2 \rangle - \langle R_g^2 \rangle)$$

Fig.11 Effect of monopole interaction on the energy levels of source and absorber

### 1.3.2 Electric quadrupole interaction

The electric quadrupole interaction Hamiltonian is given by

$$\mathcal{H}_Q = \frac{1}{6} \sum_{j,k} Q_{jk} \cdot V_{jk} \quad (1.7)$$

where

$$V_{jk} = \frac{\partial^2 V}{\partial x_j \partial x_k}$$

$$Q_{jk} = 3Q'_{jk} - \delta_{jk} \sum_e Q'_{ee}$$

$$Q'_{jk} = \int d^3\bar{x} \rho(\bar{x}) x_j x_k$$

The Hamiltonian can be written in the terms of the irreducible components of  $Q$  and  $v$

$$Q_2^0 = \frac{eQ}{2I(2I-1)} [3I_z^2 - I^2]$$

$$Q_2^{\pm 1} = \frac{eQ}{2I(2I-1)} \frac{\sqrt{6}}{2} [I_z I_{\pm} + I_{\pm} I_z]$$

$$Q_2^{\pm 2} = \frac{eQ}{2I(2I-1)} \frac{\sqrt{6}}{2} (I_{\pm})^2$$

$$V'_0 = \frac{1}{2} V_{zz}$$

$$V'_{\pm 1} = \pm \frac{1}{\sqrt{6}} (V_{xz} \pm i V_{yz})$$

$$V'_{\pm 2} = \frac{1}{2\sqrt{6}} (V_{xx} - V_{yy} \pm 2i V_{xy})$$

where

$$Q = \frac{1}{e} \langle II | Q_{33} | II \rangle$$

$$= \frac{1}{e} \int \rho_{II}(\vec{r}) (3z^2 - r^2) d^3\vec{r}$$

On transformation of these tensors to the set of principal axes of electric field gradient (EFG) tensor, the irreducible components of  $V_{jk}$  become

$$V_0 = \frac{1}{2} V_{zz} = \frac{1}{2} eq$$

$$V_{\pm 1} = 0$$

$$V_{\pm 2} = \frac{1}{2\sqrt{6}} (V_{xx} - V_{yy}) = \frac{1}{2\sqrt{6}} \eta eq$$

The quantities  $\eta$  and  $q$  are defined by the above equations.

The Hamiltonian then becomes

$$\mathcal{H}_Q = \sum_m Q_2^m V_2^{-m}$$

$$= \frac{e^2 Qq}{4I(2I-1)} [3I_z^2 - I^2 + \frac{\eta}{2} (I_+^2 + I_-^2)] \quad (2.8)$$

The separation of nuclear energy levels is usually much larger than the magnitude of  $\mathcal{H}_Q$ . So, to a good approximation, the perturbation calculations require only the matrix elements of the form  $\langle Im | \mathcal{H}_Q | Im' \rangle$  which are diagonal in all quantum numbers except  $m$ .

For axially symmetric EFG ( $\eta = 0$ ) the matrix of this Hamiltonian is diagonal in  $|Im\rangle$  representation. The energy shift in the state  $|I_{\pm m}\rangle$  for  $I > 1/2$  is



$$\frac{e^2 Qq}{4I(2I-1)} [3m^2 - I(I+1)]$$

which for  $I = \frac{3}{2}$ ,  $m = \pm \frac{3}{2}$  is  $\frac{e^2 Qq}{4}$  and  $I = \frac{3}{2}$ ,  $m = \pm \frac{1}{2}$  is  $-\frac{e^2 Qq}{4}$ . There is no shift in energy of the states having  $I = \frac{1}{2}$ .

Thus the quadrupole split spectrum is a doublet (Fig. 1.2).

The situation may be complicated if the asymmetry parameter  $\eta$  is non zero. The matrix for  $\mathcal{H}_Q$  is not diagonal in  $|Im\rangle$  representation and the off diagonal terms are

$$\langle Im' | \mathcal{H}_Q | Im \rangle = \frac{A\eta}{2} [(I+m-1)(I+m)(I+m+1)(I+m+2)]^{\frac{1}{2}} \cdot \delta_{m', m+2}$$

where  $A = \frac{e^2 Qq}{4I(I-1)}$ . This causes mixing between states having  $\Delta m = 2$ . The secular equation for some of the half integral values of  $I$  are given below [8].

$I$	Secular equation
$\frac{3}{2}$	$(E/A)^2 - 3\eta^2 - 9 = 0$
$\frac{5}{2}$	$(E/2A)^3 - (3\eta^2 + 21)(E/2A)^2 - 20(1-\eta^2) = 0$
$\frac{7}{2}$	$(E/3A)^4 - 42(1+\eta^2/3)(E/3A)^2 - 64(1-\eta^2) + 105(1+\eta^2/3)^2 = 0$
$\frac{9}{2}$	$(E/6A)^5 - 33(1+\eta^2/3)(E/6A)^3 - 44(1-\eta^2)(E/6A)^2$ $+ 44(1+\eta^2/3)^2(E/6A) + 144(1+\eta^2/3)(1-\eta^2) = 0$

For  $I = \frac{3}{2}$  the exact solution is

$$\begin{aligned} E_{3/2} &= 3A(1 + \eta^2/3)^{\frac{1}{2}} \\ E_{1/2} &= -3A(1 + \eta^2/3)^{\frac{1}{2}} \end{aligned} \quad (2.9)$$

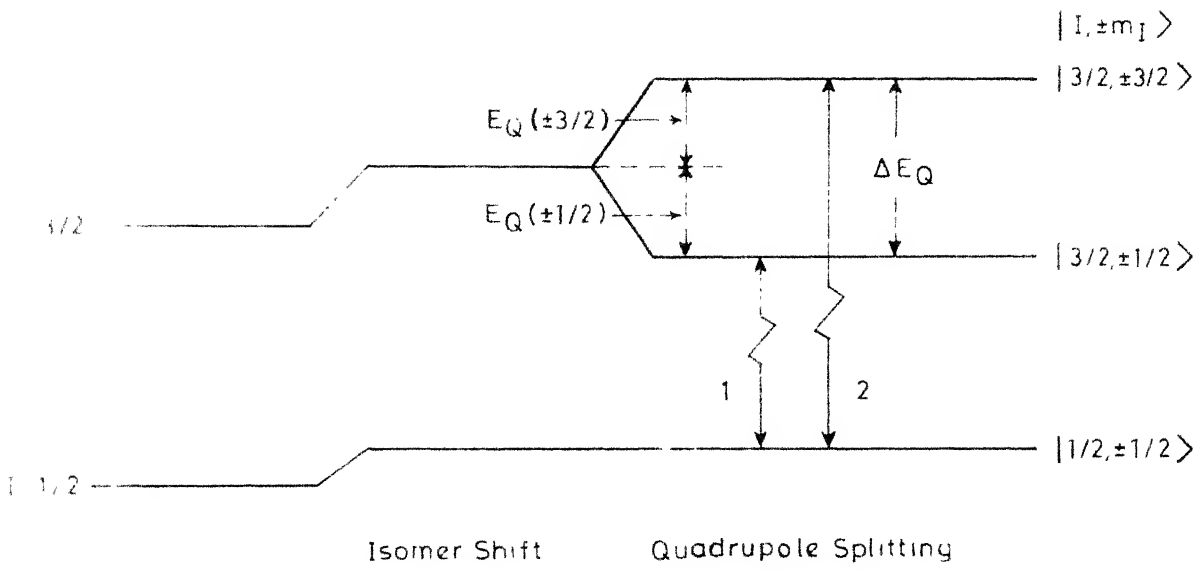


Fig.12a Quadrupole splitting in  $^{57}\text{Fe}$  with spin  $I = 3/2$  in the excited state.

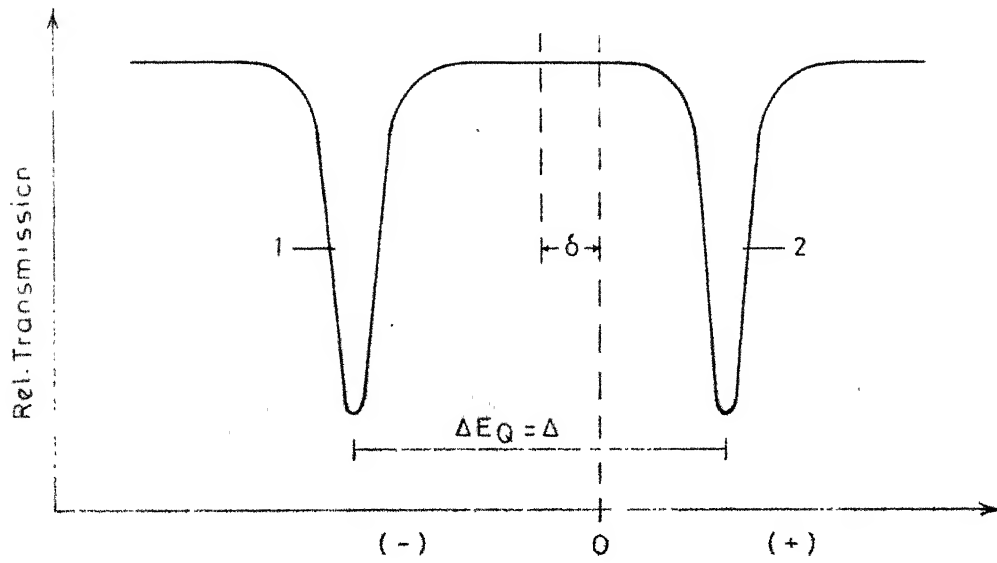


Fig.12b The quadrupole split Mössbauer spectrum with isomer shift.

For other values of nuclear spin, the secular equation is solved numerically.

The quadrupole interaction does not remove the ( $\pm m$ ) degeneracy.

### 1.3.3 Sternheimer antishielding factors

The strength of the quadrupole interaction at the nuclear site will be considerably affected due to the presence of the atomic electrons. The effective EFG at the nuclear site is usually written as

$$V_{zz}^{\text{nuc}} = (1 - \gamma_{\alpha}) V_{zz}^{\text{ext}} + (1-R) V_{zz}^{\text{local}}$$

where  $V_{zz}^{\text{ext}}$  is the EFG at the nuclear site due to the ions of the lattice in the absence of atomic electrons. An additional field ( $-\gamma_{\alpha} \cdot V_{zz}^{\text{ext}}$ ) results at the nuclear site due to the polarisation of the electron cloud. The values of  $(1-\gamma_{\alpha})$  for the medium and heavy ions are in the range 10-80 showing that the field at the nucleus is considerably enhanced and therefore  $(1-\gamma_{\alpha})$  is called the antishielding factor. If the field sources are not entirely external, as in the case of rare-earth metals or in the case of ions having non-spherical outer shells, significant local contributions to the EFG are present. The factor  $R$  corresponds to the atomic shielding of the EFG at the nucleus due to the unfilled orbital ( $V_{zz}^{\text{local}}$ ). The values of  $R$  range from  $-0.2$  to  $+0.2$ . The above picture is not valid for metals and alloys because the EFG contribution at the nuclear site

cannot be pictured wholly as due to local and non-local sources and it is well established that very significant contributions come from the conduction electrons.

#### 1.3.4 Magnetic dipole interaction

A nucleus with spin  $I > 0$  has a magnetic dipole moment  $\mu$ , which can interact with a magnetic field  $H$  at the nucleus, resulting in the splitting of energy levels (Nuclear Zeeman effect). This interaction Hamiltonian

$$\mathcal{H} = -\vec{\mu} \cdot \vec{H} = -g_N \beta_N \vec{I} \cdot \vec{H} \quad (2.9)$$

where  $g_N$  is the nuclear splitting factor and  $\beta_N = \frac{e\hbar}{2Mc}$  is the nuclear Bohr magneton. Using first-order perturbation theory the eigen values of  $\mathcal{H}(m_I)$  are given by

$$\begin{aligned} E_m(m_I) &= -\mu H m_I/I \\ &= -g_N \beta_N H m_I \end{aligned} \quad (2.10)$$

This dipole interaction splits a nuclear state  $|I\rangle$  into  $2I+1$  equally spaced states having nuclear magnetic spin quantum number  $m_I = I, I-1, \dots, -I$ . The gamma transitions corresponding to these sublevels are subject to the selection rule

$I = 1, \Delta m = 0, \pm 1$ . For  $^{57}\text{Fe}$  with  $I = \frac{3}{2}$  and  $I_g = \frac{1}{2}$  magnetic dipole interaction gives altogether six allowed transitions (Fig. 1.3).

The relative intensities of the six transitions are given by

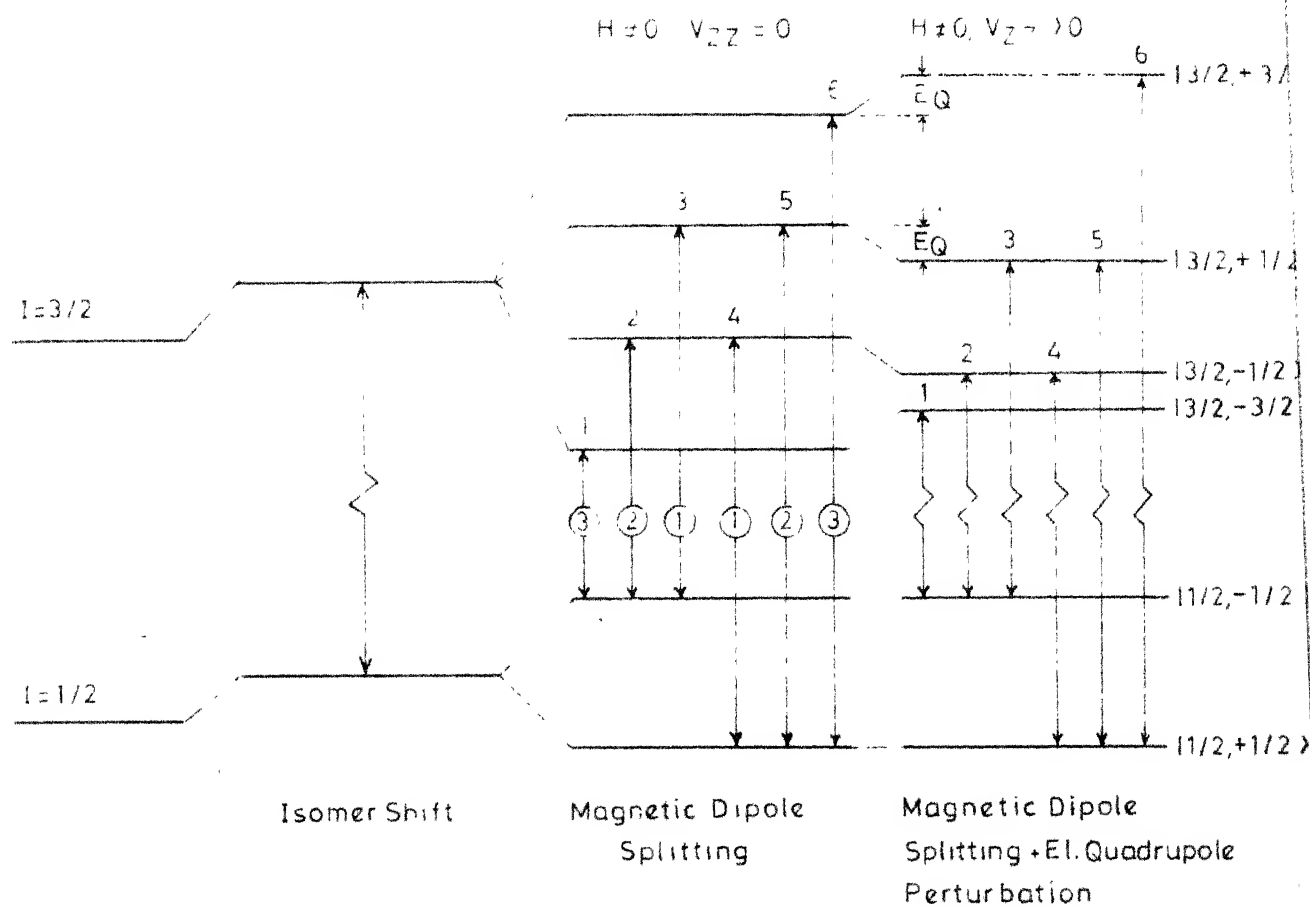


Fig.13 Magnetic hyperfine splitting without and with electric quadrupole interaction.

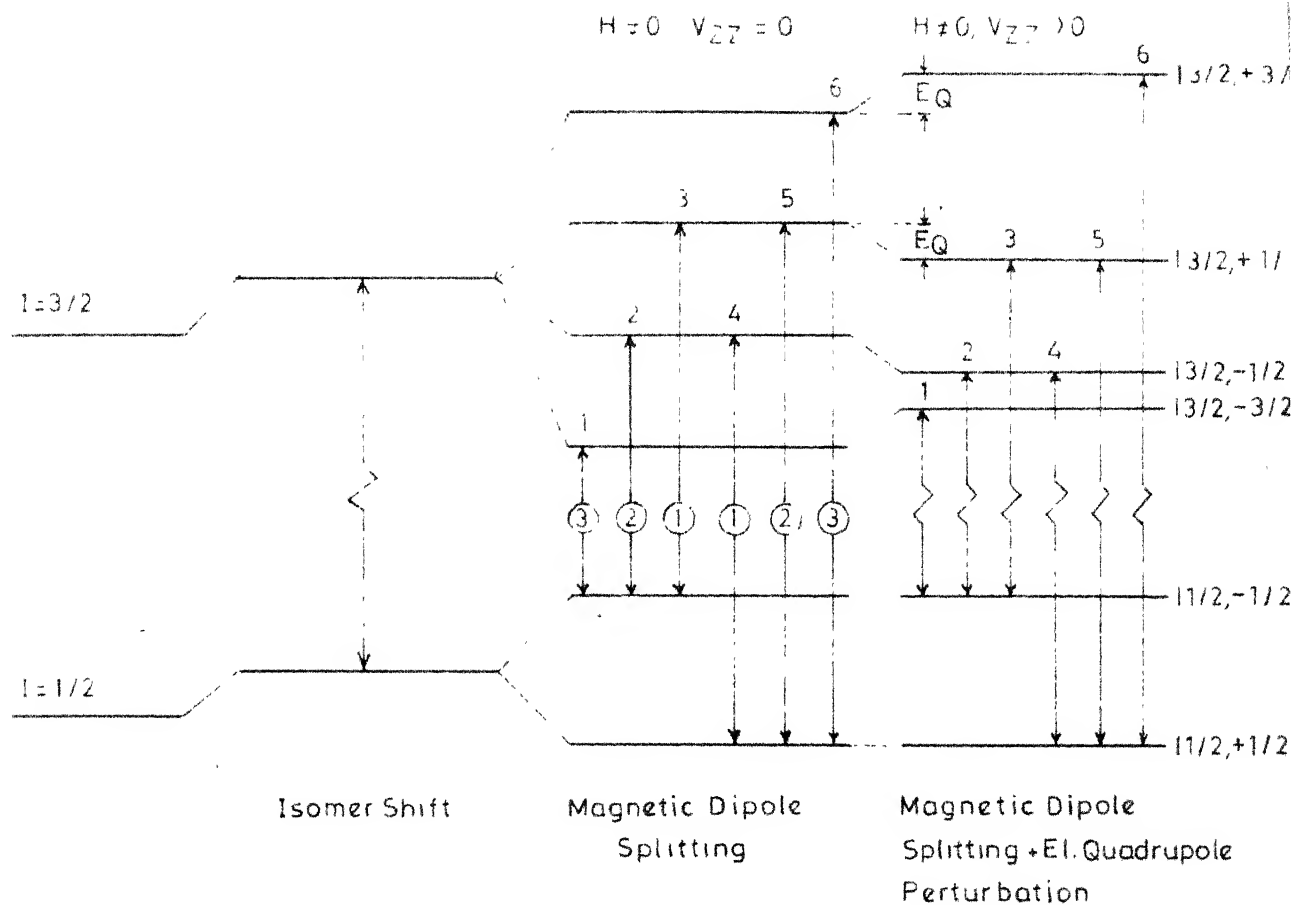


Fig 13 Magnetic hyperfine splitting without and with electric quadrupole interaction.

$$\begin{aligned}
 & \left(\frac{3}{2} \frac{3}{2} \quad \frac{1}{2} \frac{1}{2}\right) : \left(\frac{3}{2} \frac{1}{2} \quad \frac{1}{2} \frac{1}{2}\right) : \left(\frac{3}{2} \frac{1}{2} \quad \frac{1}{2} \frac{-1}{2}\right) : \left(\frac{3}{2} \frac{-1}{2} \quad \frac{1}{2} \frac{1}{2}\right) : \\
 & \left(\frac{3}{2} \frac{-1}{2} \quad \frac{1}{2} \frac{-1}{2}\right) : \left(\frac{3}{2} \frac{-3}{2} \quad \frac{1}{2} \frac{-1}{2}\right) = 3 : 2 : 1 : 1 : 2 : 3 \\
 & \dots\dots (2.11)
 \end{aligned}$$

where  $Z = 4/(1+\cot^2\theta)$ .

For polycrystalline samples, the values should be averaged over all possible orientations of crystallites. This gives the intensity ratios to be 3:2:1:1:2:3.

Pure nuclear magnetic dipole interactions are rarely encountered in chemical applications of the Mössbauer effect. On the other hand the nuclear state is simultaneously acted upon by both magnetic dipole and electric quadrupole interactions. So the sublevels of  $I = \frac{3}{2}$  or  $^{57}\text{Fe}$  are no longer equally spaced (Fig. 1.3). The quadrupole coupling may be treated as a first-order perturbation on the magnetic dipole interaction. If  $\langle H(e2) \rangle < \langle H(m1) \rangle$  and if the EFG tensor is axially symmetric and its principal axis makes an angle  $\beta$  with the axis of the magnetic field, from first-order perturbation calculations one gets for the eigen values

$$\begin{aligned}
 E = & -g_N \beta_N H m_I + (-1)^{m_I + \frac{1}{2}} (eQ V_{zz}/8) (3\cos^2\beta - 1) \\
 & \dots\dots (2.12)
 \end{aligned}$$

### 1.3.5 Relaxation effects in Mössbauer spectroscopy

When the environment of the Mössbauer nucleus rapidly changes, the Mössbauer spectrum is affected. The fluctuations

may be due to for example (i) time-dependent magnetic hyperfine interaction due to electronic spin-spin or spin-lattice relaxation, (ii) randomly changing electric quadrupole interaction due to Jahn-Teller distortions, (iii) interstitial or vacancy diffusion in the vicinity of the Mössbauer nucleus etc.

The lineshape may be quite ~~unusual~~ because of rapidly changing Hamiltonian. We shall discuss in somewhat detail the effect of spin-lattice and spin-spin relaxation on a quadrupole-magnetic spectrum of  $^{57}\text{Fe}$ . The probability of emission of a photon in direction  $\vec{k}$  with frequency  $\omega$  and polarisation  $p$  by a system which, in the process of emission, makes a transition from its initial state  $|\lambda\rangle$  to the final state  $|\alpha\rangle$  is given by the Wigner-Weisskopf formula [9]

$$P_{\lambda\alpha}(k, \omega, p) = \frac{|\langle\alpha| V^{(+)} |\lambda\rangle|^2}{(\omega + E_{\alpha} - E_{\lambda})^2 + \Gamma^2/4} \quad (2.13)$$

$V^{(+)}$  being the interaction Hamiltonian between the nucleus and the electromagnetic field.  $|\lambda\rangle$  and  $|\alpha\rangle$  represent in general, eigenstates of the nucleus together with the entire solid or liquid in which the gamma-emitting nucleus is embedded. The quantity  $\Gamma$  is the inverse of the lifetime of the excited state  $|\lambda\rangle$ . Since we do not observe initial and final states in the usual experiments, the observed probability is obtained by summing over final states and averaging over initial states. Algebraic manipulations finally yield the emission probability [10]



$$P(k \omega p) = \frac{2}{\pi} \operatorname{Re} \int_0^{\infty} d\tau \left[ \exp(i \omega \tau - \frac{\Gamma}{2} \tau) \overline{\langle V^{(-)} V^{(+)}(\tau) \rangle} \right]$$

where  $\operatorname{Re}$  stands for real part,  $V^{(-)}$  is the adjoint of  $V^{(+)}$  and

$$V^{(+)}(t) = \exp(i \mathcal{H} t) V^{(+)} \exp(-i \mathcal{H} t)$$

being the Hamiltonian for the entire system.

In a simple situation where the electronic state of the ion containing the Mössbauer nucleus flips between  $S_z = \frac{1}{2}$  and  $-\frac{1}{2}$ , the nucleus finds itself in a magnetic field which is  $+H$  for sometime and  $-H$  for sometime. In addition, let us introduce a constant axial electric field gradient, the principal axis being in the direction of  $+H$ .

The time-dependent Hamiltonian may be written as

$$\mathcal{H}(t) = \mathcal{H}_0 + g\mu_B I_z f(t) + Q(3I_z^2 - I^2)$$

$\mathcal{H}_0$  being the unperturbed Hamiltonian,

$$\mathcal{H}_0 |I_1 m_1\rangle = E_1 |I_1 m_1\rangle$$

$$\mathcal{H}_0 |I_0 m_0\rangle = E_0 |I_0 m_0\rangle$$

and  $E_1 - E_0$  is the energy of the unperturbed gamma ray. The function  $f(t)$  can take two values  $\pm 1$  at random. The lineshape is obtained by averaging over all functions  $f(t)$ .

$$P(k \omega p) = \frac{2}{\Gamma} \operatorname{Re} \int_0^{\infty} d\tau \left[ \exp(i \omega \tau - \frac{\Gamma}{2} \tau) \overline{\langle V^{(-)} V^{(+)}(\tau) \rangle} \right] \quad (2.14)$$

where the bar denotes stochastic average. The correlation function is calculated by inserting a complete set of states in the definition.

$$V^{(-)} V^{(+)}(t) = \frac{1}{2I_1+1} \sum_{m_0 m_1} \langle I_1 m_1 | V^{(-)} | I_0 m_0 \rangle \langle I_0 m_0 | V^{(+)}(t) | I_1 m_1 \rangle$$

where we have used the fact that the photon emission operators can only connect the excited state  $I_1$ , with the ground state  $I_0$ .

Writing

$$V^{(+)}(t) = \exp(i \int_0^t (t') dt') V^{(+)} \exp(-i \int_0^t (t') dt')$$

and inserting complete sets  $|I_0 m'_0\rangle \langle I_0 m'_0|$  and  $|I_1 m'_1\rangle \langle I_1 m'_1|$  and using

$$\begin{aligned} \langle I_0 m_0 | \exp(i \int_0^t (t') dt') | I_0 m'_0 \rangle &= \delta_{m_0 m'_0} \exp[i(E_0 + Q_0 \{3m_0^2 - I_0(I_0+1)\})t] \\ &\quad \times \exp(i g_0 \mu H m_0 \int_0^t f(t') dt') \end{aligned}$$

and

$$\begin{aligned} I_1 m'_1 \exp(-i \int_0^t (t') dt') | I_1 m_1 \rangle &= \delta_{m_1 m'_1} \exp[-i(E_1 + Q_1 \{3m_1^2 - I_1(I_1+1)\})t] \\ &\quad \times \exp(-i g_1 \mu H m_1 \int_0^t f(t') dt') \end{aligned}$$

we get

$$\begin{aligned} \overline{V^{(-)} V^{(+)}(t)} &= \exp(i \Delta E t) \cdot \frac{1}{2I_1+1} \sum_{m_0 m_1} |\langle I_0 m_0 | V^{(+)} | I_1 m_1 \rangle|^2 \\ &\quad \times \exp(i \beta(t)) \end{aligned} \quad (2.15)$$

where  $\Delta E = E_0 + Q_0 [3m_0^2 - I_0(I_0+1)] - E_1 - Q_1 [3m_1^2 - I_1(I_1+1)]$

$$\beta(t) = (g_0 m_0 - g_1 m_1) \mu H \int_0^t f(t') dt'$$

$g_0$  and  $g_1$  are respectively the  $g$ -factors for the ground and excited states and  $Q_0$  and  $Q_1$  are proportional to the quadrupole

moments of the ground and excited nuclear states.

The matrix elements of  $V^{(+)}$  are proportional to Clebsch-Gordan coefficients and the only remaining problem is the evaluation of the average of the quantity

$$\exp [i(g_0 m_0 - g_1 m_1) \mu H \int_0^t f(t') dt']$$

The average of this quantity may be expressed in terms of the probabilities  $W_{+-}$  and  $W_{-+}$  of transitions from  $+1/2$  to  $-1/2$  and from  $-1/2$  to  $+1/2$  respectively. For  $W_{+-} = W_{-+} = W$

$$\overline{\exp[i(g_0 m_0 - g_1 m_1) \mu H \int_0^t f(t') dt']} = [(\cos x)Wt + \frac{1}{x}(\sin x)Wt] \exp(-Wt) \quad \dots\dots (2.16)$$

$$\text{where } x = \left[ \frac{(g_0 m_0 - g_1 m_1)^2 \mu^2 H^2}{W^2} - 1 \right]^{1/2}$$

Substituting eqs. (2.15) and (2.16) in (2.14) gives the lineshape.

Spectra were calculated [11] using the above theory for different values of the jump time  $\tau$ . For large  $\tau$  or slow jumping the spectrum corresponds to a full six line one as if it is in steady magnetic field. For very small  $\tau$ , the spectrum is a symmetric quadrupole doublet. For intermediate jump times we get many lineshapes.

As we start from large relaxation time  $\tau$ , full six line spectrum corresponding to static magnetic field  $H$  with quadrupole modification is observed. As  $\tau$  becomes shorter the inner magnetic lines collapse onto their centre of gravity. The other magnetic

lines are still present, although they are considerably broadened. The remaining magnetic lines also go on collapsing and quadrupole pattern starts to appear as  $\tau$  becomes shorter and shorter. The  $\pi$ -line i.e.  $\pm \frac{3}{2} \rightarrow \pm \frac{1}{2}$  narrows more slowly than the  $\sigma$ -line  $\pm \frac{1}{2} \rightarrow \pm \frac{1}{2}$ . The  $\pm \frac{3}{2} \rightarrow \pm \frac{1}{2}$  transitions, which make up the  $\pi$ -line of quadrupole doublet, have a larger splitting in a magnetic field than the  $\pm \frac{1}{2} \rightarrow \pm \frac{1}{2}$  transitions. The Zeeman precession frequencies, with which relaxation frequency is compared are different for different transitions. It is possible that the relaxation time  $\tau$  is such that the  $\pm \frac{1}{2} \rightarrow \pm \frac{1}{2}$  transition feels a rapid relaxation but  $\pm \frac{3}{2} \rightarrow \pm \frac{1}{2}$  feels a comparatively slow relaxation. The high velocity components will have then already collapsed to a sharp line whereas the low velocity components will still be broad. This then results in asymmetric quadrupole doublet. Recently, calculations were reported [12-13] where the effects of the motion of the Mössbauer nucleus itself, or that of the molecules (in case of liquids) etc. have been taken into account.

### 1.3.6 Goldnski-Karyagin effect

The intensity of the Mössbauer line depends on the recoilfree fraction

$$f = \exp[-\langle (\vec{k} \cdot \vec{x})^2 \rangle]$$

If the gamma ray direction  $\vec{k}$  is expressed in polar co-ordinates  $\theta$  and  $\phi$  with respect to EFG axes, we can write

$$\langle (\mathbf{k} \cdot \bar{\mathbf{x}})^2 \rangle = k^2 \{ [\langle x_x^2 \rangle \cos^2 \phi + \langle x_y^2 \rangle \sin^2 \phi] \sin^2 \theta + \langle x_z^2 \rangle \cos^2 \theta \}$$

If the amplitudes of vibration are not equal in all the directions, the recoilfree fraction becomes a function of  $(\theta, \phi)$ . For  $^{57}\text{Fe}$  quadrupole doublet for a polycrystalline sample the intensities of the two lines have the ratio

$$\frac{M_{\pi}}{M_{\sigma}} = \frac{\int_0^{2\pi} \int_0^{\pi} f(\theta, \phi) (1 + \cos^2 \theta) \sin \theta \, d\theta \, d\phi}{\int_0^{2\pi} \int_0^{\pi} f(\theta, \phi) \left(\frac{5}{3} - \cos^2 \theta\right) \sin \theta \, d\theta \, d\phi}$$

for axially symmetric vibrations where

$$\langle x_x^2 \rangle = \langle x_y^2 \rangle = \langle x_{\perp}^2 \rangle \neq \langle x_z^2 \rangle = \langle x_{\parallel}^2 \rangle$$

$$f(\theta, \phi) = \exp[-k^2 \langle x_{\perp}^2 \rangle] \exp[k^2 (\langle x_{\perp}^2 \rangle - \langle x_{\parallel}^2 \rangle) \cos^2 \theta]$$

resulting in

$$\frac{M_{\pi}}{M_{\sigma}} = \frac{\int_0^{\pi} \exp[-k^2 (\langle x_{\parallel}^2 \rangle - \langle x_{\perp}^2 \rangle) \cos^2 \theta] (1 + \cos^2 \theta) \sin \theta \, d\theta}{\int_0^{\pi} \exp[-k^2 (\langle x_{\parallel}^2 \rangle - \langle x_{\perp}^2 \rangle) \cos^2 \theta] \left(\frac{5}{3} - \cos^2 \theta\right) \sin \theta \, d\theta}$$

We thus see that even for random orientation of crystallites, the intensities of the two lines may be different. The intensities of the magnetically split lines are also modified for the same reasons, i.e. the anisotropy of the Debye-Waller factor. This effect is known as Goldanski-Karyagin (G-K) effect. As the vibrational anisotropy is an increasing function of temperature the asymmetry in intensities related to the G-K effect also increases with temperature.

### 1.3.7 Asymmetric quadrupole doublet

The observed quadrupole doublet may be asymmetric due to the following three reasons:

- 1) Lack of randomness of crystallites
- 2) Anisotropy of Debye-Waller factor
- 3) Relaxation effects.

The first one has the distinct property that the ratio of intensities strongly depends upon the angle between the gamma ray direction and the sample surface. The second and third effects are independent of sample orientation but depends very much on temperature. The intensity ratio due to anisotropy of the Debye-Waller factor is  $\sim 1$  at low temperatures and increases with temperature. For the third case the asymmetry ratio will strongly depend upon the relaxation mechanism. If the fluctuations in the magnetic field are due to spin-lattice relaxation we expect relaxation time to decrease with increasing temperature. This means that raising the temperature will decrease the asymmetry, an effect opposite to temperature dependence of G-K effect. On the other hand if the fluctuations are due to spin-spin relaxation, the asymmetry will depend on the paramagnetic ions.

REFERENCES

- [1] R.L. Mössbauer, Z. Physik 151, 124 (1958).
- [2] ''Mössbauer isomer shifts'' (Edited by G.K. Shenoy and F.E. Wagner), North-Holland Pub. Co., Amsterdam (1978).  
''Topics in applied physics'' Vol. 5,
- [3] ''Mössbauer Spectroscopy'' (Edited by U. Gonser), Springer-Verlag, Berlin (1975).
- [4] ''Chemical applications of Mössbauer Spectroscopy'' (Edited by V.I. Goldanskii and R.H. Herber), Academic Press, New York (1968).
- [5] V.G. Bhide, ''Mössbauer Effect and its Applications'', New Delhi, 1973 (Tata McGraw-Hill).
- [6] N.N. Greenwood and T.C. Gibb, ''Mössbauer Spectroscopy'' (Chapman and Hall Ltd., London, 1971).
- [7] G.M. Bancroft, ''Mössbauer Spectroscopy an introduction for inorganic Chemists and Geochemists'' (Mc-Graw Hill, London, 1973).
- [8] E.A.C. Lucken, ''Nuclear Quadrupole Coupling Constants'', Academic Press, New York, p. 77 (1968).
- [9] W. Heitler, ''Quantum Theory of Radiation'', 3rd Ed., Oxford University Press, p. 200 (1954).
- [10] M. Blume, ''Hyperfine Structure and Nuclear Radiations'' (Eds. E. Matthias and D.A. Shirley), North-Holland, Amsterdam, p. 911 (1968).
- [11] M. Blume, Phys. Rev. Lett. 14, 96 (1965).

- [12] S. Dattagupta, Phys. Rev. B12, 47 (1975).
- [13] S. Dattagupta, Phys. Rev. B14 1329 (1976).



## CHAPTER 2

### EXPERIMENTAL

The principal components and equipment used in these experiments were : (i) a source of  $\gamma$ -ray generated by the decay of  $^{57}\text{Co}$  to  $^{57}\text{Fe}$ , (ii) the sample containing  $^{57}\text{Fe}$ , always used as the absorber, (iii) an electromechanical system acting as a drive unit to impart velocity to the source, (iv) the dewar and the furnace for keeping the absorber at the required temperature, (v) a  $\gamma$ -ray detector and (vi) a storage device (the multichannel analyzer) which stores the data as a function of the velocity of the source.

### 2.1 Instruments

#### 2.1.1 Electronic equipment

##### A) Mössbauer spectrometer

The spectrometer used in the present work contains a programmable velocity drive and an electromechanical transducer which was developed in this laboratory and constructed by M/s Encardio-Rite-Lucknow. This spectrometer has provision for constant velocity, constant acceleration and sinusoidal velocity modes. A precision velocity drive is realised, by generating signals with highly stable amplitude, frequency and phase, and connecting the transducer in a feed back loop. The block

diagram of the circuit is shown in Fig. 2.1. The drive signal is first generated in a highly stable 100 kHz crystal controlled oscillator. The output of this oscillator is scaled down by JK Flip-Flop to a 20 Hz square wave. The reference triangular wave for constant acceleration mode is generated by integrating the square wave by an active integrator using IC 741. The reference sine wave for the sinusoidal mode of the drive is obtained by extracting the fundamental component of the square wave through an active filter. The use of square wave to the input of the active filter minimises the second harmonic distortion in the output, because of the absence of even harmonics in a square wave. A reference trapezoidal wave for the constant velocity mode is generated by integrating the square wave in a suitable integrator. A trapezoidal wave, instead of square wave is used, so that the slew rate of the power amplifier and transducer is not exceeded which would otherwise result in ringing. An automatic gain control (AGC) circuit is provided after the integrator/active filter to stabilize the amplitude which is very critical for good performance. The AGC output is used as the reference signal for the transducer drive coil.

The transducer consists of a conventional double speaker arrangement, having a drive coil and a pick-up coil. The velocity is monitored by comparing the pick-up signal with the reference signal in an error amplifier. The difference between the two signals, called the error signal, is a measure of the deviation from the desired velocity. The error amplifier output is fed

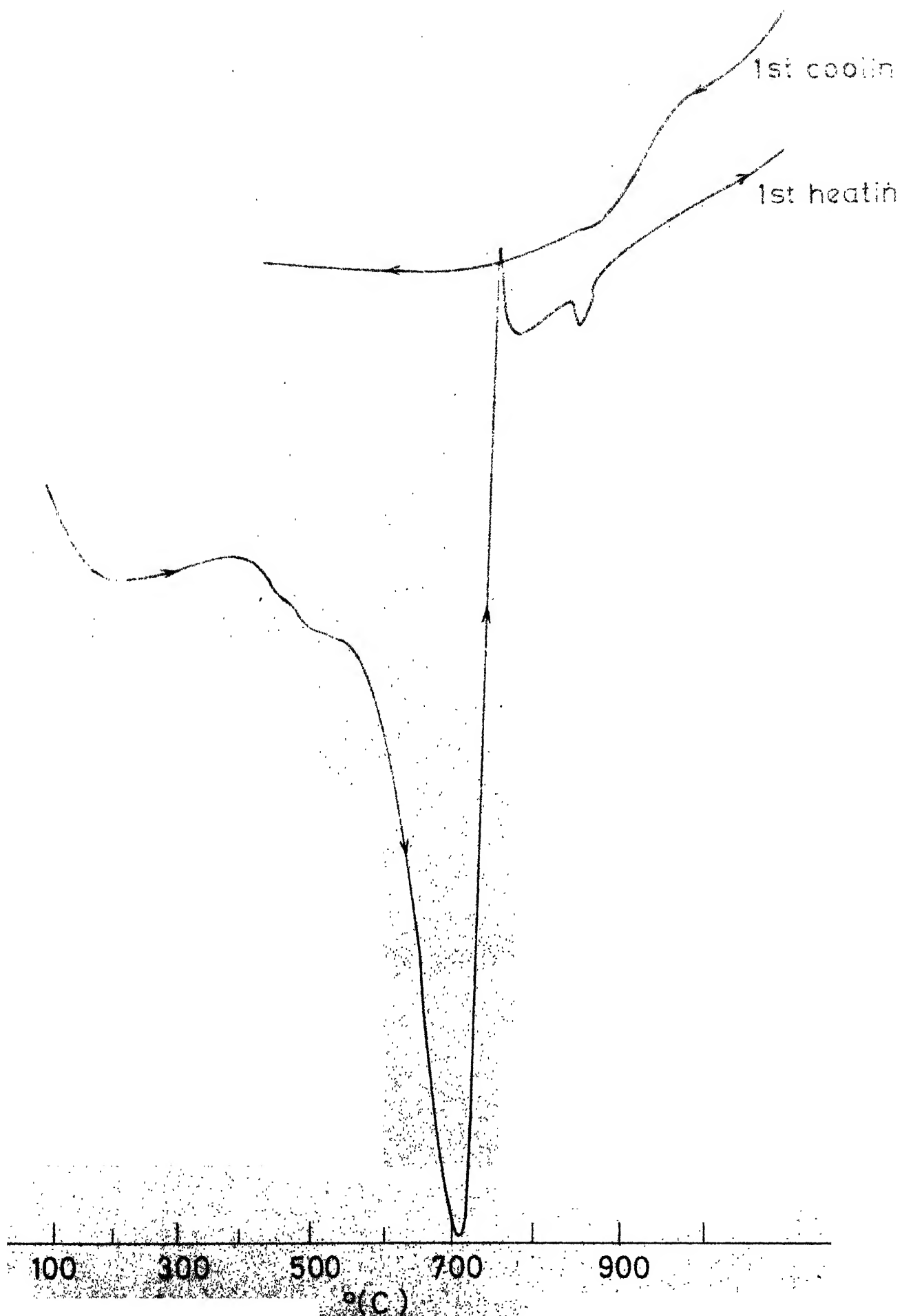


FIG. 4.7 DTA PATTERN OF RAW ALMORA MAGNESITE (-60+100

to a power amplifier which drives the transducer. Thus the transducer velocity follows the reference signal precisely in amplitude and phase. An MCS start pulse to reset the sweep in the MCA to the first channel is obtained by scaling down the complementary output of the penultimate  $\div 2$  stage by a factor of 2 which is again applied to a monostable multivibrator (74121) through a level shifter to get a narrow pulse of width 10  $\mu$ sec. The use of the complementary output synchronises the opening of the 1st channel of the MCA with the negative maxima of the velocity reference signal.

The design of the transducer is shown in Fig. 2.2. The impedance of the drive coil is matched with the output impedance of the power amplifier. The transducer is so designed that the frequency of unwanted vibrations, e.g. drum vibrations or overtones of the guided springs etc. are far away from the basic resonance frequency. The pick-up coil and drive coil are wound in grooves, at the two ends of a common holder, having diameter of 1.5'', which is made out of perspex. Each coil has a length of 0.3'' which is subdivided into three coils of length 0.1'' each. The three pick-up coils are connected in series and the drive coils are in parallel in the normal operation for impedance matching of the drive coil and to improve the linearity.

#### B. Detector and amplifier

For detection of  $\gamma$ -rays in our experiments we have used an argon-filled proportional counter with aluminised Mylar Window, procured from the Technical Physics Division, BARC,

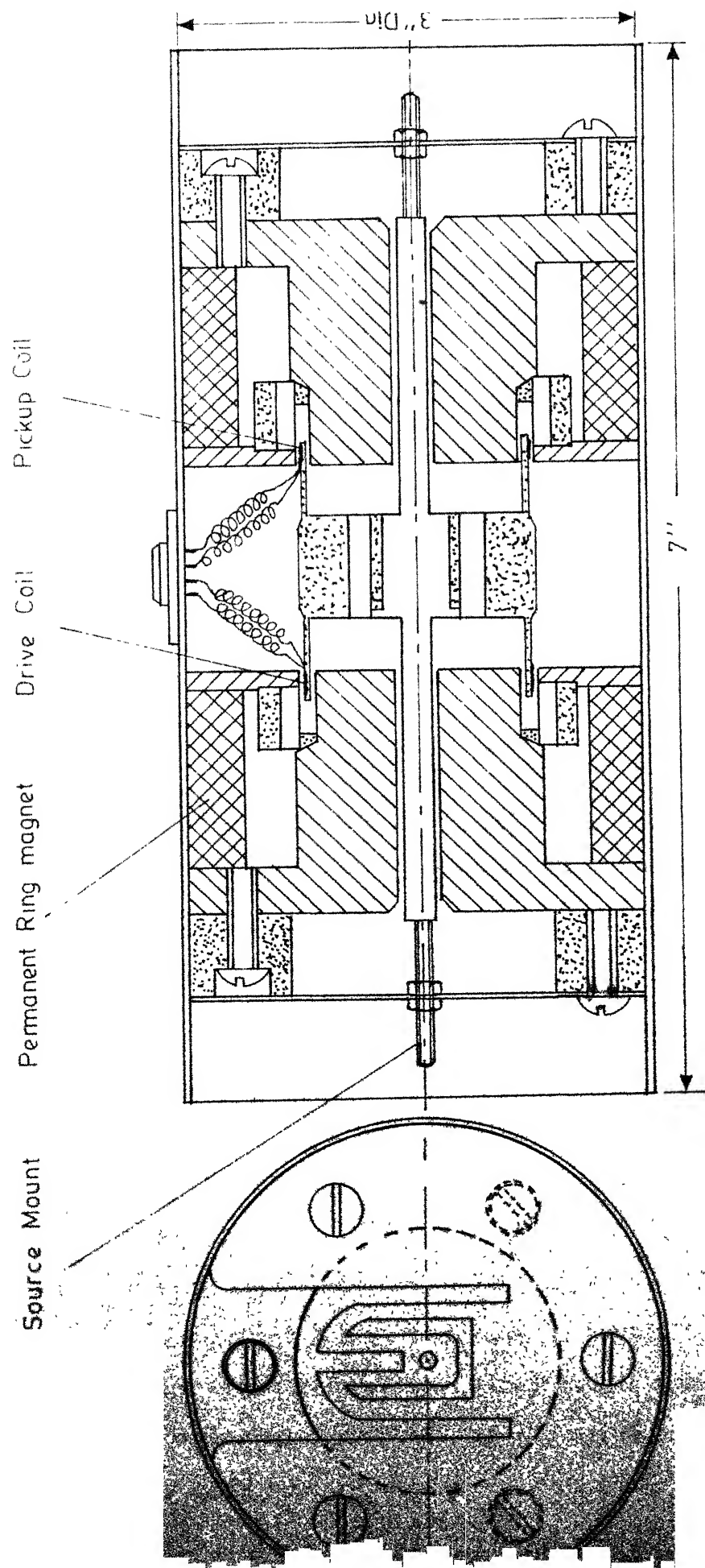


Fig. 2.2 Schematic diagram of the electromechanical transducer

Trombay, Bombay and a Krypton-filled proportional counter manufactured by Electronic Corporation of India Ltd. The author has fabricated a low noise, highly stable, temperature compensated, pre-amplifier for the proportional counter the schematic diagram of which is shown in Fig. 2.3. The signal from the pre-amplifier was amplified by an ORTEC Model 410 linear amplifier, the output of which is fed to the ND-60 multichannel analyzer. The FWHM observed for the 14 keV gamma rays with this set up is 2 keV for the argon-filled proportional counter.

#### C. Multichannel analyzer (MCA)

The ND-60 microprocessor based 2048 channel multichannel analyzer was used for selecting the 14.4 keV gamma rays and the storage of data. The MCA is operated in the multi-scaling mode with external channel reset, with a dwell time per channel of 100  $\mu$ sec for 512 channels operation and 50  $\mu$ sec for 1024 channel storage.

Multichannel scaling is comparable to counting in a series of scalers each being put into operation successively for a preset time, called the dwell time per channel. The address register in ND-60 can be advanced by the internal time base with a minimum loss of counts per channel during transition, so that the efficiency of counting is much higher. The sweep is triggered by the start pulse from the spectrometer in the MCS external mode, to get a stable peak. The counts acquired in each subsequent sweep is added.

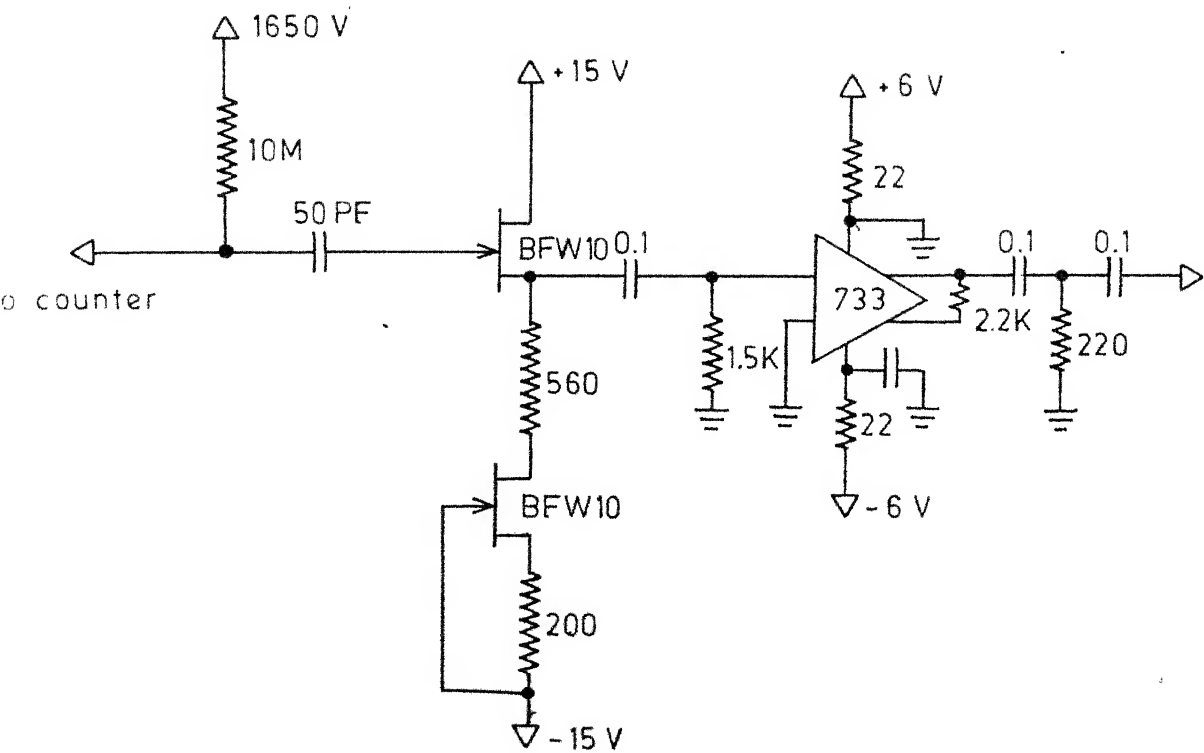


Fig. 2-3 Schematic diagram of the pre-amplifier

stored in the previous sweep.

The use of microprocessor memory in this analyser gives a better counting efficiency compared to the magnetic memory storage. The data can be printed out in a series line printer (Teletype) or can be plotted in a Hewlett Packard Model 7015A X-Y recorder.

#### D. Performance

The performance of the system was found to be good. The full width at half-maximum of the Mössbauer line obtained in the present work with Pottasium Ferrocynide absorber and  $^{57}\text{Co}$  in Rh matrix source was 0.27 mm/sec. This width includes the contributions from thickness of the source and absorber etc. The velocity per channel was found to be reproducible with in 0.1 % over a period of several weeks, once the spectrometer is set for a particular calibration.

##### 2.1.2 Furnace

The designs of vacuum furnaces for Mössbauer work at high temperatures ( $\sim 300^\circ\text{--}1300^\circ\text{K}$ ) are available in the literature [1,2,3,4]. Usually the heating coil is made of kanthal D wire wound on an alumina muffle mounted by means of ceramic flanges inside a brass cylinder (about 13 cm long and 15 cm diameter). Because of the involvement of large mass and different materials inside the furnace a large amount of power ( $\sim 1\text{ KW}$ ) is required for these furnaces and the amount of degassing and contamination of the sample is large at higher



temperatures. The outer brass cylinder requires an elaborate water cooling arrangement. The large size of the furnace brings restrictions on the versatility of its use, e.g. the geometry becomes poor with weak sources, and giving to and fro motions to the sample for recoilless fraction measurements etc. becomes difficult.

The author has designed a miniature quartz vacuum furnace [5] of light weight, requiring only small power (40 Watts), with temperature controlling facilities, and a small size giving good geometry and offering flexibility for various experimental operations. A special feature of the furnace is that it has got arrangements for induction as well as resistance heating. The induction method reduces the contamination of the sample, minimises heat losses and gives better temperature stability throughout the range of operation. The two modes of operation, i.e. induction and resistance, can be very easily interchanged. The resistance method may be used upto  $1000^{\circ}\text{K}$  whereas the induction method raise the sample temperature to  $1300^{\circ}\text{K}$  and, with suitable modifications, even higher.

The design of the furnace for resistance heating is shown in Fig. 2.4. A quartz tube of diameter 4.5 cm and length 8 cm has one end tapered to a diameter 2 cm. This end is permanently sealed with a mylar window which is shielded from thermal radiations of the heating coil by a thin sheet of beryllium. A flange is made at the other end, on which a circular brass or perspex disc with a mylar window (of diameter

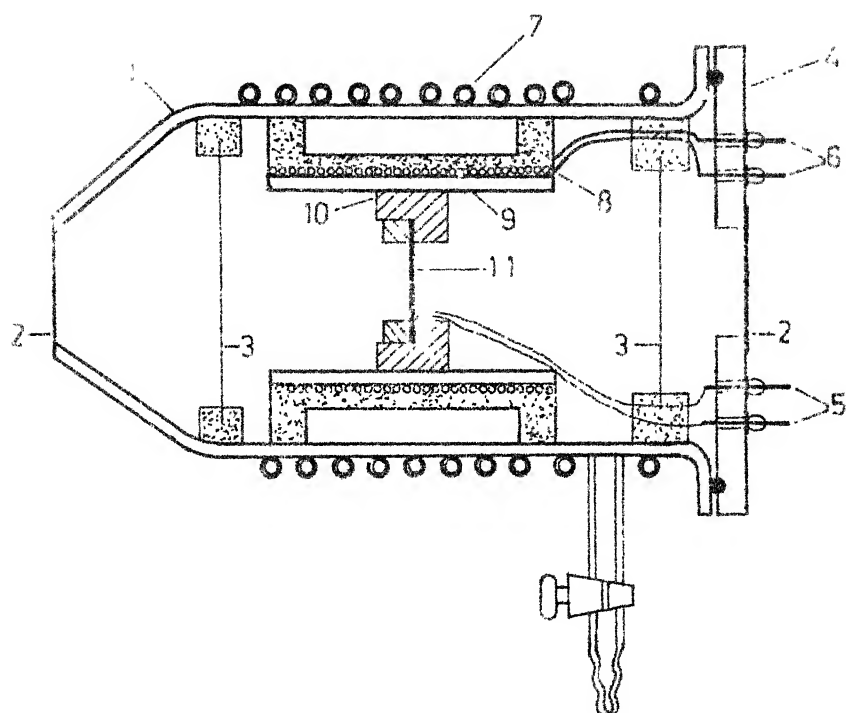


Fig. 2.4. Design of the furnace with resistance heating assembly.

2 cm) at its center, is kept pressed with an O-ring in between. The thermocouple and the heater connections are taken through the brass/perspex disc. A copper tube of diameter 6 mm is wound around the quartz tube for use as water-cooling system. This coil is also used as work coil during the induction heating. The tube can be evacuated by connecting a vacuum pump through the side tube, which can be closed by the stop cock after evacuation.

The heating assembly consists of a quartz or alumina muffle of 3 cm diameter and length 4 cm with nichrome wire wound on it non-inductively. The coil is kept in position by high temperature cement. Spacers made out of refractory brick are fixed at the two ends of the muffle.

The sample holder in the case of resistance heating is a copper disc of diameter 2.3 cm and thickness 1 cm with a groove of 2 cm diameter and an axial hole of 1 cm diameter. The Mössbauer absorber is kept between two thin discs of Fe-free synthetic mica, put on the groove and pressed by a copper ring. The sample holder is pushed snugly at the center of the muffle. The entire heating element with the sample is now put inside the outer quartz tube and the perspex/brass side disc clamped with brass clips. The temperature of the absorber is sensed by a chromel-alumel thermocouple, and kept steady by a solid state temperature-controller.

For induction heating the resistance heating system inside the quartz tube is replaced by an alumina tube of diameter 3 cm kept in position by refractory brick spacers.

The sample holder is made of two tantalum discs of diameter 2.5 cm and thickness 1 mm, kept in position inside the alumina tube by alumina rings. The high frequency (200 kHz) current is passed through the outer copper coil generating an induced eddy current in the tantalum sample holder and thus Joule heating the sample. The temperature is controlled by the temperature-controller which can switch on or off the high frequency current. The induction heating power supply is basically a plate-tuned vacuum tube (807 tetrodes) feed-back oscillator with the work coil coming as a part of the inductor in the tank circuit [Fig. 2.5].

The temperature-controller which the author has fabricated is basically a chopper stabilized amplifier working on a proportional on-off principle with the circuit as shown in Figs. 2.6a and 2.6b. When stabilized the load is switched on and off once every second. The duty cycle is controlled by the difference between the thermocouple and the reference levels. As the response time of the furnace is very long the furnace itself acts as an integrating element and the observed temperature is due to the average power being put to the system. For a miniature furnace as described above the temperature can be regulated to  $0.2^{\circ}\text{C}$  for low temperatures and within  $0.5^{\circ}\text{C}$  for high temperature. The characteristic of the design of the controller is such that it can be used with a load of any impedance.

The furnace system with the accessories has been used extensively in our laboratory for the studies of the temperature

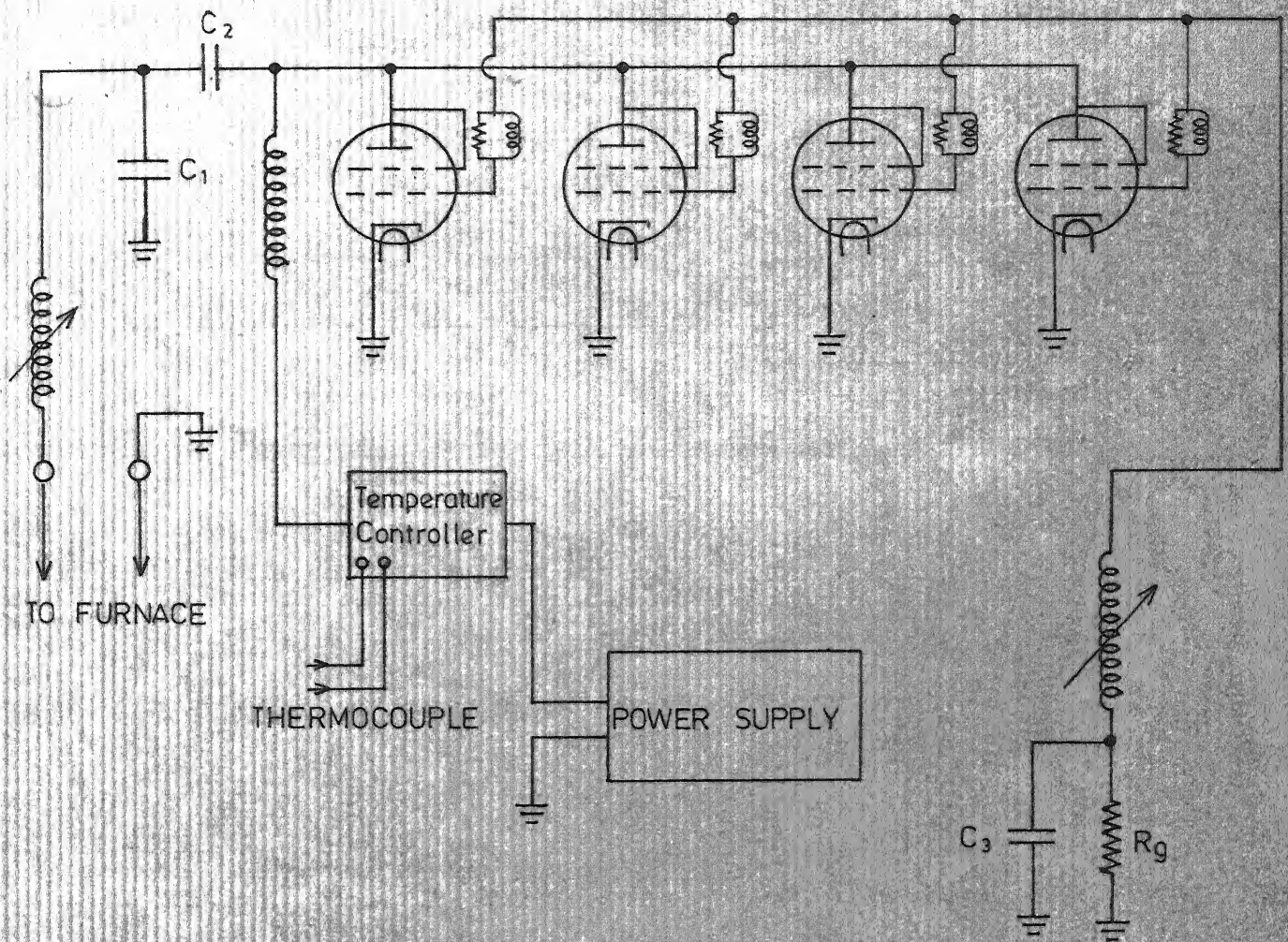


Fig.2-5 Power oscillator schematic diagram for induction heating



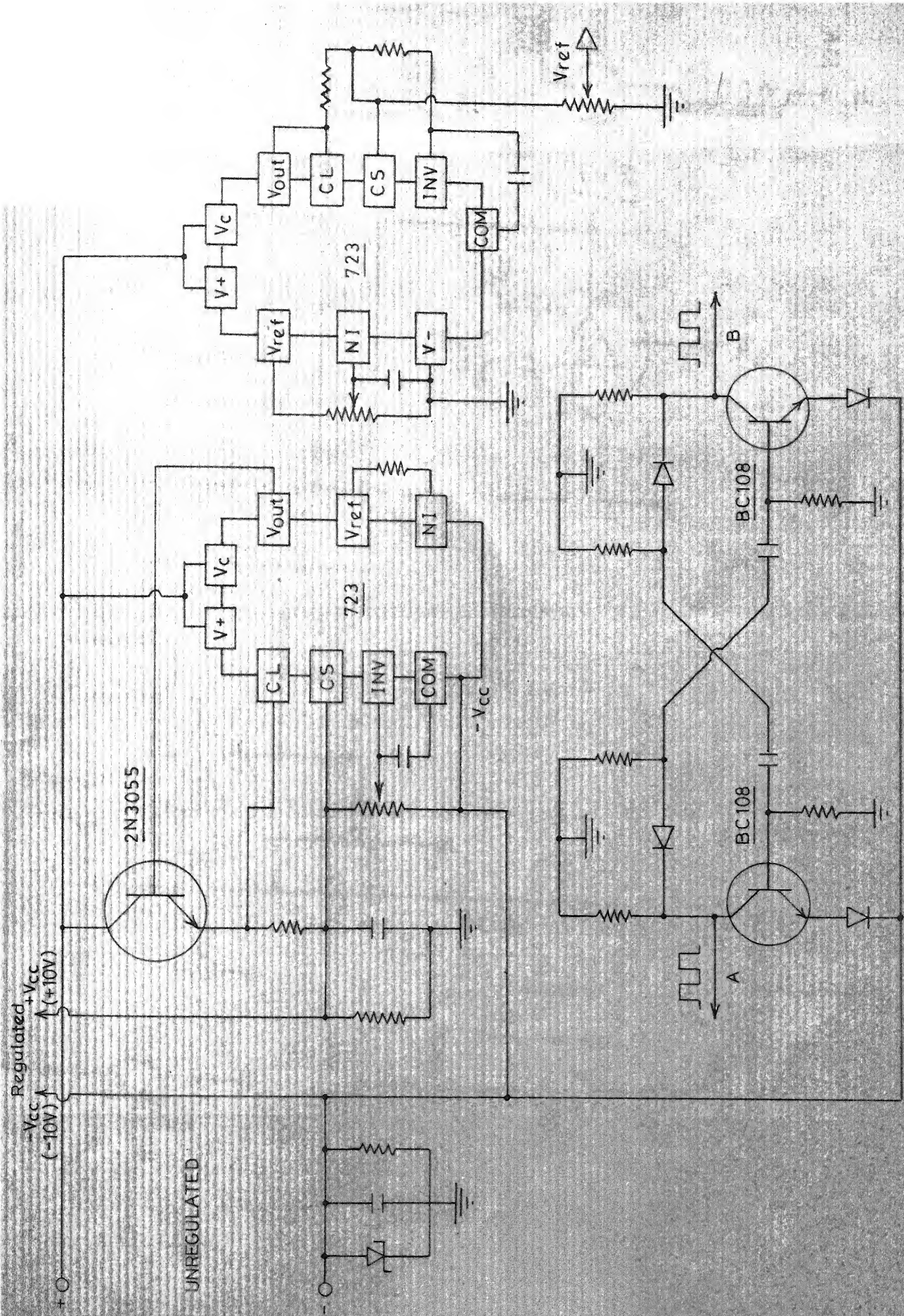


Fig 26a Power supply, oscillator and reference voltage for control amplifier.



**Fig. 2.6 Control amplifire of temperature controller (b)**

variation of Mössbauer spectra of a variety of systems. For the heating coil arrangement a 5 amp. -50 V d.c. commercial power supply was used. For a 50 Watt supply a temperature of  $700^{\circ}\text{C}$  could be attained. For the induction furnace an RF power of 250 Watts raised the temperature to  $900^{\circ}\text{C}$ . The temperature can be further raised by keeping the work coil inside the furnace. The temperature-controller was calibrated with respect to a chromel-alumel thermocouple by adjusting the reference voltage in the circuit so that each division of the ten-turn potentiometer dial corresponds to  $1^{\circ}\text{C}$ .

Some typical examples of the operation of the furnace in our laboratory are : study of the magnetic anisotropy and thermal decomposition of  $\text{Fe}(\text{NH}_4)_2(\text{SO}_4)_2 \cdot 6\text{H}_2\text{O}$  single crystals ( $300^{\circ}\text{K}$ - $500^{\circ}\text{K}$ , with heating coil), study of  $\text{Nd}_{0.33}\text{Fe}_{0.67}$  alloys at different temperatures ( $300^{\circ}\text{K}$ - $500^{\circ}\text{K}$ , with heating coil), study of Fe-Pd alloys ( $300^{\circ}\text{K}$ - $900^{\circ}\text{K}$ , with induction heating) etc. It is to be noted that there is no sideband by RF excitation [6]. This is due to the fact that the frequency used is very small ( $\sim 200$  kHz) compared to that required ( $\sim 30$  MHz) for RF excitation of magnetic materials [7].

### 2.1.3 Cryostat

A liquid nitrogen dewar was fabricated by the author for taking the Mössbauer spectra at temperature between 80-300 K. The design is shown in Fig. 2.7. It consists of two concentric cylindrical brass vessels both of which are connected by a thin walled stainless steel tube through which liquid nitrogen is



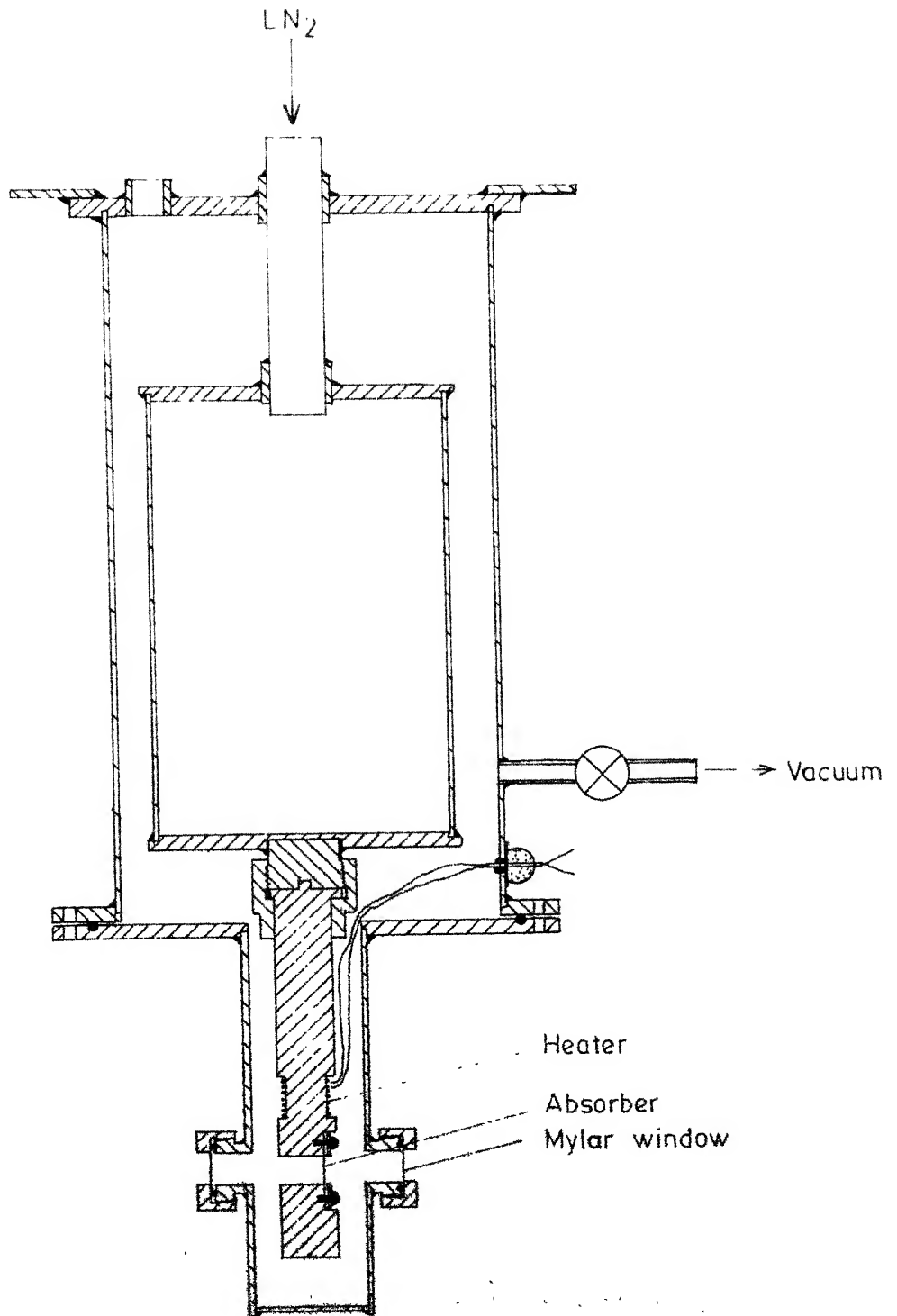


Fig.2-7 Design of the liquid nitrogen dewar used in Mössbauer experiments at temperatures between 80K and 300K

poured into the inner container. A demountable copper cold finger is attached to the inner vessel with provision for introducing suitable thermal insulation material between them, for efficient stabilisation of temperature of the cold finger at temperatures higher than  $80^{\circ}\text{K}$ . The thermal insulation between the two containers is provided by evacuating the space between them to a vacuum .02 micron which is measured by the ionisation gauge connected to the dewar at the top. The absorber can be kept pressed to the cold finger by flat thick copper square plate. This gives a better uniformity of temperature over the sample zone. Flat nichrome wire is wound on the cold finger with mica insulation near the sample zone for heating the finger. The temperature of the sample is measured by means of a copper-constantan thermocouple. The leads of the thermocouple and that of the heater are taken out through glass to metal seals fixed to the outer vessel. Demountable windows are provided on the outer vessel assembly for admitting gamma rays. Because of the demountability any type of window for the particular experiment can be easily fixed.

The bottom flange can be easily opened to change the samples. All parts of the dewar are nickel plated to prevent heating by radiation. A stainless steel stand assembly with rubber mountings for the legs is designed, and the dewar can be fixed to it at any height by the screws provided.

The temperature controller described along with the furnace is used to keep the temperature constant at any value between  $80\text{--}300^{\circ}\text{K}$  within an accuracy of  $0.4^{\circ}\text{C}$ . With one

poured into the inner container. A demountable copper cold finger is attached to the inner vessel with provision for introducing suitable thermal insulation material between them, for efficient stabilisation of temperature of the cold finger at temperatures higher than  $80^{\circ}\text{K}$ . The thermal insulation between the two containers is provided by evacuating the space between them to a vacuum .02 micron which is measured by the ionisation gauge connected to the dewar at the top. The absorber can be kept pressed to the cold finger by flat thick copper square plate. This gives a better uniformity of temperature over the sample zone. Flat nichrome wire is wound on the cold finger with mica insulation near the sample zone for heating the finger. The temperature of the sample is measured by means of a copper-constantan thermocouple. The leads of the thermocouple and that of the heater are taken out through glass to metal seals fixed to the outer vessel. Demountable windows are provided on the outer vessel assembly for admitting gamma rays. Because of the demountability any type of window for the particular experiment can be easily fixed.

The bottom flange can be easily opened to change the samples. All parts of the dewar are nickel plated to prevent heating by radiation. A stainless steel stand assembly with rubber mountings for the legs is designed, and the dewar can be fixed to it at any height by the screws provided.

The temperature controller described along with the furnace is used to keep the temperature constant at any value between  $80-300^{\circ}\text{K}$  within an accuracy of  $0.4^{\circ}\text{C}$ . With one

filling of the dewar by liquid nitrogen the liquid remains for about 12 to 14 hours.

## 2.2 Sources and Absorbers

### 2.2.1 Sources

The  $^{57}\text{Co}$  source in Rh matrix of strength 20 mCi used in these experiments was obtained commercially from New England Nuclear, Massachusetts USA. This source gave a line width of 0.26 mm/sec for Potassium Ferrocynide absorber with 0.5 mg  $^{57}\text{Fe}/\text{cm}^2$  distribution, with our set up. This width includes the width due to source, absorber and broadening due to absorber thickness. The recoilless fraction of the 14.4 keV  $\gamma$ -rays from this source is found to be 0.78, as measured by Trooster et al. [8] method, using natural iron foil 0.0005'' thick and a brass filter 0.005'' thick [9] for background correction.

This source satisfied the following requirements:

- i) The host matrix is chemically stable.
- ii) There is no electric field gradient or magnetic field at the site of the Mössbauer nuclei.
- iii) The recoil-free fraction is large.
- iv) The line width introduced by self absorption, thickness effect etc. is fairly small.
- v) The characteristic X-rays from the source matrix Rhodium (20-23.3 keV) is well above the Mössbauer gamma radiation, so that they can be easily eliminated by the single channel analyser.

$$t = \sigma n f_a \quad (2.3)$$

where  $\sigma$  is resonance cross section of the absorbing nuclei ( $^{57}\text{Fe}$ ),  $n$  is number of absorbing nuclei/cm<sup>2</sup> in the path of  $\gamma$ -rays and  $f_a$  is the recoilless fraction of the absorber.

In order that the least time is spent in Mössbauer absorption measurements, an absorber should be chosen, so that it will provide optimum statistics in a given time. That is it increases resonance absorption and reduces non-resonance absorption as far as possible.

The number of transmitted gamma rays at the resonance dip as a function of absorber thickness is given by the equation [9]

$$N(t, V_0) = (1-f) N + fN \exp(-t/2) J_0(i t/2) \quad (2.4)$$

Where  $t$  is the thickness parameter,  $V_0$  is the Doppler velocity and  $N$  is the number of  $\gamma$ -rays incident corresponding to the particular transition in the absorber. The amplitude of the Mössbauer line is then

$$N - N(t, V_0) = fN [1 - \exp(-t/2) J_0(\frac{i}{2}t)] \quad (2.5)$$

$J_0(x)$  being the zero order Bessel function of imaginary argument. The above equation expresses only the resonance effect as a function of Doppler energy. This expression suggests that the resonance absorption amplitude increases with thickness monotonically. It is obvious that as the number of active nuclei in the path of the  $\gamma$ -ray photon

increases the absorption will be more. However, if the absorber is too thick the non-resonant damping of all gamma rays will increase and the background noise will also increase resulting in masking of the spectrum. On the other hand making the absorber too thin, although increases the emergent beam, would reduce the resonance effect because of the fewer active nuclei in the path. Thus there must be an intermediate thickness, which for a given number of incident photons, will give a large absorption peak. When the non-resonant absorption is also taken into account [13] the amplitude becomes

$$N-N(d, V_0) = fN[1-\exp(-\mu_r d/2) J_0(i \frac{\mu_r d}{2})] \exp(-\mu_a d) \dots\dots\dots (2.6)$$

when  $\mu_r$  and  $\mu_a$  are the maximum resonant and non-resonant absorption coefficients. The relation between  $\mu_r$  and  $\sigma$  is

$$\mu_r = \left(\frac{n}{d}\right) \sigma f_a \quad (2.7)$$

when  $d$  is the actual thickness of the sample and  $\frac{n}{d}$  is the density of the active nuclei. Shimony [14] has maximised this with respect to  $d$  to get the highest peak for a given  $N$ . The optimum thickness in that case is given by the relation

$$\frac{\mu_r}{2\mu_a} = \frac{\exp(1/2 \mu_r d_0) - J_0(1/2 i \mu_r d_0)}{J_0(1/2 i \mu_r d_0) + J_1(1/2 i \mu_r d_0)} \quad (2.8)$$

using the identity  $\frac{d(J_0(x))}{dx} = -J_1(x)$ .

If we instead concentrate on a good spectrum with minimum statistical uncertainty a better parameter for that is

$$\alpha = \frac{\text{Amplitude of the absorption dip}}{\text{Statistical uncertainty in the counts}}$$

At velocities far away from  $V_0$  the counts are

$$N(d, \infty) = N \exp(-\mu_a d)$$

If the absorption is not too large the statistical uncertainty is given as

$$\begin{aligned} \Delta N &= [N(d, \infty)]^{\frac{1}{2}} \\ &= [N \exp(-\mu_a d)]^{\frac{1}{2}} \end{aligned}$$

$$\therefore \alpha(d) = f \sqrt{N} [1 - \exp(-\mu_r d/2) J_0(\frac{i\mu_r d}{2})] \exp(-\mu_a d/2) \quad (2.9)$$

Equating the derivative of  $\alpha(d)$  with respect to  $d$  to zero we get

$$\frac{\mu_r}{\mu_a} = \frac{\exp(1/2 \mu_r d_0) - J_0(1/2 i \mu_r d_0)}{J_0(1/2 i \mu_r d_0) + J_1(1/2 i \mu_r d_0)} \quad (2.10)$$

from this equation  $d_0$  can be found out in terms of  $\mu_r$  and  $\mu_a$ .

In the case of  $\text{FeSO}_4 \cdot 7\text{H}_2\text{O}$  using the above method and

$\mu_r = 35.96$  and  $\mu_a = 22$  and from the table in ref. [14], we get  $d \approx 40 \text{ mg/cm}^2$ .

### 2.3 Effect of Geometry

The geometry introduces two types of distortions in the Mössbauer spectrum. Because of the movement of the source the distance between the source and detector changes. The count

rate then changes with an  $1/r^2$  dependence which causes a non-flat base line in the spectrum. For example in the constant acceleration mode the velocity at any instant  $t$  is given by

$$V(t) = -V_0 + \frac{4V_0}{T} t$$

for  $0 \leq t \leq T/2$  and

$$V(t) = 3V_0 - \frac{4V_0}{T} t \quad \text{for } T/2 \leq t \leq T$$

where  $V_0$  is the amplitude of velocity and  $T$ , its time period.

The distance between source and absorber at any instant from these equations is

$$x(t) = -V_0 t + \frac{2V_0}{T} t^2 + x_0 \quad 0 \leq t \leq T/2 \quad \text{and}$$

$$x(t) = 3V_0 t - \frac{2V_0}{T} t^2 + x_0 \quad T/2 \leq t \leq T$$

$x_0$  is the distance of the source from detector at  $t = 0$ , i.e. when the source is at its equilibrium position. At  $t = T/2$

$$x_0 = x_0 - V_0 T$$

Writing  $x(t) = X_0 + x(t)$

$$x(t) = -V_0 t + \frac{2V_0}{T} t^2 \quad 0 \leq t \leq T/2 \quad \text{and}$$

$$x(t) = 2V_0 t - \frac{2V_0}{T} t^2 \quad T/2 \leq t \leq T$$

The count rate in the absence of any absorber is given by

$$C(t) = \frac{K}{[X_0 + \Delta X(t)]^2}$$

where  $K$  is a constant.



The maximum value of  $|\Delta x|$  is at  $t = T/4$  or  $3T/4$ , where the velocity is zero, i.e. at the turning points.

$$|(\Delta x)|_{\max} = \frac{V_0 T}{8}$$

In our system for  $T = 50$  millisecc. and  $V_0 = 10$  mm/sec,  $\frac{V_0 T}{8} = 0.05$  mm. If  $x_0 = 5$  cm,  $\frac{\Delta x}{x_0}$  is nearly 0.001. By expanding the expression for  $C(t)$  using binomial theorem

$$C(t) = \frac{K}{x_0^2} \left[ 1 - \frac{2 \Delta x}{x_0} + \dots \right]$$

The first order shift in base line then comes as 0.1 %.. This can be neglected for samples having good percentage absorption. In our experiments we have kept the distance between the source and detector at 10 cm. The method of nullifying this effect is to 'fold' the spectrum about the maximum velocity. This eliminates the effects due to change in count rate in the first order and improves the statistics if the lines are narrow [15]. The linearity of the velocity cycle is improved in both halves by this method.

The other effect known as the 'cosine smearing effect' is caused by the finite size of the source and the absorber. The gamma rays reaching the detector have different angles with respect to the direction of motion of the source. If this angle is  $\theta$ , the gamma ray energy as seen by the absorber will be

$$E'(\theta) = E_0 \left( 1 - \frac{v \cos \theta}{c} \right)$$

If  $\theta$  is large (when the detector and source separation is small) this effect will be pronounced and it causes a broadening of the lines in the absorption spectrum and even changes the shape of the spectrum.

## 2.4 Data Analysis

### 2.4.1 Calibration

For finding the velocity per channel of the sample, calibration spectra were taken before and after each experimental run. For calibration samples were either enriched iron or sodium nitroprusside (SNP) in our experiments.

For isomer shift measurements SNP and 310 stainless steel were used as reference materials. These standard absorbers were obtained commercially from Radio Chemical Centre Amersham, Harwell, U.K.

### 2.4.2 Computer programmes

If the relaxation effects are small, the Mössbauer absorption line can be well approximated by a Lorentzian curve. There are many programmes available now to analyse the Mössbauer data. The basic method is almost the same, where some functional form for the absorption peak is assumed, for example as Lorentzian or Lorentzian + Gaussian etc. The main purpose of these curves fittings are to find the values of the adjustable parameters (guess values), which provide the closest agreement between experimental data and the values predicted

by the assumed function.

The method used to find the best parameter in our programme is based upon the method developed by V.J. Law and R.V. Bailey [16,17]. Let  $\phi_i = \phi_i(B_1, B_2, \dots, B_m)$  be the functional form chosen for the experimental points  $Y$ . We wish to find a set of parameters  $B_k$  such that

$$S^2 = \sum_{i=1}^N S_i^2 = \sum_{i=1}^N (Y_i - \phi_i)^2$$

is minimised ( $N$  is the number of data points). The condition for this is  $(dS^2/B_k) = 0$ . If this is done a set of  $m$  simultaneous equations will be obtained. These equations are solved to get the corrections  $\Delta B_k$  and new values of the parameters  $B_k^{i+1} = B_k^i + \Delta B_k$  are obtained where the superscript  $i$  refers to the  $i^{\text{th}}$  iteration.

To ensure that the new values are better,  $\Delta B_k$  is changed in small steps at the point of convergence so that  $S^2$  is minimum.

The function  $\phi$  and its derivatives are calculated in a separate subroutine. A change in functional form can be accommodated by making changes only in this subroutine.

The programme also gives the error matrix [18] from which the standard error in the fitted parameters  $B_m$  can be calculated. All the computation are done in the DEC 1090 computer of I.I.T. Kanpur. We have developed other computer programmes for finding the  $P(H)$  distribution in magnetic hyperfine split spectra as well as EFG distribution

CENTRAL LIBRARY

I. I. T., Kanpur.

Acc. No. **A 82714**

in the case of quadrupole split spectra, which will be discussed later in this thesis. Recoilless fraction and Debye temperature of some of the samples were also found out for which computer programmes were made by the author.

REFERENCES

- [1] D.E. Nagle, Phys. Rev. Lett. 5, 364 (1960).
- [2] R.S. Preston, S.S. Hanna and J. Heberle, Phys. Rev. 128, 2207 (1964).
- [3] V.S. Sundaram and V.P. Gupta, Rev. Sci. Instr. 42, 1616 (1971).
- [4] F. Van der Woude and G. Boom, Rev. Sci. Instr. 36, 800 (1965).
- [5] N.V. Nair and D.C. Khan, Nucl. Instr. and Meth. (communicated).
- [6] L. Pfeiffer and N.D. Heiman, Phys. Rev. B6, 74 (1972).
- [7] M. Chmielowski and A. Kotlicki, Hyp. Int. 10, 1129 (1981).
- [8] J.M. Trooster and M.P.A. Vieggers, "Mossbauer Effect Reference and Data Journal", 1, 154 (1978), edited by J.G. Steven~, (IFI/Plenum, New York).
- [9] R.M. Housley, W.E. Erickson and J.G. Dasn, Nucl. Instr. and Meth. 27, 29 (1964).
- [10] S. Margulies and J.R. Ehrman, Nucl. Instr. and Meth. 12, 131 (1961).
- [11] D.A. Shirley, M. Kaplan and P. Axel, Phys. Rev. 123, 816 (1961).
- [12] D.A. O'Connor, Nucl. Instr. and Meth. 21, 318 (1963).
- [13] A.J. Stone, Nucl. Instr. and Meth. 107, 285 (1973).
- [14] U. Shimony, Nucl. Instr. and Meth. 37, 348 (1965).
- [15] Takayuki Kobayashi and Kazuko Fukumura, Nucl. Instr. and Meth. 173, 363 (1980).

- [16] V.J. Law and R.V. Bailey, Chem. Eng. Sc. 18, 139 (1963).
- [17] H.C. Verma, Ph.D. Thesis, Indian Institute of Technology, Kanpur, India (1980) (unpublished).
- [18] J.R. Wolberg, 'Prediction Analysis', D. Van Nostrand Company Inc., Princeton (1967).

## CHAPTER 3

### MÖSSBAUER STUDIES OF SOME FERROUS COMPLEXES - A NEW LOOK INTO THE OLD SYSTEMS

#### 3.1 Introduction

We present in this chapter some new findings in the well known systems such as  $\text{FeSO}_4 \cdot 7\text{H}_2\text{O}$ ,  $\text{Fe}(\text{SO}_4)_2 \cdot (\text{NH}_4)_2 \cdot 6\text{H}_2\text{O}$ , when an electric field is applied parallel to the direction of  $\gamma$ -rays [1] and also the electric field gradient distribution and isomer shift distribution in several such complexes using the model independent method. The absolute recoilless fraction in these systems are determined using the method adopted by Johnson et al. [2], with modifications.

#### 3.2 Mössbauer Studies of $\text{FeSO}_4 \cdot 7\text{H}_2\text{O}$ and $\text{Fe}(\text{SO}_4)_2(\text{NH}_4)_2 \cdot 6\text{H}_2\text{O}$ Under Applied Electric Field

Mössbauer spectra of powdered samples of  $\text{FeSO}_4 \cdot 7\text{H}_2\text{O}$  and  $\text{Fe}(\text{SO}_4)_2(\text{NH}_4)_2 \cdot 6\text{H}_2\text{O}$  under an externally applied field along the direction of the  $\gamma$ -rays were studied. Even though the internal crystal field was expected to be several orders of magnitude more than the applied field, the detection of the effect by a high-resolution spectrometer was not ruled out. As reported below, the induced ~~Stark~~ effect was clearly identifiable in one of the systems, namely,  $\text{FeSO}_4 \cdot 7\text{H}_2\text{O}$ .

Commercially available high-purity  $\text{FeSO}_4 \cdot 7\text{H}_2\text{O}$  was powdered (Merck analytical reagent) and kept between two capacitor plates as a thin layer with a distribution of  $40 \text{ mg/cm}^2$ . Mössbauer spectra were obtained at room temperature for various applied fields up to  $45 \text{ kV/cm}$  along the  $\gamma$ -ray direction using the highly stable constant-acceleration spectrometer.

The Mössbauer absorption spectrum of  $\text{FeSO}_4 \cdot 7\text{H}_2\text{O}$  at zero external field was a quadrupole doublet with  $\Delta E_Q = 3.198 \pm 0.003 \text{ mm/sec}$  and isomer shift  $1.383 \pm 0.002 \text{ mm/sec}$  [Fig. 3.1(a)]. The values agree quite well with the standard values quoted in the literature [3-7]. Under the application of the external electric field, it was found that  $\Delta E_Q$  increases up to  $3.247 \pm 0.003$  for a maximum field of  $45 \text{ kV/cm}$  [Fig. 3.1(b)]. The variation of  $\Delta E_Q$  with the applied field is shown in Fig. 3.2. The line shape is Lorentzian with full width at half maximum (FWHM)  $0.278 \pm 0.004 \text{ mm/sec}$  (for zero field) which is comparable with linewidth of  $^{57}\text{Co}$  in Rh.

The isomer shift changes from  $1.383 \pm 0.002 \text{ mm/sec}$  to  $1.411 \pm 0.002 \text{ mm/sec}$  for the same range of applied voltage (Fig. 3.3). The intensity ratio of the two peaks ( $|\frac{3}{2}, \pm \frac{1}{2}\rangle \rightarrow |\frac{1}{2}, \pm \frac{1}{2}\rangle$  and  $|\frac{3}{2}, \pm \frac{3}{2}\rangle \rightarrow |\frac{1}{2}, \pm \frac{1}{2}\rangle$  transitions) at room temperature at zero field was unity. However, with increase of field a texture effect was produced which generated an asymmetry of line shapes. The intensity ratio decreased linearly with the field, reaching a value of 0.86 at  $45 \text{ kV/cm}$  (Fig. 3.4). The texture effect cannot be due to alignment of the small crystallites



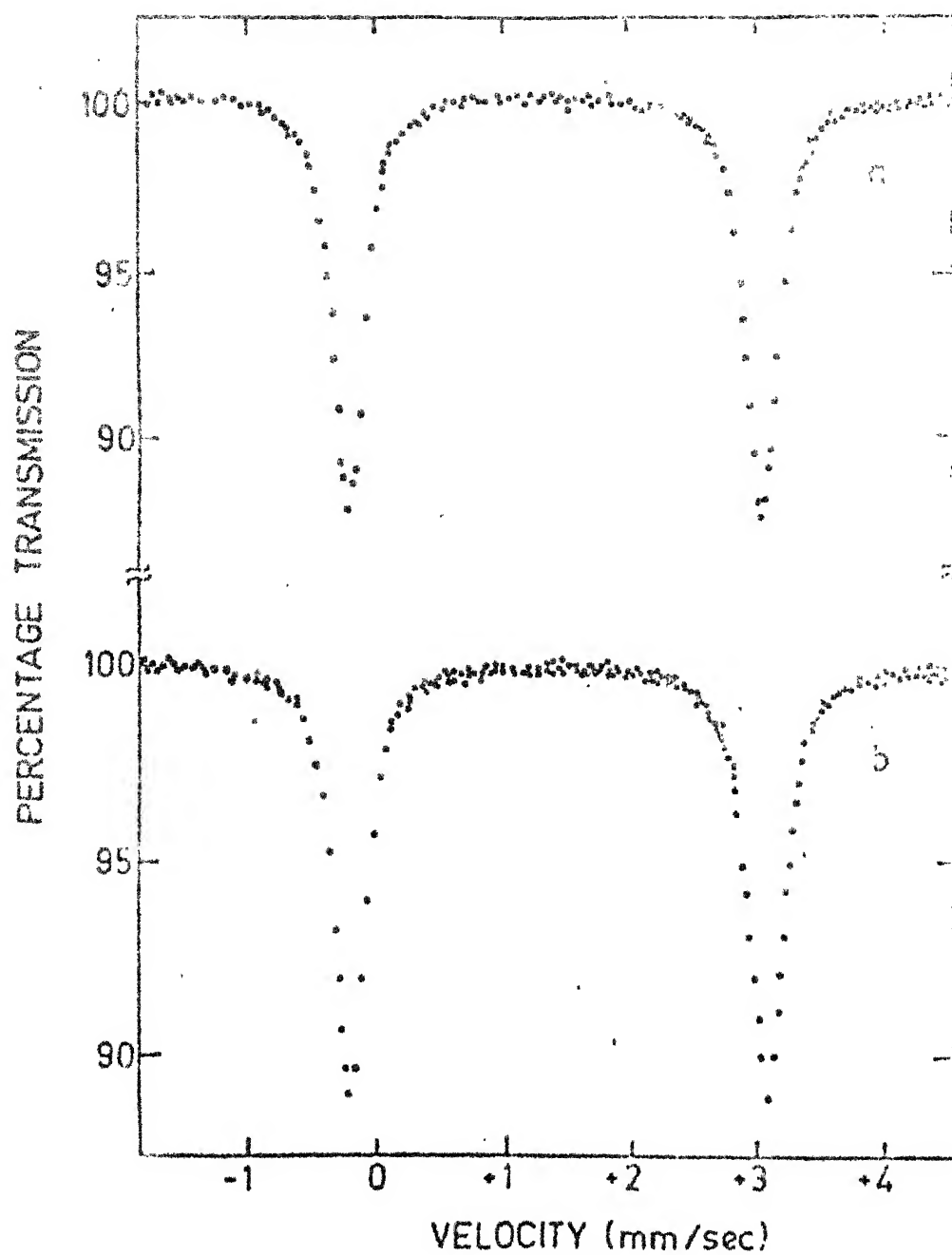


Fig 31. Mössbauer spectra of  $\text{FeSO}_4 \cdot 7\text{H}_2\text{O}$  at  
(a) Zero field (b) 45KV/cm.

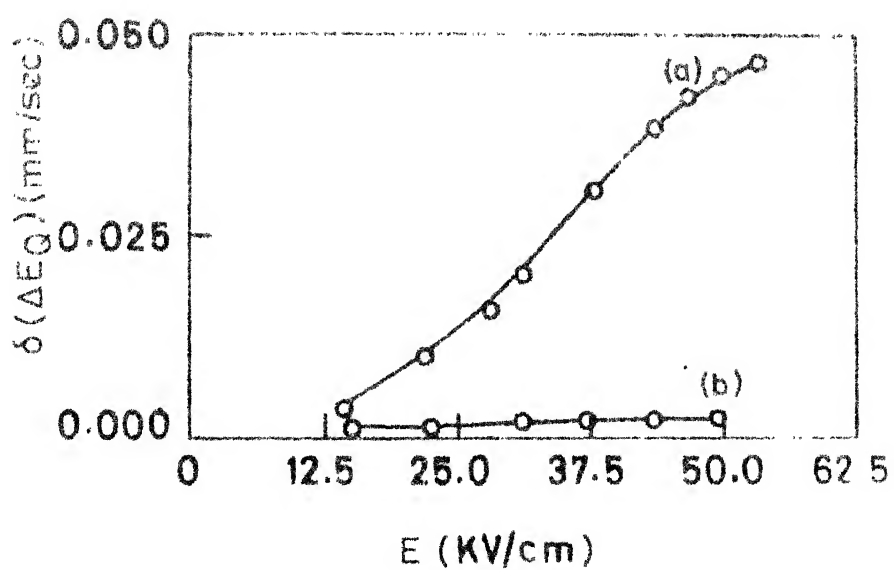
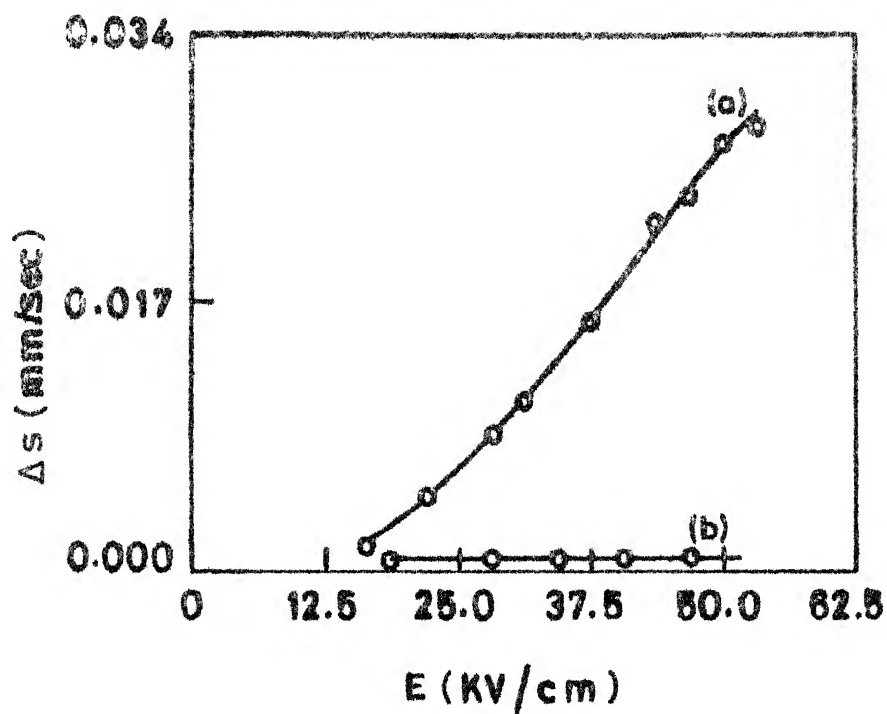


Fig.32. Change in quadrupole splitting with applied field in  $\text{FeSO}_4 \cdot 7\text{H}_2\text{O}$  (curve a) and in  $\text{Fe}(\text{SO}_4)_2 \cdot (\text{NH}_4)_2 \cdot 6\text{H}_2\text{O}$  (curve b)



**Fig.33** Change in Isomeric shift with applied field in  $\text{FeSO}_4 \cdot 7\text{H}_2\text{O}$  (curve a) and in  $\text{Fe}(\text{SO}_4)_2(\text{NH}_4)_2 \cdot 8\text{H}_2\text{O}$  (curve b)

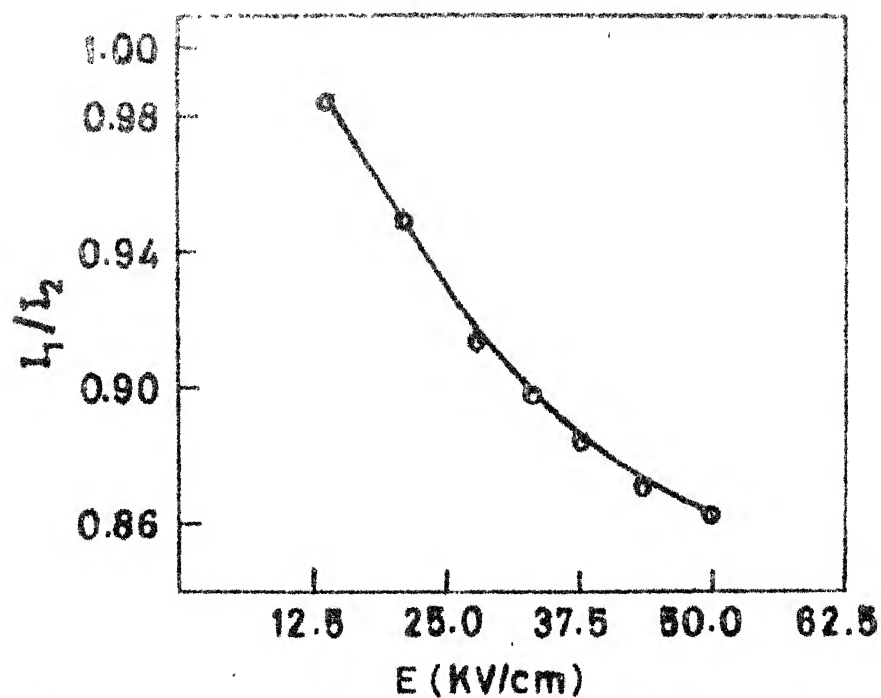


Fig.34 Variation of intensity ratio of the two peaks with applied field in  $\text{Fe SO}_4 \cdot 7\text{H}_2\text{O}$

of the powder, since they were immobilized with an epoxy binder. The effects described in the Figs. 3.2 3.3 and 3.4 were found to be reversible as the external electric field was decreased from  $V_{\max}$  to zero.

The experimental values at room temperature for  $\text{Fe}(\text{NH}_4)_2(\text{SO}_4)_2 \cdot 6\text{H}_2\text{O}$  at zero field were  $1.764 \pm 0.002$  mm/sec for quadrupole splitting and  $1.400 \pm 0.002$  mm/sec for isomer shift in agreement with the standard values [6,8]. However, there was no change in any of the above values up to an applied field of 31.4 kV/cm. Above this field two new outer peaks appeared with  $\Delta E_Q = 2.885 \pm 0.002$  mm/sec, and isomer shift  $1.317 \pm 0.002$  mm/sec. The spectrum for this system at zero and 31.4 kV/cm are shown in Figs. 3.5(a) and 3.5(b), respectively. A texture effect was observed for this system also.

Bashkirov and Lebedev [9] have recently made a perturbation calculation of the polarization of the  $\text{Fe}^{3+}$  ion 4s shell by an electric field and its contribution to the quadrupole splitting and isomer shift. For a field  $E = 45 \times 10^3$  V/cm, using their Eqs. (2) and (3), the 4s-shell polarization effect tends to zero. Hence, the contribution could be due to the 3d-shell polarization and/or the effect of the induced dipoles at the lattice sites (for  $\Delta E_Q$  only). To our knowledge, the problem of the effect of a perturbation  $E_z$  on the 3d-electron states has not been worked out yet. Another approach would be to use the axial symmetry of the operator and suitably augment the  $B_2^0$  coefficient of Eq. (7) of Ingalls [3] paper on

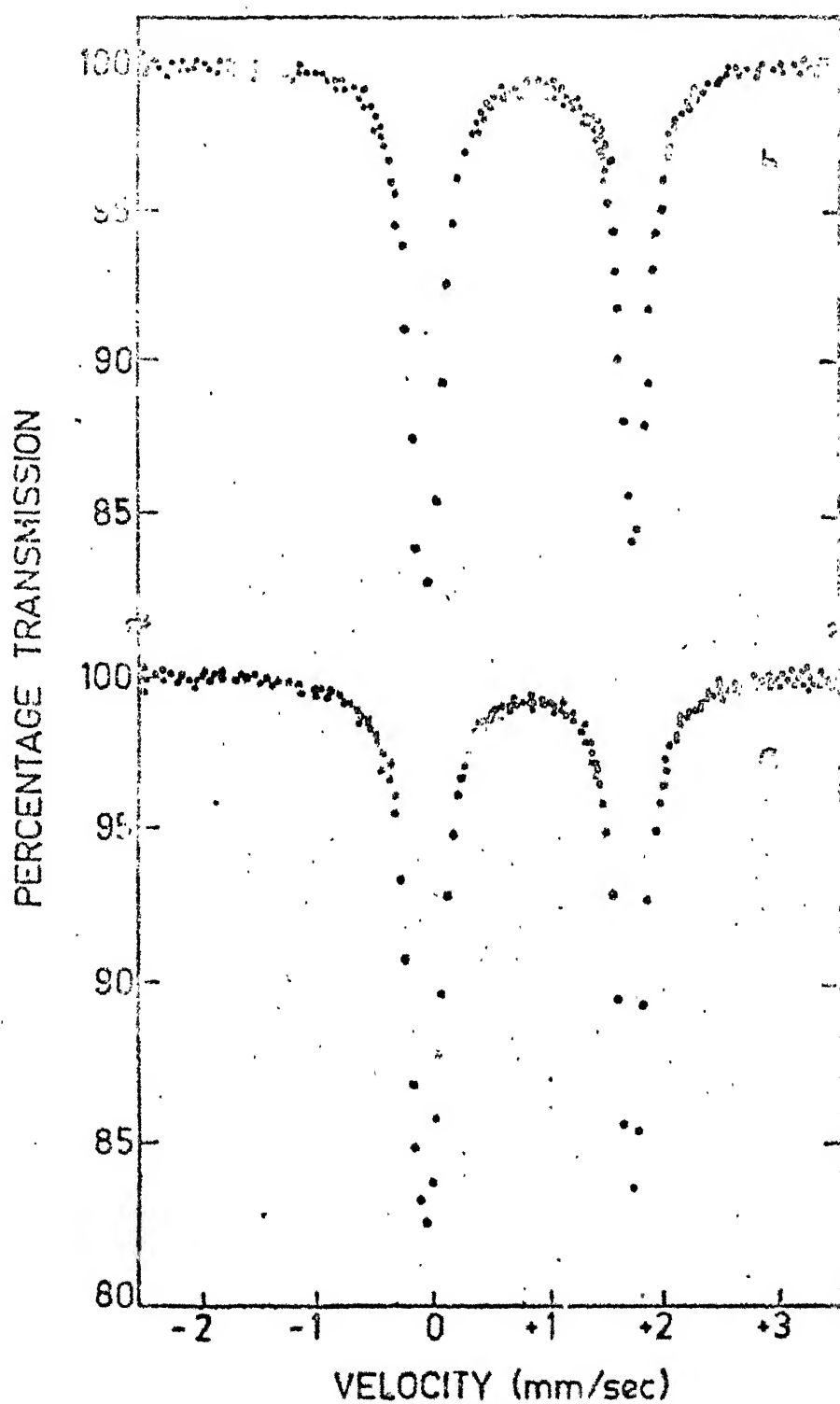


Fig.35. Mössbauer spectra of  $\text{Fe}(\text{SO}_4)_2(\text{NH}_4)_2 \cdot 6\text{H}_2\text{O}$  at (a) Zero field (b) 30KV/cm.

EFG tensor in ferrous compounds. The lattice dipole effect could be calculated classically. Experiments with other systems with larger fields up to the dielectric breakdown limit will enhance the requirement for a detailed theoretical calculation.

The extra peaks (Fig. 3.6) in the  $\text{Fe}(\text{SO}_4)_2(\text{NH}_4)_2 \cdot 6\text{H}_2\text{O}$  appearing with the application of high voltage sufficient to break the dielectric is possibly linked either with the change of the hydration states [10] or with the implantation of electrode (Al) atoms in the system.

### 3.3 Electric Field Gradient and Isomer Shift

#### Distributions from Mössbauer Spectra

##### 3.3.1 Introduction

Recently considerable attention has been paid to the line broadening of the Mössbauer spectra due to absorber thickness [11-22]. But even with very thin absorbers the line broadening can be appreciable due to the distribution of the isomer shift, the quadrupole splitting and the hyperfine field. Chien [23] has applied Window's method [24] for finding the hyperfine magnetic field distribution in amorphous ferromagnet  $\text{Fe}_{80}\text{B}_{20}$  and Narayanaswamy et al. [25] applied this method to find out hyperfine field distribution in disordered binary alloys of  $\text{Ni}_3\text{Fe}$ ,  $\text{NiFe}$  and  $\text{FeCo}$ . Eibschutz et al. [26,27] interpreted the large width of vitreous YIG as being due to the

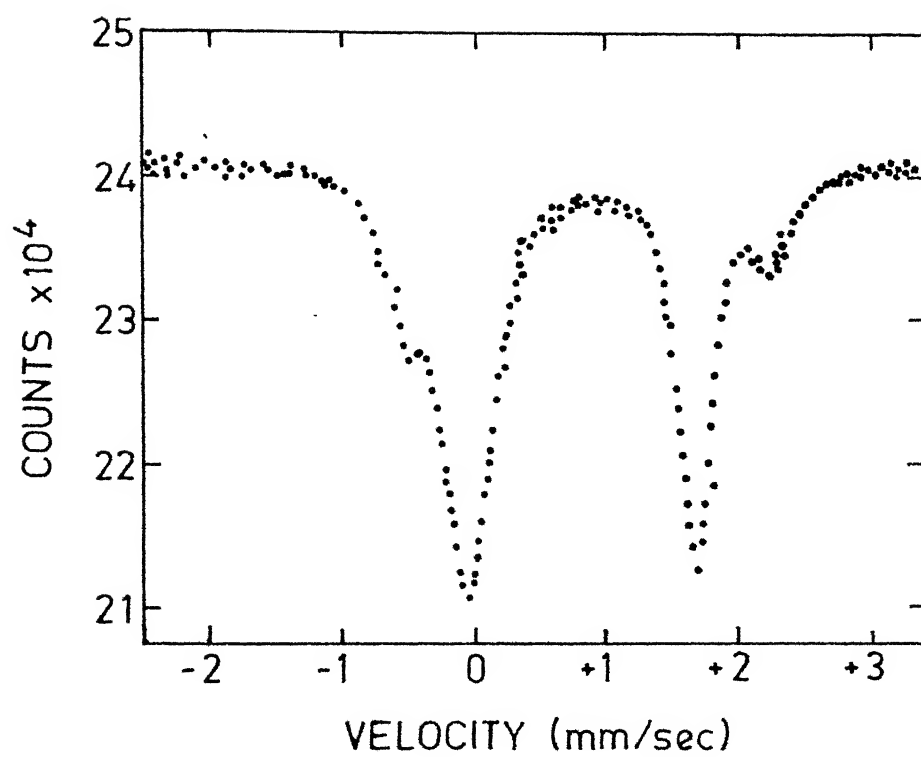


Fig. 3.6. Mössbauer spectrum of  $\text{Fe}(\text{SO}_4)_2(\text{NH}_4)_2 \cdot 6\text{H}_2\text{O}$  at 35KV/cm.



distribution of the electric field gradient at Fe sites. They described the quadrupole split doublet line shape  $f(Z)$  by a distribution  $p(|V|)$  of Lorentzian lines. The EFG distribution  $p(|V|)$  was derived from a computer model developed for the sequential addition of hard spheres [28].

The present authors have applied Window's method for determining the distribution of electric field gradient in certain well known ferrous complexes, e.g.  $\text{FeSO}_4 \cdot 7\text{H}_2\text{O}$ ,  $\text{Fe}(\text{NH}_4)_2(\text{SO}_4)_2 \cdot 6\text{H}_2\text{O}$ ,  $\text{Na}_2[\text{Fe}(\text{CN})_5\text{No}] \cdot 2\text{H}_2\text{O}$  (SNP) and an amorphous system [34]  $35 \text{ Na}_2\text{O} + 55 \text{ SiO}_2 + 10 \text{ Fe}_2\text{O}_3$ . The isomer shift distribution of  $\text{K}_4\text{Fe}(\text{CN})_6 \cdot 3\text{H}_2\text{O}$  and 310 stainless steel have also been analyzed by this method. The present work introduces the viewpoint that this distribution method need not be restricted to amorphous systems only, but can be utilized successfully for crystalline systems, improving the agreement with the experimental data as compared to standard Lorentzian fitting and giving information about the local defects or environmental changes around the Fe-ion.

### 3.3.2 Computational method

For an EFG distribution  $p(|V|)$  we can in general describe the Q.S. doublet line shape  $f(Z)$  by a distribution  $p(|V|)$  of the Lorentzian lines in the form

$$f(Z) = h \int_{-\infty}^{+\infty} \frac{p(|V|)}{1 + 4[(Z-V)/W]^2} dV \quad (3.1)$$

where  $V$  is the principal component of EFG,  $W$  is the full

Lorentzian width at half maximum and  $h$  is the amplitude of the line.

$p(|V|)$  is expanded in a cosine series with the boundary conditions

$$\left(\frac{dp}{dV}\right)_{V=0} = \left(\frac{dp}{dV}\right)_{V=V_{\max}} = 0$$

$$p(|V|) = \sum_{n=1}^N b_n \left[ \cos\left(\frac{n\pi V}{V_{\max}}\right) - (-1)^n \right] \quad (3.2)$$

$V_{\max}$  is the cutoff value of  $V$ , taken far away from the peak so that

$$p(V_{\max}) = 0$$

The Fourier coefficients  $b_n$  are calculated by the best fit to the data. If  $N \rightarrow \infty$  any  $p(|V|)$  can be represented by equation (3.2). Since the coefficients  $b_n$  are calculated by solving  $(N+1)$  simultaneous equations, the value of  $N$  is restricted by the amount of computer time one can afford and the efficiency of the computer. A value of  $N$  of the order of 15 is adequate. However the authors have tried upto a value of  $N = 40$  in the DEC-10 Computer.

For the isomer shift distribution the same method was used and hence all the above relationships hold good with  $V$  replaced by isomer shift  $S$ .

### 3.3.3 Results and discussion

The results of the EFG distribution analysis for the spectrum of the well known standard substance sodium nitroprusside (National Bureau of Standards number 725), obtained from Radio Chemical Center, Amersham, U.K., are shown in Figs. 3.7 and 3.8. Figure 3.7(a) shows the quadrupole splitting data compared with the best fit by a pair of Lorentzian lines of arbitrary position, width and height. Figure 3.7(b) shows the same data with best fit to equation (3.1). It can be seen that the experimental points are always slightly shifted outwards with respect to the Lorentzian curve where as the curve corresponding to the EFG distribution (Fig. 3.7b) passes through the experimental points at the peak. The distribution curve  $p(|V|)$ , where  $V$  is put in velocity units, is shown in Fig. 3.8. This fit is obtained with  $N = 25$  and  $\frac{1}{2} e Q V_{\max} = 6$  mm/sec. The mean quadrupole splitting at the maximum value of  $p(|V|)$  is 1.705 mm/sec which agrees well with the reported values [29,30]. The FWHM of the distribution around the mean value is 0.12 mm/sec. The knee in the distribution curve is due to the presence of dehydrated sodium nitroprusside present in the material. The position of the maximum of this minor peak is 1.970 mm/sec which agrees well with the quadrupole splitting 1.964 mm/sec of the dehydrated sodium nitroprusside [31]. The oscillations and the negative value of  $p(|V|)$  at low and high values of  $V$  are because of the truncation of the Fourier series.

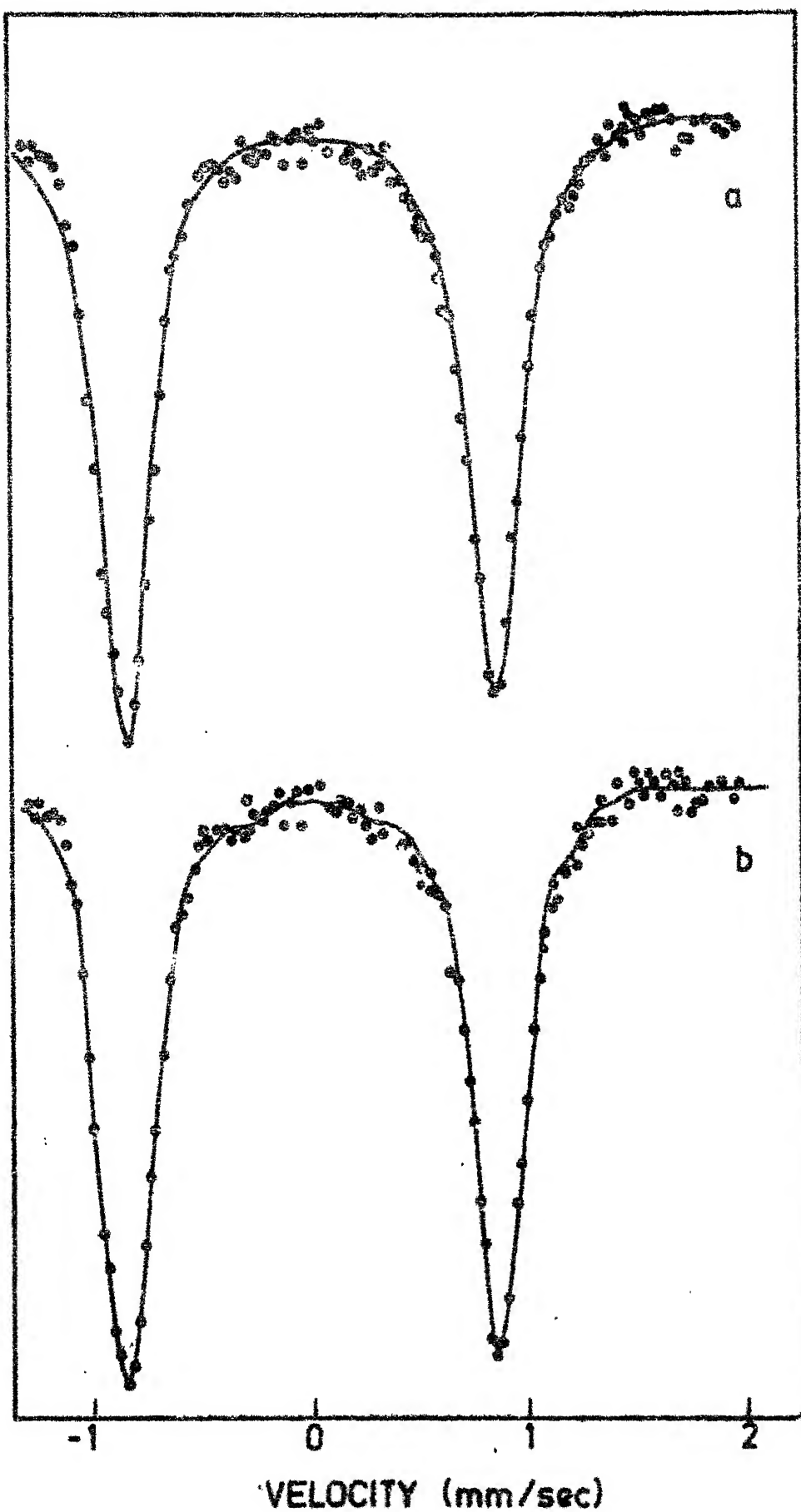
COUNTS  $\rightarrow$ 

Fig. 3.7. Mössbauer spectra of SNP (a) pure Lorentzian least squares (b) Lorentzian least squares with background

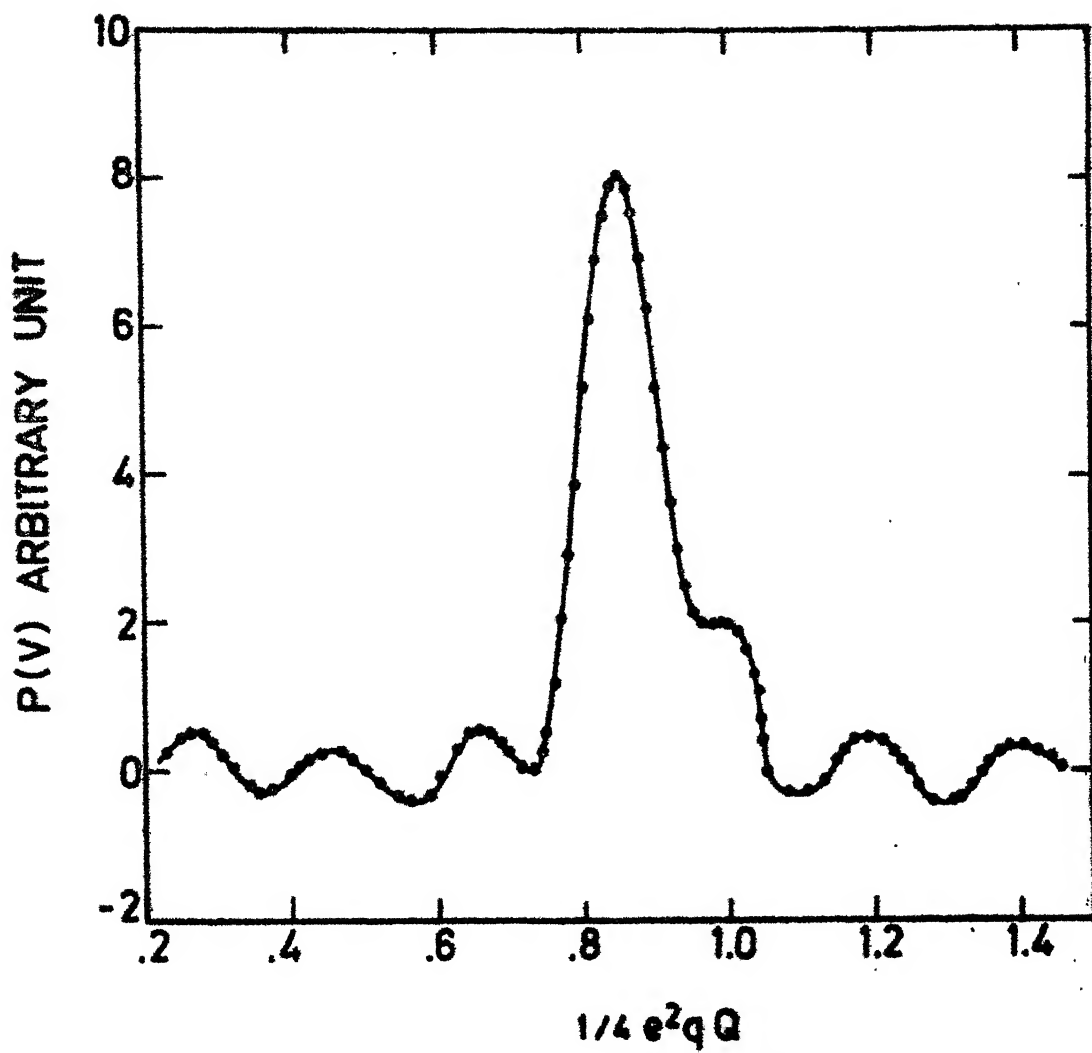


Fig. 3.8 EFG distribution in SNP at room temperature

The EFG distribution in  $\text{FeSO}_4 \cdot 7\text{H}_2\text{O}$  is shown in Fig. 3.9. The mean value of  $\frac{1}{2} e QV$  as obtained from the peak position of the distribution is 3.25 mm/sec and the FWHM of the distribution is 0.24 mm/sec. The distribution for  $\text{Fe}(\text{NH}_4)_2(\text{SO}_4)_2 \cdot 6\text{H}_2\text{O}$  is shown in Fig. 3.10. The mean value of the quadrupole splitting  $\frac{1}{2} e QV$  is 1.732 mm/sec and the FWHM is 0.235 mm/sec.

Mössbauer spectra of the amorphous  $[35 \text{ Na}_2\text{O} + 55 \text{ SiO}_2 + 10 \text{ Fe}_2\text{O}_3]$  system with the fitting curve, using equation (3.1), is shown in Fig. 3.11b. The quadrupole splitting using Lorentzian fit is 0.962 mm/sec. On careful examination of the spectrum it can be seen that the resultant spectrum is because of three overlapping quadrupole split doublets. The corresponding quadrupole splittings are precisely obtained from the distribution curve (Fig. 3.12), the values being 1.01 mm/sec, 0.45 mm/sec and 1.66 mm/sec. The first one is due to the Fe-atom at the tetrahedral site and the second one due to that in the octahedral site. The origin of the third one is still unidentified and requires other confirmatory experiments. In a normal Lorentzian fit the peaks were difficult to resolve beyond a doublet whereas the  $p(|V|)$  distribution gave clearly the three separate doublets. The octahedral site peak is the most dominant one, with FWHM of 0.41 mm/sec.

Table 3.1 gives the consolidated information on the quadrupole splittings obtained from the Lorentzian fittings as well as from EFG distribution curves for the samples

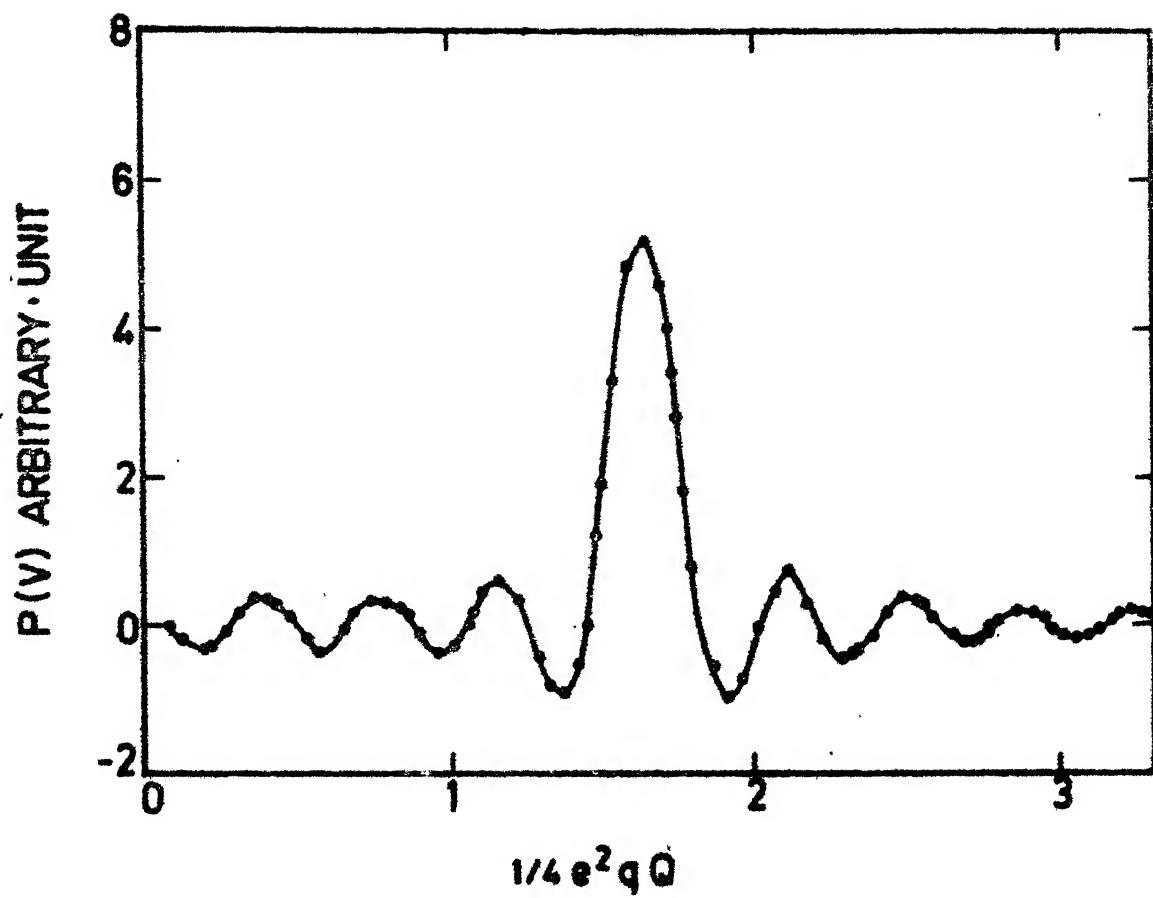


Fig. 3.9. EFG distribution in  $\text{Fe}(\text{SO}_4) \cdot 7\text{H}_2\text{O}$  at room temperature.

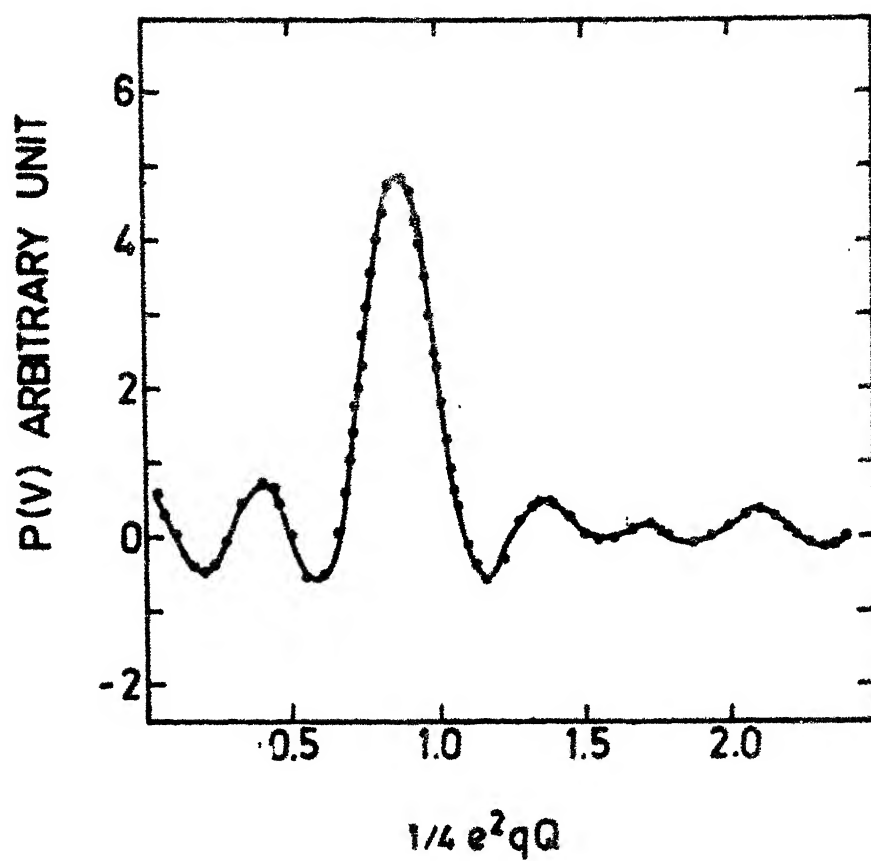


Fig. 3.10. EFG distribution in  $\text{Fe}(\text{SO}_4)_2(\text{NH}_4)_2 \cdot 6\text{H}_2\text{O}$  at room temperature.



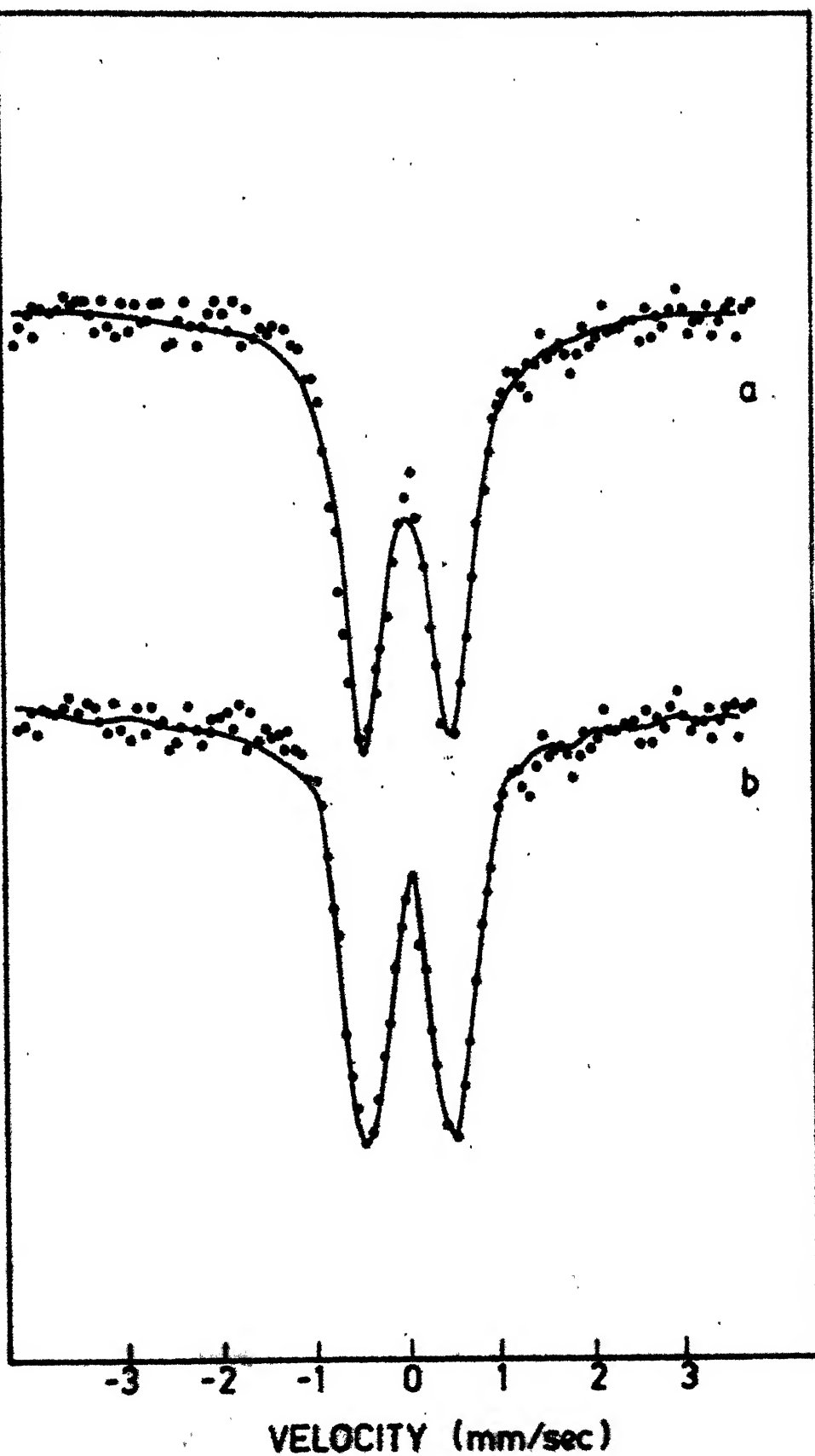
COUNTS  
↑

Fig. 3.11. Mössbauer  $\gamma$  spectrum of sodium silicate glass with (a) pure Lorentzian fit (b) fitting with HFC distribution.

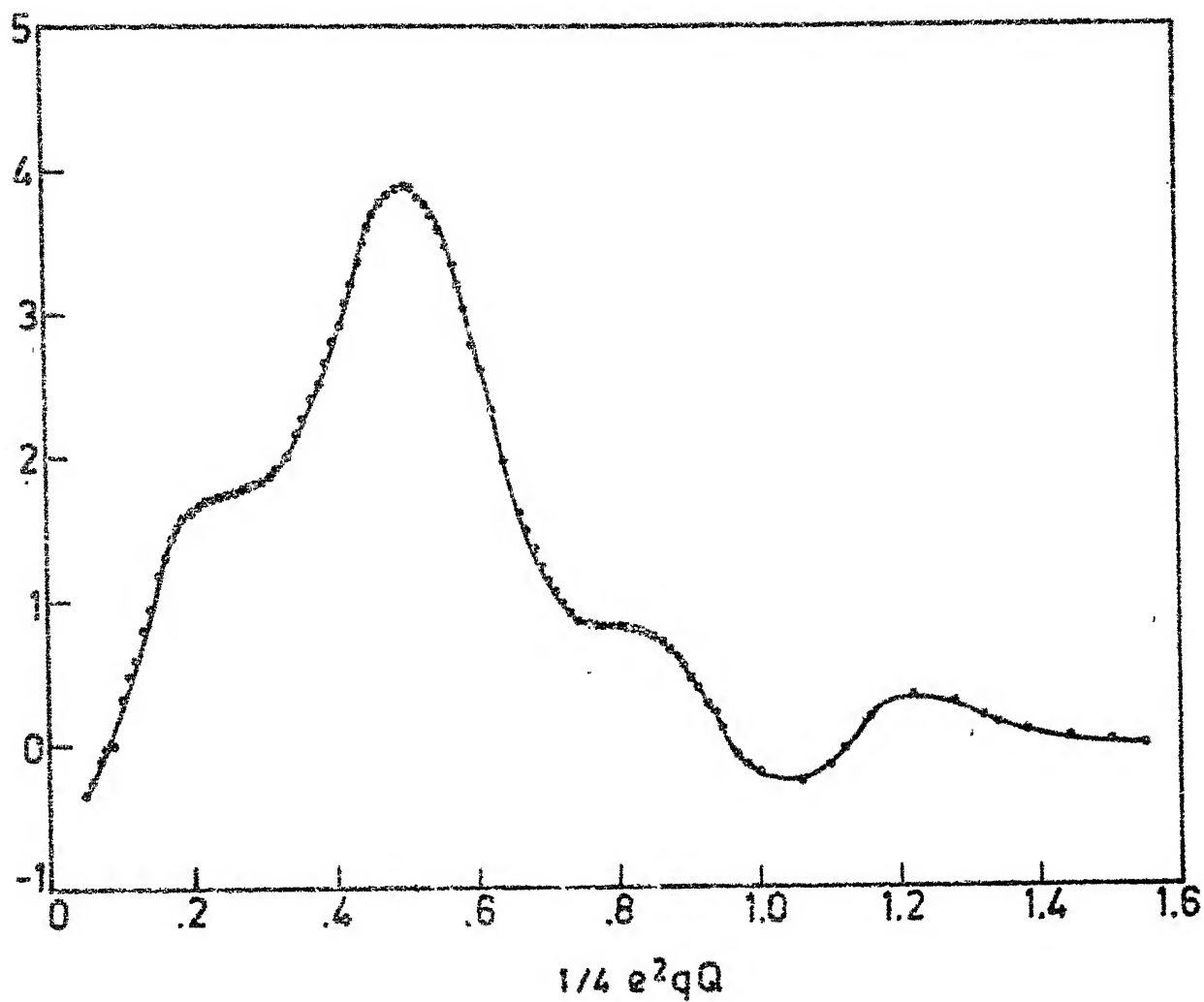


Fig. 3.12. EPZ distribution in sodium silicate at room temperature.

TABLE 3.1

The quadrupole splitting obtained by Lorentzian fit, and from  $p(|V|)$  distribution and FWHM of the P(IV) distribution.

Substance	Q.S. from Lorentzian fit  (mm/sec)	Mean Q.S. from peak position of P(IV) distribu- tion (mm/sec)	Standard value in literature (mm/sec)	F.W.H.M. of P( V ) dis- tribution (mm/sec)
SNP	1.704	1.705	1.7034 [29 ]*	0.12
Dehydrated SNP	-	1.970	1.964 [31 ]	-
FeSO <sub>4</sub> ·7H <sub>2</sub> O	3.200	3.250	3.217 [32 ]	0.24
Ferrous Ammonium Sulphate (FAS)	1.714	1.732	1.738 [32 ]	0.235
Sodium silicate glass				
(a) Tetrahedral	0.962	1.010	1.00 [33 ]	0.41
(b) Octahedral	-	0.450	0.5 [33 ]	-
(c) Unidentified	-	1.660	-	-

\*Numbers in square brackets indicates the references.

studied by us. It is evident that the distribution method gives more detailed information as well as better fit than the Lorentzian fitting method. The line widths in each case is a measure of the inhomogeneity of the EFG across the volume of the sample.

The isomer shift distribution of potassium ferrocyanide ( $K_4Fe(CN)_6 \cdot 3H_2O$ ) is obtained using the above method and is shown in Fig. 3.14. The isomer shift as determined from the least square fit with a single Lorentzian line (Fig. 3.13) is 0.220 mm/sec. with respect to sodium nitroprusside and that from the position of the peak of the distribution curve (Fig. 3.14) is 0.21 mm/sec. The FWHM is 0.32 mm/sec. The isomer shift distribution of 310 stainless steel is shown in Fig. 3.15. The peak position is 0.175 mm/sec and the FWHM is 0.42 mm/sec.

The method presented here open up the possibility of looking into the structural origin of the EFG and isomer shift again and develop Mosaic models for deviations from the ideal structure in the hitherto accepted perfect crystalline systems.

### 3.4 Recoilless Fraction

The recoilless fraction of  $\gamma$ -rays in the Ferrous Complexes  $FeSO_4 \cdot 7H_2O$ ,  $Fe(NH_4)_2 \cdot (SO_4)_2 \cdot 6H_2O$ ,  $K_4Fe(CN)_6 \cdot 3H_2O$  (PFC) and  $Na_2(Fe(CN)_5Na) \cdot 2H_2O$  were measured and the Debye

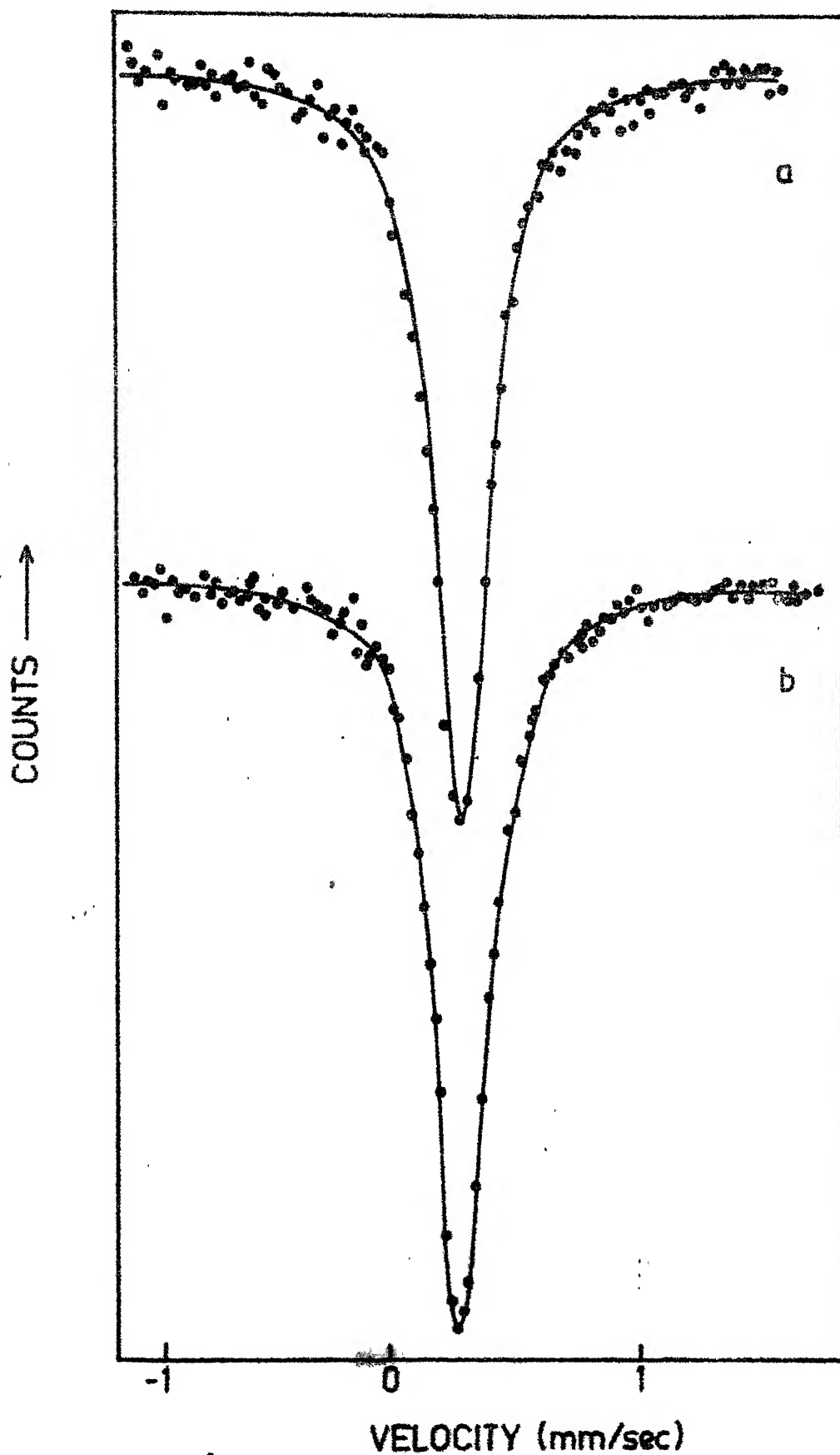
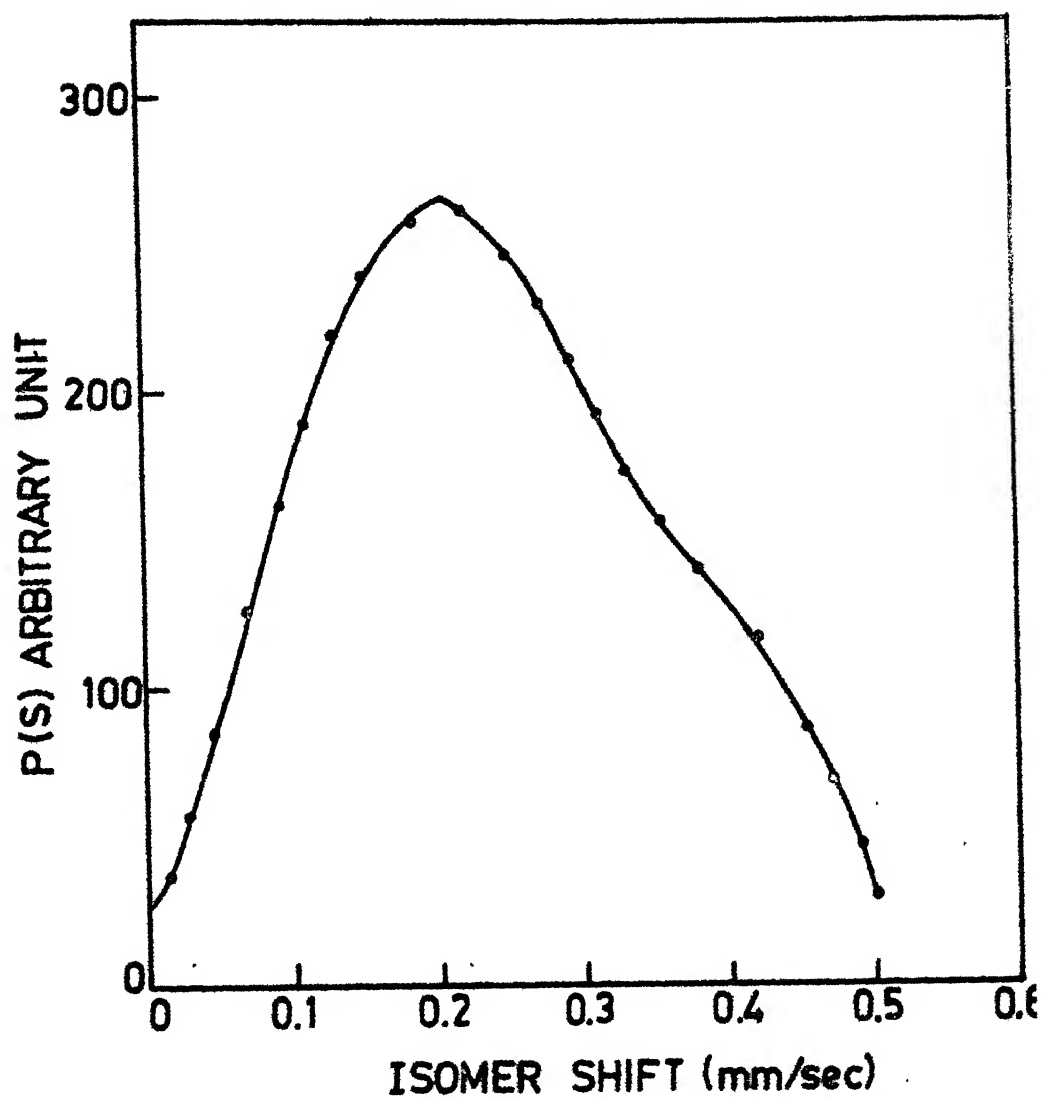


Fig. 3.13. Mössbauer spectrum of potassium ferrocyanide (a) pure Lorentzian fit and (b) fitting with isomer shift



**Fig. 3.14. Isomer shift distribution in potassium ferrocyanide at room temperature.**

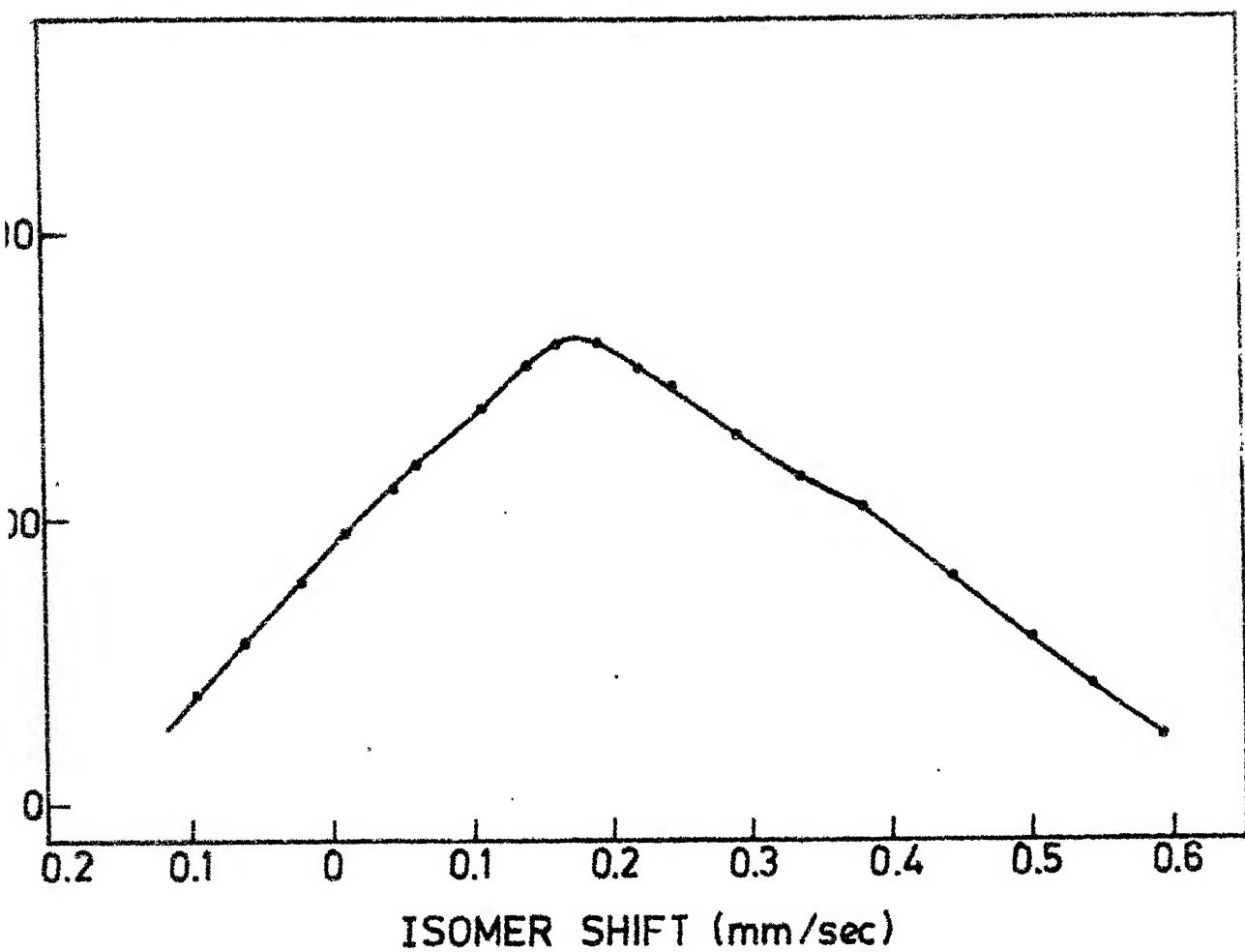


Fig. 3.15. Isomer shift distribution in 310 stainless steel at room temperature.

temperature is calculated from this. Computer programmes were made for calculating these parameter from the Mössbauer data, using the following method.

For a lattice in which all nuclei occupy equivalent lattice sites the recoilless fraction (Debye Waller factor) is given as

$$f = \exp(- \langle x^2 \rangle_T / \lambda^2) \quad (3.3)$$

where  $\lambda^2$  is reduced wavelength of  $\gamma$ -ray ( $\lambda^2 = 0.0188 \text{ \AA}^2$  for 14.4 keV  $\gamma$ -ray of  $^{57}\text{Fe}$ );  $\langle x^2 \rangle_T$  is the mean square displacement of the Mössbauer atom in the direction of  $\gamma$ -ray at temperature T, averaged over the life time of the nuclear excited state ( $\tau = 0.97 \times 10^{-7} \text{ s}$  for  $^{57}\text{Fe}$ ). The Mössbauer effect can be detected in systems satisfying the condition  $\langle x^2 \rangle_T < \lambda^2$  from Eqn. (3.3).

Expanding  $\langle x^2 \rangle_T$  in normal co-ordinates and using the Debye approximation for the phonon spectrum

$$f = \exp\left[- \frac{3R}{2k\theta_D} \left(1 + 4\left(\frac{T}{\theta_D}\right)^2 \int_0^{T/\theta_D} \frac{x dx}{e^x - 1}\right)\right] \quad (3.4)$$

where R is the recoil energy ( $R = E_\gamma^2 / 2Mc^2 = 2 \times 10^{-2} \text{ eV}$  for  $^{57}\text{Fe}$ ) k is Boltzman constant and  $\theta_D$  the Debye temperature.

The Debye Waller factor is calculated using the method in Ref. 2 by finding the integrated intensity (area) of the Mössbauer spectrum.

The total area of the Mössbauer absorption spectra is given by



$$A_{Tot} = S \pi f_s r \frac{t}{2} e^{-t/2} [I_0(t/2) + I_1(t/2)] \quad (3.5)$$

where  $I_n(t/2)$  is hyperbolic Bessel function of order  $n$  and  $T = (N f_a \sigma(0) \frac{r_0}{r})$  is the effective thickness of the absorber.  $N$  is the number of atoms/cm<sup>2</sup> of the absorber and  $f_a$  recoilless fraction of the absorber.  $r$  is the absorber line width corrected for absorber thickness using the expression given by O'Connor [12] and Shirley and Kaplan [11]

$$r_a = 2 r (1 + 0.135 t) \quad \text{for } 0 < t < 5 \quad \text{or}$$

$$r_a = 2 r (1 + 0.145 t - 0.0025 t^2) \quad \text{for } 4 < t < 10$$

$r_0$  is the natural line width of the  $\gamma$ -ray  $\sigma(0)$  is the resonance cross section for  $^{57}\text{Fe}$ . The correction of experimental data due to non-resonant radiation was taken into account by the factor  $S$ .  $S$  was determined by the filter technique given by Honsely et al. [35]. A brass filter of thickness 0.005 in. is used with the same geometry to find out the background radiation. For a source with no high energy X-rays a filter of 0.005 inch of brass will allow less than 0.02 % of the 14.4 keV gamma rays through, while removing only 4 % of the high energy radiation. The count rate obtained after putting the filter between the absorber and detector multiplied by 1.04 is the desired background rate due to high energy gammas. If  $N_\gamma(\infty)$  is the number of 14.4 keV gamma rays and  $N_x$  the background as determined, then

Knowing the recoilless fraction, the Debye temperature can be calculated using equation (3.4). In the limit of low or high temperatures compared to  $\theta_D$  Eqn. 3.4 can be approximated to

$$f = \exp\left(-\frac{3E_R}{2k_B\theta_D}\right) \quad \text{for } \theta \ll \theta_D$$

and

$$f = \exp\left(-\frac{6E_R\theta}{k_B\theta_D^2}\right) \quad \text{for } \theta \gg \theta_D \quad (3.8)$$

Using the above described method the recoilless fraction of the various iron complexes are determined and is shown in Table 3.2.

The recoilless fraction is calculated using the method of O'Connor et. al. [37,38] also as follows. The area under the absorption dip is given by

$$A = \int_{-\infty}^{\infty} \frac{I(\infty) - I(v)}{I(\infty)} dv \quad (3.9)$$

where  $I(v)$  is the intensity observed when the source-absorber relative velocity is  $v$ .

$$I(v) = I(\infty)(1-f_s) + I(\infty)f_s \cdot \int_{-\infty}^{\infty} S(v_1) \exp\left[-\frac{t \sigma(v_1-v)}{\sigma(0)} dv_1\right] \quad (3.10)$$

where  $f_s$  is the recoilless fraction of the source,  $S(v)$  is the normalised source energy distribution,  $t$  is the effective absorber thickness at its peak value and  $\sigma(v)$  is the nuclear absorption cross section

TABLE 3.2

The recoilless fraction, Debye temperature and thickness corrected FWHM of some Ferrous Complexes.

Substance	Recoilless Fraction	Debye Temperature K	Thickness Corrected Width (mm/sec.)
SNP	0.469	232	0.250
FAS	0.511	246	0.248
PEC	0.362	200	0.258
FeSO <sub>4</sub> ·7H <sub>2</sub> O	0.671	319	0.210

$$t = N f_a \sigma(0)$$

Substituting these values

$$\begin{aligned} A &= \int_{-\infty}^{\infty} dv \int_{-\infty}^{\infty} S(v+v_1) \exp\left[-\frac{t \sigma(v_1)}{\sigma(0)}\right] dv_1 \\ &= f_s \int_{-\infty}^{\infty} \exp\left[-\frac{t \sigma(v)}{\sigma(0)}\right] dv \end{aligned}$$

Expressing  $v$  in terms of  $E$ , the energy of the  $\gamma$ -rays

$$A = f_s \int_{-\infty}^{\infty} \exp\left[-\frac{t \sigma(E)}{\sigma(0)}\right] dE \quad (3.11)$$

$\sigma(E)$  is assumed to have a Voigt profile as

$$\sigma(E) = \sigma(0) \frac{P}{\pi^{1/2}} \int \frac{e^{-P^2 s^2} ds}{(S-y)^2 + 1}$$

where  $y = 2(E-E_0)/r$  where  $r$  is the natural line width and  $P$  is a Gaussian broadening parameter (equal to  $\infty$  for pure Lorentzian). The area  $A$  was computed for different values of  $P$  and  $t$  and the measured areas are fitted against  $t$  curves to determine the values of  $t$  and hence the recoilless fraction  $f_a$ .

The area  $A$  of the absorption dip was measured by the following method which is similar to the 'black absorber' method [35] for determining the recoilless fraction. In this case the black absorber is replaced by a 'white source', which has a uniform recoilless intensity over a velocity range  $\pm V$  and zero intensity elsewhere. Then the fraction of radiation

absorbed by an absorber is directly proportional to the integrated area of the absorption dip within  $\pm V$ . The white source is simulated by moving an actual source to scan the range  $\pm V$  and integrating the total intensity transmitted in this range. If the source line width is negligibly small then the effective intensity per unit velocity interval in the range  $\pm V$  when in motion would be proportional to  $(2V)^{-1}$  and the total transmitted intensity would be

$$I(v) = I(\infty) \left(1 - \frac{A}{2V}\right) \quad (3.12)$$

where  $A$  is the absorption dip area within the range  $\pm V$ . In actual source the deviation from the ideal 'white source' is less than 2 % at  $0.7 V$  for  $V$  equal to ten times the natural line width. As  $V$  increases the approximation improves and the proportion of the absorption dip area effectively spanned by the source approaches its saturation value. Measurements were made for  $V$  between 40 to 300 natural line widths over which the graph of  $I(v)$  against  $(2V)^{-1}$  was found to be linear.  $A$  was then found from this graph using the relation

$$A = - \frac{1}{I(\infty)} \left( \frac{dI(v)}{d(2V)^{-1}} \right)$$

and  $I(\infty)$  was found by extrapolation of the straight line to  $(2V)^{-1} = 0$ . The values of  $f_a$  determined using this method closely agrees with the value obtained by the method described earlier.

# REFERENCES

- [1] N.V. Nair and D.C. Khan, Phys. Rev. B24, 1 Nov. (1981).
- [2] D.P. Johnson and J.G. Dash, Phys. Rev. 172, 983 (1968).
- [3] R. Ingalls, Phys. Rev. 113, A781 (1964).
- [4] R. Ingalls, K. Ono and Louis Chandler, Phys. Rev. 172, 295 (1968).
- [5] K. Chandra and S.P. Puri, Phys. Rev. 169, 272 (1968).
- [6] V.I. Goldanskii and R.H. Herber, Chemical Applications of Mössbauer Spectroscopy (Academic, New York, 1968).
- [7] W. Kerler, Z. Phys. 167, 194 (1962).
- [8] R.W. Grant et al., J. Chem. Phys. 45, 1015 (1966).
- [9] Sh. Sh. Bhaskirov and V.N. Lebedev, Sov. Phys. Solid State 21, 158 (1979) [Fiz. Tverd. Tela 21, 263 (1979)].
- [10] D.P. Johnson and J.G. Dash, Phys. Rev. 172, 983 (1968).
- [11] D.A. Shirley and Kaplan, Phys. Rev. 123, 816 (1961).
- [12] D.A. O'Connor, Nucl. Instr. and Meth. 21, 318 (1963).
- [13] S.L. Ruby and J.M. Bicks, Rev. Sc. Instr. 33, 27 (1961).
- [14] A.J. Stone, Nucl. Instr. Meth. 107, 285 (1973).
- [15] S.A. Wender and N. Hershkowitz, Nucl. Instr. Meth. 98, 105 (1972).
- [16] R.E. Meads and B.M. Place, Nucl. Instr. Meth. 98, 29 (1972).
- [17] G. Hembree and D.C. Price, Nucl. Instr. Meth. 108, 99 (1973).
- [18] R.M. Housley, Nucl. Instr. Meth. 35, 77 (1965).

- [19] S. Margulies and J.R. Ehrman, Nucl. Instr. and Meth. 12, 131 (1961).
- [20] G. Lang, Nucl. Instr. and Meth. 24, 425 (1963).
- [21] Takayuki Kobayashi and Kazuko Fukumura, Nucl. Instr. and Meth. 173, 363 (1980).
- [22] V.N. Belogurov and V.A. Bilinkin, Nucl. Instr. and Meth. 175, 495 (1980).
- [23] C.L. Chien, Phys. Rev. B18, 1003 (1978).
- [24] B. Window, J. Phys. E4, 401 (1971).
- [25] A. Narayanasamy, T. Nagarajan, P. Muthukumarasamy and T.S. Radhakrishnan, J. Phys. F : Metal Phys. 9, 2261 (1979).
- [26] M. Eibschütz, M.E. Lines and K. Nassau, Phys. Rev. B21, 3767 (1980).
- [27] M.E. Lines, Phys. Rev. B21, 5793 (1980).
- [28] M.E. Lines, Phys. Rev. B20, 3729 (1979).
- [29] R.W. Grant, R.N. Housley and U. Gonser, Phys. Rev. 178, 523 (1969).
- [30] Mössbauer effect data index, Edited by J.G. Stevens and V.E. Stevens (North American aviation Science Centre, Thousand Oak, Calif., 1975).
- [31] C.A. Boughton, J. Inorg. Nucl. Chem., 38, 427 (1976).
- [32] R.W. Grant, H. Wiedersich, A.H. Muir, Jr., U. Gonser and W.N. Delgass, J. Chem. Phys. 45, 969 (1966).
- [33] C.R. Kurkjian and E.A. Sigety, Phys. and Chem. Glasses, 9, 73 (1968).

- [34] T. Raman, Ph.D. Thesis, Indian Institute of Technology, Kanpur, India (1977) (unpublished).
- [35] R.M. Housley, N.E. Erickson and J.G. Dash, Nucl. Instr. Meth. 27, 29 (1964).
- [36] S.V. Karyagin, Proc. Acad. Sci. U.S.S.R., Phys. Chem. Sect. 148, 110 (1964).
- [37] D.A. O'Connor, M.W. Reeks and G. Skyrme, J. Phys. F : Metal Phys., 2, 1179 (1972).
- [38] D.A. O'Connor and G. Skyrme, Nucl. Instr. and Meth. 106, 77 (1973).



## CHAPTER 4

### ELECTRIC FIELD GRADIENT AT IRON IMPURITIES IN hcp METALS

#### 4.1 Introduction

The nuclear quadrupole interaction in metals has been the subject of considerable interest in recent years. The origin of the electric field gradients (EFG) at the nuclei in metals is still not well understood. However, the extensive experimental data on EFG in non-cubic metals reported [1,2] in recent years has enabled us to draw some conclusions regarding the origin of EFG's, in particular the relative role of the lattice contribution ( $eq_{latt}$ ) and electronic contributions ( $eq_{el}$ ). In this chapter, we present a brief review of the observed systematics, and the theoretical and semi-empirical models for EFG determination and our study of the EFG at the iron impurity in some hcp metals namely Ti, Se and Nd.

##### 4.1.1 The EFG tensor

The electric field gradient tensor  $V_{ij}$  at the origin due to a point charge  $Ze$  is given by

$$V_{ij} = \frac{Ze}{r^5} [3 x_i x_j - r^2 \delta_{ij}] \quad (4.1)$$

where  $r^2 = \sum_i x_i^2$  and  $x_i$  are the Cartesian co-ordinates of the charge. Being a traceless tensor only five of the nine components of  $V_{ij}$  are independent. A unique axis system called the 'principal axes of the EFG tensor' can be defined such that

the off-diagonal elements vanish and the diagonal elements are chosen so as

$$|V_{zz}| \geq |V_{yy}| \geq |V_{xx}|$$

The EFG tensor is usually described by only two independent parameters,  $V_{zz} = eq$  and the asymmetry parameter  $\eta = (V_{xx} - V_{yy})/V_{zz}$ . With the above ordering  $\eta$  is restricted to  $0 \leq \eta \leq 1$ .

The EFG is mainly contributed by two sources [3];

(i) fixed positive ions of the crystal surrounding the Mössbauer atom in non-cubic symmetry (the lattice contribution), and (ii) the non-cubic electron distribution in partially filled valence orbitals of the Mössbauer atom (the electronic contribution). The resultant electric field gradient can be written as

$$eq = eq_{latt} (1 - \gamma_{\infty}) + eq_{el} \quad (4.2)$$

where  $(1 - \gamma_{\infty})$  is the Sternheimer antishielding factor (for iron  $\gamma_{\infty} = -9.14$ )  $eq_{latt}$  has a well defined value which can be calculated by the lattice sum method. In the case of lattice with hexagonal close packed (hcp) structure the EFG tensor is axially symmetric with the main axis along the c-direction and equal for all lattice sites. The value of  $q_{latt}$  is calculated numerically by Das and Pomerantz [4] which is given by

$$eq_{latt} = \frac{Ze}{4\pi\epsilon_0 a^3} [0.0065 - 4.3584 (\frac{c}{a} - (\frac{8}{3})^{\frac{1}{2}})] \quad (4.3)$$

The  $eq_{el}$  contribution is defined much less precisely and is difficult to calculate. Any evaluation of  $q_{el}$  would require a detailed knowledge of the wave functions of conduction electrons in the impurity-host system. One would expect that  $eq_{el}$  would strongly depend on the anisotropy of the Fermi surface, i.e. on the orbital character of conduction electrons. The spatial distribution of conduction electrons near the impurity should follow the symmetry of the host matrix. This approach has been justifiably used by Watson et al. [3] in their calculation of  $eq_{el}$  for pure metals and ordered alloys.

## 4.2 Systematic Trends of the EFG's in Metals

### 4.2.1 Correlation between $eq_{ion}$ and $eq_{el}$

Raghavan et al. [5] after studying the systematic trends of EFG in non-cubic metals pointed out that there exists an almost linear relationship between  $eq_{el}$  and  $eq_{latt}(1-\gamma_{\alpha})$  as

$$eq_{el} = -K eq_{latt} (1 - \gamma_{\alpha}) \quad (4.4)$$

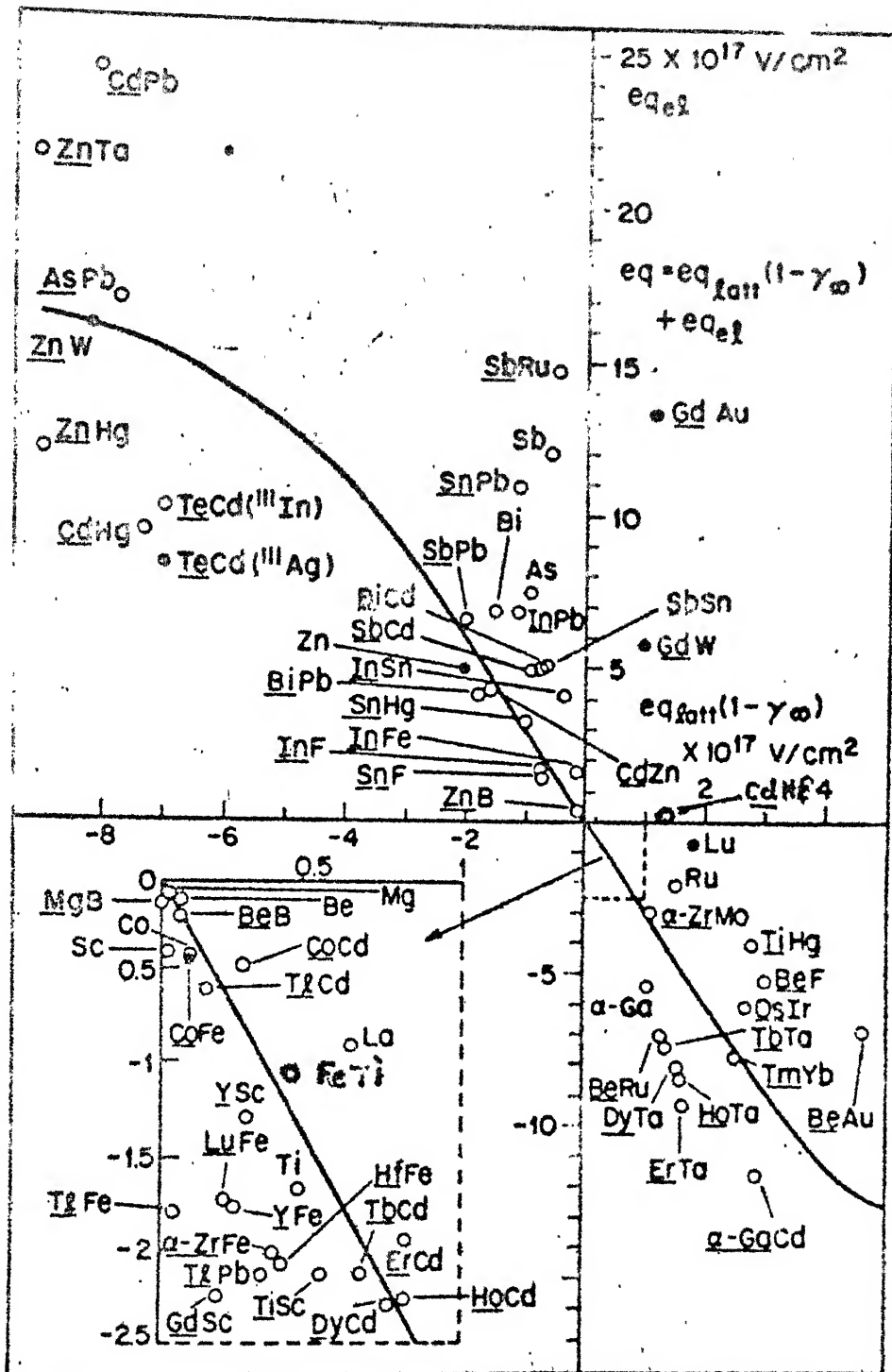
where  $K \approx 2-5$  for moderate values of  $eq_{latt}(1-\gamma_{\alpha})$ .

For the cases where both the magnitude and sign of the EFG are known experimentally,  $eq_{el}$  is determined by subtracting the theoretically calculated values of  $eq_{latt}(1-\gamma_{\alpha})$  from the experimental data.  $eq_{el}$  is then plotted against  $eq_{latt}(1-\gamma_{\alpha})$  (Raghavan's universal correlation). However Raghavan et al. did not consider the rare-earth metals since

the unfilled 4f shell quite delinked with the lattice, is the dominant source of the electronic part of the EFG. Gd has been included because the  $4f^7$  configuration of  $Gd^{+3}$  ion is spherical, making 4f contribution to EFG equal to zero. On the other hand cases such as Te and TeI are omitted since the EFG in these cases is dominated by local covalency effects [6].

The recent data on non-cubic metals are plotted in a similar way by Kaufmann and Vianden [1] and are reproduced in Fig. 4.1 with minor modifications. It is seen that most of these data support the correlation suggested between the electronic and ionic contributions.

Recently, Krusch and Forker [7] have shown that there are cases in which either the sign or the magnitude of the electronic EFG are incompatible with this correlation. In all those cases studied the host metal or the probe atom belong to a transition element series which suggests that in transition element systems the electronic EFG may be dominated by contributions, which do not arise in simple sp-metals. In the case of scandium host and iron impurity the constant  $K = 18$  [7]. In a theoretical study Piecuch and Janot [8,9] have shown that the magnitude of the local contribution to the EFG at transition element impurities should be proportional to the occupation of the d-states of the impurity, which depends on the density of states of the host.



g. 4.1. Correlation between the electronic and ionic contributions to the EFG based on recent data.

Figure taken from ref.[1].

#### 4.2.2 Dependence of EFG on the probe used

The experimental data on EFG in non-cubic metals shows that it is probe-dependent in the form of valence difference between impurity and host. Over and above the host electronic contribution an additional local electronic contribution may be present from the valence electrons of the probe atom which remain spatially correlated to the host atom. An expression which reveals the possible influence of the impurity on the resulting EFG is the ratio of this EFG at an impurity site P in a host H to the EFG of the pure metal ( $P = H$ ), i.e.

$$V_{zz} (P,H)/V_{zz} (H,H) \quad (4.5)$$

It is evident that the EFG at an impurity site should be very sensitive to changes in the conduction electron wave functions around this site. These changes can be brought out by the electron redistribution around impurities by which the charge difference between impurity and host matrix is screened out within short distance around the impurity atom. To show that this charge screening manifests in the EFG, a plot of the set of ratios of Eq. (4.5) for the different probes P in each matrix H as a function of the valence difference between impurity and host  $\delta z$  is reproduced [10] in Fig. 4.2. Somewhat similar plot of Collins [11] is also reproduced in Fig. 4.2, which brings out the fact that in sp metals, the electronic EFG is approximately proportional to the valence of the impurity which in turn

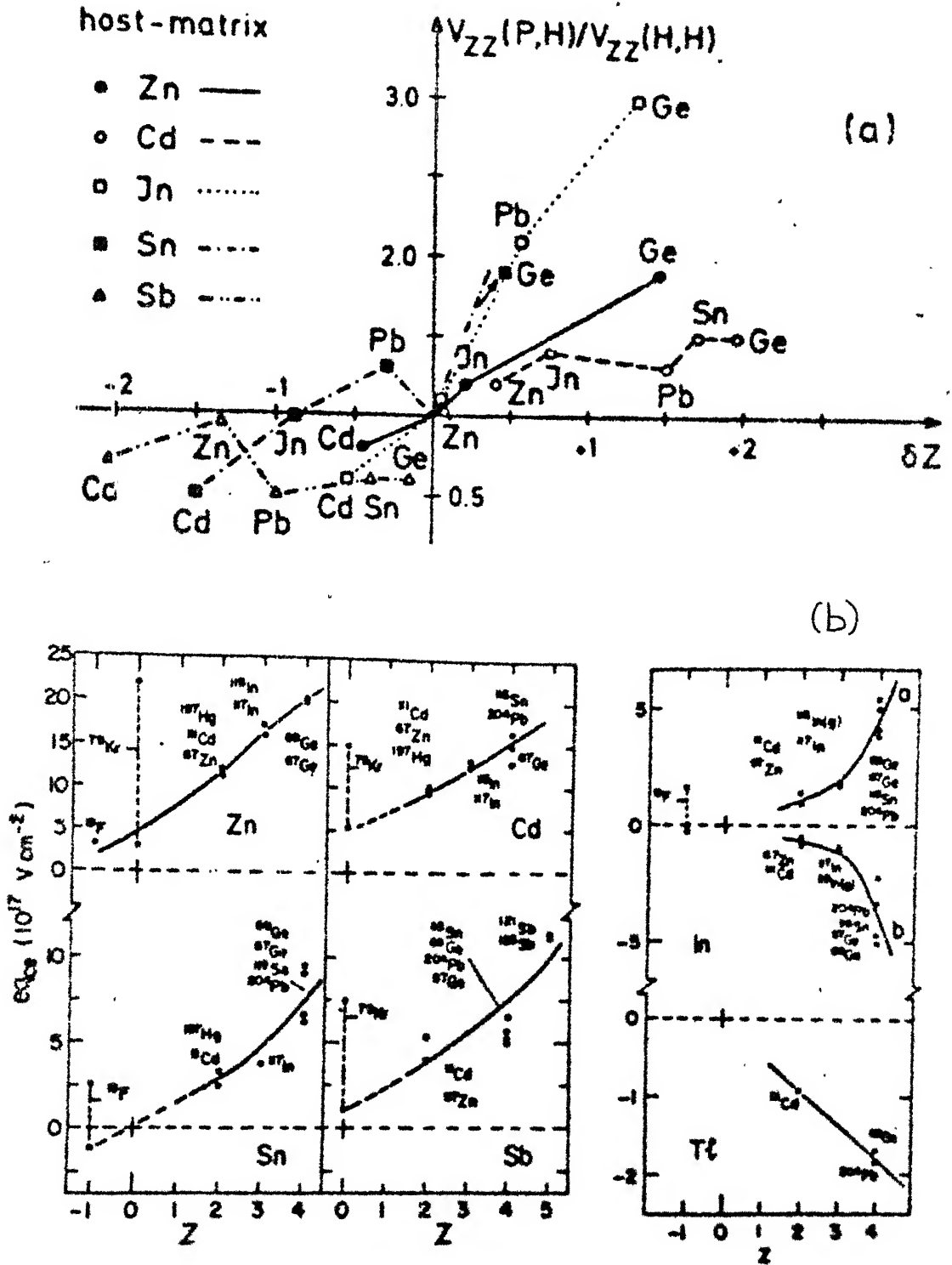


Fig.4.2 Correlation between the EFG and the impurity valence. a) The ratio ( $V_{ZZ}$  at impurity/ $V_{ZZ}$  in pure metal.) vs. impurity valence. Figure taken from ref.[10].  
b) Electronic contribution to EFG vs. impurity valence. Figure taken from ref.[11].

is related to the number of conduction electrons screening the impurity.

#### 4.2.3 Dependence of the EFG on temperature

The quadrupole interaction frequency (QIF) is found to vary with temperature. For pure metals and dilute impurity alloys the variation approximately obeys a simple empirical relation by Christiansen et al. [12]

$$eq(T) = eq(0) [1 - BT^{3/2}] \quad (4.6)$$

where  $T$  is the temperature and  $B$  is the slope parameter. Besides this expression another test function

$$eq(T) = eq(0) [1 - B_1 T - B_2 T^2], \quad (4.7)$$

where  $eq(0)$ ,  $B_1$  and  $B_2$  being free fit parameters, was also found suitable for many systems.

The slope parameter  $B$  in Eq. (4.6) is positive excepting  $^{181}\text{TaBe}$  [13] and the magnitude of  $B$  is related to the strength of the coupling between the probe and the host. The values of  $B$  were found to be different for different impurities in the same host for some systems. Also, for a given impurity the values are different in different host matrices. In the case of rare-earth systems with partially filled 4f-shells the above relation does not hold good. Since most of the EFG contribution is likely to come from the 4f-shells delinked from the lattice. Nishiyama et al. [14] used a pseudopotential approach including the influence



of lattice vibrations to find the temperature dependence of the EFG in non-cubic metals. The resulting  $eq(T)$  factorizes into a Debye-Waller factor and a lattice sum over screened ions as

$$eq(T) = (1-\gamma_{eff}) eq_{ion}^{sc}(T) \exp \left[ -\frac{4}{3} k_F^2 \langle u^2 \rangle_T \right] \quad (4.8)$$

where  $eq_{ion}^{sc}(T)$  is the lattice sum over screened ions,  $\vec{k}_F$  the Fermi vector and  $\langle u^2 \rangle_T$  is the mean-square atomic displacements at temperature  $T$ .

An exact explanation for the observed changes in the slope parameter  $B$  is difficult to give, since a large number of mechanisms are responsible for the observed temperature dependence. While interpreting the data, one should exercise caution to observe that the changes are not because of some changes in the phase of the matrix, the lattice location of the probe atoms etc.

### 4.3 Theoretical Estimates of EFG's

#### 4.3.1 The lattice contribution

The lattice contribution to the field gradient  $eq$  is

$$eq_{latt} = \sum_N Ze^2 \left[ \frac{3 \cos^2 \theta_N - 1}{r_N^3} \right]$$

where  $r_N$  and  $\theta_N$  being the polar position coordinates of the  $N^{th}$  ion with respect to the EFG principal axes and summation has to be carried out over all ions in the lattice except one at the origin. Nijboer and de Wette [15] used the Fourier

transform method to calculate the lattice sum. This sum has been evaluated numerically by T.P. Das et al. [4] to get the value for an hcp lattice (Eq. (4.3)).

#### 4.3.2 Electronic contribution

The electronic contribution to the EFG at nuclear site in metals can be written as

$$e_{q_{el}} = -e \int_{\tau} \rho_c(\vec{r}) \left[ \frac{3 \cos^2 \theta - 1}{r^3} \right] d\tau$$

where  $\rho_c(\vec{r})$  is the conduction electron density, the calculation of which is complicated due to the lack of exact wave functions [16]  $\rho(\vec{r})$  is given by

$$\rho(\vec{r}) = 2 \sum_{n\vec{k}} \varphi_{n\vec{k}}(\vec{r})^2$$

where the summation over  $n$  refers to bands and that over  $\vec{k}$  to the states in each band that are occupied, that is those lying below the Fermi surface. The factor of 2 takes care of the two spin states for each electron. Using the above expression for  $\rho(\vec{r})$

$$q_{el} = -e \sum_{n\vec{k}} \langle \varphi_{n\vec{k}}(\vec{r}) | \frac{3 \cos^2 \theta - 1}{r^3} | \varphi_{n\vec{k}}(\vec{r}) \rangle \quad (4.9)$$

The wave functions  $\varphi_{n\vec{k}}(\vec{r})$  could be obtained using appropriate crystal potential and OPW method.

Recently Thompson et al. [17] have presented a first principle analysis of the contributions from the isotropic, anisotropic and anharmonic lattice vibrations to the lattice

and electronic EFG. The temperature-dependent pseudopotential was incorporated to account for the temperature dependence. It is found that the lattice EFG is primarily affected by the anisotropic phonons, but not by the isotropic vibrations. However, the isotropic component almost entirely accounts for the variation of the electronic EFG with temperature.

#### 4.3.3 Pseudopotential approach and charge screening effects

The pseudopotential method can avoid the difficulties in the calculation of the exact crystal potentials, by constructing explicit electron wave functions which may be used to evaluate the EFG's. The basic method in these calculation is to find the electronic charge distortion which causes a new charge distribution. An impurity ion in a metal having an impurity-host valence difference results in a redistribution of the conduction electrons around the impurity to screen the effective charge differences.

Nishiyama et al. [14,18] have suggested a basically different model for EFG. This model is based on the simultaneous treatment of electronic screening along with the lattice vibrations. The effect of conduction electrons is to shield the valence ions so that their effective charge becomes

$$Ze \delta(\vec{r}-\vec{R}) - e \rho_{sc}(\vec{r}-\vec{R}) \quad (4.10)$$

$\rho_{sc}$  is the screening charge distribution.

The EFG at the origin due to a single screened ion at position  $\vec{R}$  with respect to the probe is given by

$$F(\vec{R}) = \int [Ze \delta(\vec{r}-\vec{R}) - e \rho_{sc}(\vec{r}-\vec{R})] \vec{r}^3 2P_2(\cos\theta_r) d^3\vec{r}$$

The net EFG at the probe nucleus is evaluated by taking contributions from all the screened ions antishielded by the screened probe ion. A new enhancement factor  $\gamma_{eff}$  is also used in these calculations. So the time dependent EFG at temperature T is given as

$$eq(t,T) = (1-\gamma_{eff}) \int \sum_i' \delta(\vec{R}-\vec{R}_i(t)) F(\vec{R}) d^3\vec{R}$$

in which  $\vec{R}_i(t)$  is the instantaneous position of the  $i^{th}$  ion. Since the frequency of the lattice vibrations ( $\sim 10^{12}$  Hz) is large compared to the QIF ( $\sim 10^8$  Hz), we have to take the time average over the ionic vibrations which are regarded approximately as uncorrelated and isotropic [19], so that we get the result

$$eq(T) = eq(t,T) = (1-\gamma_{eff}) \int \overline{\sum_i' \delta(\vec{R}-\vec{R}_i(t))} F(\vec{R}) d^3\vec{R} \quad (4.11)$$

The Fourier transform of this equation leads to

$$eq(T) = (1-\gamma_{eff}) \int (S_0(\vec{k})-1) \exp[-(\vec{k} \cdot \vec{x})^2/3] F(\vec{k}) d^3\vec{k} \quad \dots (4.12)$$

where  $F(\vec{k})$  is the Fourier transform of  $F(\vec{R})$  and  $S(\vec{k})$  the structure factor of the non vibrating lattice. The influence of the lattice vibrations on the EFG at the probe ion is described by the Debye-Waller factor with  $\langle x^2 \rangle$  being the

isotropic mean square displacement. By the use of a simple pseudopotential  $V(R)$  derived from a Coulomb potential  $V^C(R)$  screened by a free-electron gas

$$V(R) = \frac{1}{2\pi^2} \int_0^\infty \frac{V^C(\vec{k})}{\epsilon(\vec{k})} \frac{\sin(\vec{k} \cdot \vec{R})}{k R} k^2 d\vec{k}$$

equation (4.12) may be finally written as

$$eq(T) = (1-\gamma_{eff}) eq_{ion}^{sc}(T) \exp\left[-\frac{4}{3} k_F^2 \langle u^2 \rangle_T\right] \quad (4.13)$$

where  $eq_{ion}^{sc} = \sum_i V_2(\vec{R}_i) 2P_2(\cos\theta_i)$  over the screened ions, and  $k_F$  is the Fermi radius.  $\epsilon(\vec{k})$  is the dielectric function [20].

This model has not given results consistent with experimental data for the magnitude of EFG but the temperature dependence agrees with that of many systems.

#### 4.3.4 Conduction electron charge shift model of Bodenstedt and Perscheid

Bodenstedt and Perscheid [21] suggested a model for the origin of EFG in hcp metals essentially in terms of the charge shift of the conduction electrons; this shift is related to the deviation of  $\frac{c}{a}$  from the ideal value of  $\frac{c}{a} = \left(\frac{8}{3}\right)^{\frac{1}{2}}$  for an hcp lattice. They started from the assumption that the conduction electrons fill the space between the ions. For an easy analysis the conduction electron distribution is separated into charge clouds, the centres of which are situated in the middle between nearest

neighbour ions as shown in Fig. 4.3. Each positive ion is thus surrounded by six negative charge clouds in its own hexagonal plane and three clouds above and below. The latter ones form planes of pure negative charge in the middle between subsequent hexagonal planes of ions. The charge clouds in hexagonal plane are on equivalent sites and must therefore bear the same charge  $Q_{hp}$ . The same argument holds for the charge clouds between the hexagonal planes, let that charge be called  $Q_{el}$ . Since the total lattice is neutral

$$Q_{hp} + Q_{el} = -\frac{1}{3} Z_{eff} e$$

where  $Z_{eff} e$  is the effective charge of the ion. The conduction electron charge shift  $\delta$  is defined by

$$Q_{hp} = -\frac{1}{6} Z_{eff} e (1+\delta) \quad \text{and}$$

$$Q_{el} = -\frac{1}{6} Z_{eff} e (1-\delta)$$

By using the approximation that each of the conduction electron charge clouds and the ionic charge distribution have spherical symmetry, a lattice sum calculation can be done for each of them yielding

$$eq = eq^{ion} - \frac{1}{6} eq_{hp}(1+\delta) - \frac{1}{6} eq_{el}(1-\delta) \quad (4.14)$$

In order to estimate the charge shift  $\delta$  for a given metal lattice with a given  $c/a$ , one can start from measured elastic coefficients and calculate the stress needed in order to deform the ideal hcp lattice into the shape with

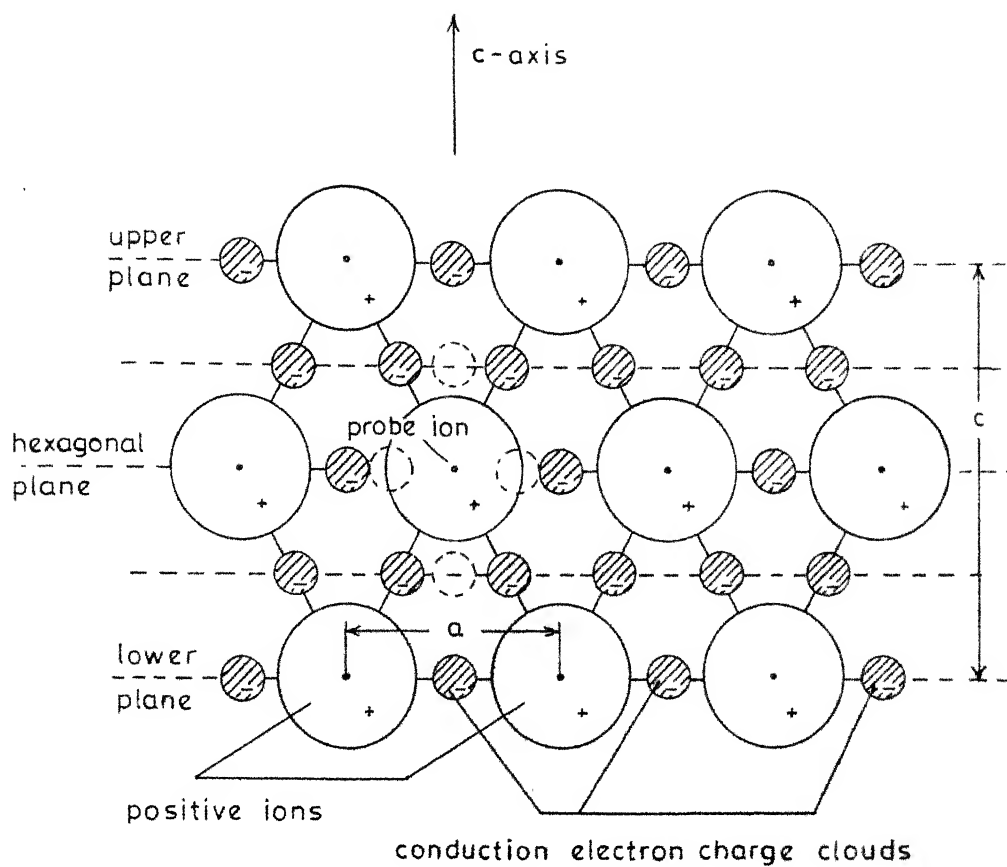


Fig.43 Charge distribution in an hcp metal idealized for the Charge Shift model. Figure taken from ref. [21]

observed  $c/a$ . Then one can calculate the charge shift  $\delta$  which produces this stress by the electrostatic forces. For a hexagonal close packed lattice the value of  $\delta$  obtained in this way is given by

$$\delta = \frac{c/a - (\frac{8}{3})^{\frac{1}{2}} 36\epsilon_0 a^4}{z_{\text{eff}}^2 e^2 (\frac{8}{3})^{\frac{1}{2}} [\frac{1}{6} (-2s_{13} + s_{12} + s_{11}) + s_{33} - s_{13}]} \quad (4.15)$$

$s_{ik}$  are the elastic coefficients of the host lattice.

For comparison with experimental data one has to apply the Sternheimer correction factor  $(1-\gamma_\infty)$  as

$$eq_{\text{tot}} = eq(1-\gamma_\infty)$$

since all charges contributing to  $eq$  are outside the probe ion sphere.

The effect of the vibrations of the probe nucleus is incorporated by calculating the average value of  $eq(\vec{r})$ ,  $\vec{r}$  representing the instantaneous position of the probe ion. Then one gets

$$eq(\vec{r}) = eq(0) + 1/2! \frac{\partial^2 eq}{\partial x_3^2} \langle x_{||}^2 \rangle (1-\epsilon)$$

$$\text{with } \epsilon = \frac{\langle x_{\perp}^2 \rangle}{\langle x_{||}^2 \rangle}$$

The quantity  $\frac{\partial^2 eq}{\partial x_3^2} = \sum_i \frac{\partial^2 eq_i}{\partial x_3^2}$  and by lattice sum method

$$\frac{\partial^2 eq}{\partial x_3^2} = \frac{1}{4\pi\epsilon_0} \sum_i \frac{Q_i}{R_i^2} 24 P_4(\cos\theta_i)$$

for the positive ions and conduction electron charge clouds.



This model of conduction electron charge clouds also allow us to estimate the probe dependence of the EFG for probe ions with an ionic radius not larger than that of the lattice ion. To incorporate the probe effect, first the total lattice sum in pure metal  $eq$  is determined and the EFG due to the twelve surrounding charge clouds carrying the effective charge of the host ion,  $eq^P(Z_{eff})$ , is subtracted. Then the EFG of the twelve surrounding charge clouds with the effective charge of the probe  $eq^P(Z'_{eff})$ , is added. In order to get the total EFG this is multiplied with  $(1-\gamma_\alpha)$  of the probe.

$$eq_{probe}^{Total} = (1-\gamma_\alpha)[eq - eq^P(Z_{eff}) + eq^P(Z'_{eff})] \quad (4.16]$$

$eq^P$  is calculated using the lattice sum method as

$$eq^P = \frac{1}{4\pi\epsilon_0} \frac{Z_{eff}e}{a^3} 4 [(1+\delta) - (1-\delta) \frac{\frac{1}{2} (c/a)^2 - \frac{1}{3}}{[\frac{1}{3} + \frac{1}{4} (c/a)^2]^{5/2}}]$$

The results of such calculations for zinc are reproduced in Fig. 4.4.

The different models which are discussed have only limited success in predicting the EFG in metals. Experimental determination of EFG's in different systems will be valuable in studying the various systematic trends which enables us to have a better understanding of the origin of the resultant EFG observed in metals. However, our experimental results and discussions would be better understood in view of these discussions.

eq. (1) -  $\gamma_{\infty}(\text{probe})$   
 $[10^{17} \text{ V/cm}^2]$

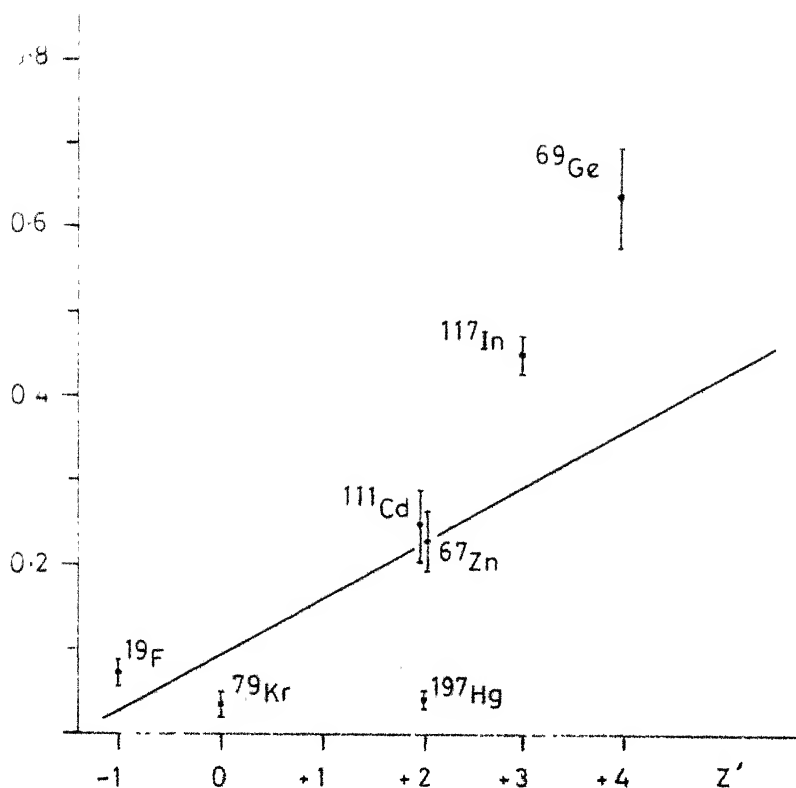


Fig 4.4 The dependence of EFG in Zinc on the probe used. The solid line represents the prediction of the Charge Shift model. Figure taken from ref. [21]

## 4.4 Quadrupole Interactions at $^{57}\text{Fe}$ in Titanium Metal

### 4.4.1 Introduction

The main objective of the work reported here is to measure the electric field gradient experienced by  $^{57}\text{Fe}$  probe doped in Titanium metal as a dilute impurity, using Mössbauer spectroscopy. The results are discussed in the framework of the available theoretical and semi-empirical models. The distribution of EFG at the probe nuclei is also determined from which an estimate of the different locations in which the iron atom has gone is found out.

Titanium is a transition metal in 3d-series with a hexagonal close packed structure. Piecuch and Janot [9] have calculated the EFG and its temperature dependence in transition metals of the 3d, 4d and 5d series using a first order perturbation dynamical theory in random phase approximation. The anisotropy of the metal was treated as a weak perturbation to the electronic Hamiltonian with respect to a cubic environment. The EFG obtained in this way in pure titanium is  $(-7.6 \text{ to } +2.5) \times 10^{15} \text{ V/cm}^2$ .

Three measurements of the quadrupole splitting in  $^{57}\text{FeTi}$  at room temperature are available in literature. Quim [22] reported a fairly large value for the quadrupole splitting  $\Delta E_Q = 0.32 \pm 0.03 \text{ mm/sec}$ , while Wortmann and Williamson [24] got a very small splitting of  $0.1 \pm 0.02 \text{ mm/sec}$  through their Mössbauer experiments. Both of them used the method of electroplating  $^{57}\text{Co}$  activity on Ti foils

## 4.4 Quadrupole Interactions at $^{57}\text{Fe}$ in Titanium Metal

### 4.4.1 Introduction

The main objective of the work reported here is to measure the electric field gradient experienced by  $^{57}\text{Fe}$  probe doped in Titanium metal as a dilute impurity, using Mössbauer spectroscopy. The results are discussed in the framework of the available theoretical and semi-empirical models. The distribution of EFG at the probe nuclei is also determined from which an estimate of the different locations in which the iron atom has gone is found out.

Titanium is a transition metal in 3d-series with a hexagonal close packed structure. Piecuch and Janot [9] have calculated the EFG and its temperature dependence in transition metals of the 3d, 4d and 5d series using a first order perturbation dynamical theory in random phase approximation. The anisotropy of the metal was treated as a weak perturbation to the electronic Hamiltonian with respect to a cubic environment. The EFG obtained in this way in pure titanium is  $(-7.6 \text{ to } +2.5) \times 10^{15} \text{ V/cm}^2$ .

Three measurements of the quadrupole splitting in  $^{57}\text{FeTi}$  at room temperature are available in literature. Quim [22] reported a fairly large value for the quadrupole splitting  $\Delta E_Q = 0.32 \pm 0.03 \text{ mm/sec}$ , while Wortmann and Williamson [24] got a very small splitting of  $0.1 \pm 0.02 \text{ mm/sec}$  through their Mössbauer experiments. Both of them used the method of electroplating  $^{57}\text{Co}$  activity on Ti foils

and diffusing at 1200°C. Devere and De Waard implanted the  $^{57}\text{Co}$  activity in a single crystal of Ti at an energy of 130 keV and got an upper limit of  $\Delta E_Q = 0.12$  mm/sec by Mössbauer measurements, after annealing at 700°C for a period of 1 hour and assuming that the  $^{57}\text{Co}$  activity has gone to unique substitutional sites.

Since the above experiments with source matrix as titanium, gave such widely varying results we have done the measurements, by preparing an absorber of pure titanium with  $^{57}\text{Fe}$  as a very dilute impurity for the first time, and using the  $^{57}\text{Co}$  in Rh matrix as the source.

#### 4.4.2 Sample preparation

Titanium of 99.99 % purity and iron ( $\sim 0.2$  at %) enriched in  $^{57}\text{Fe}$  isotope, were melted in a fused alumina crucible in an induction furnace at high vacuum. The melting was repeated a couple of times to get a homogeneous alloy. The alloy thus obtained was powdered with a diamond file and Mössbauer measurements were done with this unannealed sample. The quadrupole splitting of this sample was measured at room temperature. The resultant spectrum obtained showed a quadrupole doublet spectrum of appreciable line broadening.

The alloy was then annealed at 800°C for 6 days after sealing it in a quartz tube under high vacuum and slowly cooled to room temperature. This alloy was powdered and the samples were prepared by keeping the powder in a copper ring with cellophane tape with a distribution of  $30 \text{ mg/cm}^2$  of powder

and also by mixing the powder with the araldite adhesive followed by drying in the form of a thin plate. This method ensures the homogeneity of the sample and helps the sample to be perfectly random in orientation.

X-ray diffraction patterns of titanium and of the prepared alloys were recorded and compared. The analysis showed that the alloy has the same crystal structure as that of pure titanium.

#### 4.4.3 Experimental

The details of the experimental set-up were given in Chapter 2. The data were collected for sufficiently long time to ensure good absorption peaks and the effects of the statistical fluctuations were small. Pfeiffer et al. [25] and Kobayashi et al. [26] pointed out that if the peaks are not well separated with overlapping broad lines and the statistics is poor, an independent fit of Lorentzian parameters to the data may lead to erroneous results. A parameter  $\xi = D\sqrt{N}$  was set for statistical quality of the spectrum where  $D$  is the amplitude and  $N$  is the number of counts per channel at the peak. It was shown that independent fit procedure is valid only if  $\xi > 10$ . In all our measurements this parameter was kept well above this limit.

#### 4.4.4 Results and Discussion

##### (a) Quadrupole splitting at room temperature

The Mössbauer parameters obtained in our measurements

is shown in Table 4.1. The average Q.S. at room temperature [Fig. 4.5a] in the unannealed sample is  $0.343(8)$  mm/sec. An electric field gradient of  $1.63 \times 10^{17}$  V/cm<sup>2</sup> is deduced assuming the asymmetry parameter to be zero.

The annealed sample Mössbauer spectra [Fig. 4.5b] clearly showed the presence of two different well defined sites for the iron atom corresponding to Q. splitting of  $0.112(8)$  mm/sec or to an EFG of  $0.53(4) \times 10^{17}$  V/cm<sup>2</sup> for the inner lines and  $0.380(8)$  mm/sec corresponding to an EFG of  $1.86(4) \times 10^{17}$  V/cm<sup>2</sup> for the outer lines.

Following the arguments of Devare et al. if we assume that the smaller quadrupole splitting corresponds to the substitutional site of the iron atom the value of Q.S. obtained agrees quite well with the value reported by Wortmann and Williamson. Moreover this method of sample preparation adopted reduces very much the chances of iron forming clusters. Comparing the results with the reported intermetallics of Ti with Fe [27] it is most probable that the other site of iron in our alloy is interstitial which gives a quadrupole splitting of  $0.39(1)$  mm/sec. The agreement of the observed line widths ( $0.275$  mm/sec) with the expected values further shows that the  $^{57}\text{Fe}$  has gone to unique substitutional and interstitial sites in Titanium matrix for the absorbers prepared by us. Further, after preparing several samples it is found that getting a unique substitutional site alone for  $^{57}\text{Fe}$  in the host matrix

TABLE 4.1

Observed Mössbauer parameters for  $^{57}\text{FeTi}$  system.

Temperature $^{\circ}\text{K}$	Quadrupole Splitting mm/sec	Isomer Shift* mm/sec	$eq(1+\eta^2/3)^{1/2}$ in $10^{17}$ V/cm <sup>2</sup>
80	0.128 (6)	0.172 (7)	0.613 (28)
123	0.126 (6)	0.160 (8)	0.602 (28)
293	0.112 (8)	-0.016 (5)	0.538 (38)
360	0.103 (6)	-0.16 (8)	0.491 (28)
386	0.098 (8)	-0.21 (9)	0.468 (38)

\*With respect to iron metal. Numbers in paranthesis show the errors.



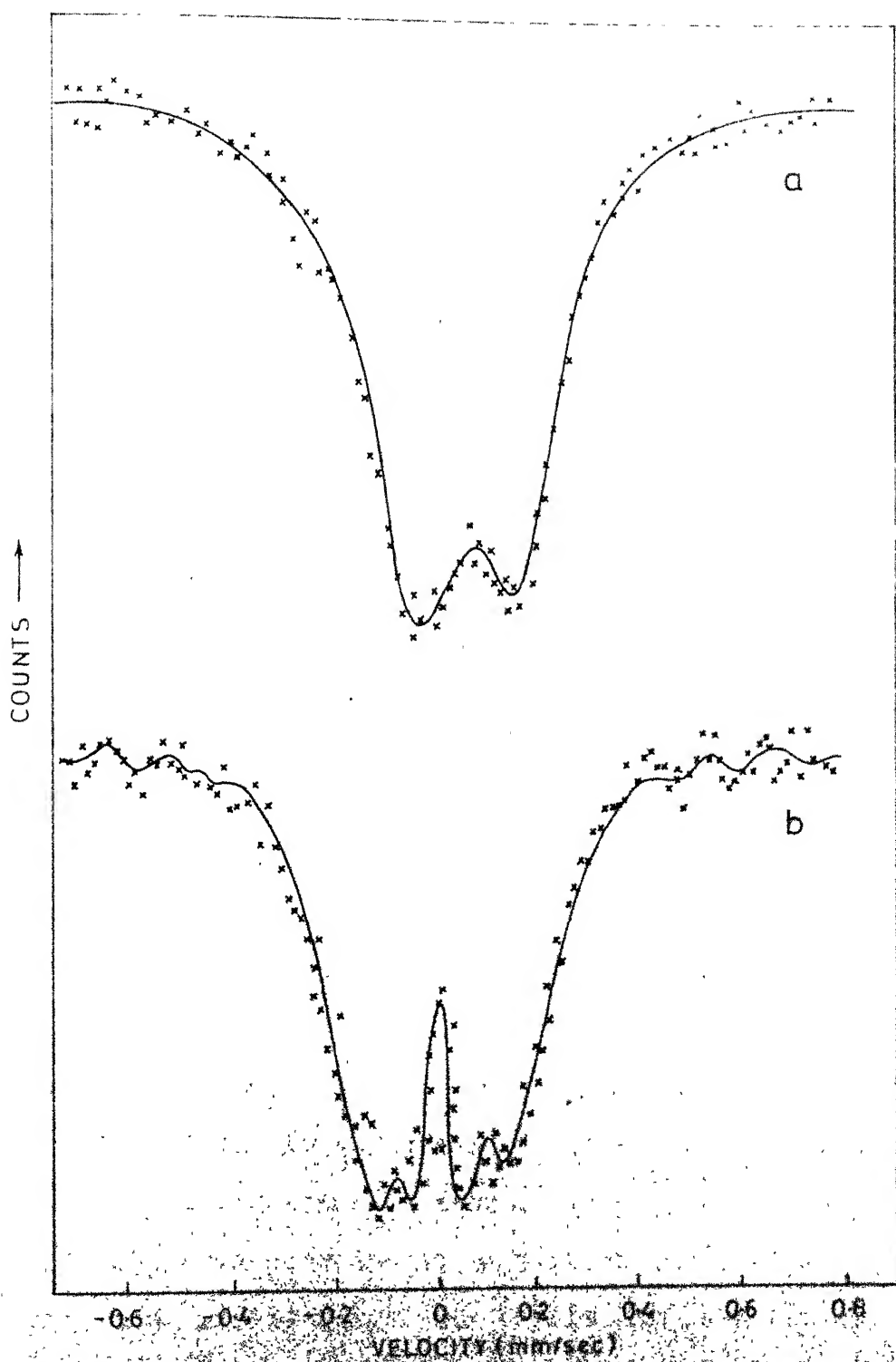


Fig. 4.5 The Mössbauer spectra  $^{57}\text{FeTi}$  (a) unannealed (b) after annealing

titanium is very difficult with the usual methods of alloy preparations.

b) Comparison with EFG's at other probes in titanium

Since titanium is an hcp metal the field gradients are expected to be axially symmetric. Therefore we have analysed our data assuming  $\eta = 0$ . Using the known value of the quadrupole moment of the 14.4 keV state of  $^{57}\text{Fe}$  (0.192 b) and the measured quadrupole splitting, the electric field gradient  $eq$  is obtained. The ionic contribution is calculated using the Das and Pomerantz [4] formula

$$eq_{\text{latt}} = \left(\frac{eZ}{a^3}\right) [0.0065 - 4.3584 \left(\frac{c}{a} - 1.633\right)] \quad (4.17)$$

and the known Sternheimer antishielding connection factor  $(1-\gamma_\infty) = 10.14$  for  $^{57}\text{Fe}$ . The ionic contribution  $eq_{\text{ion}}$  for  $^{57}\text{FeTi}$  system is  $0.47 \times 10^{17} \text{ V/cm}^2$ . If we assume that the signs of  $eq_{\text{ion}}$  and  $eq_{\text{el}}$  are opposite as observed for most of the other systems, the electronic contribution  $eq_{\text{el}}$  is obtained to be  $1.01 \times 10^{17} \text{ V/cm}^2$ .

Table 4.2 shows the EFG at different probes in titanium host reported so far. It seems that  $^{57}\text{Fe}$  in titanium produces the minimum EFG at the impurity site if we assume that the minimum Q.S. observed corresponds to a substitutional site. On the other hand if the larger Q. splitting is taken as the one corresponding to substitutional site the EFG is  $1.86 \times 10^{17} \text{ V/cm}^2$  which is comparable with the EFG obtained with other probes. Since the atomic volume of Fe is comparatively smaller

The available data at present on quadrupole interactions at different probes in titanium host.

Probe	$eq_{exp}$	$eq_{ion}$	$eq_{cl}^I$	$eq_{cl}^{II}$	$\frac{eq_{cl}^I}{eq_{ion}}$	$\frac{eq_{cl}^{II}}{eq_{ion}}$	$\frac{eq_{cl}^I}{eq_{ion}}(1-\gamma_\alpha)$	Ref.
Fe	-0.53	+0.47	-	-1.01	-	2.15	-	Present Work
Sc	$\pm 1.59$	+0.485	+1.105	-2.075	2.28	4.28	23.80	[28]
Ti	$\pm 1.20$	+0.46	+0.74	-1.66	1.60	3.60	16.00	[29]
Cd	+1.59	+1.4	+0.19	(-2.99)	0.14	(2.14)	4.24	[30]
Ta	$\pm 5.61$	+2.92	+2.69	-8.53	0.92	2.92	57.96	[31]
Hf	+8.60	+3.20	+5.40	(-11.80)	1.69	(3.69)	116.80	[32]
Ir	$\pm 6.5$	+2.04	+4.46	-8.59	2.19	4.18	96.60	[33]
Hg	$\pm 1.22$	+2.84	-1.62	$\pm 4.06$	0.57	1.43	34.90	[34]
Ru	$\pm 5.3$	+0.85	+4.45	-6.15	5.24	7.24	96.36	[35]
Au	$\pm 4.53$	+3.08	+1.45	-7.61	0.47	2.47	31.29	[35]

The EFG's are in units of  $10^{17}$  V/cm<sup>2</sup>. The quantities  $eq_{cl}^I$  and  $eq_{cl}^{II}$  are the electronic contributions to the EFG assuming the EFG to be positive and negative respectively.

(7.1 compared to 10.6 for Ti) there is enough possibility of Fe going interstitially in a diffusion process. Considering the Hume-Rothery rules for solid solution formation  $\frac{\Delta R}{\Delta R}$  is to be less than 0.15 and in this case for Fe and Ti  $\frac{\Delta R}{\Delta R} \sim 0.13$  which is not very much lower than 0.15. The above studies indicates that further ion channeling experiments have to be done to locate the exact site of the Fe atoms before arriving at a conclusion regarding the substitutional position of iron atoms in titanium host. The calculated value  $[(-7.6 \text{ to } 2.5) \times 10^{15} \text{ V/cm}^2]$  of EFG in pure titanium by Pieuch and Janot [9] is much smaller than the measured field gradients in titanium. Table 4.2 also shows the electronic contributions to the EFG obtained by subtracting the ionic contribution from the total EFG. The quantities  $eq_{el}^I$  and  $eq_{el}^{II}$  are the electronic parts obtained by taking the signs of  $eq_{ion}$  and  $eq_{el}$  to be same and opposite respectively. The sign of EFG at  $^{57}\text{Fe}$  probe in titanium is negative [23]. The sign of EFG at Cd and HF impurities are given as positive [30,32]. But the  $eq_{el}$  calculations reveal that if the resultant EFG is positive at Cd the ratio of  $|eq_{el}/eq_{ion}| = 0.14$  which deviates much from the Raghavan's systematics [5] where as if it is assumed to be negative the ratio  $|eq_{el}/eq_{ion}|$  comes to 2.14 which agrees well with the systematics.

### c) Correlation between $eq_{ion}$ and $eq_{el}$

Table 4.3 gives the measured EFG's in the hcp transition metal hosts/so far in literature. The electronic contributions

TABLE 4.3

Electric field gradients in hcp transition metal hosts.

HOST	PROBE	Sc	Fe	Cd	Ta	Hf	Ir	Ru	Au
Sc	(0.38)	0.38	4.0	-	5.16	8.1	42.9	19.2	-
Ti	(1.2)	1.59	-0.53 <sup>*</sup>	+1.59	5.61	+8.6	6.5	5.3	4.53
Y	(-)	0.99	1.51	0.83	5.91	-	+20.8	5.5	+21.00
Zr	(3.68)	-	3.16	0.75	5.15	8.9	6.8	4.5	18.24
Tc	(0.70)	-	-0.65	-	-	-	-	-	-
Ru	(0.49)	-	-0.71	-	-4.0	4.86	2.9	0.49	3.54
Hf	(+9.3)	-	1.66	+1.38	+4.7	+9.3	11.5	5.6	15.7
Re	(-4.7)	-	-0.50	-1.68	-5.52	-	-4.56	-	-3.04
Os	(-4.55)	-	-0.75	3.29	-6.0	7.0	-2.94	-	-

The values in paranthesis show the field gradients in pure metals. The values of field gradients are given in units of  $10^{17}$  V/cm<sup>2</sup>.

<sup>\*</sup>Present work.

to the EFG in hcp transition metal hosts are plotted against the ionic contributions in Fig. 4.6. The quantity  $K = |eq_{el}/eq_{ion}|$  has a value of 2.15. This shows that the system  $^{57}\text{FeTi}$  agrees well with the systematic correlation between  $eq_{ion}$  and  $eq_{el}$ . Considering the other site corresponding to an observed EFG of  $1.86 \times 10^{17} \text{ V/cm}^2$  if the sign of this is positive, the ratio of  $|eq_{el}/eq_{ion}|$  comes to 2.95, and if the sign is negative  $eq_{el}/eq_{ion}$  is 4.9.

#### d) Temperature dependence

From the measurements done between room temperature and liquid nitrogen temperature it is seen that this system almost obeys the  $T^{3/2}$  law for the variation of EFG (Fig. 4.7) as

$$eq(T) = eq(0) [1 - B T^{3/2}]$$

The parameters obtained from these measurements are

$$eq(0) = 0.63 \times 10^{17} \text{ V/cm}^2 \quad \text{and}$$

$$B = 32 \times 10^{-6} / T^{3/2}$$

The experimental findings of Q.S. are compared with the predictions of the charge shift model, later in this Chapter (Table 4.7).

#### e) EFG distribution at the impurity site in titanium host

Using the method described in Chapter 3 the distribution of EFG at the two different sites of  $^{57}\text{Fe}$  in titanium is

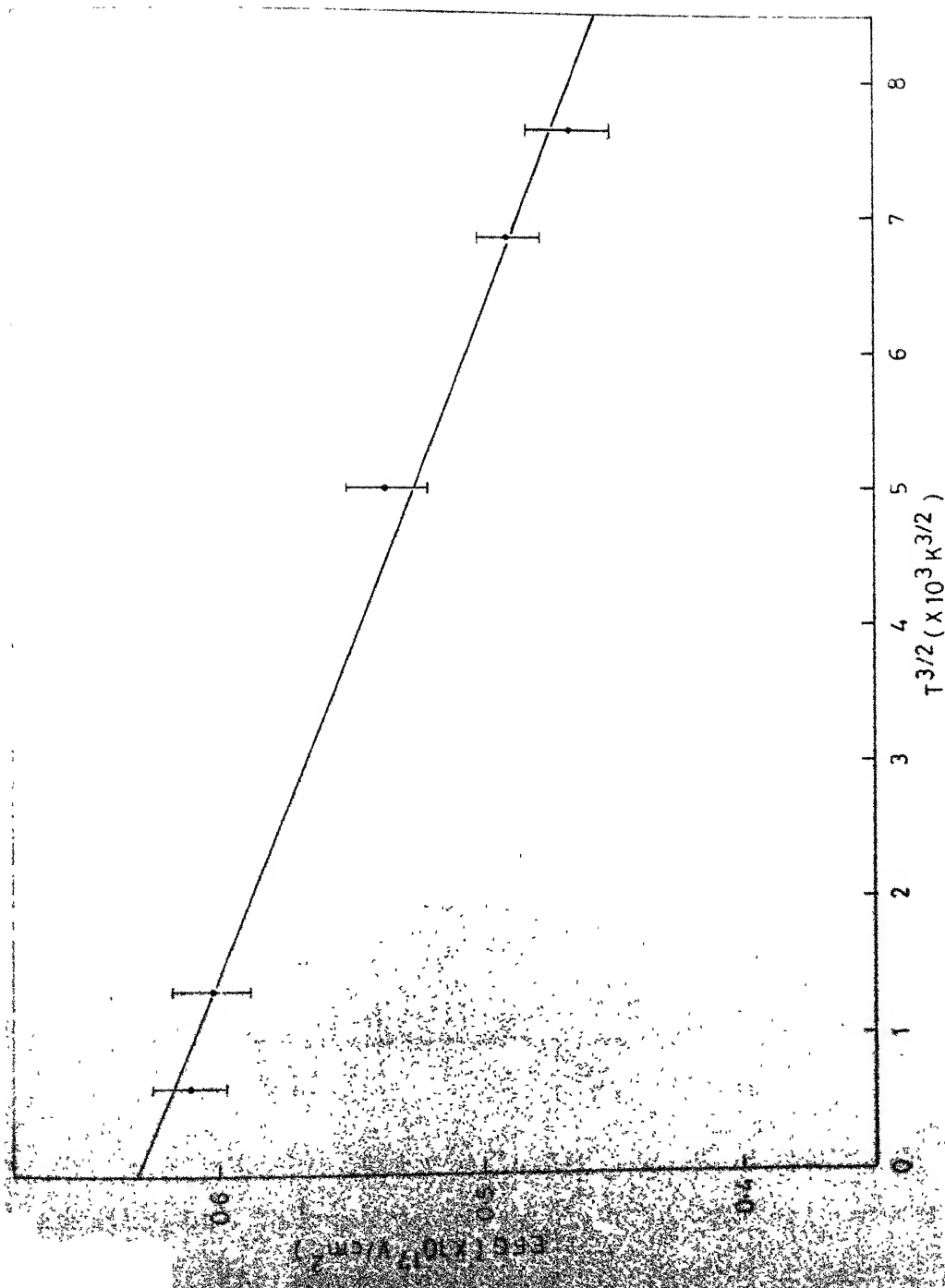


Fig.4.7 Temperature dependence of EFG in  $^{57}FeTi$  system.

found out, and is shown in Fig. 4.8. The width of the distribution for the site corresponding to the smaller value of Q.S. is 0.012 mm/sec and that for other site 0.016 mm/sec.

f) Comparison of experimental data with conduction electron charge shift model

The charge shift model calculations described earlier are done to find out the EFG in titanium and its temperature dependence.

The compliance constants are determined from the known values of the elastic constants  $C_{ij}$  of titanium at different temperatures as

$$S_{11} = \frac{C_{11}C_{33} - C_{13}^2}{(C_{11}-C_{12})(C_{11}C_{33} + C_{12}C_{33} - 2C_{13}^2)}$$

$$S_{12} = \frac{C_{13}^2 - C_{12}C_{33}}{(C_{11}-C_{12})(C_{11}C_{33} + C_{12}C_{33} - 2C_{13}^2)}$$

$$S_{13} = \frac{-C_{13}}{C_{11}C_{33} + C_{12}C_{33} - 2C_{13}^2}$$

$$S_{33} = \frac{C_{11} + C_{12}}{C_{11}C_{33} + C_{12}C_{33} - 2C_{13}^2}$$

Table 4.4 gives the values of  $a$  and  $c/a$  of titanium at various temperatures. The values of  $eq_{ion}$ ,  $eq_{hp}$  and  $eq_{el}$  are taken from Ref. 21 for the known values of  $c/a$  for titanium. Table 4.5 gives these values in units  $\frac{Z_{eff} e}{4\pi\epsilon_0 a^3}$  as a function of temperature or  $c/a$  value.



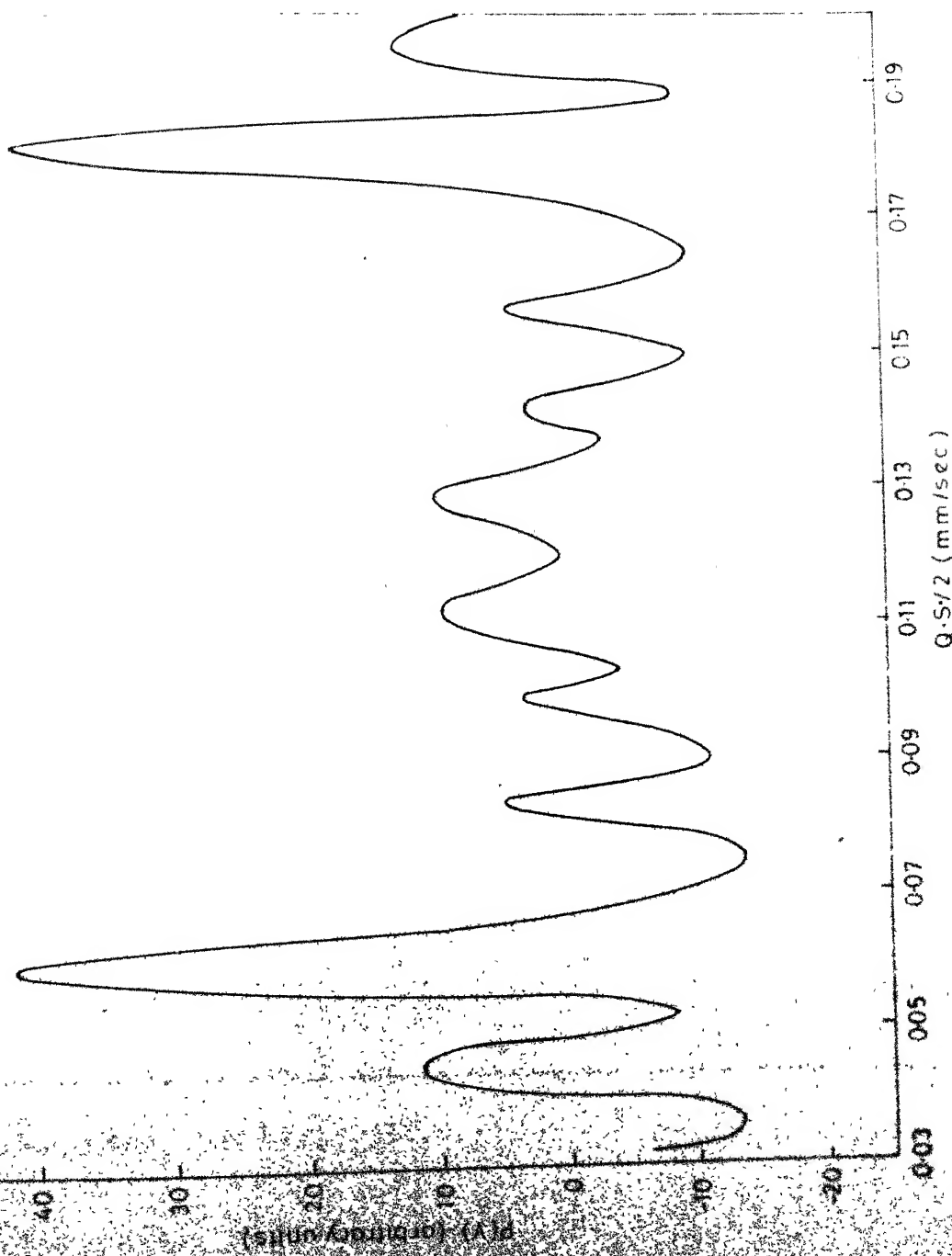


Fig.48 EFG distribution at  $^{57}\text{Fe}$  in titanium host (EFG in energy units of Q.S.)

TABLE 4.4

Lattice parameters of titanium at different temperatures.

Temperature °K	a Å	c/a
4	2.9416	1.5843
73	2.9435	1.5850
123	2.9449	1.5856
293	2.9496	1.5874
386	2.9526	1.5878
523	2.9558	1.5882
656	2.9593	1.5886
774	2.9634	1.5894
920	2.9670	1.5941

Data taken from Ref. [36].

TABLE 4.5

The value of  $eq_{ion}$ ,  $eq_{hp}$  and  $eq_{el}$  for different  $c/a$  values of titanium at different temperatures in units of  $Z_{eff} e/4\pi\epsilon_0 a^3$ .

Temperature $^{\circ}K$	$c/a$	$eq_{ion}$	$eq_{hp}$	$eq_{el}$
4	1.5843	0.2195	-39.566	41.701
73	1.5850	0.2164	-39.597	41.691
123	1.5856	0.2138	-39.600	41.682
293	1.5874	0.2059	-39.647	41.656
386	1.5878	0.2041	-39.658	41.650
523	1.5882	0.2024	-39.668	41.644
656	1.5886	0.2006	-39.679	41.638
774	1.5894	0.1971	-39.699	41.626
920	1.5941	0.1765	-39.823	41.556

The values of the elastic constants of titanium at different temperatures are shown in Table 4.6. Table 4.7 shows the calculated values of EFG at  $^{57}\text{Fe}$  probe in titanium host as a function of temperature for different values of  $Z'_{\text{eff}}$ . The Sternheimer antishielding factor  $(1-\gamma_{\infty})$  is taken to be 10.14 for the  $^{57}\text{Fe}$  probe in these calculations.

In the above calculations we have neglected the effects of the vibrations of the probe ions. Unlike the Nishiyama et al. [18] model, the isotropic vibrations of probe ions do not contribute to the EFG in charge shift model. The contributions from the anisotropic vibrations may be expressed as

$$\text{eq(vibrations)} = \frac{1}{2} \frac{\partial^2 \text{eq}}{\partial x_3^2} (1-\epsilon) \langle X_{\parallel}^2 \rangle$$

where  $\epsilon = \langle X_{\perp}^2 \rangle / \langle X_{\parallel}^2 \rangle$  and  $X_{\perp}^2$  and  $X_{\parallel}^2$  are the mean squared displacements of the probe ions perpendicular to the c-axis and parallel to the c-axis respectively

There are two factors which mainly contribute to the temperature dependence of EFG. The contributions come from the variations of the elastic constants and the lattice parameters with temperature and from the anisotropic vibrations of the probe ions. The temperature dependence of EFG is quite sensitive to the anisotropic vibrations of the probe ions.

The measured values of the field gradient at  $^{57}\text{Fe}$  in titanium host agrees well with the experimental values for  $\frac{Z_{\text{eff}}}{2} = 1$  and  $Z'_{\text{eff}} = 2$ . The charge shift model calculations are applied to other hcp metals and the results are shown along

TABLE 4.6

The values of elastic constants of titanium at different temperatures in units of  $10^{12}$  dynes/cm<sup>2</sup>.

Temperature °K	$C_{11}$	$C_{12}$	$C_{13}$	$C_{33}$
4	1.761	0.869	0.683	1.905
73	1.749	0.871	0.68	1.894
123	1.726	0.877	0.681	1.876
298	1.624	0.92	0.69	1.807
373	1.579	0.934	0.694	1.774
523	1.495	0.961	0.692	1.715
673	1.416	0.978	0.69	1.661
773	1.368	0.985	0.688	1.627
923	1.299	0.992	0.688	1.567

Data taken from Ref. [37].

TABLE 4.7

The values of electric field gradients at  $^{57}\text{Fe}$  in titanium host at different temperatures calculated using the charge shift model. The value of  $Z_{\text{eff}}$  is taken as 4.

Temperature (°K)	$Z'_{\text{eff}}$				Experimental
	0	1	1.5	2	
4	0.375	0.502	0.566	0.63	-
73	0.364	0.484	0.552	0.615	0.61
123	0.361	0.483	0.545	0.606	0.602
293	0.335	0.448	0.504	0.561	0.538
386	0.325	0.435	0.489	0.544	0.468
523	0.313	0.418	0.470	0.523	-
656	0.300	0.401	0.451	0.502	-
774	0.290	0.387	0.435	0.484	-
920	0.253	0.337	0.3787	0.420	-

with the experimental values in Table 4.8.

#### 4.4.5 Conclusions

The electric field gradient at  $^{57}\text{Fe}$  doped substitutionally in the transition metal titanium as a dilute impurity is measured to be  $0.538(38) \times 10^{17} \text{ V/cm}^2$  at room temperature. The results of the measurements of EFG for  $^{57}\text{FeTi}$  agrees with the charge shift model calculations. The ratio of  $e_{\text{el}}/e_{\text{ion}}$  agrees well with the universal correlation relation of Raghavan et al.

### 4.5 Quadrupole Interactions at $^{57}\text{Fe}$ in Trigonal Selenium

#### 4.5.1 Introduction

In the last few years considerable progress has been made in the understanding of the physical properties of selenium. It is known that selenium exists in the amorphous, hexagonal (trigonal) and  $\alpha$ - and  $\beta$ -monoclinic forms. The growth morphology and physical properties are reported in detail in references [38,39]. Trigonal selenium with its chain lattices and strong anisotropy have a number of peculiar and interesting physical properties. Since selenium is a semiconductor, it will be interesting to study the EFG produced at an impurity of the transition metal group, and to find out the electronic contribution to the EFG, because of the more localised nature of the conduction electrons.

TABLE 4.8

Calculated values of EFG at  $^{57}\text{Fe}$  probe at room temperature using charge shift model in various hcp metals and its comparison with experimental results.

Host	$Z_{\text{eff}}$	$Z'_{\text{eff}}$								Experi- mental
		0	1	1.5	2	2.5	3	4	5	
Zn	2		1.324	1.683	2.042	2.401				2.341
Cd	1.5		1.642	2.079	2.515	2.952				2.584
In	1		1.215	1.439	1.663	1.887				1.43
Sc	1		1.451	1.881	2.311	2.774	3.170	4.030	4.890	4.01
Tl	3						0.83	1.06	1.29	1.78
Y	1	0.70	1.75	2.27	2.79					1.697
Re	7		0.38	0.41	0.44	0.475	0.506	0.567		0.506
Ru	4	0.92	1.26	1.43	1.6	1.89				0.71
Ti	4	0.335	0.448	0.504	0.561	0.617				0.538
Hf	2	1.063	1.288	1.512	1.738					1.579

The value of  $Z_{\text{eff}}$  is chosen such that the results agrees closely with the experimental values.



#### 4.5.2 Crystal structure of hexagonal selenium

A molecule of hexagonal selenium consists of atomic chains displaced in Zig-Zag fashion in the direction  $[0001]$  (Fig. 4.9). The shortest interatomic distance in the chain and the shortest distance between the chains of hexagonal selenium are  $2.32 \text{ \AA}$  and  $3.53 \text{ \AA}$  respectively. The covalent bond angle Se-Se-Se is  $103^\circ$ . Between the atoms in the rings and chains, in the case of hexagonal selenium, there exist homopolar links and the rings and chains themselves are bound to one another by considerably non-polar forces. Hexagonal selenium belongs to the space group  $P3_121$  with unit cell dimensions  $a = 4.3662 \text{ \AA}$  and  $c = 4.9536 \text{ \AA}$  with  $\beta = 120^\circ$ . The unit cell has three molecules lying on a helical chain of symmetry  $3_1$  or  $3_2$ . These chains pass through the corners of a hexagonal lattice. The atoms lie on special positions on a two-fold rotation axis so that only one position parameter  $x$ , needed to be determined.

#### 4.5.3 Sample preparation

Trigonal selenium crystals were grown by the method described by C.H.Griffiths and B. Fitton [40]. Selenium 99.99 % purity and iron powder ( $\sim 0.1 \text{ at } \%$ ) enriched to 91 % in  $^{57}\text{Fe}$  were sealed in a quartz tube under high vacuum. The sealed samples were kept at  $600^\circ\text{C}$  for about 10 days, after which the ampoules were transferred to a furnace kept at  $90^\circ\text{C}$ , for 4 days, in which case it crystallizes in the form of spherulites. This was cooled to room temperature and the spherulites were powdered.

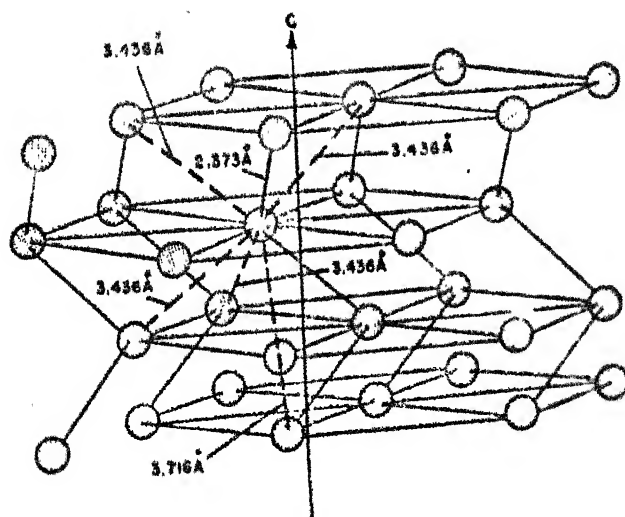
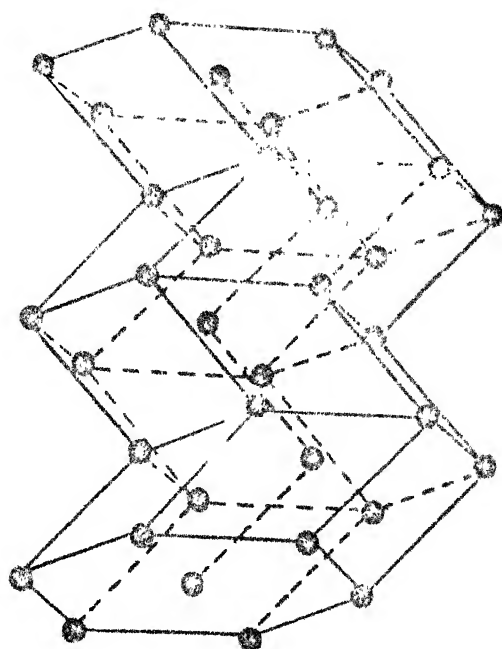


Fig. 4.9. Crystal Structure of Hexagonal Selenium.

The X-ray diffraction pattern was obtained using the XRD-5 X-ray diffractometer to determine the crystal structure. The results of X-ray analysis shows that selenium has grown into the trigonal form with the unit cell dimensions given earlier. About 30 mg of powder was sandwiched between two celloctapes covering an area of nearly one square cm. The thickness of the active material was therefore about  $0.05 \text{ mg/cm}^2$ , which was quite small so that the broadening due to sample thickness could be neglected. A separate sample was prepared by thoroughly mixing the powder specimen with araldite adhesive for getting a distribution of pure random orientation. This sample was used for the measurements from liquid nitrogen temperature to room temperature.

#### 4.5.4 Results and discussions

Since the melting point of selenium is  $217^\circ\text{C}$ , the range of temperatures at which the Mössbauer spectra can be studied, is limited to comparatively low temperatures.

For pure electric quadrupole interaction, the quadrupole splitting in the case of  $^{57}\text{Fe}$  may be written as

$$\Delta E_Q = \frac{e^2 q Q}{2} \left(1 + \frac{\eta^2}{3}\right)^{\frac{1}{2}}$$

where  $eq$  is the electric field gradient at the nuclear site and  $\eta$  is the asymmetry parameter. Values of  $eq$  and  $\eta$  cannot be determined separately from  $^{57}\text{Fe}$  Mössbauer spectra alone and therefore one has to obtain the value of  $\eta$  from some other experiments to obtain the magnitude of the electric field

with  $^{129}\text{I}$  obtained a value of  $\eta = 0.5 \pm 0.02$  for trigonal selenium.

A typical Mössbauer spectra obtained by us is shown in Fig. 4.10. The Mössbauer parameters derived from the data are given in Table 4.9. The values of isomer shift are given with respect to iron metal. Using the known quadrupole moment  $Q = 0.192$  barn of the 14.4 keV state of  $^{57}\text{Fe}$ , the experimental values of  $eq(1 + \eta^2/3)^{1/2}$  were calculated.

Earlier experiments [41,42] by Boolchand et al. in trigonal selenium yielded a value  $110 \times 10^{17} \text{ V/cm}^2$  for the EFG with  $^{125}\text{Te}$  in Se, and  $69.2 \times 10^{17} \text{ V/cm}^2$  with  $^{129}\text{I}$ . In these experiments the line widths are  $\sim 6$  mm/sec. in the case of  $^{125}\text{Te}$  and 2 mm/sec in the case of  $^{129}\text{I}$ . In the present experiment from the observed line widths and solubility data, it appears that  $^{57}\text{Fe}$  is substitutional in selenium matrix. The EFG obtained with the above values for  $\eta$  and  $Q$  at room temperature is  $eq = 0.749(9) \times 10^{17} \text{ V/cm}$ . Boolchand et al. [41] reported recently that the sign of EFG on  $^{129}\text{I}$  in selenium is negative. At present it appears to be difficult to comment on the sign of EFG for  $^{57}\text{Fe}$  in selenium. The lattice contribution to the EFG,  $eq_{\text{ion}} = 0.763 \times 10^{17} \text{ V/cm}^2$ , using Das and Pomerantz relation [Eq. 4.17] and with  $(1-\gamma_{\infty})$  for  $^{57}\text{Fe}$  equal to 10.14. Using this value we obtain  $eq_{\text{el}} = 1.512$ , if the sign of EFG is positive and sign of  $eq_{\text{ion}}$  negative, and  $eq_{\text{el}} = 0.014$  if the sign of EFG is positive and sign of  $eq_{\text{ion}}$  is also positive. That is, in the case the electronic contribution becomes negligible and

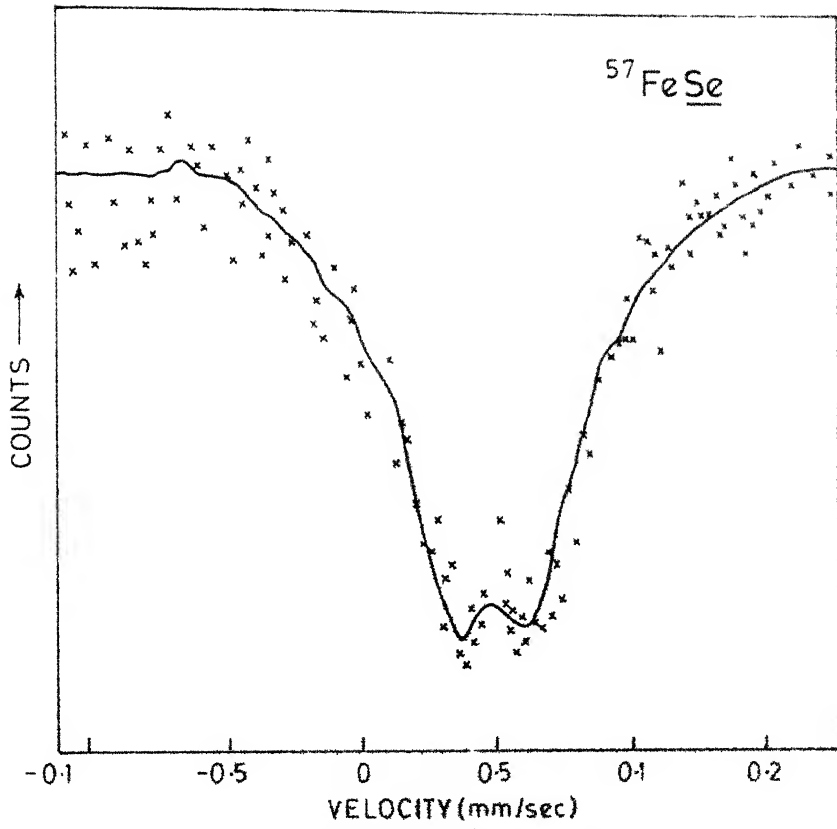


Fig.4.10 Mössbauer spectrum of  $^{57}\text{FeSe}$  at room temperature

TABLE 4.9Observed Mössbauer parameters of  $^{57}\text{FeSe}$ .

Temperature K	Quadrupole Splitting (mm/sec)	Isomer Shift* (mm/sec)	$eq(1 + \frac{\eta}{3})^{\frac{1}{2}}$ in $10^{17} \text{ V/cm}^2$	$eq$ in $10^{17} \text{ V/cm}^2$
82	0.175 (6)	0.450 (5)	0.837 (28)	0.804 (27)
123	0.170 (6)	0.451 (6)	0.813 (28)	0.781 (27)
195	0.167 (8)	0.456 (7)	0.799 (38)	0.767 (36)
298	0.163 (7)	0.467 (6)	0.779 (33)	0.749 (32)

\*With respect to iron metal.

all the EFG is of ionic origin. Table 4.10 gives the EFG for different probes in selenium host. It is seen that besides the ionic part, the  $eq_{el}$  values are highly probe dependent. This is not unexpected because, the co-valent bonding between the atoms on the same chain play an important role in determining the EFG, and the bonding of the probe atom with nearest host atoms could change the EFG considerably.

a) Correlation between  $eq_{el}$  and  $eq_{ion}$

The present data on selenium seem to qualitatively support the Raghavan's correlation if we assume that  $eq_{ion}$  and  $eq_{el}$  are of opposite signs.

b) Temperature variation of QIF

The temperature dependence of the QIF's [14,17,43] may be expected from the changes in lattice parameters, from the lattice vibrations, or possibly from the interactions of the neighbouring quadrupoles. Since the number of observations between room temperature and liquid nitrogen temperature is small, it is difficult to establish the actual relation for the temperature dependence of QIF. However, we checked that our data fit with empirical relation

$$eq(T) = eq(0) (1 - B T^{3/2}).$$

c) Recoilless fraction

The recoilless fraction of  $^{57}\text{FeSe}$  absorber is measured by using the method adopted by Trooster et al. [44] with some

TABLE 4.10

The currently available data on quadrupole interactions for different probes in Selenium host.  $eq_{el}^I$  and  $eq_{el}^{II}$  are calculated values assuming the total EFG to be positive and negative respectively. All the values of EFG are in  $10^{17}$  V/cm<sup>2</sup>.

Probe	$eq_{exp}$	$eq_{ion}$	$eq_{el}^I$	$eq_{el}^{II}$
<sup>125</sup> Te	$\pm 110.0^a$	1.45	108.55	-111.45
<sup>129</sup> I	+ 69.2	1.34	67.86	-
<sup>57</sup> Fe	$\pm 0.749^b$	0.763	- 0.014	- 1.512

(a) Reference 1      (b) Present work.



modifications. The method described in Chapter 3 can be applied only if we know the number of active nuclei ( $^{57}\text{Fe}$  /cm) of the absorber which is difficult to determine in this case. So the following method is used to determine the recoilless fraction ( $f_a$ ).

$f_a$  is related to the mean square displacement of the Mössbauer atom in the absorber by the expression

$$f_a = \exp [-K^2 \langle x^2 \rangle_T] \quad (4.18)$$

and  $\ln f_a$  is proportional to the absolute temperature  $T$  for  $T/\theta_D > 0.5$  as

$$- \ln f_a(T) = \frac{6RT}{k_B \theta_D^2} \quad (4.19)$$

where  $R$  is the recoil energy of the Mössbauer atom;  $\theta_D$  the Debye temperature and  $k$  is the Boltzmann constant. In other words

$$- \ln f_a(T) = - \lambda T$$

$f_a(T)$  is also given by the equation

$$f_a(T) = \frac{t_a}{N\sigma_0}$$

where  $t_a$  is the effective thickness of the absorber,  $N$  the number of Mössbauer atoms/cm<sup>2</sup> and  $\sigma_0$  is the resonance absorption cross section for the Mössbauer radiation [Chapter 3].

$$\ln t_a = \ln N\sigma_0 + \ln f_a(T)$$

$$= \ln N\sigma_0 + \lambda T$$

at temperature  $T_1$

$$\ln t_{a_1} = \ln N\sigma_0 + \lambda T_1$$

and at temperature  $T_2$

$$\ln t_{a_2} = \ln N\sigma_0 + \lambda T_2$$

from which

$$\ln N\sigma_0 = \frac{T_2 \ln t_{a_1} - T_1 \ln t_{a_2}}{T_2 - T_1} \quad (4.20)$$

$t_{a_1}$  and  $t_{a_2}$  are calculated from the Mössbauer spectra areas at two temperatures. The area of an absorption peak can be calculated from the transmission integral as

$$N(V_s) = B [1 - F_s [1 - \frac{2}{\pi r_0} \int \frac{(r_0/2)^2}{(V - V_s)^2 + (r_0/2)^2} \times \exp \{- t_a \frac{(r_0/2)^2}{V^2 + (r_0/2)^2} \} dV]] \quad (4.21)$$

where  $N(V_s)$  is the number of  $\gamma$ -quanta that reach the detector when source and absorber have a relative velocity  $V_s$  with respect to each other,  $F_s$  is given by

$$F_s = \frac{f_s N_\gamma(\infty)}{N_x + N_\gamma(\infty)}$$

which is the recoilless fraction of the incident radiation corrected for background.  $N_\gamma(\infty)$  is the number of  $\gamma$ -quanta reaching the detector per unit time when the relative velocity between source and absorber is very large,  $N_x$  is the background

rate when a 0.005 inch brass plate is introduced between the absorber and detector for the same geometry.  $F_s$  can also be determined from the Mössbauer spectrum of a substance like SNP or natural iron foil where the distribution and the recoilless fraction are known,  $r_0$  is the natural line width of the source and  $V$  is the energy variable expressed in equivalent Doppler velocity.

For small values of  $t_a$  the exponential can be approximated by

$$N(V_s) = B \left[ 1 - F_s \frac{t_a}{2} \cdot \frac{(r/2)^2}{V_s^2 + (r/2)^2} \right] \quad (4.22)$$

where  $r = 2 r_0$ . The peak intensity and absorption area are given by

$$I_0 = 1/2 F_s t_a \quad \text{and} \quad A_0 = 1/2 \pi F_s t_a r_0$$

Trooster et al. [44] made a table of  $t_a$  for various values of area  $A$ , of a Lorentzian line fitted to  $N(V_s)$  as given in Eq. (4.21). These values were obtained by calculating  $N(V_s)$  numerically and subsequently fitting a Lorentzian line to the calculated spectra. If the source line width deviates from  $r_0$  by an amount  $\Delta r_s$ , as a first approximation the measured line width should be corrected by this amount, before it is used for the determination of  $t_a$ , i.e.  $(r - \Delta r_s)$  should be used instead of  $r$ .

Using the above method the recoilless fraction of  $^{57}\text{Fe}$  in Se is determined at room temperature and the average value

comes out to be  $f_a = 0.18$ . The Debye temperature of the probe atom in the host lattice can be determined using Eq. 4.19. The mean square displacement of the host is related to that of the probe through the relation

$$\frac{\langle x^2 \rangle_{\text{imp}}}{\langle x^2 \rangle_{\text{host}}} = \left[ \frac{m_{\text{host}}}{m_{\text{imp}}} \right]^{\frac{1}{2}} \quad \text{for } T \rightarrow 0^\circ\text{K}$$

where  $m_{\text{host}}$  is the mass of the host atom and  $m_{\text{imp}}$  is that of the impurity atom. The Debye temperature of the host can be calculated from  $\langle x^2 \rangle_{\text{host}}$  using eq. 4.19.

The Debye temperature of the probe atom in the host can also be determined from the slope of, logarithm of the effective thickness against temperature graph. From Eq. 4.19 the slope of this straight-line graph is

$$\frac{6 E_R}{k\theta_D^2} = \frac{\ln t_{a2} - \ln t_{a1}}{T_1 - T_2}$$

from which  $\theta_D$  can be found out. Using the above method the calculated value of Debye temperature of  $^{57}\text{Fe}$  in selenium is  $120^\circ\text{K}$ .

The author has also applied this method to find the recoilless fraction of  $^{57}\text{Fe}$  in the isoelectronic host tellurium and the value of  $f_a$  thus obtained at room temperature is 0.43.

#### 4.5.5 Conclusion

The electric field gradient at  $^{57}\text{Fe}$  doped in the semiconductor selenium as a dilute impurity is measured to be  $0.749(43) \times 10^{17} \text{ V/cm}^2$ . The electronic contribution to the total EFG is

negligible if the experimental and ionic EFG's are taken as positive. Otherwise it obeys the universal correlation of Raghavan et al.

#### 4.6 Quadrupole Interaction at $^{57}\text{Fe}$ in the hcp Rare-Earth Neodymium as a Dilute Impurity

##### 4.6.1 Introduction

Neodymium is a rare earth metal of the group IIIb series with a double hexagonal close packed structure, which means that the layer sequence is ABCABC instead of ABAB. Therefore two inequivalent lattice sites with  $e_{\text{latt}}$  differing by 10 % should exist [45]. Raghavan et al. [5] showed that the EFG in rare earth metals does not obey the universal correlation proposed by them because the electronic part of EFG is mainly contributed by the unfilled 4f shell. Recently Ernst et al. [45] proposed a new classification for hexagonal metals. They have shown with the available data at present that the electronic contribution to the total EFG is proportional to the ionic part, the proportionality constant  $K$  being positive for all group IIIb and IVb hexagonal metals and negative for all group IIb, VIIb and VIIIb metals. In rare earths the studies are mainly concentrated on the heavy rare earth metals from Gd to Lu with more than half filled 4f shell where one expects the conduction bands to be quite similar. These hcp metals have lattice structures with almost the same  $c/a$  ratio. To check the validity of these proposed systematics for a light

rare-earth we have taken the system  $^{57}\text{FeNd}$  and measured the EFG by Mössbauer effect.

#### 4.6.2 Sample preparation

Neodymium (99.9 % purity and iron ( $\sim 0.2$  at %.) enriched in  $^{57}\text{Fe}$  were melted in an induction furnace in Zirconia Crucible under high vacuum. The resulting alloy was sealed in a quartz tube under high vacuum and annealed at  $500^\circ\text{C}$  for 4 days. Since neodymium oxidises very easily in atmosphere the alloy, after breaking the seal, was kept in mineral oil. This shining alloy ball was powdered with a diamond file in mineral oil and later mixed with epoxy resin to prevent oxidation and to have a uniform distribution. The quadrupole splitting of this sample was measured at room temperature and at liquid nitrogen temperature.

X-ray diffraction pattern of this sample was studied and the analysis showed that this alloy has the same crystal structure as that of pure neodymium and no other intermetallic compounds are formed in significant proportions.

#### 4.6.3 Results and discussions

The typical Mössbauer spectra of the  $^{57}\text{FeNd}$  system at room temperature is shown in Fig. 4.11. The observed Mössbauer parameters at room temperature and liquid nitrogen temperature are shown in Table 4.11. The quadrupole splitting at room temperature is  $0.30(1)$  mm/sec which is an average value obtained from many independent runs. An electric field gradient of  $1.45(5) \times 10^{17}$  V/cm<sup>2</sup> is deduced from this, assuming the asymmetry

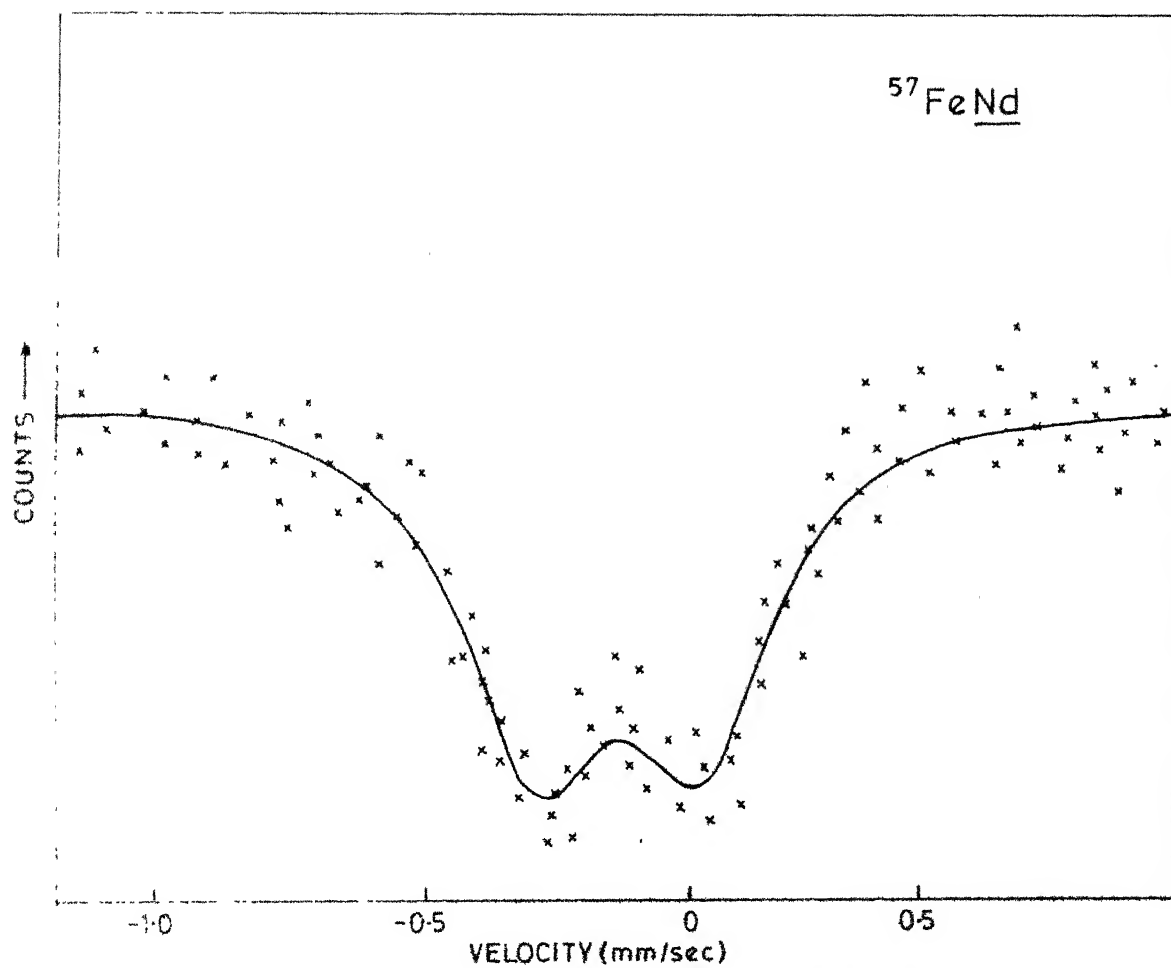


Fig 4.11 Mössbauer spectrum of  $^{57}\text{FeNd}$  at room temperature.

TABLE 4.11Observed Mössbauer parameters of  $^{57}\text{FeNd}$ .

Temperature $^{\circ}\text{K}$	Quadrupole Splitting mm/sec	Isomer Shift <sup>*</sup> mm/sec	$eq(1+\eta^2/3)^{1/2}$ in $10^{17}$ V/cm <sup>2</sup>
295	0.304 (9)	-0.140 (8)	1.454 (43)
173	0.317 (8)	0.06 (7)	1.516 (38)
82	0.331 (8)	0.209 (6)	1.584 (38)

<sup>\*</sup>With respect to iron metal.



parameter to be zero. The FWHM of the absorption lines observed 0.32 mm/sec which is comparable with the natural line width at room temperature of  $^{57}\text{Co}$  source in rhodium matrix and natural iron absorber, which shows that the  $^{57}\text{Fe}$  has gone to unique positions, most probably substitutional, in the alloy. The isomer shift at room temperature obtained is  $-0.140(8)$  mm/sec with respect to iron metal and it changes to  $0.209(6)$  mm/sec at 82 K.

The lattice contribution to the EFG by using the Das and Pomerantz relation for hcp metals is  $0.08 \times 10^{17}$  V/cm<sup>2</sup> which is very small compared to the experimental value. This shows that the electronic contribution is the major source of EFG in this case and the ratio of  $eq_{el}$  to  $eq_{ion}$  is  $\approx 17$ . The systematics proposed by the Ernst et al. [45], gives for heavy rare earth metals, a value for  $|eq_{el}/eq_{ion}| \sim 2$ . The value of  $eq_{ion}$  and  $eq_{el}$  with this systematic behaviour is reproduced in Table 4.12. Our results of  $^{57}\text{FeNd}$  shows that the electronic contribution is very much augmented for the less than half filled 4f shell.

#### 4.6.4 Some theoretical aspects of EFG in rare earth metals

Pelzl [46] has given some insight into the role played by the conduction electrons and the 4f electrons in heavy rare earth metals. The total EFG is because of three sources. 1. The EFG produced by the 4f electrons, 2. The EFG arising from the point charges surrounding the rare-earth ions, and 3. The EFG produced by the conduction electrons. Each of these

TABLE 4.12

Systematics of electric field gradients in pure hexagonal group IIb, IIIb (including the rare earths), IVb, VIIb, and VIIIb metals. The experimental EFG data  $eq_{\text{exp}}$ , the ionic contribution  $eq_{\text{ion}} = eq_{\text{latt}}(1-\gamma_{\infty})$ , and the electronic part  $eq_{\text{el}} = eq_{\text{exp}} - eq_{\text{ion}}$  are listed. All the values are given in units of  $10^{17}$  V/cm<sup>2</sup>. Predicted signs for  $eq_{\text{exp}}$ , whose signs have not been measured, and the corresponding values for  $eq_{\text{el}}$  are put in parentheses.

Group	lattice	$eq_{\text{exp}}$	$eq_{\text{ion}}$	$eq_{\text{el}}$
IIb	Zn	+3.0(2)	-1.96	+5.0
	Cd	+6.7(9)	-3.63	+10.3
	Cd (24 kbar)	+6.0(9)	-2.90	+8.9
	Cd (50 kbar)	+5.4(8)	-2.60	+8.0
	Cd (74 kbar)	+4.8(8)	-2.50	+7.3
IIIb	Sc	(+)0.38(2)	+0.22	(+0.16)
	La	(+)1.5(2)	+0.50	(+1.0)
	Gd	+2.8(3)	+1.06	+1.7
	Tb	+3.4(1.7)	+1.32	+2.1
	Dy	+4.3(1.5)	+1.53	+2.8
	Tm	+5.0(8)	+1.64	+3.4
	Lu	+3.6(5)	+1.36	+2.2
IVb	Ti	(+)1.2(1)	+0.40	(+0.8)
	Hf	+9.5(4)	+2.84	+6.7
VIIb	Tc	(-)0.7(4)	+1.56	(-2.3)
	Re	-4.9(2)	+2.08	-7.0
VIIIb	Fe ( $\epsilon$ phase)	(-)0.26(5)	+0.44	(-0.70)
	Co	-0.29(2)	+0.15	-0.44
	Ru	(-)0.49(14)	+1.41	(-1.90)
	Os	-4.5(3)	+3.24	-7.7

Data taken from Ref. [45].

gradients are, modified aspherical distributions of the closed electron shells (Sternheimer effect). The resulting EFG is given as

$$q = (1 - R'_Q) q_{4f} + (1 - R''_Q) q_{CE(int)} + (1 - \gamma'_\infty) (q_{latt} + q_{CE(ext)})$$

$q_{4f}$  is the gradient produced by the 4f electrons,  $q_{latt}$  is that due to the positive ions in the neighbourhood,  $q_{CE(int)}$  and  $q_{CE(ext)}$  are the contribution of the conduction electrons inside and outside the atomic sphere. The Sternheimer factor  $R_Q$  and  $\gamma_\infty$  account for the induced distortions

The two field gradients can be related by introducing a parameter  $\delta$  as

$$(q_{latt} + q_{CE(ext)}) = q_{latt}(1+\delta)$$

From a non-relativistic APW calculation Das and Ray [48] obtained  $\delta = 0.4$  for Dy metal. A nearly free electron behaviour is a good approximation for the conduction electrons, and a vanishing  $q_{CE(int)}$  is expected in heavy rare-earth metals. The electric field gradient produced by the 4f electrons which are well located inside the atomic sphere can be calculated using the relation [46]

$$(1 - R'_Q) q_{4f} = -3 e \langle J | \alpha | J \rangle$$

$$\langle J_2^2 - 1/3 J(J+1) \rangle \langle r^{-3} \rangle Q_{4f}$$

the effective radial integral is defined as

$$\langle r^{-3} \rangle_{4f} = \langle r^{-3} \rangle_{4f} (1 - R'_Q)$$

where  $R'_Q$  is the Sternheimer factor which accounts for the contributions from the induced distortions of all other core shells due to the aspherical 4f electron distribution in the metal. An empirical relation is proposed which fits with the radial integral as  $\langle r^n \rangle = D_n (Z - \sigma_n)^{-n/4}$  for  $64 \leq Z \leq 70$ . For rare-earth metals the best fit yields  $D_n = 1.940$  and  $\sigma_n = 58.41$ .

From these theoretical consideration Pelzl [46] found that in the heavy rare-earth metals, the EFG due to lattice and conduction electrons should be due to the point charge contribution and an enhanced electron charge density at interstitial sites respectively, and is given by

$$q = (1 - \gamma'_\alpha) (1 + \delta) q_{\text{latt}} \approx 200 q_{\text{latt}}$$

It is also found that the conduction electrons also enhance the field gradient at the 4f site.

#### 4.6.5 Conclusions

The EFG at  $^{57}\text{Fe}$  as a dilute impurity in the light rare-earth metal neodymium was determined for the first time as  $0.30(1) \times 10^{17} \text{ V/cm}^2$ . The lattice contribution is  $0.08 \times 10^{17} \text{ V/cm}^2$  and the ratio of  $|eq_{\text{el}}/eq_{\text{latt}}| = 17$ , which violates the systematics proposed by Raghavan et al. [5] and also of Ernst et al. [45]. The EFG in this case may be originating mainly from the less than half filled 4f shell. A systematic study

of the EFG in other hcp rare-earth metals with less than half filled 4f shell (Pr and Pm) will give a better insight to this behaviour.

#### 4.7 Comparisons

The three hcp structures chosen to serve as the hosts of  $^{57}\text{Fe}$ , represent three different categories. Ti is a transition metal of the 3d-series with  $c/a = 1.5873$  and has interesting properties. The sign of field gradient in Ti depends on probe. For  $^{57}\text{FeTi}$  it is negative where as for  $^{111}\text{CdTi}$  it is positive. The ionic and electronic contributions follow the general trend observed by Raghavan et al. Selenium is a semiconductor which is isoelectronic in nature with Tellurium and Sulphur. The observed EFG has the same value as the ionic contribution to EFG (if  $eq_{\text{exp}}$  is taken as positive) which suggests that the conduction electron contribution is practically zero in this case. Neodymium is from the rare-earth group with a less than half filled 4f shell and the results of our study shows that the 4f electron contribution is very much predominant over the other contributions to the total EFG.

# REFERENCES

- [1] E.N. Kaufmann, R.J. Vianden, Reviews of Mod. Phys. 51, 161 (1979).
- [2] R. Vianden, Hyp. Int. 10, 1243 (1981).
- [3] R.E. Watson, A.C. Gossard and Y. Yafet, Phys. Rev. 140, A375 (1965).
- [4] T.P. Das and M. Pomerantz, Phys. Rev. 123, 2070 (1961).
- [5] P. Raghavan, E.N. Kaufmann, R.S. Raghavan, E.J. Ansaldò and R.A. Naumann, Phys. Rev. B13, 2835 (1976).
- [6] P. Boolchand, B.L. Robinson and S. Jha, Phys. Rev. B2, 3463 (1970).
- [7] K. Krusch and M. Forker, Z. Physik, B37, 225 (1980).
- [8] M. Piecuch and C. Janot, J. Phys. Colloq. C6, 359 (1976).
- [9] M. Piecuch and C. Janot, Hyp. Int. 5, 69 (1977).
- [10] W. Leitz, W. Semmler, R. Sielemann and Th. Wichert, Phys. Rev. B14, 5228 (1976).
- [11] G.S. Collins, Hyp. Int. 4, 523 (1978).
- [12] J. Christiansen, P. Heuber, R. Keitel, W. Klinger, W. Loeffler, W. Sander and W. Witthuhn, Z. Physik, B24, 177 (1976).
- [13] K. Krien, J.C. Soares, K. Freitag, R. Tischler, G.N. Rao, H.G. Muller, E.N. Kaufmann, A. Hanser and B. Feurer, Phys. Rev. B14, 4782 (1976).
- [14] K. Nishiyama, F. Dimmling, Th. Kornrumpt and D. Riegel, Phys. Rev. Lett. 37, 357 (1976).
- [15] B.R.A. Nijiboer and F.W. de Wette, Physica, 24, 1105 (1958).

- [16] T.P. Das, Physica Scripta 11, 121 (1975).
- [17] M.D. Thompson, P.G. Pattnaik and T.P. Das, Hyp. Int. 4, 515 (1978).
- [18] K. Nishiyama and D. Riegel, Hyp. Int. 4, 490 (1978).
- [19] W. Kohn and L.J. Sham, Phys. Rev. 140, A1133 (1965).
- [20] W. Kohn, Phys. Rev. 87, 472 (1950).
- [21] E. Bodenstedt and B. Perscheid, Hyp. Int. 5, 291 (1978).
- [22] S.M. Qaim, J. Phys. C, 2, 1434 (1969).
- [23] G. Wortmann and D.L. Williamson, Hyp. Int. 1, 167 (1975).
- [24] H.G. Devare and H. De Waard, Hyp. Int. 3, 63 (1977).
- [25] L. Pfeiffer and C.P. Lichtenwalner, Rev. Sc. Instr. 45, 803 (1974).
- [26] Takayuki Kobayashi and Kazuko Fukumura, Nucl. Instr. and Meth. 173, 363 (1980).
- [27] I. Vincze and I.A. Campbell, J. Phys. F. 3, 647 (1973).
- [28] R.C. Reno, R.L. Raseria and G. Schmidt, Phys. Lett. A50, 243 (1974).
- [29] A. Narath, Phys. Rev. 162, 320 (1967).
- [30] E.N. Kaufmann, P. Raghavan, R.S. Raghavan, K. Krien and R.A. Naumann, Phys. Stat. Sol. B63, 719 (1974).
- [31] E.N. Kaufmann, Phys. Rev. B8, 1387 (1973).
- [32] B. Perscheid and G.K. Kaindl, J. de Phys. C1, C1-139, (1980).
- [33] M. Forker and K. Krusch, Phys. Rev. B21, 2090 (1980).
- [34] K. Krien, J.C. Soares, K. Freitag, R. Vianden, and A.G. Bibiloni, Hyp. Int. 1, 217 (1975).

- [35] G. Wortmann, B. Perscheid, G. Kaindl and F.E. Wagner, Contrib. Hyp. Int. 9, 343 (1981).
- [36] W.B. Pearson, 'A Hand Book of Lattice Spacings and Structure of Metals and Alloys', Vol. II, Pergamon Press, Oxford (1967).
- [37] G. Simmons and H. Wang, 'Single Crystal Elastic Constants and Calculated Aggregate Properties', Second Edition, The MIT Press Cambridge England (1971).
- [38] 'The Physics of Selenium and Tellurium', Proceedings of International Symposium, Montreal, 1967, edited by W.C. Cooper (Pergamon Press, New York, 1969).
- [39] 'The Physics and Selenium and Tellurium', Proceedings of the International Conference, Königstein, 1979, edited by E. Gerlack and P. Grosse (Springer-Verlag, Berlin, 1979).
- [40] C.H. Griffiths and Brian Fitton, 'The Physics of Selenium and Tellurium', Proceedings of the International Symposium, Montreal 1967, edited by W.C. Cooper, p. 163 (Pergamon Press, New York, 1969).
- [41] C.S. Kim and P. Boolchand, Phys. Rev. B19, 3187 (1979).
- [42] P. Boolchand, T. Henneberger, and J. Oberschmidt, Phys. Rev. Lett., 30, 1292 (1973).
- [43] P. Jena, Phys. Rev. Lett. 36, 418 (1976).
- [44] J.M. Trooster and M.P.N. Vieggers, Mössbauer Effect Reference Data Journal, 1, 154 (1978), edited by Dr. J.G. Stevens. (IFI/Plenum, New York).
- [45] H. Ernst, E. Hagn, E. Zech, G. Eska, Phys. Rev. B19, 4460 (1979).



- [46] J. Pelzl, Z. Phys. 251, 13 (1972).
- [47] K.C. Das and D.K. Ray, Phys. Rev. 187, 777 (1969).
- [48] K.C. Das and D.K. Ray, Solid State Comm. 8, 2025 (1970).
- [49] J. Pelzl, S. Hufner and S. Scheller, Z. Phys. 231, 377 (1970).

## CHAPTER 5

### HYPERFINE INTERACTIONS AND PHASE TRANSITIONS IN BINARY IRON ALLOYS

#### 5.1 Introduction

In recent years Mössbauer spectroscopy has been found to be very useful in the investigation of order-disorder transitions in alloys and its effect on hyperfine magnetic field and quadrupole interaction. The broad distribution of magnetic hyperfine fields in the disordered alloys is notably reduced by atomic ordering, and the change in hyperfine field is explained as the result of the change in Fe moment which increases with the increase in the number of Fe nearest neighbours.

Of all the ME parameters,  $H_{hf}$  is the most sensitive for the microscopic changes in the structure of the alloys, and so the variation of  $H_{hf}$  with temperature and heat treatment, and its distribution because of the varying environment in the sample, will give a better understanding of the metallurgy of the alloy.

Metal atoms coagulate some times in the non crystalline form which is in an extraordinarily disordered state i.e. in an amorphous state. The spectral lines of the hyperfine pattern of ferromagnetic amorphous alloys are very broad. At present there is general agreement that the broadening is caused by the

hyperfine field distribution. The poor resolution in the spectra led the scientists to apply different models for the interpretation and evaluation of the spectra. There are in general three approaches [1,2,3] using the basic elements: 1. microcrystallites, 2. molecules, molecular units, chemical compound clusters, embryos, 3. dense random packing. Kemeny et al. [4] suggested a "quasi-crystalline structure based on a locally distorted off-stoichiometric lattice".

The presence of microcrystallites in these alloys seems unlikely because it would require that all the microcrystallite arrangements exhibit essentially the same spectra independent of the constituents. More over in contrast to experimental findings one would expect the spectra should be composed of a broad contribution, from the resonance atoms being located in rather distorted in between regions, and a rather sharp contribution of the atoms with in the grains.

In the case of molecular models also one faces the same difficulty to envisage the solid as a whole with the molecules in their manifold of arrangements and orientations. The dense random packing model (Bernal model) seems suitable for fitting the spectra.

The amorphous materials can be divided into two principal classes:

- i) the metglass alloys with composition typically of one transition metal (Fe, Co, Ni) and one or several metalloids (B, C, N, P, Si.....). The composition usually

alloy shows an interesting behaviour closely related with the order-disorder transition which appears at 600 °C. As the long range order parameter of the fcc based  $L1_2$  type ordered structure of the  $Fe_3Pt$  alloy increases from 0 to 1, the martensitic transformation changes from the burst type to the thermoelastic type [7]. Since Pd lies between Ni and Pt in the VIII column of the periodic table the study of Fe-Pd alloy will be useful with respect to martensitic transformations.

At high temperatures, iron and palladium form a continuous series of binary alloys with an fcc lattice. At temperatures below 1100 K, however, a preference for surrounding with dissimilar neighbours becomes pertinent in the concentration range from 50 to 80 % Pd. Around the FePd composition the alloy adopts the  $L1_0$  structure, and around the  $FePd_3$  composition the  $L1_2$  structure. The crystal structures as well as the regions of existence are shown in Fig. 5.1a. The fcc-bcc martensitic transformation was reported [8] for an alloy of this type containing less than 20 at % Pd. Recently Sohumura et al. [9] reported a thermoelastic fcc-fct martensitic transformation of Fe-Pd alloy which has not been observed before. The transformation is of the first order, but the axial ratio of  $c/a$  of the fct gradually decreases as the temperature lowers, which is typical of the second order transition. The shape memory effect is also reported in this alloy.

In order to elucidate the general features of the lattice transformation  $fcc \Rightarrow L1_0 \Rightarrow fct$ , some details of the electron-microscopic observations in CuAu-I by Herabayashi et al. will be of interest [10]. In an early stage of the ordering treatment itself, small tetragonal crystallites of

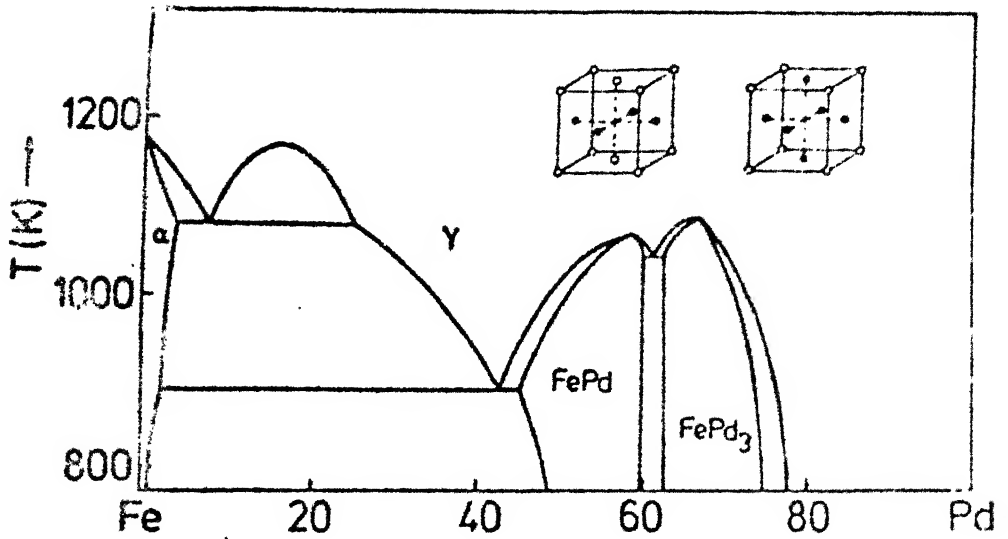


Fig. 5.1a. The phase diagram of Fe-Pd system (after Shunk[41], 1969)

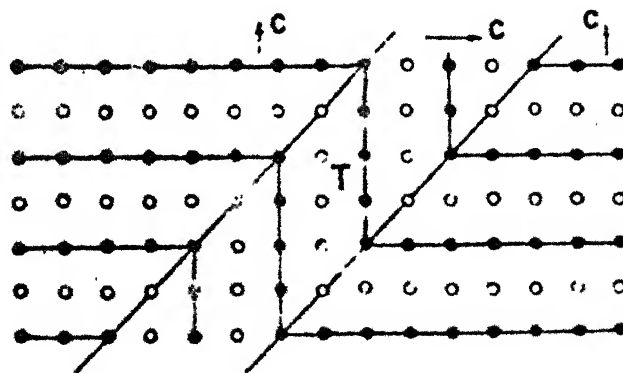


Fig. 5.1b. Schematic drawing of twinning (after Hirabayashi et al.[10])

the ordered phase come into existence. These ordered crystallites are formed coherently with the disordered matrix, and due to the different lattice parameters an elastic strain energy develops. Since the c-axis contracts and the a- and b-axis expand during the fcc  $\Rightarrow$  fct transformation, the elastic energy can be reduced when the ordered regions preferably form thin lamellae, lying in {110} planes of the fcc matrix with the tetragonal c-axis along one of the cubic {100} directions. Nevertheless, some elastic strain will build up around the tetragonal regions and this leads to microtwinning (Fig. 5.1b). In this process the c-axis of the tetragonal crystallites changes direction regularly between two of the three cubic axes, thus reducing appreciably the strains in the plane of Fig. 5.1b. Perpendicular to this plane, however the strains remain, these are accommodated in a more advanced stage of the ordering by the interposition of the ordered material with the tetragonal c-axis in this direction. The atomic rearrangements within the disordered phase preceding the transformation to the tetragonal structure remain undetermined. According to Zenes [11], one might expect the tetragonal distortion to arise from the anisotropy of the ordering, and therefore a fair amount of ordering should occur within the fcc phase before the fcc  $\Rightarrow$  fct transformation takes place. Hence a systematic study of the fcc phase during an ordering treatment will be of considerable interest.

### 5.2.2 Sample preparation

The alloy of Fe-31.2 at %. Pd was prepared by melting 99.9 % pure iron and 99.9 % pure Pd in an induction furnace. This alloy was homogenised at 1100 °C for 3 days. This alloy was powdered with a diamond file and annealed at 900 °C for 4 hours and quenched into iced water. This powder was mixed with araldite adhesive resin so as to form a thin plate with a distribution of 30 mg/cm<sup>2</sup> of Fe-Pd alloy, for Mössbauer measurements. Another absorber was also made in a copper ring with a distribution of 30 mg/cm<sup>2</sup> which is kept in position by celotape for comparison.

X-ray diffraction pattern of this alloy was recorded by the X-ray diffractometer and the structure agrees well with that reported for the same alloy by Sohumura et al. [9] and Matsin et al. [21]. The diffraction peak corresponding to 220 is shown in Fig. 5.2.

### 5.2.3 Results and discussions

#### A) Results

The observed Mössbauer parameters for the Fe-31.2 at %. Pd alloy are shown in Table 5.1. The hyperfine field distribution were analysed by means of the procedure developed by Window [13]. In this, model independent evaluation, the observed line shapes are represented by a continuous probability  $P(H)$  for the distribution of hyperfine fields, as

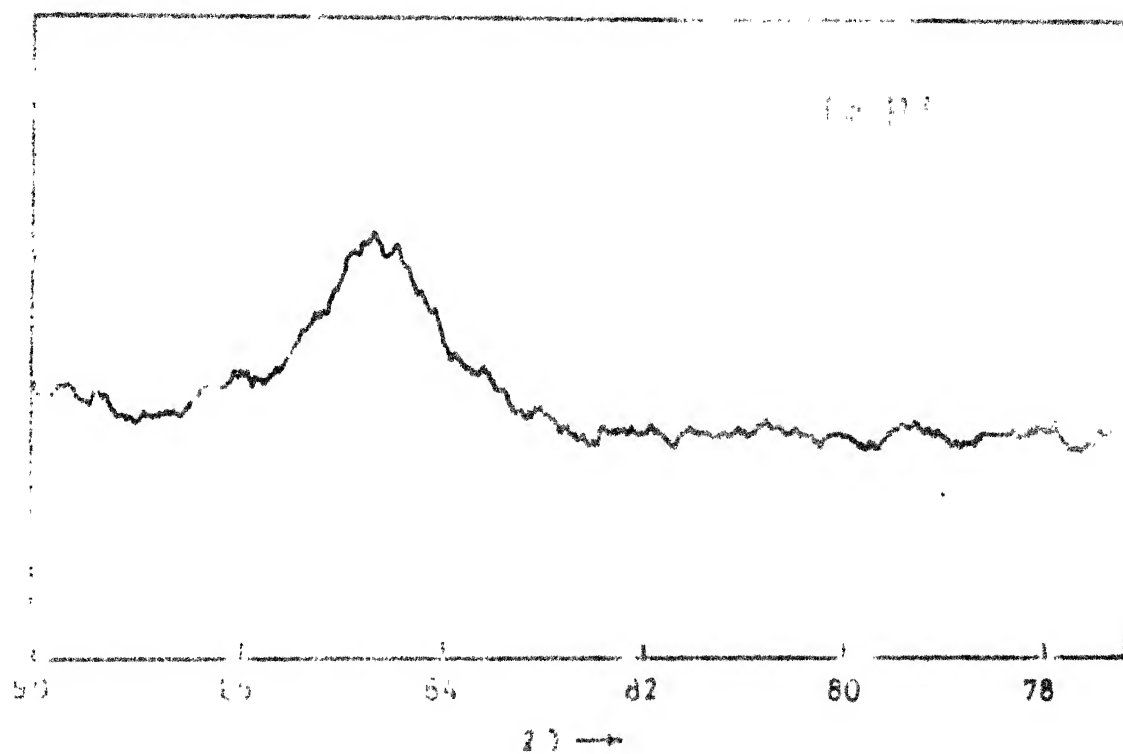


Fig. 52 X-ray diffraction pattern corresponding to  $\{220\}$  peak of Fe-31.2%Pd alloy



TABLE 5.1

The observed Mössbauer parameters of Fe-31.2 % Pd alloy at different temperatures.

Temperature	$H_{\text{eff}}$	Q.S.	Isomer Shift*
K	KOe	(mm/sec)	(mm/sec)
113	307(2)	0.44 (1)	0.35 (1)
126	302(1)	0.42 (1)	0.31 (1)
145	299(3)	0.32 (2)	0.30 (2)
169	300(3)	0.21 (2)	0.26 (2)
173	299(2)	0.19 (1)	0.26 (2)
198	295(3)	0.16 (2)	0.23 (2)
295	299(2)	0.11 (2)	0.19 (1)
389	266(1)	0.11 (2)	0.16 (2)
430	237(3)	0.09 (2)	0.16 (2)
470	206(1)	0.09 (2)	0.14 (2)
508	167(2)	0.04 (2)	0.06 (1)
527	99(1)	-	0.05 (2)
540	86(2)	-	0.06 (2)
549	39(1)	-	0.06 (2)
600	0	-	0.05 (2)

\*With respect to iron metal.

$$P(H) = \sum_{n=1}^N b_n \left[ \cos \frac{n\pi H}{H_{\max}} - (-1)^n \right]$$

with the boundary conditions

$$\left( \frac{dP(H)}{dH} \right)_{H=0} = \left( \frac{dP(H)}{dH} \right)_{H=H_{\max}} = 0.$$

The hyperfine spectrum with this distribution can be then expressed as the modified Lorentzian form

$$S(E) = \sum_{i=1}^6 \int \frac{D_i P(H) dH}{1+4[(E-a_i H)/W_0]^2} \quad (5.1)$$

where the spectrallines are assumed to be Lorentzian with position  $a_i H$ , width  $W_0$ , and height  $D_i$ .  $E$  is the resultant doppler energy corresponding to each point in the spectrum.  $H_{\max}$  is taken far away from the peaks so that

$$P(H_{\max}) = 0$$

The Fourier coefficients  $b_n$  are calculated by the best fit to the data. Since the coefficients  $b_n$  are calculated by solving a set of  $N+1$  simultaneous equations,  $N$  cannot be too large. With the computer programme developed by the author data was analysed with  $N$  of the order of 25.

The Mössbauer spectra of Fe-Pd alloy at various temperatures with fitting using the distribution programme is shown in Fig. 5.3. The corresponding hyperfine field distribution is shown in Fig. 5.4. When the temperature is near the

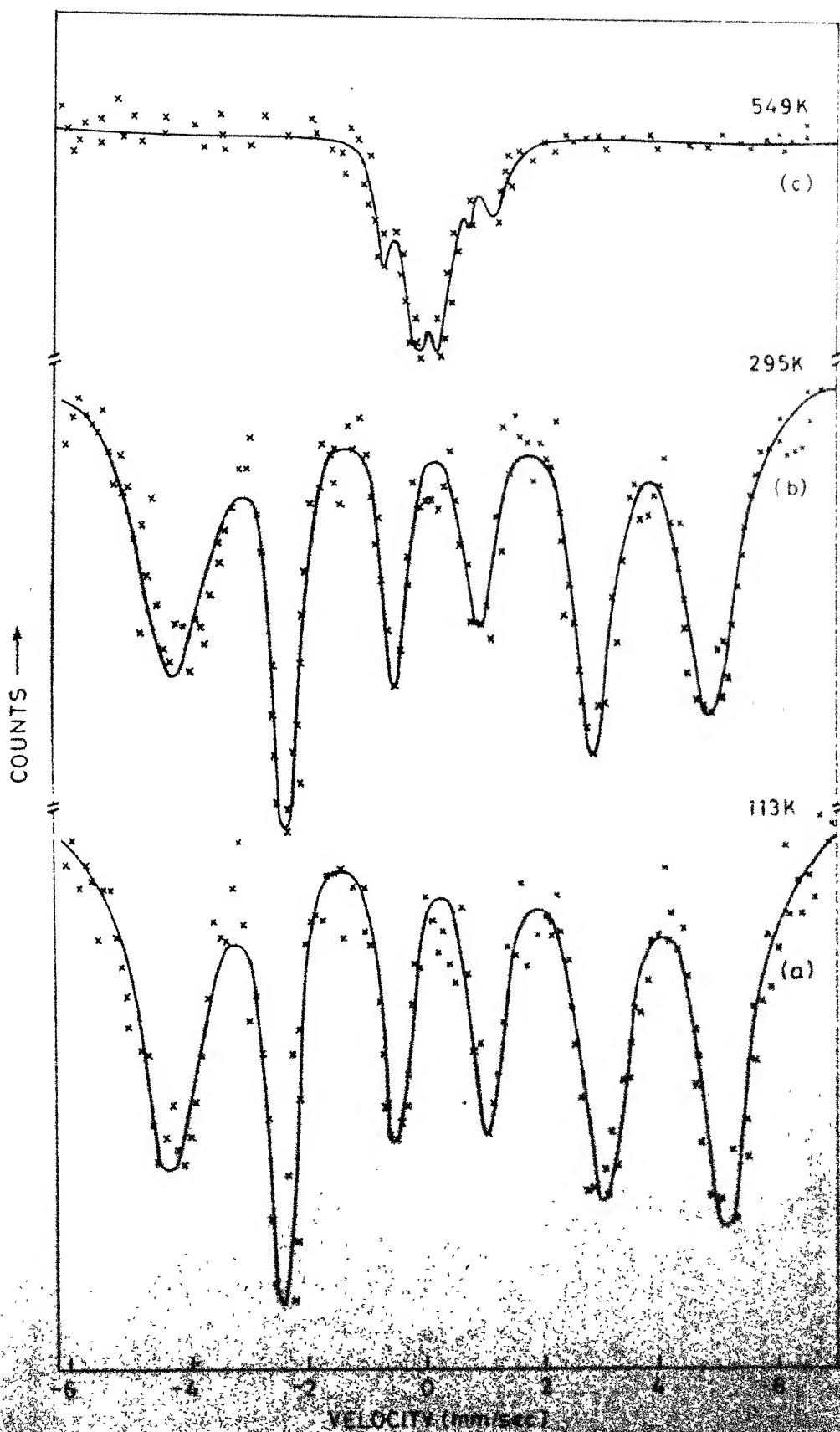


Fig. 5.3 Mössbauer spectra of Fe-3124Pd. The spectrum (c) is fitted with isomer shift distribution.

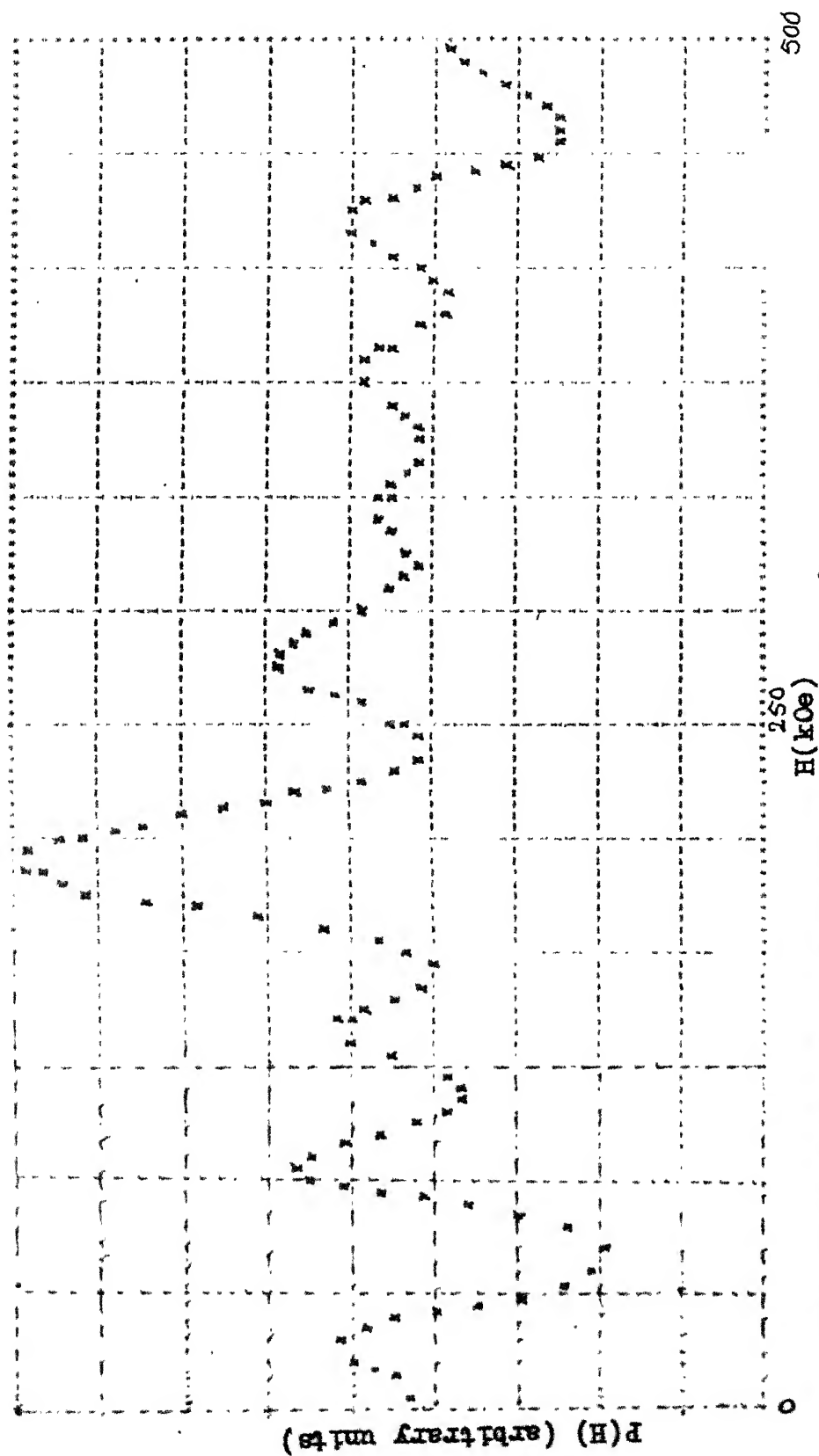


Fig. 5.4 Hyperfine field distribution in Fe-31.2 % Pd alloy at 470 K.

Curie temperature the spectra appears to be of a broad single line which fits into a single line using the Lorentzian fitting programme. The data is again analysed using the isomer shift distribution programme described in Chapter 3 and the analysis shows clearly the hyperfine split spectrum at 549 °K. The variation of  $H_{\text{eff}}(T)/H_{\text{eff}}(295)$  with  $T$  is shown in Fig. 5.5. The paramagnetic Curie temperature determined from this graph is 554 °K. The isomer shift in Fe-Pd is found to change with temperature. The variation of which is shown in Fig. 5.6.

The temperature dependence of magnetisation of Fe-Pd was determined in residual field using the PARC vibrating sample magnetometer. The curie temperature,  $T_c$  of the sample is determined using the interpolation programme. The value obtained for  $T_c$  in this way is 515 °K. The variation of magnetisation  $\sigma$  with temperature is shown in Fig. 5.7. The value of  $T_c$  obtained agrees well with the extrapolated value of Fe-Pd alloys studied by Matsui et al. [14].

In order to study the fcc  $\Rightarrow$  fct martensitic transformation the Mössbauer spectra of the sample was taken down upto 11 °K. The quadrupole splitting is found to increase from 0.07(2) mm/sec to 0.44(1) mm/sec as the temperature is decreased from room temperature to 113 °K. The Mössbauer spectra of the sample shows that the fcc phase is still present even below the reported [9] transition temperature 173 °K and at 113 °K it almost completely changes to the fct phase. The variation of Q.S. with temperature is shown in Table 5.2. The corresponding

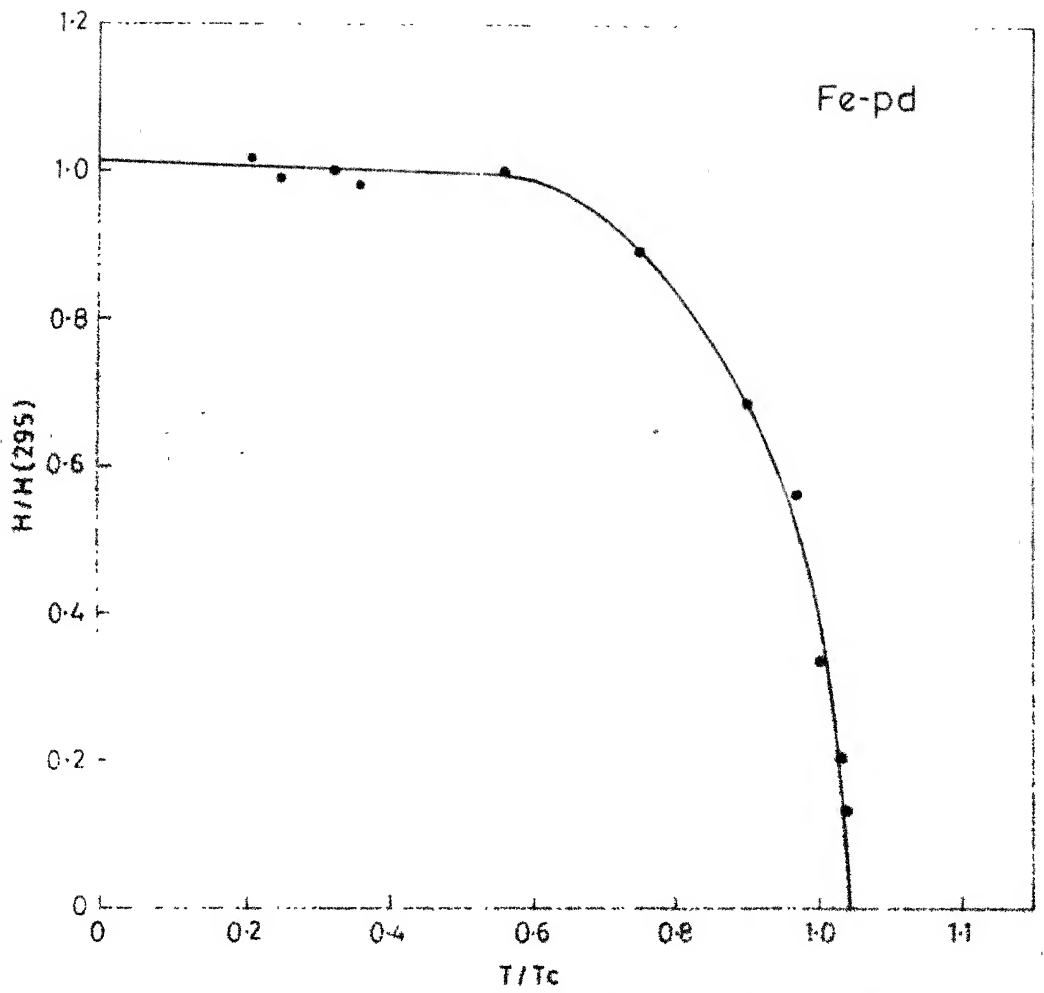


Fig.5-5 The variation of  $H_{eff}(T)/H(295)$  with  $T/T_c$  in Fe-31.2%Pd alloy

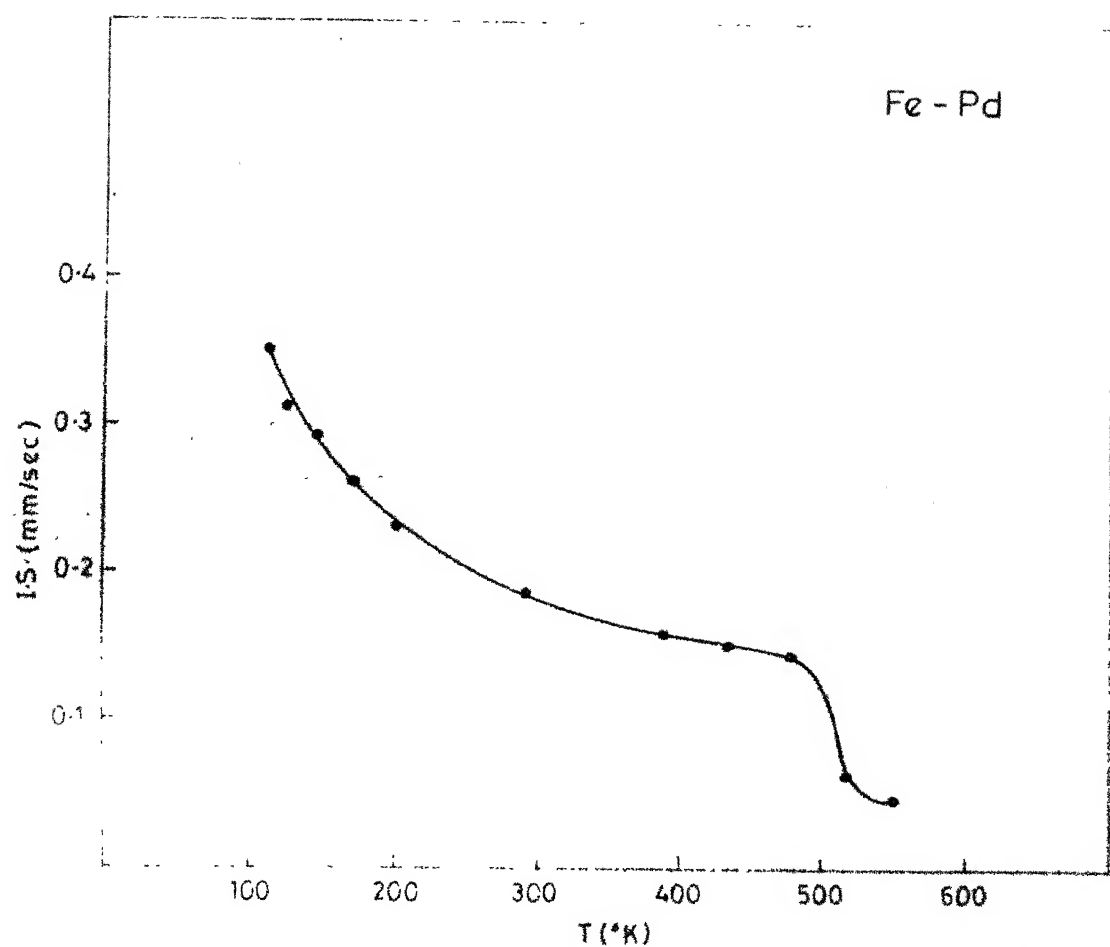


Fig 56 Variation of isomer shift with temperature in the Fe-312% Pd alloy

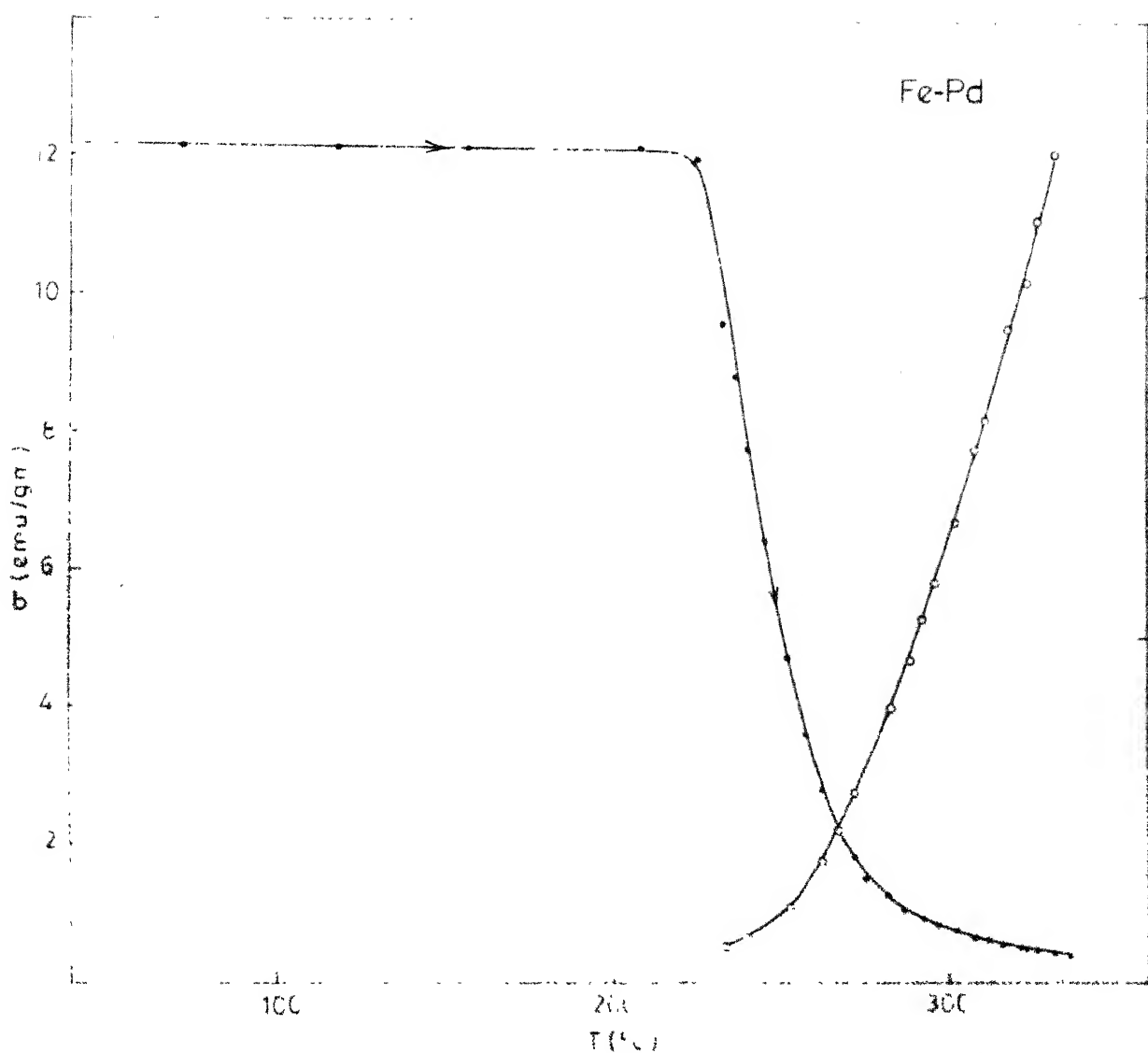


Fig 5.7 Variation of magnetisation and inverse susceptibility with temperature of Fe-31.2% Pd alloy



TABLE 5.2

The quadrupole splitting of the fct phase of Fe-31.2 % Pd alloy at different temperatures with the corresponding  $c/a$  values.

Temperature K	$c/a$	Q.S. (mm/sec)
113	0.965	0.44(1)
126	0.97	0.42(1)
145	0.975	0.32(2)
169	0.99	0.21(2)
173	0.995	0.19(2)

c/a values from ref. [9] is also shown in the same table.

## B) Discussions

The analysis of the Mössbauer spectrum at various temperatures shows that the fcc austenite phase of Fe-Pd transforms to a fct structure as can be seen from the changes in the Q.S. at around 173 °K. However the spectrum also shows the coexistence of the fcc and fct phases, at low temperature.

### (a) Temperature dependence of EFG

The temperature dependence of the quadrupole interaction with temperature [Table 5.2] is fitted with the empiric relation

$$eq(T) = eq(0) [1 - B T^{3/2}]$$

A fitting of this equation with the experimental values of the fct phase gave a value of

$$B = - 0.32 \times 10^{-3} \text{ K}^{-3/2}$$

the value of  $eq(0) = 3.48 \times 10^{17} \text{ V/cm}^2$ .

The dependence of EFG in Fe-Pd system on temperature is shown in Fig. 5.8 where the observed EFG's are plotted against  $T^{3/2}$ .

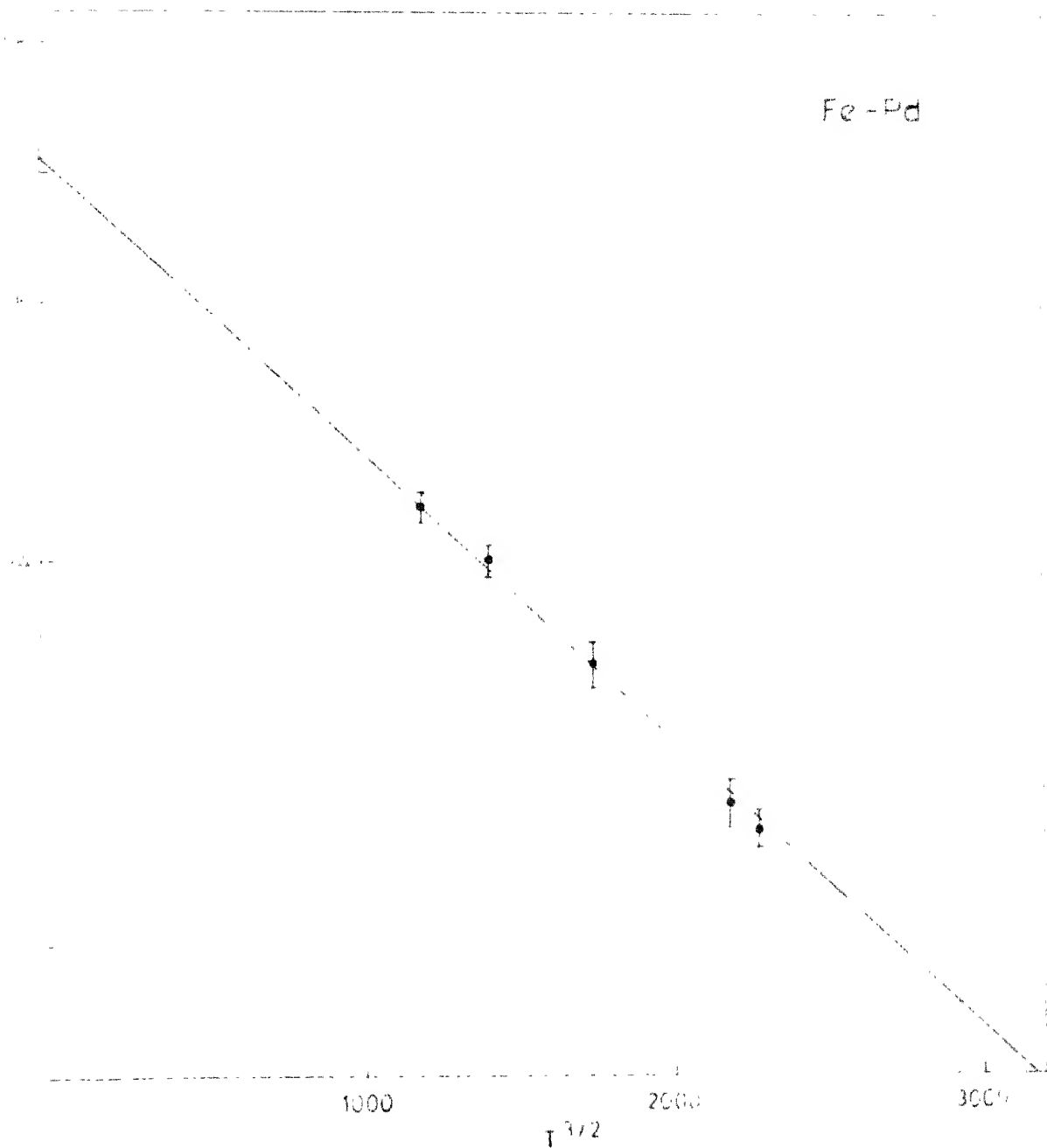


Fig. 1. G vs.  $T^{-1/2}$  change with temperature in the fct phase of Fe-31.2%Pd alloy

## (b) Universal correlation of EFG in tetragonal lattices

The total EFG in tetragonal alloys is proportional to the lattice contribution to the EFG [15]. The temperature dependence of EFG in the fct phase of Fe-Pd shows that it varies almost linearly with the variation of the  $c/a$  ratio. A least squares fit of the function

$$V_{zz} = C_1 (c/a - C_2)$$

to the experimental points of the fct phase yields  $C_2 = 1.01$ . This agrees with the vanishing quadrupole splitting in the case of cubic symmetry. The variation of EFG for different values of  $c/a$  is shown in Fig. 5.9. Fig. 5.10 shows the variation of the lattice parameters and the  $c/a$  ratio for the Fe-31.2 % Pd alloy at various temperatures.

## (c) The distribution of hyperfine field and its temperature dependence

The spectrum of Fe-Pd shows the following characteristics. Numbering the lines from negative to positive velocity, the following relations hold:  $\Gamma_1 > \Gamma_6$ ,  $\Gamma_2 > \Gamma_5$  and  $\Gamma_3 > \Gamma_4$ ; the effect is even easier to see in the different depths of the lines, this pattern can be understood from the model given by Window [16]. The distribution of the number of similar and dissimilar neighbours in the first shell causes a distribution of isomer shifts and hyperfine fields. The results of the

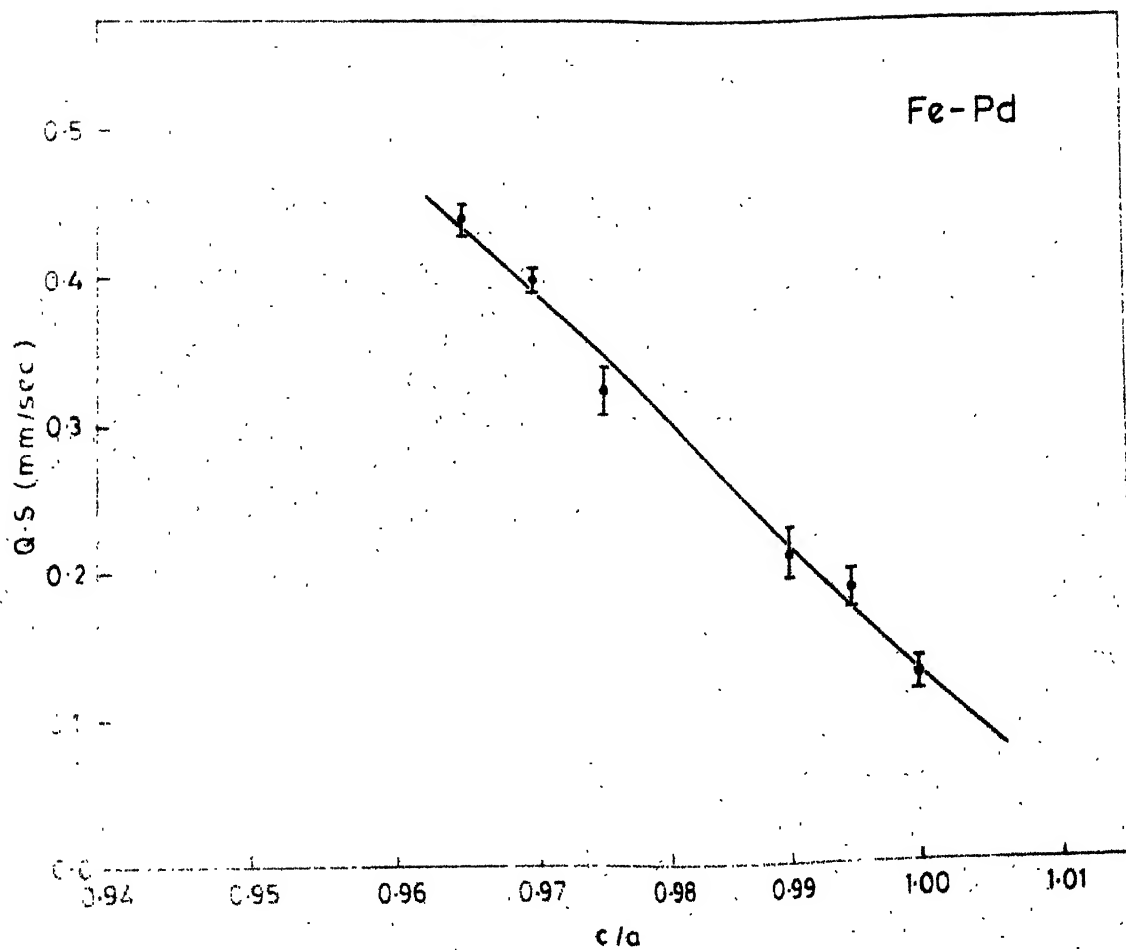


Fig.5.9 Variation of  $Q \cdot S$  with variation of  $c/a$  value in Fe-31.2%Pd

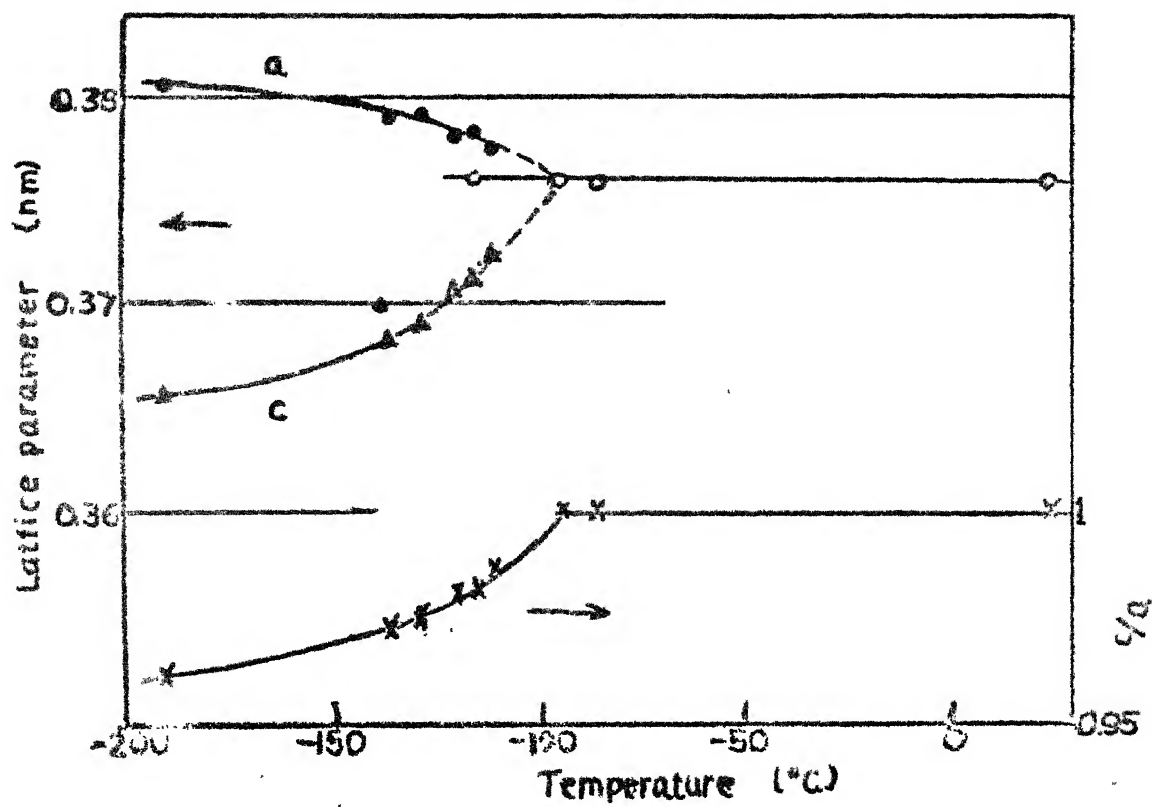


Fig. 5.10. Variation of lattice parameters and  $c/a$  ratio in Fe-31.2% Pd.

distribution studies is summarised by the values of  $\bar{H}$  and  $\Delta H$ , the position of the main peak in the  $P(H)$  distribution and its full width at half maximum respectively, which is given in Table 5.3. It is seen that the most probable field coincides with the mean field within error limits in all cases. The width of distribution goes on increasing in the fcc phase with increase of temperature which suggests a more disordered phase. Whereas at low temperature side the width almost remain constant.

In a disordered binary alloy, the Fe atom finds itself in different nearest-neighbour and next-neighbour environments. Hence in the disordered alloy the Fe magnetic moments have a distribution giving rise to a distribution of hyperfine fields. A complete random distribution is expected in the fcc phase, since the order parameter is zero. At low temperatures, the distribution produces a spread in the saturation values of the hyperfine field [17]. If there exists a common ordering temperature for all ions and if the temperature dependence of the hyperfine field for all ions is identical, then  $\bar{H}$  should follow this temperature dependence and one expects that  $\Delta H$  should steadily decrease as one goes from low temperature to  $T_c$ . Timoyoshi et al. [18] pointed out that the thermal average of the magnetic moments on which the weaker exchange field is acting decreases more rapidly with increase of temperature than the one on which the stronger exchange fields. Therefore

TABLE 5.3

The mean field  $H_{\text{eff}}$ , most probable field ( $\bar{H}$ ) and the FWHM ( $\Delta H$ ) of  $P(H)$  distribution in Fe-31.2 % Pd as a function of temperature.

Temperature	$H_{\text{eff}}$	$\bar{H}$	$\Delta H$
K	kOe	kOe	kOe
295	299(1)	298	53
389	266(1)	257	62
430	237(3)	216	68
470	206(1)	197	69
508	167(3)	142	71
527	99 (1)	112	75
540	86 (2)	-	-



if the exchange field has local fluctuations at various lattice sites, the reduced magnetisation has a broad distribution at high temperature. The range of the exchange interaction is a very important factor in considering the fluctuations of the exchange field. If the exchange interaction is a very long range one, the local fluctuation of the exchange field should be small even if the exchange interaction between different kinds of atom pairs has large differences, so that the magnetisation and hence the internal field have no distribution at high temperatures. On the other hand if the interaction is a very short range one, the alloy should have a large local fluctuation of the exchange field according to the neighbouring atomic configuration. Thus the variations in the near neighbours environment also cause a distribution in exchange fields through out the material, and so, different ions may have hyperfine fields that show quite different temperature dependences. This will have a tendency to cause  $\Delta H$  to increase as the temperature increases and  $\bar{H}$  will follow some average temperature dependence. It is difficult to decide which of the above mechanisms is dominant. The appearance of two peaks in the  $P(H)$  distribution with two different values of  $\bar{H}$  is an indication that there are two kinds of iron atoms with two different average magnetic moments and two different mean values for the hyperfine field at this temperature. The appearance of the peak in the  $P(H)$  distribution centered near  $\bar{H} = 0$  along with the peak with non-zero  $\bar{H}$  value near the

Curie temperature tells us that ferromagnetism does not vanish suddenly in these alloys and also the existence of non-magnetic iron in the alloy [19]. Some iron atoms which are weakly coupled by exchange interaction go to paramagnetic state at a comparatively lower temperature than the remaining iron atoms.

The hyperfine field  $H(0)$  at  $0^\circ\text{K}$  was found by extrapolating  $H$  to  $0^\circ\text{K}$  and the value obtained in this way is 314 kOe. The asymmetry in the widths and heights of the peaks in the Mössbauer spectrum of Fe-Pd alloy is due to the combined presence of the distributions of both quadrupole and dipole interactions.

(d) Recoilless fraction and Debye temperature of the Fe-Pd alloy

The recoilless fraction is determined using the method of Trooster et al. described in Chapter 4. The average value of the recoilless fraction  $f_0$  at room temperature of the alloy is 0.588 and as the temperature is increased the value decreases to 0.42 at  $470^\circ\text{K}$ . It is interesting to note that for the fct phase the recoilless fraction goes on decreasing with decrease of temperature. The Debye temperature at room temperature is calculated from the recoilless fraction as  $279^\circ\text{K}$ .

The recoilless fraction of the Fe-Pd alloy at various temperatures is shown in Table 5.4.

TABLE 5.4

Recoilless fraction ( $f_a$ ) and effective thickness ( $t_a$ ) of the fcc phase of Fe-31.2 % Pd as a function of temperature.

Temperature K	$t_a$	$f_a$
295	2.305	0.558
389	1.975	0.478
430	1.792	0.434
470	1.729	0.419

#### 5.2.4 Conclusion

The fcc=> fct martensitic transformation in the Fe-31.2 at % Pd has been studied by the Mössbauer analysis. The Q.S. clearly shows an increase after the transformation. The variation of the EFG in the fct phase obeys the universal correlation between lattice contribution and electronic contribution. The variation of Q.S. with temperature obeys the  $T^{3/2}$  law in the fct phase. The distribution of hyperfine fields has been studied by the model independent method of analysis. The width of the distribution increases with increase of temperature which reveals that the range of exchange interaction is shorter in the Fe-Pd alloy. The development of the paramagnetic peak even before the bulk curie temperature is reached shows that there is a distribution of curie temperatures in the Fe-Pd alloy studied.

### 5.3 Mössbauer and Magnetic Studies of the Amorphous

#### Nd<sub>0.33</sub>Fe<sub>0.67</sub> Alloy

##### 5.3.1 Introduction

During the past twenty four years the class of compounds formed between rare-earths and 3d transition metals has gained particular interest, since one can benefit here from the intrinsic properties of both components, i.e. from the high magnetic moment per atom and the strong single-ion magnetocrystalline anisotropy of the rare-earth partner, and

from the high magnetic coupling strength of the moments of the 3d-transition metal partner. A subclass is formed by those compounds in which the rare-earth partner bears no magnetic moment (La, Lu, Y and tetravalent Ce). Because of the use in making permanent magnets much work has been done in the investigation of intermetallic compounds between rare-earths and transition metals [20,21]. Strong interest in amorphous rare-earth (R)-Fe alloys began with the work of Rhyme et al. [22] who used sputtered samples of  $\text{TbFe}_2$  and showed that these samples are structurally amorphous and magnetically ordered. They reported that both the magnetization (M) and the critical temperature ( $T_c$ ) were reduced in amorphous state. The reduction in magnetization and  $T_c$  was attributed to the strong random local anisotropy [23]. Later investigations [24-26] have established that the reduced  $T_c$  is due to a reduced Fe-Fe exchange interaction. Heiman and Lee [27] from their studies on amorphous LaFe found that in contrast to YFe and LuFe the sample were ferromagnetic with  $T_c$  near room temperature. This suggested that the Fe-Fe exchange interaction somehow depends on the size of the rare-earth because the most obvious difference between La, Y and Lu is only in the size. The radius of the R atoms decreases with the atomic number from  $1.87 \text{ \AA}$  for La to  $1.74 \text{ \AA}$  for Lu (with the exception of multiple-valence elements). The spin values and so the de Gennes factor [ $\text{DGF} = (g-1)^2 J(J+1)$ ] also varies systematically, rising from La to Gd and then decreasing from Gd to Lu.

The systematic decrease of  $T_c$  with increasing atomic number is attributed to the decrease of the DGF. The extent to which each of the parameters, radius and DGF, contribute to the systematic decrease of  $T_c$  has not yet been established. Recently Cullen [28] had introduced a model in which the magnetic interaction of the R atom aligns nearest neighbour Fe atoms in a spin-glass-like state. The work on amorphous YFe system by Coey et al. [29] suggests a local co-ordination model in which the moment on the Fe atom is a function of the number of Fe nearest neighbours.

Another interesting result obtained by Chappert et al. [30] is the observation of transition metal moments larger in amorphous state than in crystalline counter part. A qualitative explanation for this observation is given in terms of the consequences of charge transfer from the rare-earth R to the empty d-orbitals of the transition metal [31]. The evidences available thus far suggests that all these models should be taken into account along with more experimental evidences for a comprehensive understanding of the amorphous RFe systems.

Generally all these materials are ferromagnetic so that  $M$  is difference between the two sublattice magnetisations (R sublattice and Fe sublattice) and so they are highly composition dependent.. More over the spins with in a given sublattice are not necessarily aligned. In the case of Fe, the non alignment apparently results from large exchange fluctuations. The degree of non-alignment with in the two sublattices depend

upon the concentration and species of R.

In many of the experiments reported above the amorphous R-Fe alloys were prepared by two-source co-evaporation of the elements and were deposited on substrate of fused-quartz or on polyparabanic acid sheets. A number of recent studies have demonstrated the potential of using an amorphous rapidly quenched alloy for the magnetic hardening of the rare-earth-iron or rare earth-iron based alloys [32-35]. In this work the magnetic and Mössbauer studies on rapidly quenched amorphous  $\text{Nd}_{0.33}\text{Fe}_{0.67}$  alloy is described. The properties of these alloys as well as those of the other light rare-earths, are of particular interest because of their natural abundance makes them considerably less expensive.

### 5.3.2 Experimental

$\text{Nd}_{0.33}\text{Fe}_{0.67}$  alloy was prepared by first melting in an induction furnace high purity Nd(99.9 %) and Fe(99.99 %) (total 2 gm) under high vacuum in a flat bottomed Zirconia crucible. The melting is repeated 2-3 times to get uniformity. The quenching was done by passing purified argon gas at low temperature through the molten alloy. The resulting brittle alloy was made into small pieces and annealed at 500 °C for 32 hours under high vacuum and quenched in water. X-ray diffraction patterns of the powdered specimens were taken after taking precautions to prevent oxidations. The X-ray diffractographs were characteristic of the amorphous state (Figs. 5.11 and 5.12). A rectangular piece of this material

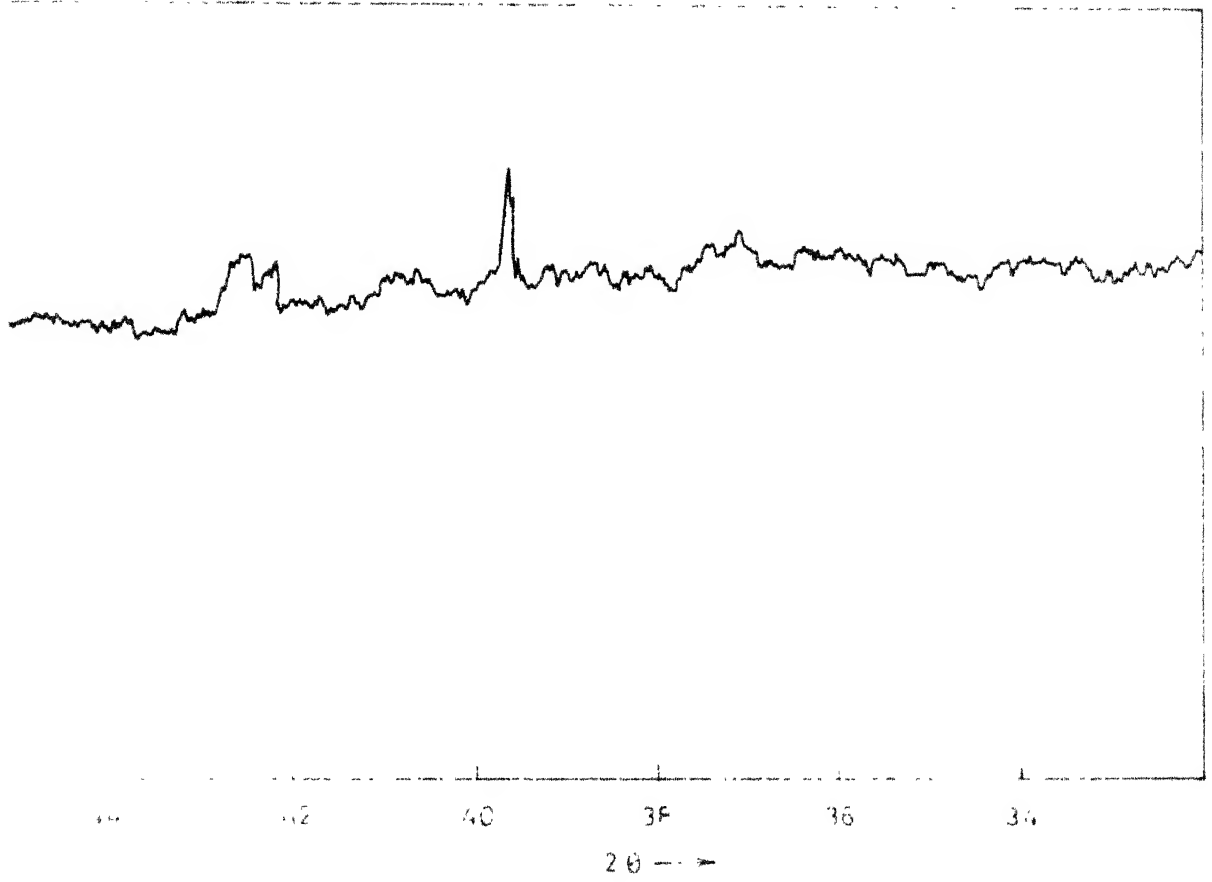


Fig 5.11 X-ray diffraction pattern of pure neodymium



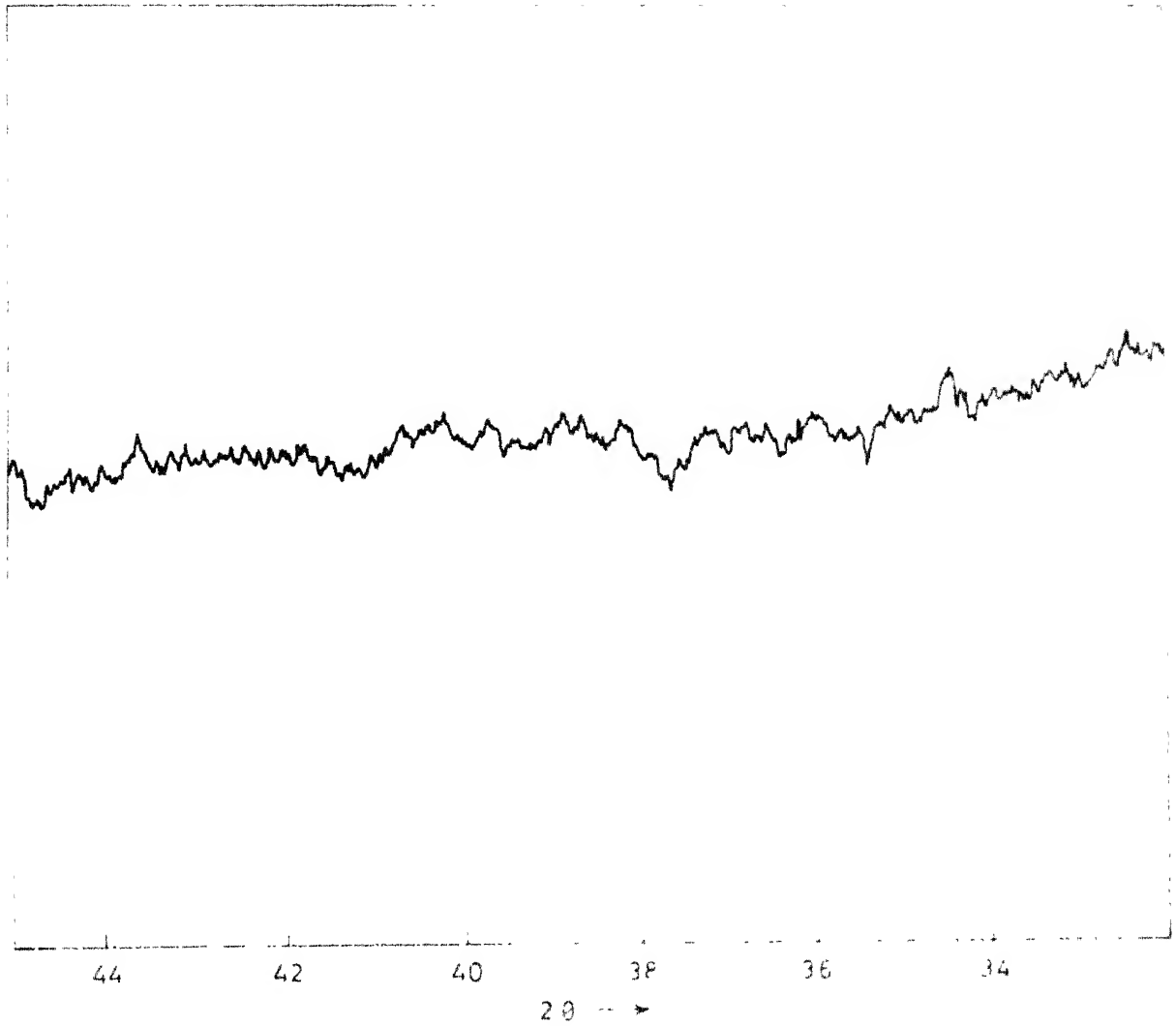


Fig.5.12 X-ray diffraction pattern of amorphous  $\text{Nd}_{33}\text{Fe}_{67}$  alloy

of size 0.214 x 0.294 x 0.132 cm was made out of this for magnetisation measurements in the PARC vibrating sample magnetometer (VSM). Powdered sample of this alloy was mixed with epoxy resin to form a thin plate for Mössbauer studies.

Mössbauer spectra were taken at different temperatures and the comparison with spectra taken with normal powdered sample kept between celotape showed that the adhesive does not modify the spectrum. More over it prevents oxidation of the sample and ensures homogeneity in distribution.

Magnetisation measurements were carried out from room temperature to 425 K on the PARC vibrating sample magnetometer in fields upto 6.5 kOe.

Mössbauer effect measurements were made with the set up described in Chapter 2 in the constant acceleration mode from liquid nitrogen temperature to 475 °K.

### 5.3.3 Results and discussions

#### (a) Results

The temperature dependence of magnetisation of the amorphous  $\text{Nd}_{0.33}\text{Fe}_{0.67}$  alloy is determined under residual field ( 40 gauss) during the increase and decrease of temperature. The results shows (Fig. 5.13) a sharp transition at around 333 °K. The thermal hysteresis present during heating and cooling is found to be negligibly small in this alloy. The Curie temperature ( $T_c$ ) was obtained from the

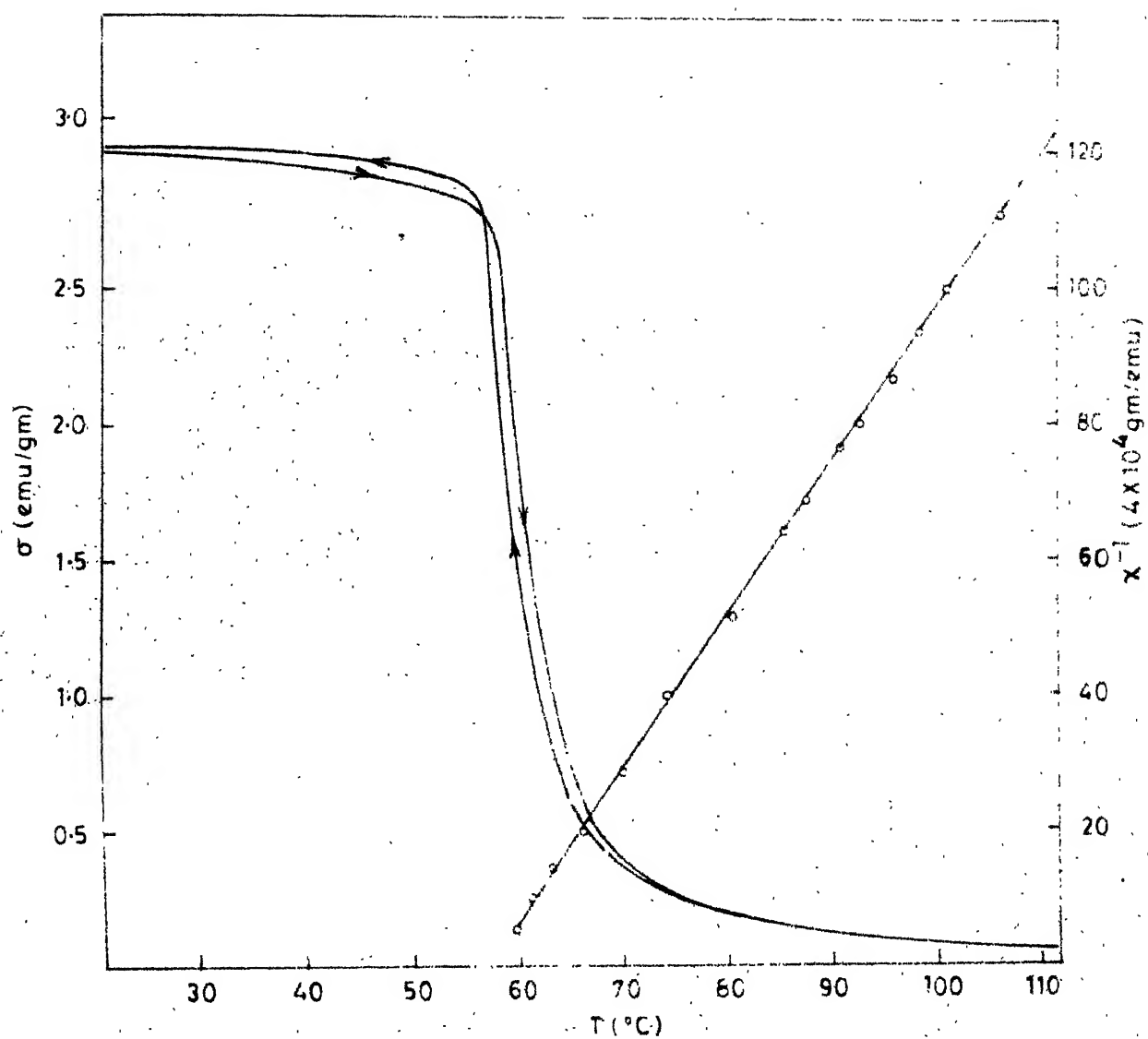


Fig.5-13 Temperature dependence of magnetisation and inverse susceptibility of amorphous  $\text{Nd}_{33}\text{Fe}_{67}$  alloy.

$d\sigma/dT$  vs  $T$  curve (Fig. 5.14) and from the variation of  $\frac{d^2\sigma}{dT^2}$  with  $T$ . The value of  $T_c$  obtained in this way is 332.89 K. The temperature dependence of the inverse susceptibility is also shown in Fig. 5.13 and a linear dependence is observed. The Curie temperature of the recently synthesized  $\text{NdFe}_2$  compound [21] is higher than this value ( $T_c = 578 \text{ K}$ ) as expected.

Magnetisation measurements ( $\sigma$  versus  $H$ ) for  $\text{Nd}_{0.33}\text{Fe}_{0.67}$  alloy at several temperatures near  $T_c$  are also taken with the VSM and are shown in Fig. 5.15. The temperature was kept stable within  $0.2^\circ\text{C}$ , with the temperature controller developed by the author. It is observed that the sample is not getting saturated upto 6.5 kOe. The temperature dependence of magnetisation at various values of the applied field near the Curie temperature is shown in Fig. 5.16. The effective field acting on the sample is different from the applied field by a quantity called the demagnetising field of the sample. The demagnetising field is given by  $H_{Di} = 4\pi N \cdot (\text{magnetisation})$  where the magnetisation is in gauss and  $N$  is the geometrical demagnetisation factor which depends on the definite geometry of the sample. The geometric demagnetisation factor for a rectangular sample was determined by using the expression [36]

$$N = \frac{2}{\pi} \cot^{-1} \left[ \frac{(a^2 + b^2 + c^2)^{1/2} c}{ab} \right]$$

where the  $c$  axis is kept parallel to the magnetic field.

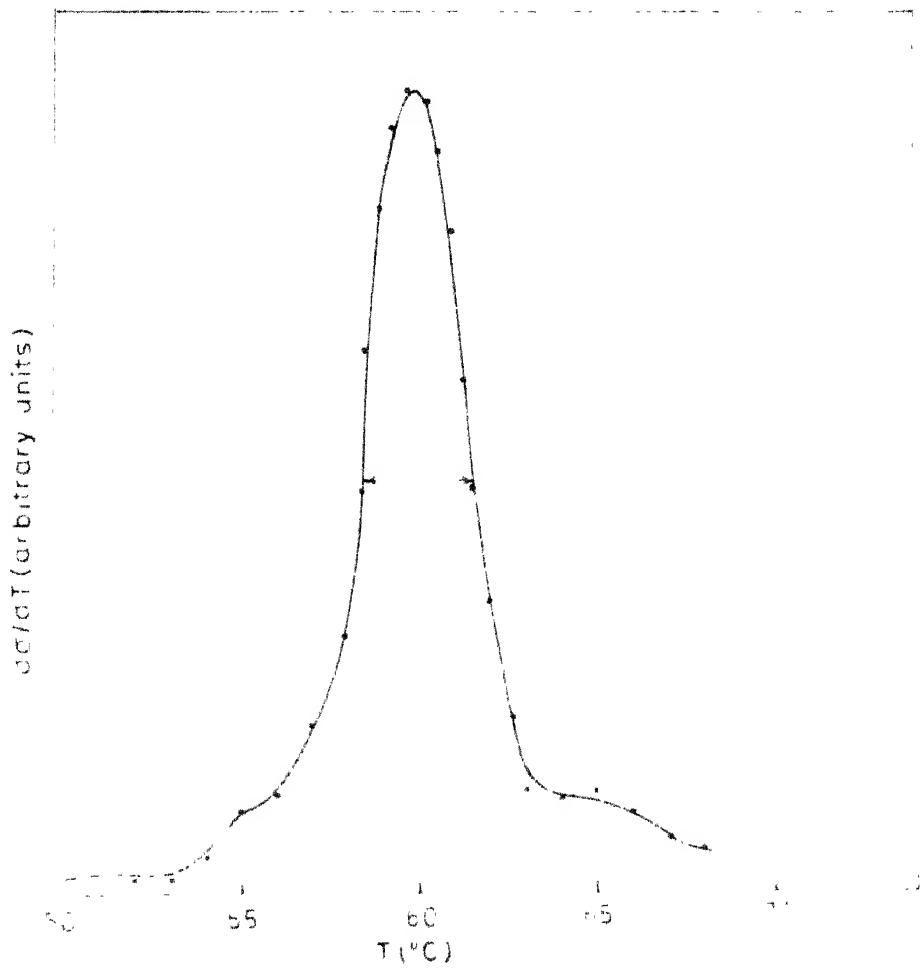


Fig 514. Variation of  $d\sigma/dT$  with temperature in  $\text{Nd}_{33}\text{Fe}_{67}$  alloy

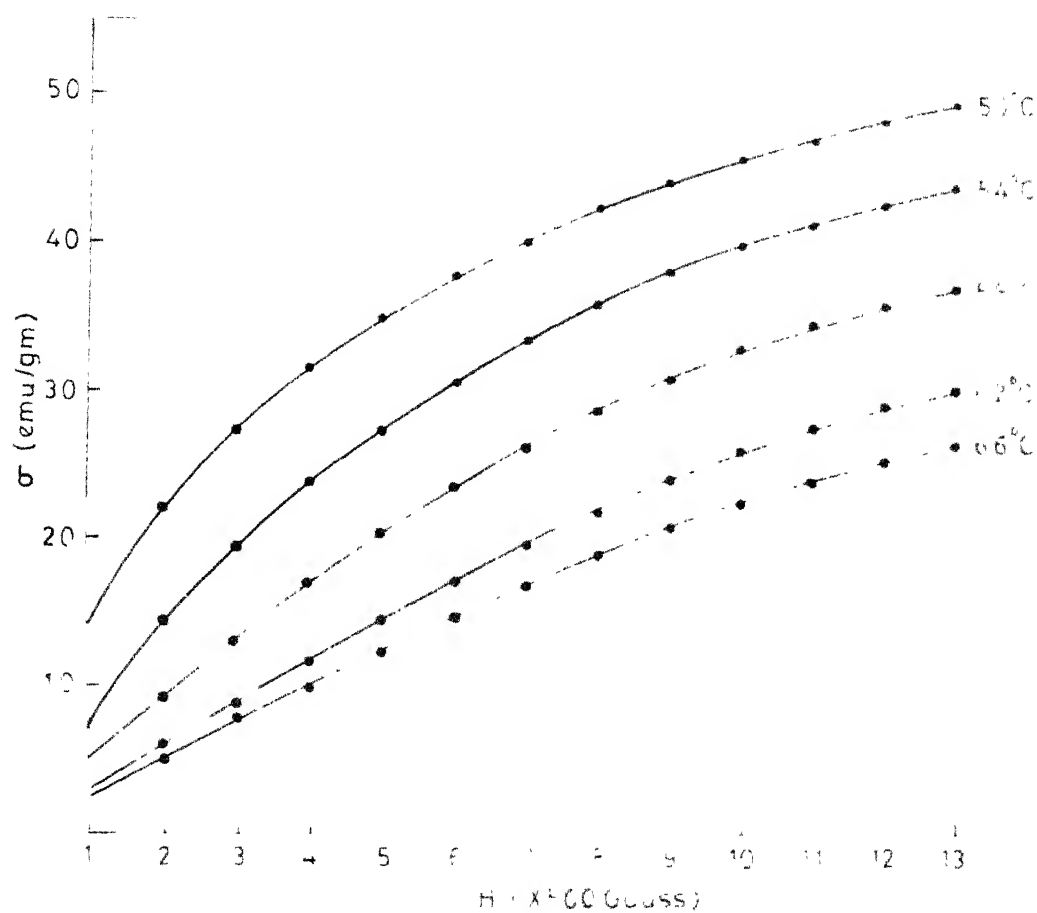


Fig 5.15  $\sigma$  vs  $H$  in the amorphous  $\text{Nd}_{3.5}\text{Fe}_{2.5}$  alloy (note the lack of saturation)

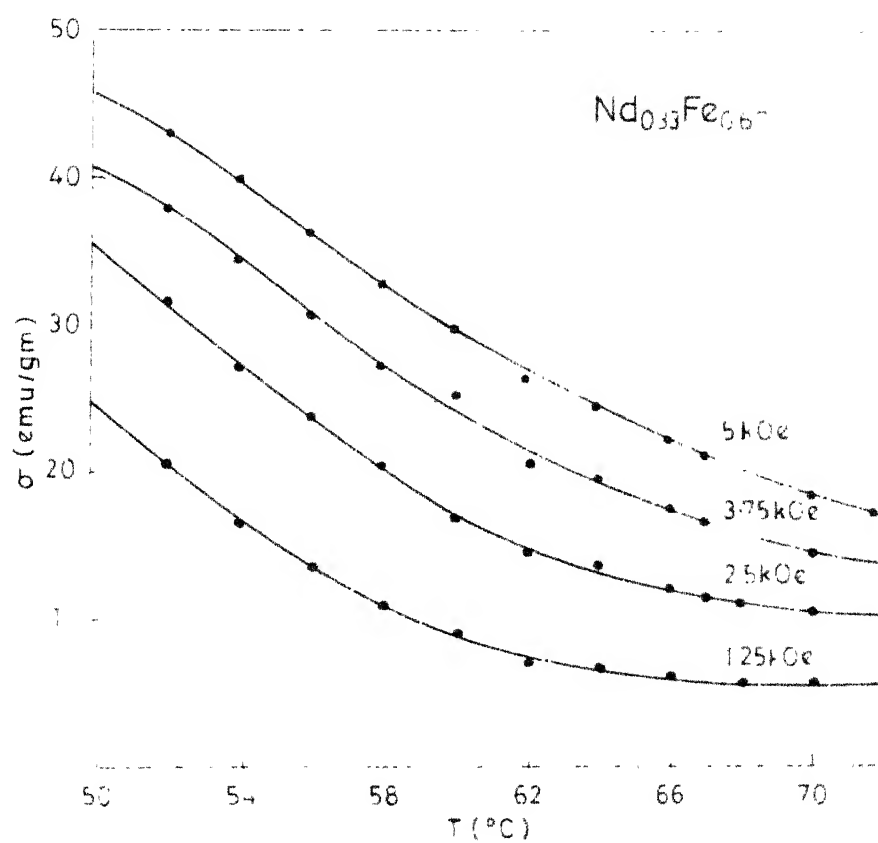


Fig 546 Temperature dependence of magnetisation at various values of the applied field in  $\text{Nd}_{0.33}\text{Fe}_{0.67}$  amorphous alloy

The isotherms near the temperature  $T_c$ , drawn with  $\sigma^2$  against  $\frac{H}{\sigma}$ , called the Arrotts plots, are shown in Fig. 5.17. Beyond 2 KGauss the Arrott plots are straight lines showing that the relation  $H/\sigma = \alpha + \beta\sigma^2$  is very closely followed. The slope of these straight lines give  $\frac{1}{\beta}$  and the intercept on the  $\sigma^2$  axis gives  $-\frac{\alpha}{\beta}$ , where  $\alpha$  and  $\beta$  are called the thermodynamic coefficients. The transition temperature is that where the thermodynamic coefficient  $\alpha$ , changes sign and passes through zero (Fig. 5.18). The transition temperature ( $T_c$ ) obtained by this method is 322 K, which is less than that obtained from the  $\frac{d\sigma}{dT}$  vs T curve by about 10 K.

The  $^{57}\text{Fe}$  Mössbauer spectra at different temperatures of the amorphous  $\text{Nd}_{0.33}\text{Fe}_{0.67}$  alloy is shown in Fig. 5.19. The spectrum is typical of the amorphous structure where the line width goes on increasing as we go from the centre of the spectrum. The spectra was recorded from 90 K to 473 K. The data were analysed by a least square fit with Lorentzian line shape and also with the field distribution programmes developed by the author. From 315 K up wards the spectrum shows the presence of both magnetic hyperfine splitting and quadrupole splitting superposed. The Mössbauer parameters obtained at various temperature upto 320 K are shown in Table 5.5. The hyperfine field distribution  $P(H)$  clearly shows the presence of two distinct environments for the Fe ion with two different values for the mean field  $\bar{H}$ . The average  $H_{hf}$  varies from 317(1) KOe at 90 K to 109(3) KOe at 320 K and the corresponding



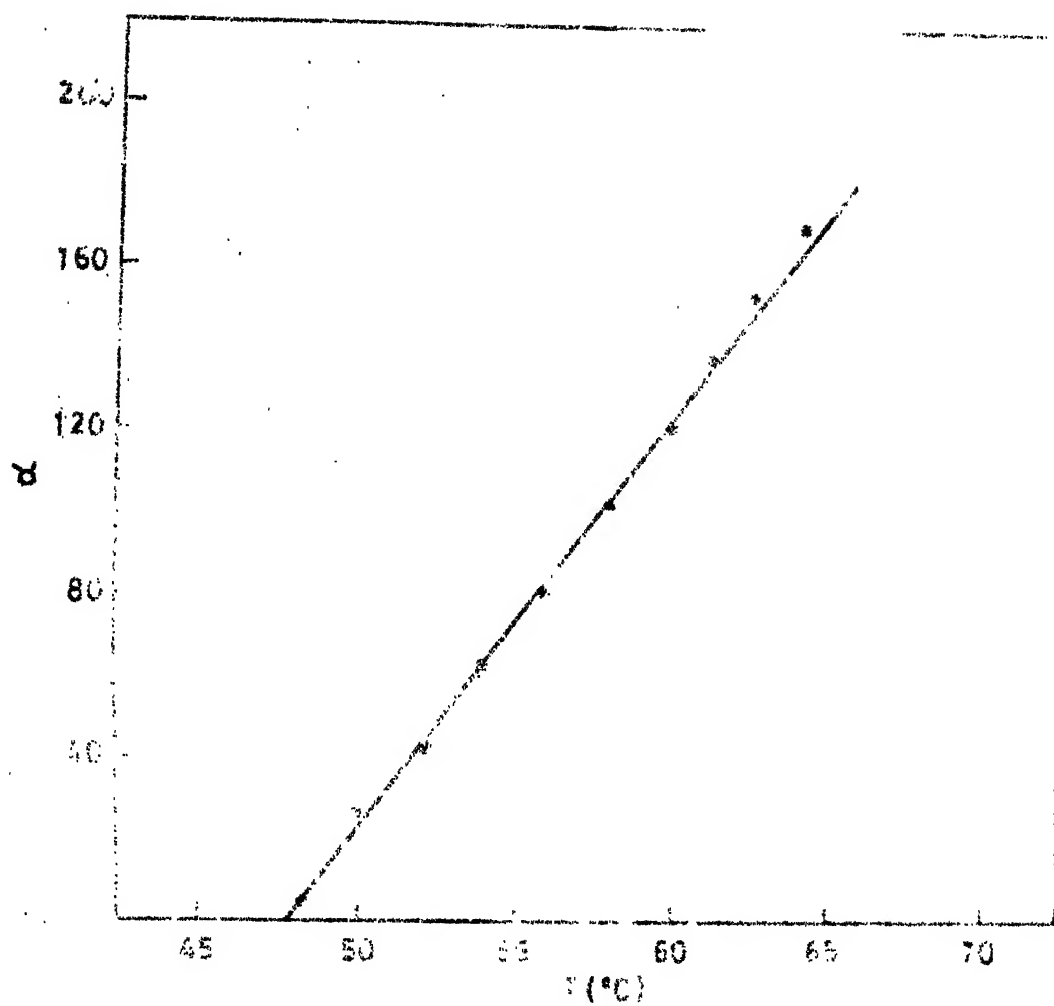


Fig.5-18 Variation of thermodynamic coefficient  $\alpha$  with temperature in the amorphous  $\text{Ni}_{33}\text{Fe}_{67}$  alloy

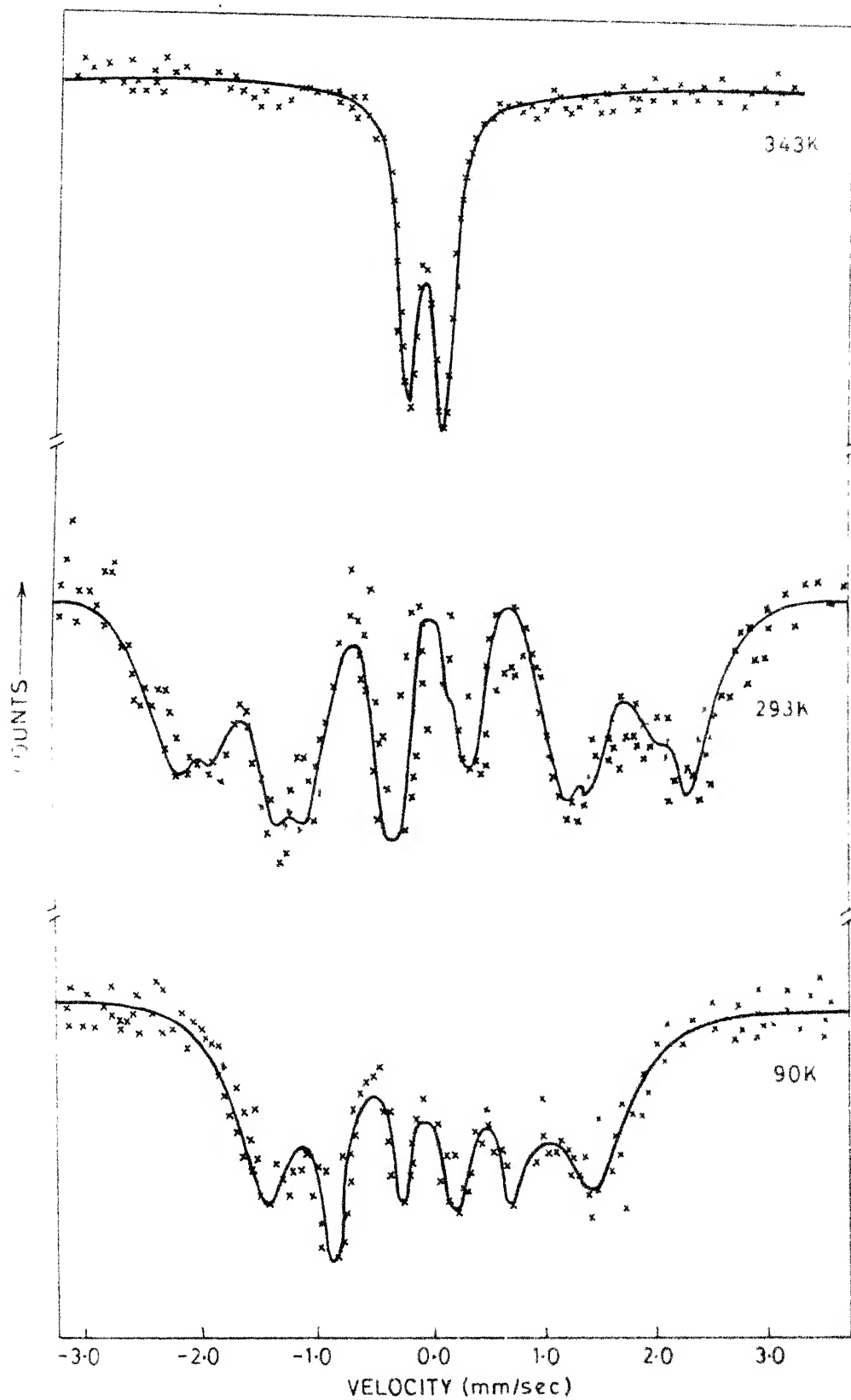


Fig 5-19 Mössbauer spectra of amorphous  $\text{Nd}_{33}\text{Fe}_{67}$  alloy at different temperatures

TABLE 5.5

Observed Mössbauer parameters of the ferromagnetic phase of  $\text{Nd}_{0.33}\text{Fe}_{0.67}$  amorphous alloy.

Temperature K	$H_{\text{eff}}$	Isomer Shift <sup>*</sup> (mm/sec)	Q.S. (mm/sec)
90	317(1)	0.29 (1)	0.273(8)
159	279(2)	0.074(9)	0.356(9)
168	267(2)	0.132(8)	0.50 (1)
216	261(3)	0.050 (1)	0.26 (1)
222	251(2)	0.050(1)	0.24 (1)
293	173(3)	-0.087(9)	0.174(8)
306	155(2)	-0.11 (1)	0.26 (1)
320	109(3)	-0.13 (1)	-

<sup>\*</sup>With respect to iron metal.

isomer shift change from + 0.29(1) to -0.13(1) (with respect to iron metal) as the temperature is increased in the above range. Figure 5.20 shows the variation of  $H_{\text{eff}}$  with temperature in  $\text{Nd}_{0.33}\text{Fe}_{0.67}$ . The value of  $H_{\text{eff}}(0)$  obtained by extrapolation to zero degree Kelvin is 320 KOe and the value of  $T_c$  obtained from this curve for  $H_{\text{eff}}$  to be zero is 345 K. The hyperfine field distributions at various temperatures are shown in Fig. 5.21. The values of  $\bar{H}$  (mean field and the full width at half maximum of the  $P(H)$  distribution ( $\Delta H$ ) are shown in Table 5.6.

In the paramagnetic phase  $\text{Nd}_{0.33}\text{Fe}_{0.67}$  amorphous alloy shows quadrupole splitting with well defined peaks. The quadrupole splitting at 333 K is 0.66 mm/sec with an isomer shift of -0.13 mm/sec with respect to iron metal. The quadrupole splitting and the corresponding isomer shift obtained at various temperatures is shown in Table 5.7. The variation of quadrupole splitting with temperature obeys the empirical relation

$$Q.S.(T) = K(1 - B T^{3/2})$$

as can be seen from the Fig. 5.22. The value of the slope parameter obtained from this graph is  $6.93 \times 10^{-5} \text{ K}^{-3/2}$ .

The iron moment  $\mu_{\text{Fe}}$  in the amorphous  $\text{Nd}_{0.33}\text{Fe}_{0.67}$  alloy using the relation by Gubbens et al. [37,35] is  $\mu_{\text{Fe}} = \frac{H_{\text{eff}}}{1.5}$  is  $2.17 \mu_B$ .

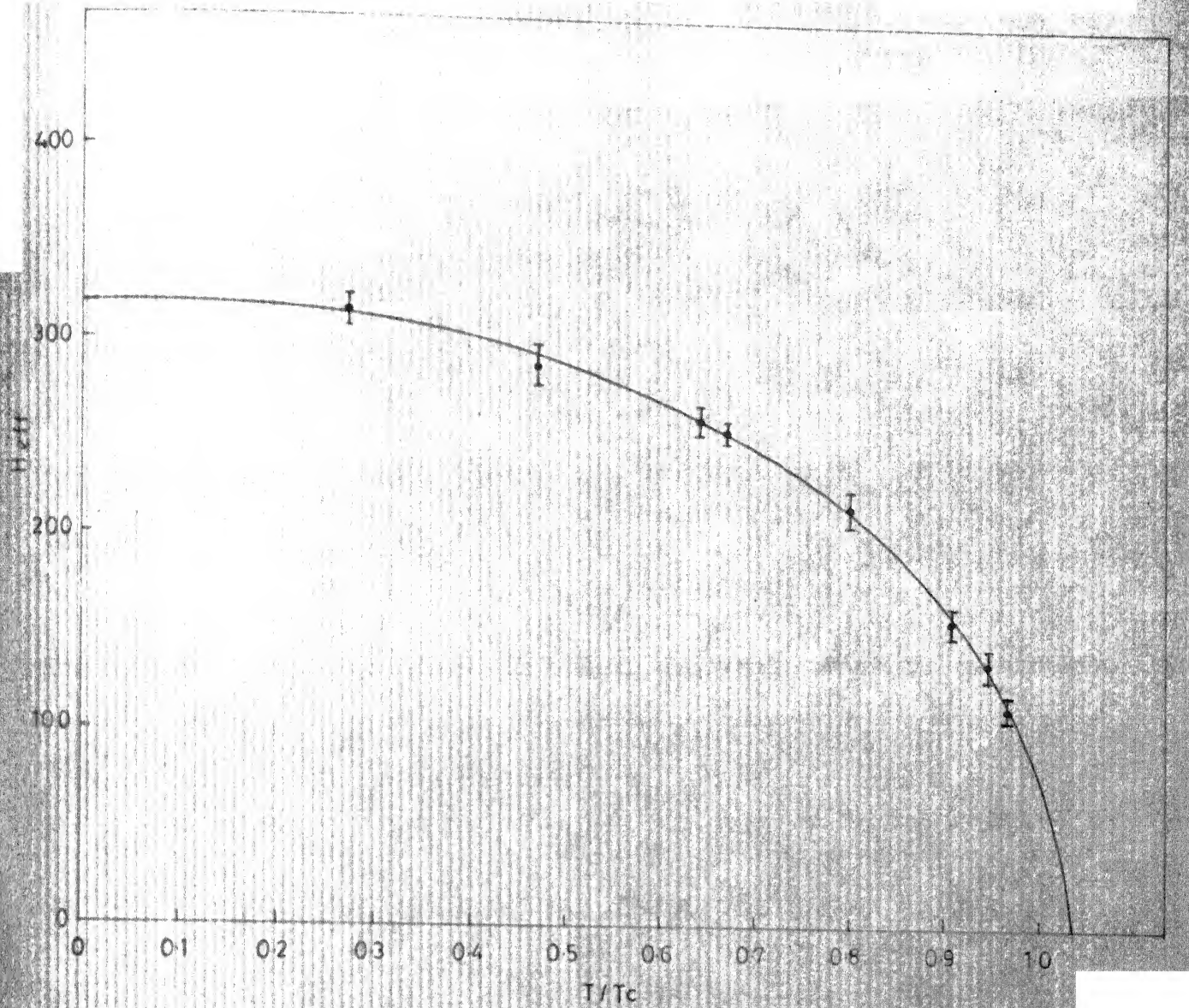


Fig.5-20 Variation of  $H_{eff}$  with  $T/T_c$  in the amorphous  $Nd_{33}Fe_{67}$  alloy

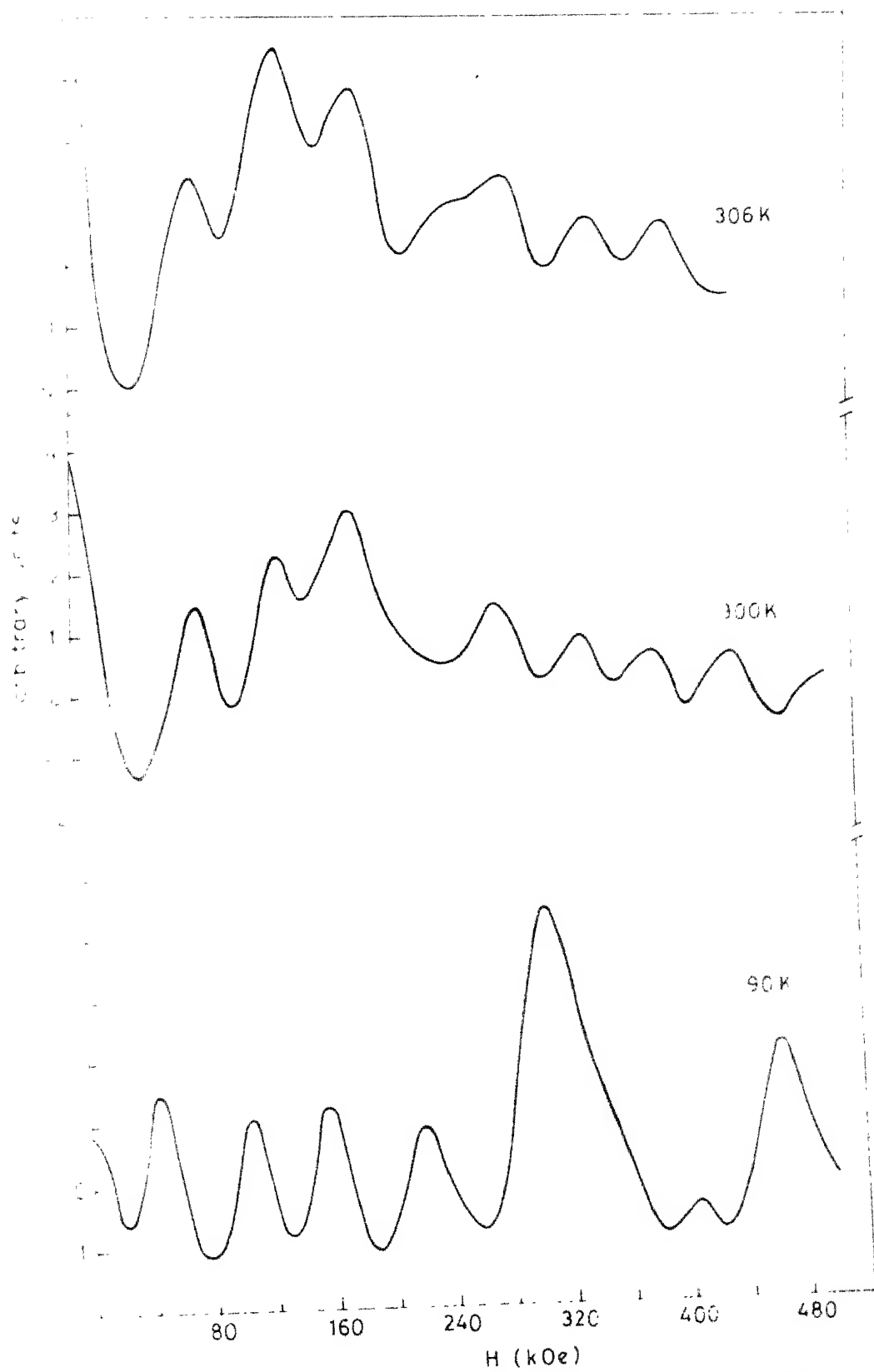


Fig 5.21 Hyperfine field distribution in amorphous  $\text{Nd}_{33}\text{Fe}_{67}$

TABLE 5.6

Temperature dependence of the most probable field ( $H_{\text{eff}}$ )  
 mean fields ( $\bar{H}$ ) and FWHM ( $\Delta H$ ) of the hyperfine field  
 distribution in  $\text{Nd}_{.33}\text{Fe}_{0.67}$  amorphous alloy.

Temperature K	$H_{\text{eff}}$ kOe	$\bar{H}_1$ kOe	$\bar{H}_2$ kOe	$\Delta H_1$ kOe
90	317	306	-	45
159	279	299	240	56
168	267	299	247	42
216	261	259	225	60
222	251	257	223	50
293	174	188	140	35
306	155	135	-	34
315	139	128	-	48

TABLE 5.7

Quadrupole splitting and isomer shift in the paramagnetic phase of  $\text{Nd}_{0.33}\text{Fe}_{0.67}$  amorphous alloy.

Temperature K	Q.S. (mm/sec)	Isomer Shift <sup>*</sup> (mm/sec)
325	0.672 (8)	0.15 (1)
333	0.662 (6)	0.13 (1)
343	0.64 (1)	0.12 (1)
363	0.609 (9)	0.116(8)
423	0.53 (1)	0.11 (1)
473	0.45 (1)	-

<sup>\*</sup>With respect to iron metal.



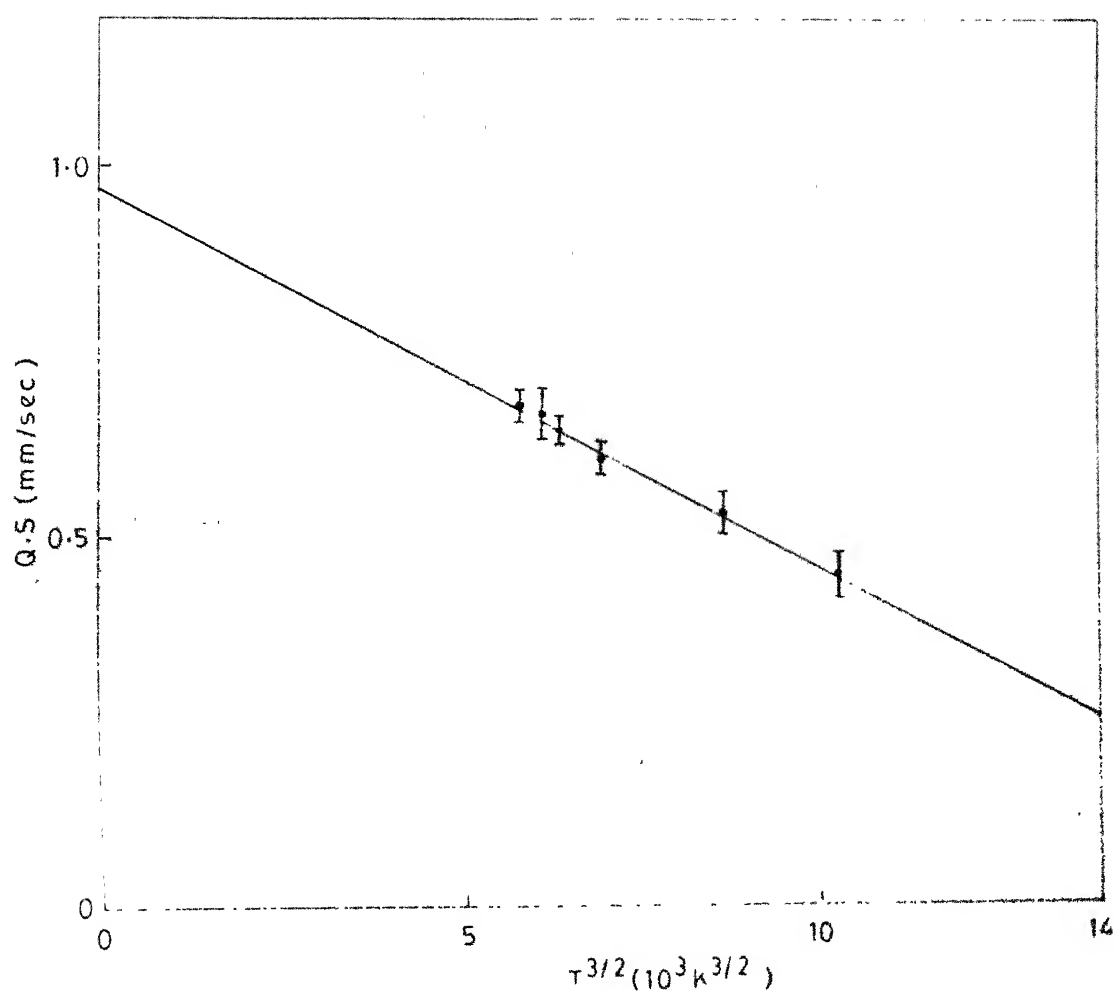


Fig 5.22 Quadrupole splitting in paramagnetic  $Nd_{33}Fe_{67}$  ; plotted against the corresponding  $T^{3/2}$

## (b) Discussions

The  $RFe_2$  systems are generally ferrimagnets. The magnetisation measurements provide the global moment of a domain which is the sum of the net moments of the sublattices. On the other hand Mössbauer measurements provides the net moment of the sublattice which depends on the magnitude and distribution in the direction of the individual atomic moments.

In the crystalline phase R is aligned antiparallel to Fe. In the amorphous phase there is still antiparallel exchange between R and Fe, and there are also negative Fe-Fe bonds and the  $R-R$  coupling. Competition between these two produces disorder and non-saturation and produces a random ferrimagnet or from Coey's classification [29] a speromagnet ( Mössbauer spectra shows spatial isotropy in distribution ).

Another specific characteristic of the amorphous R-Fe alloys is that it shows a strong dependence on the size of R on  $H_{hf}$ . Fig. 5.23 shows  $H_{hf}$  as a function of the atomic radius of the R-atom. The solid circles are data taken from Ref. [38]. The open circles are points for other R-Fe alloys. In these cases the contributions to  $H_{hf}$  is from the magnetic nature of the R-element such as core polarisation and dipolar terms because of the non zero value for the DGF. Whereas for Lu, Y and La the DGF = 0. Even then the trend is obeyed by these alloys also.

The finite quadrupole interaction in the paramagnetic state of amorphous R-Fe systems are observed earlier also [39].

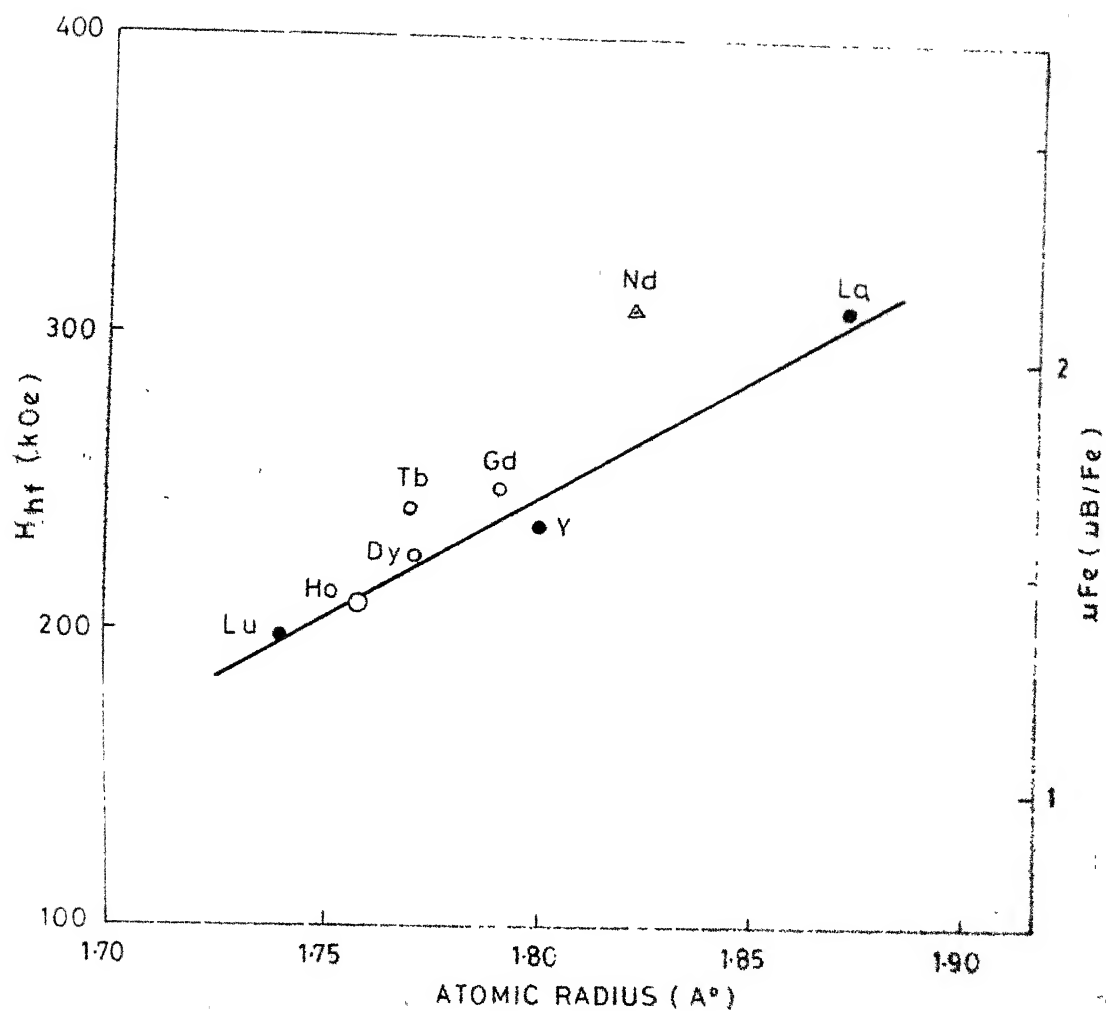


Fig.5.23 Dependence of  $H_{hf}$  at the Fe site upon the size of R

Our measurements also shows the evidence for a non zero EFG at the Fe sites. The presence of a quadrupole interaction in the magnetic state shows strong local anisotropy at the Fe site.

If the material has a common ordering temperature for all ions and if the temperature dependence of the hyperfine field for all ions is identical then  $\bar{H}$  should follow this temperature dependence and  $\Delta H$  should decrease monotonically as one goes from low temperature to  $T_c$ . Tomiyoshi et al. [40] have shown that the thermal average  $\langle \mu \rangle$  of the magnetic moments on which the weaker exchange field is acting decreases more rapidly with increase of temperature than the one with the stronger exchange fields. Therefore if the exchange field has local fluctuations at various lattice sites, the reduced magnetisation has a broad distribution at high temperature and also different ions may have hyperfine fields that show quite different temperature dependence and there will be a distribution of Curie temperatures in the system which is observed in the case of the  $\text{Nd}_{0.33}\text{Fe}_{0.67}$  amorphous system.

The distribution of EFG is evidenced by the  $P(|V|)$  distribution shown in Fig. 5.24. The distribution is broad near the transition temperature and goes on decreasing with increase of temperature since more and more Fe atoms comes to the paramagnetic state as the temperature is increased.

#### 5.3.4 Conclusion

The magnetic properties of R-Fe alloys are quite varied and sensitive to the variation of temperature and other

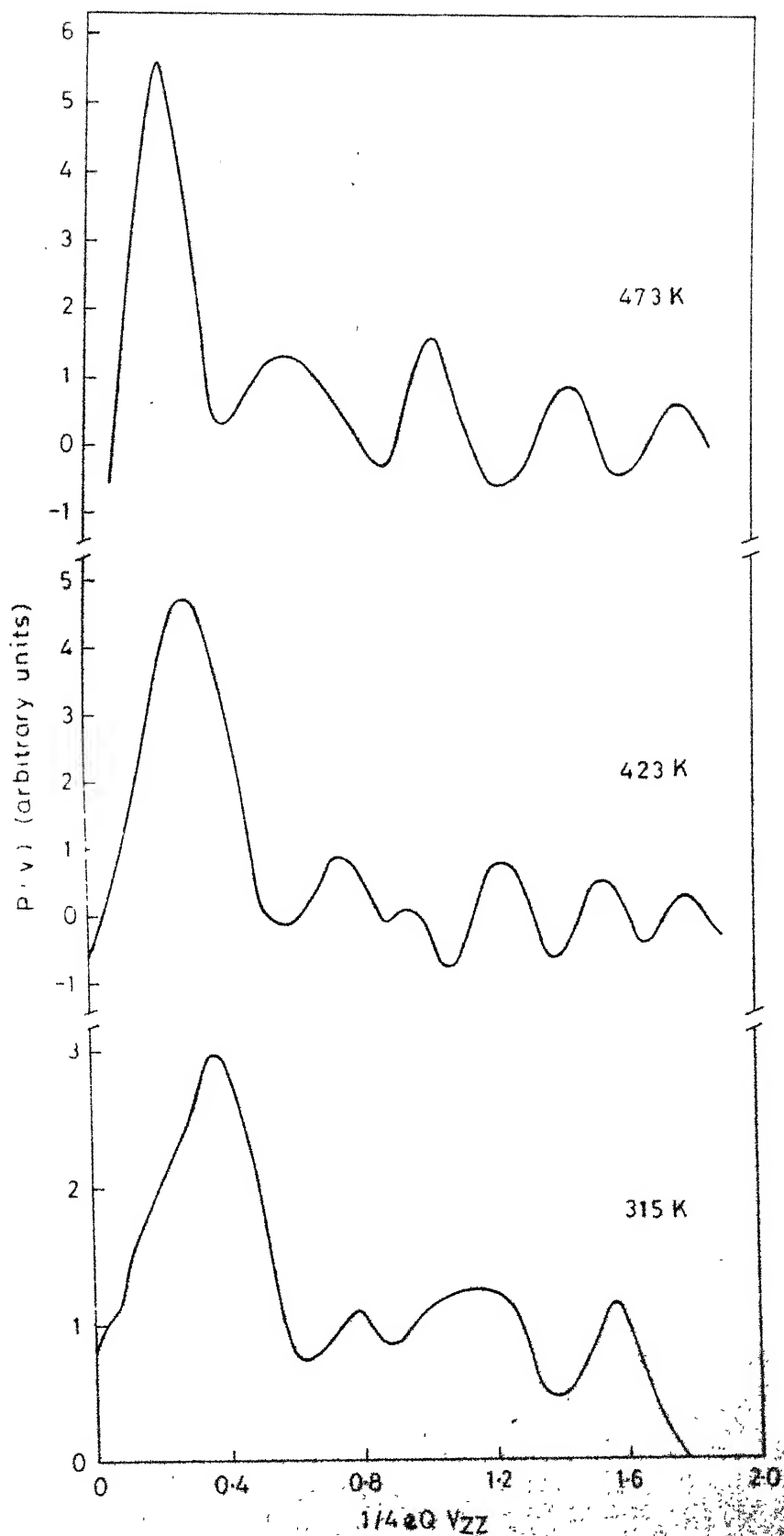


Fig. 5.24 EFG distribution in paramagnetic  $\text{Nd}_{33}\text{Fe}_{67}$  amorphous alloy

parameters. Mössbauer spectroscopy can be used as a tool to probe into these amorphous systems to determine the individual magnetic moments. The study of an amorphous system also leads to a critical re-examination of the role of lattice in crystalline solids in the structural origin of hyperfine fields.

It is hoped that the present work has contributed to our knowledge on the systematics of hyperfine interactions in metals, alloys and compounds and has helped bring us closer to the understanding of the origin of the hyperfine fields.

REFERENCES

- [1] F.E. Fujita, Supplement of Sci. Rep. RITU, A28, 1, (1980).
- [2] D.S. Boudreau, Phys. Rev. B18, 4038 (1978).
- [3] U. Gonser, M. Gafari and H.G. Wagner, J. Magn. Magn. Mat. 8, 175 (1978).
- [4] T. Kemeny, I. Vincze, B. Fogarassy and S. Arajcs, Phys. Rev. B20, 476 (1979).
- [5] P. Chaudhari, J.J. Cuomo and R.J. Gambino, IBM J. Res. Dev. 11, 66 (1973).
- [6] Y. Minura, N. Inamura, T. Kobayashi, A. Okada, and Y. Kushiro, J. Appl. Phys. 49, 1208 (1978).
- [7] D.P. Dunne and C.M. Wayman, Met. Trans. 4, 137 (1973).
- [8] R. Hultgren and C.A. Zapffe, Nature 142, 395 (1938).
- [9] T. Sohumura, R. Oshima and F.E. Fujita, Scripta Met. 14, 855 (1980).
- [10] M. Hirabayashi and S. Weissmann, Acta Met. 10, 25 (1962).
- [11] C. Zener, 'Phase Stability in Metals and Alloys', Editors, P.S. Rudman, J. Strenger and R.I. Jaffee, McGraw Hill (1967).
- [12] Masaaki Matsui, Hajime Yamada and K. Adachi, J. Phys. Soc. Japan 48, 2161 (1980).
- [13] B. Window, J. Phys. E. Sci. Instr. 4, 401 (1971).
- [14] M. Matsui, T. Shimizu, H. Yamada and K. Adachi, J. Magn. Magn. Mat. 15, 1201 (1980).

- [15] S. Hoth, W. Engel, R. Keitel, W. Klinger, R. Seebock and W. Witthuhn, Z. Phys. B41, 99 (1981).
- [16] B. Window, J. Phys. F (Metal Phys.) 4, 329 (1974).
- [17] R. Nemanich, C.W. Kimball, B.D. Dunlap and A.T. Aldred, Phys. Rev. B16 , 124 (1977).
- [18] S. Tomiyoshi, H. Yamamoto and H. Watanabe, J. Phys. Soc. Japan 30, 1605 (1971).
- [19] J. Chappert, J. Physique Colloq. 40, C<sub>2</sub>-107 (1979).
- [20] K.H.J. Buschow, Rep. Prog. Phys. 40, 1179 (1977).
- [21] C. Meyer, F. Hartmann-Boutron, Y. Gros, Y. Berthier, J. Physique 42, 605 (1981).
- [22] J. Rhyne, S. Pickart, and H. Alperin, Phys. Rev. Lett. 29, 1962 (1972).
- [23] R. Harris, M. Plischke and M.J. Zuckermann, Phys. Rev. Lett. 31, 160 (1973).
- [24] K. Lee and N. Heiman, AIP Conf. Prog. 24, 108 (1974).
- [25] N. Heimann, K. Lee and R. Potter, AIP Conf. Proc. 29, 130 (1976).
- [26] J. Rhyne, AIP Conf. Proc. 29, 182 (1976).
- [27] N. Heiman and K. Lee, AIP Conf. Proc. 34, 319 (1976).
- [28] J.R. Cullen, G. Blessing, S. Rinaldi and E. Callen, J. Magn. Magn. Mat. 7, 160 (1978).
- [29] J. Coey, J. Appl. Phys. 49, 1646 (1978).
- [30] J. Chappert, R. Arrese-Boggiano, J.M.D. Coey, A. Lienard J.P. Reboullat. J. Physique Colloq. 37, C6-771 (1976).



- [31] L.J. Tao, S. Kirkpatrick, R.J. Gambino and J.J. Cuomo, Solid State Commun. 13, 1491 (1973).
- [32] A.E. Clark, Appl. Phys. Lett. 23, 642 (1973).
- [33] J.J. Croat, Appl. Phys. Lett. 37, 1096 (1980).
- [34] J.J. Croat, J. Appl. Phys. 52, 2509 (1981).
- [35] K.H.J. Buschow, A.M. Van der Kraan, J. Magn. Magn. Mat. 22, 220 (1981).
- [36] S.M. Bhagat, M. Meichle and M.B. Salamon, 23rd Conf. on Magn. and Magn. Mat., Minneapolis, Minnesota (1977) p. 8.
- [37] P. Gubbens, J. Van Apeldorn, A. Van der Kraan, and K. Buschow, J. Phys. F4, 921 (1974).
- [38] N. Heiman and N. Kazama, Phys. Rev. B19, 1623 (1979).
- [39] D.W. Forester, W.P. Papa and R. Segnan in "'Amorphous Magnetism'", Eds. R.A. Levy and R. Hasegawa (Plenum Press (1977))p. 135.
- [40] S. Tomiyoshi, H. Yamamoto and H. Watanabe, J. Phys. Soc. Japan 30, 1605 (1971).
- [41] F.A. Shunk in "'Constitution of Binary Alloys'", McGraw Hill (1969).

## PUBLICATIONS

1. Mössbauer studies of  $\text{FeSO}_4 \cdot 7\text{H}_2\text{O}$  and  $\text{Fe}(\text{SO}_4)_2 \cdot (\text{NH}_4)_2 \cdot 6\text{H}_2\text{O}$  under applied electric field.  
N.V. Nair and D.C. Khan, Phys. Rev. B, 1st Nov. 1981 (Rapid Communications).
2. A miniature furnace for Mössbauer measurements at high temperatures.  
N.V. Nair and D.C. Khan (Communicated to Nucl. Instr. and Methods).
3. Electric field gradient and isomer shift distributions from Mössbauer spectra.  
N.V. Nair and D.C. Khan (Communicated to Phys. Rev. B).
4. Mössbauer and magnetisation studies of  $\text{Nd}_{0.33}\text{Fe}_{0.67}$  alloy.  
**N.V. Nair and D.C. Khan**  
(Communicated to International Conference on the applications of Mössbauer effect, Jaipur, India (1981)).
5. Quadrupole interaction at  $^{57}\text{Fe}$  in titanium metal.  
N.V. Nair and D.C. Khan (Communicated to Nuclear Physics and Solid State Symposium, India (December 1981)).
6. Mössbauer studies of zirconium iron alloys.  
B.M. Lal, N.V. Nair, S.N. Gupta and H.C. Verma  
(Communicated to Nuclear Physics and Solid State Symposium, India (Dec. 1981)).
7. Recoilless fraction measurements in  $^{57}\text{FeTe}$ .  
N.V. Nair and H.C. Verma (Communicated to International Conference on the applications of Mössbauer effect, Jaipur India (1981)).

CENTRAL LIBRARY

Acc. No. A-8271A

PHY-1981-D-NAI-MOS